DYNAMICAL MODELS OF WINDS FROM ROTATING HOT STARS

by

Steven Robert Cranmer

A dissertation submitted to the Faculty of the University of Delaware in partial fulfillment of the requirements for the degree of Doctor of Philosophy in Physics

Fall 1996

DYNAMICAL MODELS OF WINDS FROM ROTATING HOT STARS

by

Steven Robert Cranmer

Approved: _____

Henry R. Glyde, Ph.D.
Chairman of the Department of Physics and Astronomy

Approved: _____

John C. Cavanaugh, Ph.D.
Interim Associate Provost for Graduate Studies

I certify that I have read this dissertation and that in my opinion it meets the academic and professional standard required by the University as a dissertation for the degree of Doctor of Philosophy.

Signed: _____

Stanley P. Owocki, Ph.D.
Professor in charge of dissertation

I certify that I have read this dissertation and that in my opinion it meets the academic and professional standard required by the University as a dissertation for the degree of Doctor of Philosophy.

Signed: _____

James MacDonald, Ph.D.
Member of dissertation committee

I certify that I have read this dissertation and that in my opinion it meets the academic and professional standard required by the University as a dissertation for the degree of Doctor of Philosophy.

Signed: _____

Derck Massa, Ph.D.
Member of dissertation committee

I certify that I have read this dissertation and that in my opinion it meets the academic and professional standard required by the University as a dissertation for the degree of Doctor of Philosophy.

Signed: _____

David Seckel, Ph.D.
Member of dissertation committee

I certify that I have read this dissertation and that in my opinion it meets the academic and professional standard required by the University as a dissertation for the degree of Doctor of Philosophy.

Signed: _____

Gary Zank, Ph.D.
Member of dissertation committee

ACKNOWLEDGEMENTS

First and foremost I would like to express my gratitude to my advisor and friend, Dr. Stanley Owocki, for essential guidance and insight throughout my graduate career. More than anyone else, his influence has contributed to my development as a scientist.

Sincere appreciation is due to Dr. Alex Fullerton and Dr. Kenneth Gayley, who have enlarged my sphere of understanding of astrophysics with their fresh perspectives. I also wish to thank Dr. James MacDonald, Dr. Derck Massa, Dr. David Seckel, and Dr. Gary Zank for taking the time to serve on my thesis committee and also for many useful conversations. I am also indebted to Dr. George Collins and Dr. Dermott Mullan for their helpful advice, original ideas, and encyclopaedic knowledge.

Additionally, I thank everyone at the Bartol Research Institute for the unique and stimulating environment they have provided, and most notably: Nick Arge, Dr. Steve Barr, Sujit Basu, Dave Huber, Dave McKenzie, Dr. Louis Pauls, Dr. Todd Story, and Dr. Lance Williams. I am especially grateful to Dr. Norman Ness, the NASA Space Grant Committee, and the NASA Graduate Student Researchers Program for making my work at Bartol possible.

Needless to say, my family deserves a great deal of credit for my development. I thank my mother Patricia and my father Roy for all their love and support. Finally, I offer my most genuine thanks to my wife Janet, whose unwavering compassion, faith, and love carries me through life.

TABLE OF CONTENTS

LIST OF FIGURES

LIST OF TABLES

ABSTRACT

The hottest and most massive stars (spectral types O, B, Wolf-Rayet) have strong stellar winds that are believed to be driven by line scattering of the star's continuum radiation field. The atmospheres and winds of many hot stars exhibit the effects of rapid rotation, pulsation, and possibly surface magnetic fields, inferred from observations of ultraviolet spectral lines and polarization. The complex time variability in these observations is not yet well understood. The purpose of this dissertation is to model the dynamics of winds around rotating hot stars and synthesize theoretical observational diagnostics to compare with actual data.

Before dealing with rotation, however, we derive the theory of radiative driving of stellar winds, and uncover several new useful aspects of the theory for spherical, nonrotating stars. The presence of *limb darkening* of the stellar radiation is found to be able to increase the mass flux $\dot{M}$ by 10–15% over standard models assuming a uniformly-bright star, and the wind's asymptotic terminal velocity v_∞ should decrease by the same amount. We also introduce a new approximation method for estimating the terminal velocity, which is both conceptually simpler and more physically transparent than existing approximation algorithms. Finally, from theoretical line profile modeling we find that observational determinations of v_∞ may be underestimated by several hundred km s^{-1} if *unsaturated* P Cygni lines are used.

Rotation affects a star by introducing centrifugal and Coriolis forces, decreasing the effective gravity and making the star oblate. This in turn redistributes the emerging radiative flux to preferentially heat the stellar poles, an effect known as *gravity darkening.* Although previous models have computed the increase in equatorial mass flux due to the lower effective gravity there, none have incorporated gravity darkening. We find that the brighter (darker) flux from the poles (equator) has a much stronger impact on the mass flux, increasing (decreasing) the mass loss and local wind density. This, in addition to the existence of *nonradial* radiation forces from a rotating star, which tend to point latitudinally away from the equator and azimuthally opposite the rotation, produces a net *poleward* deflection of wind streamlines. This is contrary to the "wind compressed disk" model of Bjorkman

and Cassinelli, and also seems incompatible with observational inferences of equatorial density enhancements in some systems. This work is ongoing, and we are endeavoring to include all the relevant physics in hydrodynamical simulations.

We also dynamically model spectral-line *time variability* by inducing corotating nonaxisymmetric structure in the equatorial plane of a hot-star wind. By varying the radiation force over localized "star spots," the wind develops fast and slow streams which collide to form corotating interaction regions (CIRs) similar to those in the solar wind. We synthesize P Cygni type line profiles for a stationary observer, and find that "discrete absorption components" (DACs) accelerate slowly through the profiles as complex nonlinear structures rotate in front of the star. We also examine the photospheric origin of such variability, in a preliminary manner, by deriving the theory of stellar pulsations, waves, and discontinuities. Although most observed low-order pulsation modes are evanescently damped in the photosphere, we find that the presence of an accelerating wind can allow waves of *all* frequencies to propagate radially. We thus make a first attempt at outlining the possible "photospheric connection" between interior and wind variability that observations are beginning to confirm.

Chapter 1

INTRODUCTION

Every man and every woman is a star.

Every number is infinite; there is no difference.

E. A. Crowley, *Liber A.L. vel Legis*

All stars possess expanding outer atmospheres known as *stellar winds.* This continual mass loss has a significant impact on stellar evolution, the mass and energy balance of the interstellar medium, and even the overall chemical evolution of the Universe. Although the hottest and most luminous stars (spectral types O, B, A, and Wolf-Rayet) are rare, their strong winds play a dominant role in this interstellar and galactic "ecology." By studying the physical mechanisms driving these outflows, as well as their interaction with such stellar processes as rotation, pulsation, and magnetic fields, we are able to better understand the importance of stellar winds to astrophysics as a whole.

The subject of this work is the dynamical interaction between stellar winds, rotation, and pulsation. By synthesizing spectral line profiles from multidimensional hydrodynamical models of winds, we are able to test and compare various theories of time-variable and nonspherical outflow. This Chapter introduces the subject of winds from early-type stars by discussing their astrophysical importance (Section 1.1), providing a brief historical review of the observation of stellar winds (Section 1.2), and outlining the research presented in the remainder of this dissertation (Section 1.3).

1.1 Motivation for Hot Star Wind Research

It is worthwhile to examine briefly how the study of winds from hot stars fits into the broader aims of astronomy. On the largest scale, each generation of

stars contributes significantly to the chemical enrichment of its host galaxy. Stellar winds and supernova explosions release heavy elements that were produced by nucleosynthesis in the cores of stars, and the most massive ($M_* \approx 10$–$100\,M_\odot$) and luminous ($L_* \approx 10^4$–$10^6\,L_\odot$) stars, known historically as "early-type," lose mass at a rate of $\dot{M} \approx 10^{-7}$ to 10^{-4} solar masses per year. This implies that a substantial fraction of the star's initial mass can be dispersed during its main sequence lifetime. Maeder (1981) and Abbott (1982b) found that the effect of hot-star winds must be included to accurately model observed He, C, and O mass fractions in the interstellar medium. The high ^{22}Ne/^{20}Ne ratio observed in Galactic cosmic rays has been attributed to the predicted overabundance of ^{22}Ne in the winds of Wolf-Rayet stars (Casse & Paul 1982). Even the overall ionization state of the Galaxy is strongly influenced by wind-dominated H II regions around O stars (Miller & Cox 1993). The details of stellar mass loss are thus quite important to theories of galactic chemistry, structure, and evolution.

On smaller scales, stellar winds strongly affect the mass and energy balance of the interstellar medium in their immediate vicinity. The massive, but short-lived winds from pre-main sequence stars can disrupt the surrounding dense molecular cloud and induce additional star formation. The fast winds from hot main sequence stars and supergiants plow through the interstellar medium and evacuate "bubbles" of rarefied gas (Weaver et al. 1977) which also affect surrounding ionized H II regions (e.g., Yorke 1986). Even the comparatively feeble solar wind, with $\dot{M} \approx 10^{-14}\,M_\odot \mathrm{yr}^{-1}$, leaves its mark on the local interstellar medium (Holzer 1989).

As stars evolve, their mass loss usually increases dramatically. Low-mass stars are believed to form planetary nebulae by ejecting, and subsequently ionizing, the extended envelope of their red supergiant stage (Shklovskij 1956). More massive stars can evolve into luminous blue variables (LBVs), which can expel mass in episodic bursts of up to 1–2 $M_\odot$, or Wolf-Rayet stars, which are inferred to lose up to $\sim 10^{-4}\,M_\odot \mathrm{yr}^{-1}$ (see, e.g., Langer et al. 1994), before eventually becoming supernovae. The massive stellar ejecta associated with these stages of evolution often form observable emission nebulae which provide invaluable diagnostics of the history and dynamics of the star's evolution (Dorland & Montmerle 1987; Marston 1995; Garcia-Segura et al. 1996).

Mass loss also strongly affects the evolution of the stars themselves. Chiosi & Maeder (1986) review how stellar winds influence the internal structure, evolutionary tracks, and ultimate fate of massive stars. Main sequence lifetimes are somewhat longer when mass loss is taken into account, mainly because the progressive reduction of the star's mass reduces the mass of the convective core and decreases the luminosity. Whether a star evolves into a blue or red supergiant, an LBV, or a Wolf-Rayet star sensitively depends on the wind's history, but the more

advanced and rapid stages of nuclear burning are less dependent on the dynamics of the outer envelope. Note also that mass loss in close binary systems has another consequence: accretion onto the companion. Some types of binaries (e.g., "semidetached" systems such as Algol or β Lyrae) undergo several evolutionary phases of mass transfer, and winds can be an important part of the overall budget of available circumstellar matter (Eggleton & Pringle 1985; De Greve 1986; Mazzali 1990).

Knowledge about the theoretical mechanisms of stellar wind driving, combined with detailed spectrum synthesis techniques, leads to valuable diagnostics of fundamental stellar parameters: mass, radius, luminosity, and elemental abundance. Such "quantitative spectroscopy" of hot stars is discussed by Kudritzki & Hummer (1990), and has been found to be a highly reliable means of determining these quantities for large samples of stars. This opens the way to using the winds of O, B, A, and Wolf-Rayet stars as standard candles to infer extragalactic distances (see, e.g., Kudritzki et al. 1992; McCarthy et al. 1995).

In addition to the above benefits of understanding hot-star winds to astronomy as a whole, there is another (perhaps more fundamental) reason to study these outflows: they serve as unique laboratories for *radiation hydrodynamics.* Although this term is often used in a broad sense to refer to the quite common situation where radiation affects the energy balance of a fluid (as in Mihalas & Mihalas 1984), here it applies more strictly to the case of photons imparting energy *and* momentum to the system. The physics involved in such coupling is relatively unexplored outside the field of hot-star winds, and we are just beginning to be able to apply results from these models to other luminous systems, such as protostellar jets, pulsars, and active galactic nuclei.

1.2 Overview of the Observations

1.2.1 The Existence of Stellar Winds

The first indirect observations of mass outflow from a star occurred in prehistory. When primitive peoples saw the crown-like solar corona during a total eclipse, and shimmering aurorae in the northern and southern skies, they were viewing the beginning and end points of the solar wind flow that intercepts the earth. Historical records of novae and supernovae also represent observations of dramatic bursts of mass loss from evolved stars, and some objects labeled as novae ("new" stars) were actually hot stars experiencing strong variability in their winds. In 1600, the luminous blue variable P Cygni first appeared as a second magnitude star, and Christian Huygens named it the *"Revenante of the Swan"* because of its ghostly variability (Allen 1899). Between 1830 and 1860, η Carinae experienced remarkable luminosity variations which we now interpret as characteristic of an episodic mass loss of 1–2

solar masses (see Humphreys & Davidson 1994).

However, the first scientific understanding of stellar winds came with the application of spectroscopy to starlight in the late nineteenth century. Many bright lines in the optical spectrum of P Cygni were observed to have redshifted emission peaks combined with blueshifted absorption troughs, and Beals (1929, 1931) interpreted this pattern in terms of continuous ejection of high-velocity material from various types of hot stars (see Section 3.1 for a quantitative derivation). Swings & Struve (1940) estimated the supersonic outflow velocities from several O, B, and LBV stars, and interpreted these as characteristic of an "expanding shell" several stellar radii from the photosphere. Adams & MacCormack (1935) and Deutsch (1956) identified narrow "P Cygni type" profiles in the cores of strong Fraunhofer lines from cool supergiants (spectral types G, K, M), and similarly inferred the presence of winds from these stars. Finally, the existence of a continuously outflowing *solar wind* was realized by Parker (1958, 1963), both from theoretical considerations and mounting observational evidence (see Hundhausen 1972 for a historical review), and was confirmed by *in situ* spacecraft experiments in the early 1960s (Brandt 1970; Ness 1987; Burlaga 1993).

Because stars hotter than $T_{\rm eff} \approx 9000\,{\rm K}$ (spectral type $\sim$A2) emit their peak radiation in ultraviolet, rather than optical wavelengths, it was not until the rocket ultraviolet observations of Morton (1967a, b) and Morton, Jenkins, & Brooks (1969) that the presence of strong winds from O and B supergiants was directly inferred. The broad P Cygni line profiles of, e.g., the C IV $\lambda\lambda$1548, 1551Å doublet indicate mass loss rates as high as 10^{-6}–$10^{-5}\,M_\odot{\rm yr}^{-1}$ and wind terminal velocities between 600 and 3500 km s^{-1}. Subsequent observations with the *Copernicus* and *IUE* satellites, as well as supporting radio, infrared, and X-ray measurements, have confirmed many details about the nature of winds around hot stars (Cassinelli 1979; Conti & Underhill 1988; Kudritzki & Hummer 1990; Moffat et al. 1994).

Early-type stars do not exhibit the strong sub-surface convection that is present in solar- and late-type stars, so there is negligible evidence for mechanically-heated chromospheres or ultra-hot ($T \approx 10^6$–$10^7\,{\rm K}$) coronae surrounding these objects. Thus, the high thermal pressure which drives the solar wind is not thought to be an important factor in hot-star wind dynamics. However, the relatively high luminosities of O, B, and Wolf-Rayet stars are of crucial importance to the dynamical and ionization states of the circumstellar gas. In this dissertation I will outline and derive the theory of *radiative driving* of stellar winds, i.e., of momentum transfer between the strong radiation field and the atoms and ions surrounding the star. This mechanism is presently believed to be the dominant cause of large-scale continuous mass outflow from all main sequence, giant, and supergiant stars hotter than spectral type $\sim$B5.

1.2.2 The Effects of Rotation

The study of rotating stars began with the telescopic discovery of sunspots, and their slow motion across the solar disk, by Galileo, Fabricius, and Scheiner in the early 1610s. However, the rotation of other stars was not thought to be detectable until Abney (1877) suggested that the Doppler effect could *broaden* stellar absorption lines from rotating stars. Wavelengths in the light coming from the approaching (receding) edge of the star are blueshifted (redshifted), and some of the weakest spectral lines may disappear below the threshold of detectability. Note that this Doppler broadening is affected only by the projected component of the star's equatorial rotation velocity $V_{\rm eq}$ in the line of sight of the observer. Thus, all that can be theoretically measured from this effect is the product $V_{\rm eq} \sin i$, where i is the inclination angle between the line of sight and the star's rotation axis. The Doppler effect interacts with stellar rotation in another manner in observations of eclipsing binary systems. During partial eclipses only one approaching or receding edge of the occulted star is visible, and the observed radial velocity shifts of spectral lines depart from their systemic values. Following the initial predictions of Holt (1893), Schlesinger (1909, 1910) and Rossiter (1924) confirmed this effect relatively independently.

The strong dynamical effect of *rapid* rotation was suspected when several early-type stars were measured to have projected rotational velocities of 200–400 km s^{-1}, in contrast to the relatively slow (about 2 km s^{-1}) equatorial rotation of the Sun. These extreme velocities, measured primarily in B-type binaries (Shajn & Struve 1929) and single stars (Struve 1930, 1931), are a significant fraction of the "critical" or Keplerian equatorial velocity, which occurs when the outward apparent centrifugal force balances gravity. The theory of the equilibrium form of rapidly rotating fluid bodies has been discussed since Newton's *Principia* (see Tassoul 1978), and the idea that centrally-condensed gaseous spheres will rotationally deform into *oblate* configurations was well-known when Struve (1931) applied it to stars with large $V_{\rm eq} \sin i$.

A distorted gaseous star in radiative and hydrostatic equilibrium exhibits a change in its net radiative flux which is proportional to the local gravity over its surface (von Zeipel 1924; Chandrasekhar 1933). Although this simple picture of "gravity darkening" is not completely time-steady (Eddington 1929; Sweet 1950) and does not take convection into account (see, however, Lucy 1967; Anderson & Shu 1977; Zhou & Leung 1990), it has been seen to provide reliable estimates for the flux variations from early type stars. Slettebak (1949) discussed the variation in effective temperature $T_{\rm eff}$ over the surface of rotationally distorted stars, and computed modified rotationally broadened line profiles. Further refinements in modeling the observable parameters from rapidly rotating stars are reviewed by Tassoul (1978),

but note the more recent work of Collins, Truax, & Cranmer (1991) and Collins & Truax (1995).

Stars of spectral type B which exhibit emission in hydrogen Balmer lines are known as *Be stars,* and this subclass has exercised a fascination over spectrographic observers since the nineteenth century. Be stars are among the fastest rotators, and Struve (1931) explained the strong emission in terms of a dense circumstellar disk ejected by a critically rotating "lens-shaped" star. However, it is now generally accepted that most Be stars are rotating at only 60–80% of their critical equatorial velocity (see Slettebak & Snow 1987), and thus some other mechanism is required to produce a dense disk. Like other O and B stars, the ultraviolet spectral lines of Be stars show evidence for substantial stellar winds, with velocities of the order 1000 km s^{-1} and mass loss rates $\dot{M} \approx 10^{-11}$–$10^{-8}\, M_{\odot}\mathrm{yr}^{-1}$ (Snow 1981). Empirical models based on these observations thus generally suggest a two-component envelope, with a low-density, fast polar wind and an orbiting equatorial disk of high-density material with only slow radial outflow (Poeckert & Marlborough 1976; Waters 1986; Waters, Coté, & Lamers 1987; Waters et al. 1988).

The wind from a rapidly rotating star is significantly affected by centrifugal forces. The resulting smaller effective gravity tends to increase the mass loss rate and decrease the wind speed. Gerasimovič (1934) first predicted such a rotational wind enhancement for Be stars, and Limber (1964) constructed phenomenological models of axisymmetric Be-star envelopes based on such a "rotational ejection" paradigm. However, in actual dynamical models of wind acceleration over the equator, this effect is limited to factors of a few, and thus it fails to explain the quite strong (factors of 100–1000) observed equatorial density enhancements in Be star disks (Friend & Abbott 1986). Bjorkman & Cassinelli (1993) have proposed the simple and powerful "wind compressed disk" (WCD) paradigm, which is a two-dimensional model of how rotation can deflect wind flow streamlines toward the equatorial plane to possibly form a shocked disk. Although an important step forward, it seems that some added mechanism, such as magnetic fields or nonradial pulsations, must distinguish the extreme "Be phenomenon" from other, more ubiquitous rotational effects.

Although magnetic fields have only been observed in a relatively small fraction of hot stars (see Moss & Smith 1981; Bohlender 1994), the presence of even quite weak fields can have a strong impact on modulating the circumstellar material. In the solar wind, the detailed field structure in the lower corona determines how the density and velocity vary throughout the entire heliosphere (Hundhausen 1972; Zirker 1977). Models of open magnetic fields in O- and B-star winds have been limited to one dimension (Friend & MacGregor 1984; Poe & Friend 1986), and although the wind over the equator of a rotating and magnetic star is "spun up" by

the field, only extremely rapidly rotating models ($V_{\rm eq} \approx V_{\rm crit}$) exhibit large equatorial density enhancements. A more complete magnetohydrodynamic treatment of the near-star *dipole* nature of the field is definitely needed, akin to the solar wind model of Pneuman & Kopp (1971), in order to accurately assess the importance of magnetic fields in rotating hot stars.

1.2.3 Variability and Inhomogeneity

The atmospheres and winds of most early-type stars are intrinsically variable on time scales ranging from hours to years. Periodic variability in photospheric absorption lines is often identified with radial or nonradial pulsations of the underlying star, while the more complex variability in P Cygni type wind lines is still poorly understood. Most theories concerning the origin of these variations involve the existence of highly-structured, non-spherically symmetric winds. Because there are many physical mechanisms that can lead to wind structure and variability, it is useful to distinguish between (1) *small-scale* stochastic fluctuations, intrinsic to the wind itself, and (2) *large-scale* quasi-regular variability, induced by changes in the underlying star. In the former category is the shocked structure arising from the strong instability of the radiation-driving mechanism (Rybicki 1987; Owocki 1992), which may explain black troughs in saturated ultraviolet P Cygni lines in O and B stars (Lucy 1982; Puls, Owocki, & Fullerton 1993), shock-heated X-ray emission (Cohen et al. 1996), and moving "bumps" in Wolf-Rayet optical emission lines (Robert 1994).

In this work, however, we will concentrate mainly on the latter, larger-scale wind structure that can be attributed to the dynamical effects of rotation, magnetic fields, or pulsations. This "wind activity" has been observed indirectly in the highly-variable emission lines of Be stars for almost a century (see Underhill & Doazan 1982; Slettebak & Snow 1987), but only recently has this variability been found to be so widespread in most O and B stars. Early repeated observations of wind diagnostics such as Hα (Ebbets 1982) and ultraviolet resonance lines (York et al. 1977; Snow 1977) showed drastic changes in line profile shapes and strengths. The relation between this wind variability and the rotation or pulsation of the underlying star has been suspected for some time, and the attendees of a workshop on Instability and Variability of Hot-Star Winds (Moffat et al. 1994) proposed that a long continuous time series was required to identify such a connection. This proposal evolved into the *IUE* "MEGA" campaign (Massa et al. 1995), which observed three hot stars nearly continuously for 16 days. This groundbreaking data set provides the major observational impetus for many of the theoretical models in this dissertation.

The most conspicuous of the variations in the blueshifted absorption troughs

of ultraviolet P Cygni profiles are the *discrete absorption components* (DACs), which appear as narrow and localized optical depth enhancements in unsaturated lines, in some stars even dominating the "mean wind" absorption. DACs are present in a majority of O-star (Howarth & Prinja 1989) and Be-star (Grady, Bjorkman, & Snow 1987) winds, and are typically seen to accelerate to the blue wing of the profile over a few days, becoming narrower as they approach an asymptotic velocity. Prinja (1988) and Henrichs, Kaper, & Zwarthoed (1988) found an apparent correlation between both the recurrence and acceleration time scales of DACs (typically of the same order as each other) and the projected rotational velocity of the star, $V_{\rm eq} \sin i$. Corresponding and often temporally-correlated variability is seen in the blue edge fluctuations of saturated ultraviolet P Cygni lines, in the low-velocity variability of subordinate-level P Cygni lines, and in optical lines such as Hα and He II λ4686, suggesting a single dynamical phenomenon reaching down to very near the photosphere (Henrichs, Kaper, & Nichols 1994).

Attempts to model DACs have been progressively constrained by better observations. By studying lines of different ionization species, Lamers, Gathier, & Snow (1982) ruled out the early supposition that DACs might be caused by ionization gradients in an otherwise spherically symmetric and time steady wind. The episodic ejection of spherical "shells" of increased mass loss was an often-invoked model for a time, but the lack of both *emission* variability in ultraviolet P Cygni lines (Prinja & Howarth 1988) and significant infrared variability (Howarth 1992) seems to rule out a spherically-symmetric disturbance (see, however, the kinematic models of Waldron et al. 1994). On the other hand, to produce the observed strong absorption dips, the structure must be large enough to cover a substantial fraction of the stellar disk. This seems to rule out the small-scale wind instability as the source of most DAC clumpiness, since global averaging would weaken the observable signature (Owocki 1994). Also, Rybicki, Owocki, & Castor (1990) showed that small-scale, lateral velocity perturbations should be strongly damped, and so should not disrupt the horizontal scale size set by base variations. Altogether, these constraints suggest that DACs originate from moderate size wind structures, e.g., spatially-localized clouds, streams, or "blobs."

Of particular interest is the apparent acceleration rate of DACs. When compared to the acceleration of the mean wind inferred from line-driven flow theory and detailed profile fitting, some (typically weaker) DACs seem to be passively carried along the same velocity law (see, e.g., Kaper 1993). But most strong DACs accelerate much more *slowly* (Prinja 1994), suggesting they may not represent a single mass-conserving feature, but rather might arise from a slowly evolving *pattern* or perturbation through which wind material flows. The enhanced optical depth could result from either a higher density or a lower wind velocity gradient (a "plateau"), or by a combination of the two (Fullerton & Owocki 1992; Owocki, Fullerton, & Puls

1994), as is found in the dynamical models presented in this dissertation (Chapter 6).

Mullan (1984a, b; 1986) proposed that DACs and related phenomena could arise from "corotating interaction regions" (CIRs) analogous to those commonly observed *in situ* in the solar wind. In the solar corona, regions of open magnetic field cause the flow from coronal holes to be accelerated faster than the mean ecliptic-plane wind, resulting in colliding fast and slow streams strung into spiral CIR patterns by rotation (Hundhausen 1972; Zirker 1977). These nonlinear interacting streams eventually steepen into oblique corotating shocks, through which the wind flows nearly radially. Mullan (1984a) showed that CIRs can form in winds from a wide variety of stars, and depend primarily on a longitudinal asymmetry in wind velocity or density. Because hot stars do not have the strong surface convection and coronae known to exist in the sun, the "seed" mechanism for large-scale azimuthal perturbations may be quite different.

In this work we do not adhere to any particular model for these photospheric variations, but several plausible scenarios have been proposed. Underhill & Fahey (1984) modeled assumed time-steady DAC velocities in terms of varying acceleration above small patches of enhanced magnetic field. Henrichs et al. (1994) found that DAC accelerations correlate well with a corotating magnetic dipole configuration on the stellar surface. Indeed, Henrichs et al. (1995) have recently begun to detect these weak time-variable surface fields. Nonradial pulsations have also been observed in many OB stars, and have been shown to be able to induce localized increased mass loss and outward angular momentum transfer (Castor 1986; Willson 1986; Ando 1991). Henrichs (1984) discussed the possible connection between pulsations and DACs, and the ubiquity and strength of these oscillations in the outer layers of hot stars makes them likely to influence the wind. Also, circumstellar disks exhibit many natural large-scale instabilities, e.g. Okazaki's (1991) global one-armed normal modes, which may be correlated with DAC variability in Be stars (Telting & Kaper 1994). Finally, Dowling & Spiegel (1990) discuss the possible existence of Jupiter-like zonal bands and vortices in the atmospheres of hot stars, and give order-of-magnitude estimates of the flux enhancement over a "Great Red Spot" type of shear pattern.

Several qualitative attempts have been made to apply the CIR picture to observations of time variability in early-type stellar winds, but all have been *kinematic* in nature. Prinja & Howarth (1988) fit slowly-accelerating spiral streamlines to DACs in time series spectra from the O7.5 giant 68 Cyg, and showed that the narrowing of the absorption feature as it accelerates can be explained roughly by the decrease in the line-of-sight velocity gradient of the CIR. Harmanec (1991) extended this analysis and discussed possible observational signatures of CIRs in other classes

of early-type stars. Rotationally-modulated gas streams or "spokes" have been proposed in models of Be star circumstellar material (see, e.g., Štefl et al. 1995) and in the time variability of Herbig Ae star spectra (Catala et al. 1991). Of course, the physics of circumstellar streams in Be and Herbig Ae stars will most likely be very different from that of corresponding structures around O stars, and we will focus mainly on the latter.

1.3 Goals of this Work

This dissertation represents research performed between 1992 and 1996 at the Bartol Research Institute. Herein I address several problems in the observations of hot-star winds by constructing radiation hydrodynamical models of these winds and synthesizing spectroscopic and polarization diagnostics to compare with observations. Chapter 2 outlines the current state of the theory of radiatively driven stellar winds and concentrate on spherically-symmetric solutions to the equations of radiation hydrodynamics. I derive the radiative force in the "Sobolev approximation," consider driving by various forms of continuum and line opacity, and present analytic and numerical solutions for the wind's velocity and density. In Chapter 3, I utilize such solutions for the purpose of synthesizing observational diagnostics of stellar winds. The major goal of this Chapter is the derivation of several techniques of creating theoretical ultraviolet P Cygni line profiles, but I also discuss the importance of the linear polarization of stellar envelopes, and provide a straightforward means of approximating this polarization for general circumstellar gas distributions.

The role of rapid stellar rotation is central to the formation of nonspherical and temporally variable circumstellar structures. In Chapter 4, I describe three physical consequences of the strong *centrifugal* force from a rotating star: (1) oblateness and gravity darkening in the interior and photosphere, (2) the modulation of the flux and effective gravity in the wind and the possible loss of steady-state flow solutions, and (3) the existence of nonradial line forces which can remove large amounts of angular momentum from a rotating and expanding wind. Another important rotational effect is discussed in Chapter 5: the two-dimensional "wind compressed disk" model of Bjorkman & Cassinelli (1993). This was the first original research with which I was involved at Bartol, and this Chapter outlines my contribution to the work of Owocki, Cranmer, & Blondin (1994), Cranmer & Owocki (1995), and Owocki, Gayley, & Cranmer (1996).

Subsequent research has been concerned with modeling the complex variability observed in P Cygni spectral lines, and Chapter 6 contains the results of hydrodynamical simulations of corotating interaction regions (CIRs) in the equatorial plane of a rotating wind. We find that a "bright spot" of enhanced mass loss

from the photosphere leads to rotating circumstellar structure which reproduces many of the observed properties of discrete absorption components (DACs) in ultraviolet P Cygni profiles. This work has been published as Cranmer & Owocki (1996). Chapter 7 begins to address the question of the physical origin of the photospheric base perturbations of Chapter 6, and I outline the theory of *nonradial oscillations* in the interior, photosphere, and wind of a rotating star. Some of the insight gained from the recent results of Owocki, Cranmer, & Fullerton (1995) and Cranmer, Massa, & Owocki (1996) is included, but this work is still in progress. Finally, Chapter 8 contains a brief overview and discussion of this dissertation work, as well as an outline of future research that would address important questions about the radiation hydrodynamics of rotating hot-star winds.

Chapter 2

THE THEORY OF RADIATIVELY DRIVEN STELLAR WINDS

You must take the will for the deed.
With a heart and a half
if I could raise the wind anyhow.

James Joyce, *Ulysses*

2.1 Equations of Radiation Hydrodynamics

Stellar winds are driven by net outward forces on photospheric and circumstellar gas, and the resulting motion is determined by solving the dynamical equations of mass, momentum, and energy conservation. To apply the solutions of these partial differential equations to actual physical systems, however, it is important to understand their mathematical structure. In many cases the equations admit *time steady* wind solutions whose topology is characterized in terms of singular and critical points of the flow. In other cases no steady-state solutions exist, and the wind's velocity and density must either become non-analytic (discontinuous in value or derivatives) or time-variable. Studying various analytic and numerical methods of solving the dynamical equations can even lead to the discovery of underlying physical laws which govern the acceleration of stellar winds; e.g., we suspect, but have not yet proven, that certain time-steady wind solutions represent nonlinear "attractors" governed by new variational principles. A wealth of complex physics lies just beneath the surface of hot-star wind theory, and the present work only scratches this surface.

The first question to address, then, is that of the origin or initiation of stellar winds. We find below that both static and accelerating solutions may be possible

in some cases, but the observations clearly point to the existence of winds whenever possible. Cannon & Thomas (1977) and Andriesse (1981) propose the existence of inherent nonthermal subphotospheric instabilities that rapidly accelerate small perturbations to generate a wind, but such "sources" of mass loss are unnecessary in early-type stellar environments because of the strong force exerted by the radiation field. The maximum amount of possible mass loss is determined *in the wind* by the stellar radiation, and as much material as needed (from the near-hydrostatic atmosphere) can be "pulled up" from above. In fact, this radiation force is itself unstable to small perturbations (see Section 2.4), which may be able to amplify small deviations from a static atmosphere into a full-blown supersonic wind. Abbott (1979) and Babel (1995, 1996) investigated the limits of wind maintenance and initiation in the HR diagram, and verified that whenever radiation-driven mass loss is possible, it invariably occurs.

The idea that material can be ejected from the star by the absorption and scattering of radiation was first suggested by Milne (1924, 1926) and Johnson (1925, 1926) who found that the force on selected ions due to the absorption of photons can greatly exceed gravity. These forces, though, were assumed to be impulsive in nature, and that the accelerated ions eventually fell back down onto the star. However, Milne (1926) also predicted that these ions may be Doppler shifted out of the core of their photospheric absorption line, and thus experience a much greater force from the unattenuated continuum. Contrary to the prevailing notions, then, Milne anticipated a steady ionic outflow with an asymptotic terminal velocity v_∞ two to three times the surface escape velocity, i.e., that "the prodigal never returns."

When these theories were revived by Lucy & Solomon (1970), Castor (1974), and Castor, Abbott, & Klein (1975, hereafter CAK) in the hopes of explaining observed mass loss from O stars, the treatment was of a *single* hydrodynamic fluid driven by stellar radiation, not a heterogeneous collection of ions. This assumption of a fully-mixed, or collisionally-coupled plasma was examined by Castor et al. (1976) and justified for O-star winds. The motion of the heavy ions driven by line radiation (C, N, O, Fe, etc.) induce electrostatic forces which carry along an appropriate number of electrons, which themselves are also weakly driven by Thomson scattering. Collisions with the remaining protons and helium nuclei create a net frictional force which damps out relative motion between the various species. For winds from O and Wolf-Rayet stars, the drift velocities between these populations are found to be much smaller than the associated thermal velocities, and the one-fluid approximation is valid. For the lower-density winds around B and A stars, however, decoupling between the ions and the bulk plasma can occur and lead to "frictional heating" and high temperatures (Springmann & Pauldrach 1992; Gayley & Owocki 1994) or fully-separated multicomponent winds that may appear chemically peculiar (Babel 1995, 1996).

In this work we will assume a single-fluid treatment of a stellar wind. Starting from first principles, the hydrodynamic equations of mass, momentum, and energy conservation (Landau and Lifshitz 1987) form the basis of our wind models. For simplicity, we neglect forces due to electric and magnetic fields in these equations and defer consideration of plasma and magnetohydrodynamic effects to future work. Expressed in differential form, these equations are as follows:

$$\frac{\partial \rho}{\partial t} + \nabla \cdot (\rho \mathbf{v}) = 0 \tag{2.1}$$

$$\frac{\partial \mathbf{v}}{\partial t} + (\mathbf{v} \cdot \nabla)\mathbf{v} = -\frac{1}{\rho}\nabla P + \mathbf{g} + \frac{1}{\rho}\left[\eta \nabla^2 \mathbf{v} + (\zeta + \tfrac{1}{3}\eta)\nabla(\nabla \cdot \mathbf{v})\right] \tag{2.2}$$

$$\frac{\partial P}{\partial t} + \mathbf{v} \cdot \nabla P - \left(\frac{\gamma P}{\rho}\right)\left[\frac{\partial \rho}{\partial t} + \mathbf{v} \cdot \nabla \rho\right] = H(T) \ , \tag{2.3}$$

where the fluid velocity $\mathbf{v}$, the mass density ρ, and the gas pressure P are functions of position and time. The vector acceleration $\mathbf{g}$ includes external body forces such as gravitation and radiation forces, and the viscosity coefficients η and ζ are often considered constant. Note, however, that the low-density gas surrounding most stars is often assumed inviscid ($\eta = \zeta = 0$), and this simplification will be utilized herein (see Castor et al. 1976). Equation (2.3) represents the conservation of internal (microscopic) energy, and the constant γ is the ratio of specific heats c_P/c_V (usually 5/3 for a monatomic gas). $H(T)$ is a temperature-dependent rate of net heating or cooling.

Although the equation of energy conservation is formally required to complete the hydrodynamic system to be solved, the conditions in stellar winds often allow for an immediate, if approximate, solution to this equation. In the regions surrounding early-type stars, *radiative* heating and cooling terms in $H(T)$ dominate the energy balance, and the time scale for the gas to gain or lose energy is short when compared to the time scale of the flow. These conditions allow radiative equilibrium to be assumed throughout large parts of the wind, and a solution for the gas temperature $T(\mathbf{r})$ is thus simpler to evaluate. Klein & Castor (1978) solved the full radiative equilibrium problem for hydrogen in a spherical stellar wind, and they concluded that the electron temperature is approximately constant with radius, and slightly less than the photospheric effective temperature $T_{\rm eff}$.

This work has been extended (Stewart & Fabian 1981; Drew 1989) using more accurate statistical and thermal equilibrium calculations, and more extensive atomic data. Drew (1989) finds that the ratio of the wind temperature to the stellar $T_{\rm eff}$ shows a slow decline with radius, from $\sim$0.8 at the stellar surface to nearly $\sim$0.6 at twice the stellar radius, and is not sensitively dependent on the heavy element abundances. Bunn & Drew (1992) fit the computed temperature variation with

a function which depends only on the local wind velocity; this implies a constant asymptotic temperature as $r \rightarrow \infty$. Fortunately, the highly supersonic hydrodynamic structure of the stellar wind is relatively insensitive to these temperature variations, and we safely assume a simple isothermal $T(\mathbf{r}) = T_{\rm eff}$ in the remainder of this work.

Thus, the inviscid hydrodynamic equations of mass and momentum conservation, together with an appropriate equation of state, can be considered a closed set of five equations in five unknowns (P, ρ, $\mathbf{v}$). The spherical (or near-spherical) symmetry of stellar environments naturally leads us to express these equations in spherical polar coordinates, and in component form, as

$$\frac{\partial \rho}{\partial t} + \frac{1}{r^2}\frac{\partial}{\partial r}(\rho v_r r^2) + \frac{1}{r\sin\theta}\frac{\partial}{\partial \theta}(\rho v_\theta \sin\theta) + \frac{1}{r\sin\theta}\frac{\partial}{\partial \phi}(\rho v_\phi) = 0 \qquad (2.4)$$

$$\frac{\partial v_r}{\partial t} + v_r\frac{\partial v_r}{\partial r} + \frac{v_\theta}{r}\frac{\partial v_r}{\partial \theta} + \frac{v_\phi}{r\sin\theta}\frac{\partial v_r}{\partial \phi} - \frac{v_\theta^2 + v_\phi^2}{r} = -\frac{1}{\rho}\frac{\partial P}{\partial r} + g_r \qquad (2.5)$$

$$\frac{\partial v_\theta}{\partial t} + v_r\frac{\partial v_\theta}{\partial r} + \frac{v_\theta}{r}\frac{\partial v_\theta}{\partial \theta} + \frac{v_\phi}{r\sin\theta}\frac{\partial v_\theta}{\partial \phi} + \frac{v_r v_\theta}{r} - \frac{v_\phi^2\cot\theta}{r} = -\frac{1}{\rho r}\frac{\partial P}{\partial \theta} + g_\theta \qquad (2.6)$$

$$\frac{\partial v_\phi}{\partial t} + v_r\frac{\partial v_\phi}{\partial r} + \frac{v_\theta}{r}\frac{\partial v_\phi}{\partial \theta} + \frac{v_\phi}{r\sin\theta}\frac{\partial v_\phi}{\partial \phi} + \frac{v_r v_\phi}{r} + \frac{v_\theta v_\phi\cot\theta}{r} = -\frac{1}{\rho r\sin\theta}\frac{\partial P}{\partial \phi} + g_\phi \ . \qquad (2.7)$$

To model the wind surrounding a hot star, several additional simplifying assumptions are commonly made to facilitate solutions to the above equations. In this Chapter we examine the problem of a spherically symmetric wind (with $v_\theta = v_\phi = 0$ and all angular derivatives also zero) and explore possible time-steady configurations. Even at this simplified level, however, the equations of motion are highly nonlinear, and various methods of solution will be discussed. In subsequent Chapters we investigate multidimensional and time-dependent models of hot-star winds, which usually can only be constructed numerically.

Consider a spherical star of mass M_*, radius R_*, and bolometric luminosity L_*, with a time-steady and spherically-symmetric wind. The hydrodynamic equations reduce to one-dimensional (radial) forms. The equation of mass conservation is thus

$$\frac{1}{r^2}\frac{\partial}{\partial r}(\rho v_r r^2) = 0 \ , \qquad (2.8)$$

which can be easily integrated and formed into a constraint on the total outward *mass flux* (the amount of mass lost by the entire star per unit time),

$$\dot{M} \equiv -\frac{dM_*}{dt} = 4\pi\rho v r^2 = \text{constant} \ , \qquad (2.9)$$

replacing v_r by v in this one-dimensional analysis. This constraint will later allow us to eliminate the density ρ from the momentum equation.

The radial component of the momentum equation is given by

$$v\frac{\partial v}{\partial r} = -\frac{1}{\rho}\frac{\partial P}{\partial r} + g_r \quad . \tag{2.10}$$

To evaluate the pressure P it is useful to assume an ideal gas equation of state of the form

$$P = \frac{\rho k_B T}{\mu m_H} = \rho a^2 \quad , \tag{2.11}$$

where a is the isothermal sound speed, k_B is Boltzmann's constant, μ is the mean molecular weight of gas particles, and m_H is the mass of a hydrogen atom. The mean molecular mass in the case of complete ionization can be approximated by

$$\frac{1}{\mu} = 2X + \tfrac{3}{4}Y + \tfrac{1}{2}Z \quad , \tag{2.12}$$

where X, Y, and Z represent the mass fractions of hydrogen, helium, and heavy elements in the wind (Mihalas 1978). In all models of O and B stars in this work we assume solar-like elemental abundances ($X = 0.73$, $Y = 0.24$, $Z = 0.03$), but in models of Wolf-Rayet winds we assume a pure helium state ($Y = 1$) for simplicity.

If the gas temperature T, and thus the sound speed a, is assumed to be a known function of radius, the mass flux constraint above can be used to eliminate the density ρ, and the resulting equation of motion reduces to

$$\left(v - \frac{a^2}{v}\right)\frac{dv}{dr} = \frac{2a^2}{r} - \frac{da^2}{dr} + g_r \quad . \tag{2.13}$$

The external acceleration g_r can be written as a sum of gravitational and radiation forces, where the radiation field is naturally separable into that due to the continuum and spectral lines,

$$g_r = -\frac{GM_*}{r^2} + g_{\rm rad}^C + g_{\rm rad}^L \quad . \tag{2.14}$$

The radiative force terms are derived in their entirety in Section 2.2, but can be parameterized in some cases rather simply. In contrast to the stellar interior, where thermodynamic equilibrium allows the radiation force to be expressed as the gradient of a scalar isotropic "radiation pressure," the nonlocal character of the radiation field in the expanding circumstellar gas (and its associated dependence on the wind *velocity*) does not allow this simplification, and knowledge of the dynamic properties of the fluid is required.

2.2 The Sobolev Radiation Force

2.2.1 The Continuum and Individual Lines

Radiation is able to transfer momentum to matter via the absorption and scattering of photons. The acceleration (force per unit mass) due to a radiation field at a point $\mathbf{r}$ (Mihalas 1978) is given by

$$\mathbf{g}_{\rm rad}(\mathbf{r}) = \frac{1}{c} \oint \int_{\nu=0}^{\infty} \kappa_\nu I_\nu(\mathbf{r},\hat{\mathbf{n}})\, \hat{\mathbf{n}}\, d\Omega\, d\nu \tag{2.15}$$

$$= \frac{1}{c} \int_{\nu=0}^{\infty} \kappa_\nu \boldsymbol{\mathcal{F}}_\nu(\mathbf{r}) d\nu \quad , \tag{2.16}$$

where κ_ν is the total (absorption plus scattering) mass extinction coefficient (in $\rm cm^2/g$) which is assumed to be isotropic (i.e., independent of direction Ω). The variables I_ν and $\boldsymbol{\mathcal{F}}_\nu$ are the monochromatic radiative intensity and flux, respectively, and the unit vector $\hat{\mathbf{n}}$ is the direction of flow of the radiation, over which the intensity moment is integrated over solid angle Ω.

We can separate the opacity and radiation field into continuum (in hot stars, presumed dominated by electron scattering) and line processes. Although spectral lines subtend only narrow bands of wavelength, they play an important role in wind driving. This is because bound atoms *resonate,* or constructively interfere with continuum photons. This broad-band excitation of a resonance is the same effect that makes a whistle loud or a laser bright; the response remains significant even when averaged over the entire continuum (see Gayley 1995). Thus, treatment of both continuum and line radiation driving is important in hot-star wind theory, and the force can be separated into two general components:

$$\mathbf{g}_{\rm rad} = \mathbf{g}^C_{\rm rad} + \mathbf{g}^L_{\rm rad} \tag{2.17}$$

$$= \frac{\sigma_e}{c} \oint \int_{\nu=0}^{\infty} I_\nu(\mathbf{r},\hat{\mathbf{n}})\, \hat{\mathbf{n}}\, d\Omega\, d\nu \;+ \sum_{\rm lines} \frac{\kappa_L}{c} \oint \int_{\nu=0}^{\infty} \tilde{\phi}(\nu-\nu')\, I_\nu(\mathbf{r},\hat{\mathbf{n}})\, \hat{\mathbf{n}}\, d\Omega\, d\nu \quad , \tag{2.18}$$

where σ_e is the Thomson scattering opacity, κ_L is the mass absorption coefficient of a single line, and $\tilde{\phi}(\nu)$ is a normalized line profile function. Note that if the gas at position $\mathbf{r}$ is *in motion,* the frequency of radiation ν' seen at $\mathbf{r}$ will be Doppler shifted, to first order, by

$$\nu' = \nu_o \left[1 + \frac{1}{c} \hat{\mathbf{n}} \cdot \mathbf{v}(\mathbf{r}) \right] \quad . \tag{2.19}$$

Here, ν_o is the emitted frequency and $\mathbf{v}(\mathbf{r})$ is the flow velocity of the gas, assumed nonrelativistic. Let us make the standard change of variables, defining the dimensionless frequency displacement (from line center) in Doppler units as

$$x \equiv \left(\frac{\nu - \nu_o}{\Delta\nu_D} \right) \ , \tag{2.20}$$

where the Doppler width $\Delta\nu_D = \nu_o v_{th}/c$, and v_{th} is the ion thermal speed in the gas. This thermal velocity is a sensitive parameter in many wind models, and is defined from kinetic theory in a similar way as the isothermal sound speed a (eq. [2.11]),

$$v_{th} \ = \ \sqrt{\frac{2k_B T}{A_i m_H}} \ , \tag{2.21}$$

where A_i is the mean atomic weight of the driving ions in question. For ions of heavy elements such as carbon, nitrogen, and oxygen, the ratio v_{th}/a is of the order 0.2–0.3. However, many authors define a "fiducial" thermal speed of a gas composed primarily of hydrogen ions ($A_i = 1$), with a ratio $v_{th}/a \gtrsim 1$. We see below (Section 2.2.3) that definitions of other important wind variables depend on this choice of v_{th}, but the radiative force *itself* does not depend on v_{th}. The radiative acceleration can thus be written as

$$\begin{aligned} \mathbf{g}_{\rm rad} \ &= \ \frac{\sigma_e}{c} \oint\!\!\int_{\nu=0}^{\infty} I_\nu(\mathbf{r},\hat{\mathbf{n}})\,\hat{\mathbf{n}}\,d\Omega\,d\nu \\ &\quad + \sum_{\rm lines} \frac{\kappa_L \Delta\nu_D}{c} \oint\!\!\int_{x=-\infty}^{\infty} \phi\!\left(x - \frac{\hat{\mathbf{n}}\cdot\mathbf{v}(\mathbf{r})}{v_{th}} \right) I_\nu(\mathbf{r},\hat{\mathbf{n}})\,\hat{\mathbf{n}}\,d\Omega\,dx \ . \end{aligned} \tag{2.22}$$

Note that the line profile functions $\tilde{\phi}$ and ϕ are both normalized such that

$$\int_{\nu=0}^{\infty} \tilde{\phi}(\nu) d\nu = \int_{x=-\infty}^{\infty} \phi(x) dx = 1 \ , \tag{2.23}$$

and the lower limit of integration of the variable x is extended from $-c/v_{th}$ to $-\infty$ without appreciable error, because of the finite extent of the line's opacity in the overall spectrum. (See Section 3.1.3 for more details about the line profile function and opacity.)

Assuming the wind is optically thin to continuum radiation (as is the case in O and B stars), the continuum integral is simply the continuum bolometric flux $\boldsymbol{\mathcal{F}}_*$. The integral for the lines, however, is more complicated. Note that the general equation of radiative transfer,

$$\frac{dI_\nu}{d\tau_\nu} = -I_\nu + S_\nu \ , \tag{2.24}$$

has the formal solution (with a diffuse term and a "core" boundary term),

$$I_\nu(\tau_\nu) = \int_0^{\tau_\nu} S_\nu(t_\nu) e^{-(\tau_\nu - t_\nu)} dt_\nu \; + \; I_\nu^{\rm core} e^{-\tau_\nu} \quad , \tag{2.25}$$

where $S_\nu(\tau_\nu)$ is the source function of the medium, and the geometry-independent optical depth τ_ν is defined, in the moving medium along a general ray of path length s, as

$$\tau_\nu = \int_0^s \kappa_L \, \rho(s') \, \phi\left(x - \frac{\hat{\mathbf{n}} \cdot \mathbf{v}(\mathbf{r})}{v_{th}} \right) ds' \quad . \tag{2.26}$$

With the assumptions of isotropic scattering and local thermodynamic equilibrium (LTE), the source function is given by

$$S_\nu = \epsilon_\nu B_\nu(T) + (1 - \epsilon_\nu) J_\nu \quad , \tag{2.27}$$

where ϵ_ν is the photon destruction probability per scattering (absorption albedo), $B_\nu(T)$ is the Planck function, and J_ν is the mean intensity,

$$J_\nu = \frac{1}{4\pi} \oint I_\nu(\mathbf{r}, \hat{\mathbf{n}}) \, d\Omega \quad . \tag{2.28}$$

In the frame of reference of a moving atom, we assume the scattering can be considered coherent. But the thermal Doppler motion of the gas tends to produce a nearly complete frequency redistribution in the rest frame (Hummer 1969; Castor 1970; Hummer & Rybicki 1992), which greatly simplifies the form of the source function. Because the wind is an *expanding* medium, photons scattered into all directions will be systematically red-shifted in comoving wavelength. Thus, whether the line is dominated by absorption or scattering processes, photons will "drift" from the blue to red edge, and emerge with roughly fore-aft symmetry. The net diffuse component of the *force*, which is proportional to the integral of the now direction-independent intensity, times the "odd" factor of $\hat{\mathbf{n}}$, will be negligibly small. Castor (1974) estimates the ratio of the diffuse force to the "direct" core force, and finds it to be of the order of $(v_{th}/|\mathbf{v}|)$, which is indeed negligible in most of the wind.

Let us then keep only the direct term $I_\nu^{\rm core} e^{-\tau_\nu}$ from the formal solution for the intensity, and the radiative acceleration can be written as

$$\mathbf{g}_{\rm rad} = \frac{\sigma_e \boldsymbol{\mathcal{F}}_*}{c} + \sum_{\rm lines} \frac{\kappa_L \Delta\nu_D}{c} \oint \int_{x=-\infty}^{\infty} \phi \left(x - \frac{\hat{\mathbf{n}} \cdot \mathbf{v}(\mathbf{r})}{v_{th}} \right) I_\nu^{\rm core} e^{-\tau_\nu} \, \hat{\mathbf{n}} \, d\Omega \, dx \quad . \tag{2.29}$$

In a wind with a monotonically increasing velocity, one can simplify the optical depth integral (eq. [2.26]), by invoking the *Sobolev approximation* (Sobolev 1957, 1960), assuming that the variables κ_L and ρ do not change appreciably over a "Sobolev length" $L_{\rm Sob}$. If the fluid velocity is large enough, the Doppler shift of

the line frequency will dominate the integrand, and it will be sharply-peaked near the point at which the frequency x is in resonance with the local component of the fluid velocity. The frequency of the line, at "observer" position $\mathbf{r}$, is changed by one Doppler width $\Delta\nu_D$ over a length scale $L_{\rm Sob}$ on which the gas velocity $\mathbf{v}$ is increased by v_{th} (the local thermal speed of the scattering ions). Thus, if $L_{\rm Sob}$ is significantly smaller than a typical hydrodynamical scale height H_ρ, then the optical depth integral becomes a function of *local* variables only, and is dominated by the Doppler shift of the line profile. If

$$L_{\rm Sob} \approx \frac{v_{th}}{dv/dr} \ll H_\rho = \frac{\rho}{d\rho/dr} \approx \frac{v}{dv/dr} \quad , \tag{2.30}$$

then a necessary condition for the Sobolev approximation is either the zero thermal speed ($v_{th} \to 0$) limit, or the roughly equivalent limit of a supersonic wind ($v \gg v_{th}$). Note the fact that $v_{th} \approx 0.3a$ for the driving ions, so the Sobolev approximation is reasonably valid at the dynamically important *sonic point* of the flow, where $v = a$. The local variables κ_L and ρ can thus be taken out of the optical depth integral, and

$$\tau_\nu(\mathbf{r}) = \kappa_L\, \rho(\mathbf{r}) \int_0^s \phi\left(x - \frac{\hat{\mathbf{n}}\cdot\mathbf{v}(\mathbf{r}')}{v_{th}}\right) ds' \quad , \tag{2.31}$$

where the path length ranges from the stellar surface at $s' = 0$ (position vector $\mathbf{r}_0$) to the "observer" in the wind at $s' = s$ (position vector $\mathbf{r}$), with the instantaneous position $\mathbf{r}' = \mathbf{r}_0 + s'\hat{\mathbf{n}}$. Because of the assumed monotonic nature of the flow, we can make a one-to-one change of variables into frequency space:

$$x' = x - \frac{\hat{\mathbf{n}}\cdot\mathbf{v}(\mathbf{r}')}{v_{th}} \quad , \tag{2.32}$$

$$dx' = -\frac{1}{v_{th}} d\left[\hat{\mathbf{n}}\cdot\mathbf{v}(\mathbf{r}')\right] = -\frac{1}{v_{th}} \hat{\mathbf{n}}\cdot\nabla\left[\hat{\mathbf{n}}\cdot\mathbf{v}(\mathbf{r}')\right] ds' \quad , \tag{2.33}$$

since $d\mathbf{r}' = \hat{\mathbf{n}}\, ds'$, and $\hat{\mathbf{n}}$ is (for now) a constant vector. The velocity gradient term $\hat{\mathbf{n}}\cdot\nabla[\hat{\mathbf{n}}\cdot\mathbf{v}(\mathbf{r})]$, which emerges from the change of variables, is an important component of the Sobolev radiative acceleration. This variable is similarly "macroscopic," or slowly-varying over the spatial scale of an acceleration through v_{th}, and can be taken out of the integral with κ_L and ρ. The optical depth in the Sobolev approximation is then

$$\tau_\nu(\mathbf{r}) = \frac{\kappa_L\, v_{th}\, \rho(\mathbf{r})}{\hat{\mathbf{n}}\cdot\nabla\left[\hat{\mathbf{n}}\cdot\mathbf{v}(\mathbf{r})\right]} \int_{x - \hat{\mathbf{n}}\cdot\mathbf{v}(\mathbf{r})/v_{th}}^{\infty} \phi(x')dx' \quad , \tag{2.34}$$

with the $s' = 0$ limit replaced by $x' \to \infty$, because the photon is most probably completely out of the line's influence far from $\mathbf{r}$. One can define the "Sobolev optical depth" by grouping the slowly-varying variables taken out of the optical depth integral,

$$\tau_o \equiv \kappa_L\, \rho \left(\frac{v_{th}}{|\hat{\mathbf{n}}\cdot\nabla\left[\hat{\mathbf{n}}\cdot\mathbf{v}(\mathbf{r})\right]|}\right) = \kappa_L\, \rho\, L_{\rm Sob} \quad , \tag{2.35}$$

which also provides a more rigorous definition for $L_{\rm Sob}$. Note that the velocity gradient term, $\hat{\mathbf{n}} \cdot \nabla [\hat{\mathbf{n}} \cdot \mathbf{v}(\mathbf{r})]$, represents the projected component of the gradient of the velocity component which is projected along the ray $\hat{\mathbf{n}}$, and can be denoted schematically as $(\partial v_n / \partial n)$. The absolute value of this quantity is taken because the Sobolev approximation works in monotonically accelerating or decelerating velocity fields. We will ignore this absolute value for the remainder of this Chapter, but will re-examine its usefulness in subsequent Chapters dealing with more complex multidimensional winds. One can also define the known integral

$$\Phi(x, \mathbf{r}) \equiv \int_{x - \hat{\mathbf{n}} \cdot \mathbf{v}(\mathbf{r})/v_{th}}^{\infty} \phi(x') dx' \ , \tag{2.36}$$

which is proportional to the error function for a pure Doppler-broadened (i.e., Gaussian) profile, or is a step function for an infinitely sharp ("delta function") line profile. Thus, the line radiation force can be written as

$$\mathbf{g}_{\rm rad}^{L} = \sum_{\rm lines} \frac{\kappa_L \Delta \nu_D}{c} \oint \int_{x=-\infty}^{\infty} \phi(x') I_{\nu}^{\rm core} e^{-\tau_o \Phi(x, \mathbf{r})} \, \hat{\mathbf{n}} \, d\Omega \, dx \ . \tag{2.37}$$

Because of the limited extent in frequency of most spectral lines, the core intensity $I_{\nu}^{\rm core}$ can be safely assumed to be constant over the line, and taken out of the integral over the *line profile* frequency variable x. This intensity can be assumed to be a continuum quantity I^C. Thus, the integral becomes analytic, since

$$\begin{aligned} \mathbf{g}_{\rm rad}^{L} &= \sum_{\rm lines} \frac{\kappa_L \, \Delta \nu_D}{c} \oint d\Omega \, \hat{\mathbf{n}} \, I^C(\Omega) \int_{x=-\infty}^{\infty} e^{-\tau_o \Phi(x, \mathbf{r})} \, d\Phi(x, \mathbf{r}) \\ &= \sum_{\rm lines} \frac{\kappa_L \, \nu_o \, v_{th}}{c^2} \oint d\Omega \, \hat{\mathbf{n}} \, I^C(\Omega) \left[\frac{1 - e^{-\tau_o}}{\tau_o} \right] \ . \end{aligned} \tag{2.38}$$

This integral thus represents the general application of the Sobolev approximation to the force from a sum of spectral lines (Castor 1974).

2.2.2 Simple Force Estimates

The radiative acceleration due to resonant line photons is most rigorously computed by summing over "line lists" of thousands or millions of individual atomic transitions. In this dissertation, however, I review several simpler methods of estimating this sum which preserve the most important physics of line driving. Let us first consider the radiation force from a "point source" of radiation on a *single* line. This approximation was the original (Lucy & Solomon 1970; CAK) and intuitively simplest way to view the stellar radiation field, and is geometrically valid in the limit of the wind very far from the star. The direct stellar intensity reduces to

$$I^C(\Omega) = \left(\frac{L_{\nu}}{4 \pi r^2} \right) \delta(\hat{\mathbf{n}} - \frac{\mathbf{r}}{|\mathbf{r}|}) \ , \tag{2.39}$$

where L_ν represents the star's source luminosity spectrum, and the delta function is merely a schematic way of saying that $\hat{\mathbf{n}}$ and $\mathbf{r}$ are parallel for rays coming from the point-star at the origin. The projected velocity gradient $\hat{\mathbf{n}} \cdot \nabla(\hat{\mathbf{n}} \cdot \mathbf{v})$ is simply $\partial v_r / \partial r$ in this limit.

The continuum radiative acceleration due to Thomson scattering of electrons can be written as a scalar quantity, since the radial components of all vectors are all that survive, and is

$$g^C_{\rm rad} = \frac{\sigma_e L_*}{4\pi r^2 c} \ , \tag{2.40}$$

where the continuum bolometric flux has been assumed to be simply $L_*/4\pi r^2$. For a mixture of ionized gases, the Thomson scattering opacity can be expressed as

$$\sigma_e = \tfrac{1}{2}\sigma_H \left(\frac{2X+Y}{X+Y}\right) \approx \tfrac{1}{2}\sigma_H (1+X) \ , \tag{2.41}$$

with $\sigma_H = 8\pi e^4 / 3 m_H m_e^2 c^4 = 0.39778$ cm^2/g for pure hydrogen (Mihalas 1978). It is common to group the gravitational and continuum radiation force terms because they both vary as the inverse square of the radius, and

$$g + g^C_{\rm rad} = -\frac{GM_*(1-\ ,\ )}{r^2} \ , \tag{2.42}$$

where the continuum Eddington ratio (L_*/L_{Edd}) is defined as

$$,\ = \frac{\sigma_e L_*}{4\pi c G M_*} \approx 1.5218 \times 10^{-5} (1+X) \frac{(L_*/L_\odot)}{(M_*/M_\odot)} \ , \tag{2.43}$$

and does not consider other continuum opacity sources (e.g., bound-free or free-free absorption) which are relatively unimportant in winds from O and early-B stars. The assumption that the wind is optically thin to continuum radiation is implicit in this development. By definition, , must be less than unity for stars which have a static "core." Stars existing above the Eddington limit of , $= 1$ have a net *outward* combined gravitational and continuum radiation force, and cannot hold themselves together in a time-steady sense. It is suspected that the strong outbursts of luminous blue variable (LBV) stars are due to a temporary breach of this Eddington limit (see Humphreys & Davidson 1994).

The force due to a single spectral line is also a purely radial scalar, and can be written

$$g^L_{\rm rad} = \frac{\kappa_L\, v_{th}}{c^2} \left(\frac{\nu_o L_\nu}{L_*}\right) \frac{L_*}{4\pi r^2} \left[\frac{1-e^{-\tau_o}}{\tau_o}\right] \ . \tag{2.44}$$

Note that the quantity $(\nu_o L_\nu / L_*)$ depends on the product of L_ν and the line frequency ν_o itself. If we assume, however, that the line in question has a frequency

near the peak of the continuum spectrum, this ratio is of order unity and can be ignored. For optically thin lines, $\tau_o \ll 1$, the expression in square brackets approaches unity, and the force falls off as the inverse square of the radius, like gravity and the continuum radiation force. For optically thick lines, $\tau_o \gg 1$, the exponential $e^{-\tau_o}$ becomes negligible, and

$$g^L_{\rm rad} = \frac{\kappa_L\, v_{th}}{c^2}\frac{L_*}{4\pi r^2}\left(\frac{1}{\tau_o}\right) = \frac{L_*}{4\pi r^2 \rho c^2}\left(\frac{\partial v_r}{\partial r}\right) \quad . \tag{2.45}$$

The linear dependence of the force on the velocity gradient can be understood by recalling how the number of photons scattered in a line depends on the red-shift due to the expanding medium, and when optically thick, all photons in resonance with the line are scattered. The counter-intuitive notion of a force which both *causes* and *requires* an acceleration is a central feature of Sobolev wind driving, and the nonlinear "feedback" of this acceleration dependency is discussed further in Section 2.3.

One can approximately consider the effect of many lines by assuming an ensemble of $N_{\rm thick}$ optically thick lines and $N_{\rm thin}$ optically thin lines. The thin lines help to "cancel out" a fraction of the gravity and result in an effective gravitational acceleration

$$g_{\rm eff} \equiv g + g^C_{\rm rad} + g^L_{\rm rad}({\rm thin}) = -\frac{GM(1-,\ -,\ {\rm thin})}{r^2} \quad , \tag{2.46}$$

where

$$,\ {\rm thin} = \frac{N_{\rm thin}\kappa_L(v_{th}/c)L_*}{4\pi c G M_*} \tag{2.47}$$

is constant throughout the wind. (Actually, there are virtually an infinite number of weak lines in the spectrum, but the opacity contribution of each is minimal; the product $N_{\rm thin}\kappa_L$, however, can be finite and appreciable.) The resulting $g_{\rm eff}$ must be negative in the near-static photosphere so that the star can hold itself together. Thus, although thin lines can help reduce the effective gravity, only thick lines (which interact with the velocity gradient) can produce actual outward *wind driving* above the stellar surface. Chen & Marlborough (1994) propose an additional radial dependence for a force due to thin lines, and are thus able to accelerate a wind artificially with only thin lines. Non-Sobolev effects may introduce such terms for the B stars discussed by Chen & Marlborough, but the large mass loss rates they attempt to model will probably not result from these corrections (Babel 1996).

Because the thick-line radiative acceleration scales with the velocity gradient $\partial v_r/\partial r$, it can balance the *inertial* term in the radial momentum equation. If we assume these two terms balance each other, then

$$v_r\left(\frac{\partial v_r}{\partial r}\right) = N_{\rm thick}\,\frac{L_*}{4\pi r^2 \rho c^2}\left(\frac{\partial v_r}{\partial r}\right) \quad , \tag{2.48}$$

and the mass loss rate is naturally given by eq. (2.9) as

$$\dot{M} = 4\pi\rho v_r r^2 = N_{\rm thick}\,\frac{L_*}{c^2} \quad . \tag{2.49}$$

Also, the asymptotic wind momentum flux can be represented by

$$\dot{M}v_\infty = N_{\rm thick}\,\frac{L_*}{c^2}\,v_\infty = \frac{L_*}{c}(N_{\rm thick}\frac{v_\infty}{c}) \quad . \tag{2.50}$$

Note that we assume that the lines do not interact with one another (and thus sum individually), but this depends crucially on their relative spacing throughout the spectrum. This "single-scattering" limit implies that a photon, which sweeps out a Doppler velocity range of width v_∞ from the stellar surface to infinity, does not encounter any other lines. The spacing of thick lines, roughly,

$$\Delta v \approx \frac{c}{N_{\rm thick}} \quad , \tag{2.51}$$

must be greater than v_∞ for single-scattering to be valid. Of course, some line overlap always exists, but its overall effect on the force should be statistically balanced by regions of line paucity. Thus, it is often useful to consider the ratio of momentum flux due to the wind to that due to photons ("momentum efficiency")

$$\frac{\dot{M}v_\infty}{L_*/c} \approx \frac{v_\infty}{\Delta v} \quad , \tag{2.52}$$

which is often less than or equal to unity in the case of O and B star winds (where the single-scattering limit is a good approximation). However, Wolf-Rayet stars can exhibit values of this ratio as large as 5 to 50, implying densely-spaced and multiply-scattered lines (Willis 1991; Lucy & Abbott 1993; Gayley, Owocki, & Cranmer 1995). The fundamental upper limit to this ratio, assuming that finding enough lines is not a problem, comes when the *energy* efficiency (ratio of wind kinetic to photon energy) approaches unity, i.e., when

$$\frac{\frac{1}{2}\dot{M}v_\infty^2}{L_*} = \left(\frac{\dot{M}v_\infty}{L_*/c}\right)\frac{v_\infty}{2c} \rightarrow 1 \quad . \tag{2.53}$$

In this limit, the energy expended by the radiation field to accelerate the wind comes at the *expense* of a reduction in the radiative energy flux itself. This "photon tiring" may be a significant effect in the near-Eddington-limit ($\Gamma \approx 1$) winds of LBV stars, but is negligible for most O, B, and Wolf-Rayet stars. The above energy ratio ranges from $\sim$ 0.1–2% for O and B stars, and can reach as high as $\sim$10% for Wolf-Rayet stars, but these values are well below the photon tiring limit.

2.2.3 General Line Ensemble Forces

Instead of a sum of thin and thick lines, the actual ensemble of driving lines exhibits a continuous range of optical depth τ_o. The significant insight of CAK was to model this as a statistical distribution function of line strengths. CAK first considered an extensive list of subordinate C^{+3} lines and parameterized their contribution via a power law fit, in terms of a scaled electron-scattering optical depth t:

$$g^L_{\rm rad} \propto kt^{-\alpha} \ , \qquad \text{where} \quad t \equiv \frac{\sigma_e \rho \, v_{th}}{\partial v_r / \partial r} \ . \tag{2.54}$$

CAK and Abbott (1980) realized that this power law could be expressed equivalently as a *number distribution* of lines, and Owocki, Castor, & Rybicki (1988, hereafter OCR) generalized this, and defined an exponentially-truncated power law number distribution of the form,

$$\frac{dN}{d\kappa_L} = \frac{1}{\kappa_o} \left(\frac{\kappa_L}{\kappa_o} \right)^{\alpha-2} e^{-\kappa_L/\kappa{\rm max}} \ , \quad 0 < \alpha < 1 \ , \tag{2.55}$$

and κ_o is related to CAK's force constant k by

$$\frac{\kappa_o v_{th}}{c} = \sigma_e \left(\frac{v_{th}}{c} \right)^{-\alpha/(1-\alpha)} \left[\frac{(1-\alpha)}{,(\alpha)} k \right]^{1/(1-\alpha)} \ , \tag{2.56}$$

where $,(\alpha)$ is the complete gamma function. The power-law exponent α characterizes the relative importance of optically thin and thick lines in the distribution: when $\alpha = 0$, all lines are thin, and when $\alpha = 1$, all lines are thick. Detailed line-list computations have found $\alpha \approx 0.5$–0.7 for various stellar environments (CAK; Abbott 1982a; Kudritzki, Pauldrach, & Puls 1987; Pauldrach et al. 1990; Shimada et al. 1994). Also, simple models of an "ensemble" of hydrogen-like resonance lines with Kramers-opacity transition strengths yield the analytic result $\alpha = 2/3$ (J. Puls, private communication).

The exponential "cut-off" parameter $\kappa_{\rm max}$ was introduced by OCR because a pure power law cannot model the fact that there must exist a single strongest optically thick line. The overall effect of $\kappa_{\rm max}$ is thus to limit the effect of strong driving lines. Theoretically, the value of $\kappa_{\rm max}$ should be equal to (or at least of the same order as) κ_o, in order to position the exponential cut-off near the point where $N(\kappa_L) = 1$, and thus avoid modeling fractions of lines. Note that the line-list distribution $dN/d\kappa_L$ assumes no overlap in the influence of the lines, and thus uses the single-scattering limit discussed above. In addition, the distribution has been "flux-weighted" in frequency such that

$$\frac{dN}{d\kappa_L} = \int_0^\infty d\nu \left(\frac{\nu L_\nu}{L_*} \right) \frac{dN_\nu}{d\kappa_L} \ , \tag{2.57}$$

and lines near the peak of the continuum spectrum have a stronger contribution to the distribution.

The sum over lines in the force is then replaced by an integral,

$$\sum_{\rm lines} \mathbf{g}^L_{\rm rad} = \int_0^\infty \mathbf{g}^L_{\rm rad} \frac{dN}{d\kappa_L} d\kappa_L \ , \tag{2.58}$$

and the *total* line force becomes

$$\begin{aligned}
\mathbf{g}^L_{\rm rad} &= \frac{v_{th}}{c^2} \oint d\Omega\, \hat{\mathbf{n}}\, I^C(\Omega) \int_0^\infty \kappa_L \frac{dN}{d\kappa_L} \left[\frac{1-\exp(-\kappa_L \rho L_{\rm Sob})}{\kappa_L \rho L_{\rm Sob}}\right] d\kappa_L \\
&= \frac{v_{th}}{c^2 \kappa_o^{\alpha-1}} \oint d\Omega\, \hat{\mathbf{n}}\, I^C(\Omega) \int_0^\infty \left(\frac{\kappa_L^{\alpha-1}}{e^{\kappa_L/\kappa \rm max}}\right) \left[\frac{1-\exp(-\kappa_L \rho L_{\rm Sob})}{\kappa_L \rho L_{\rm Sob}}\right] d\kappa_L \\
&= \frac{v_{th}}{c^2 \kappa_o^{\alpha-1}} \oint d\Omega\, \hat{\mathbf{n}}\, I^C(\Omega) (\rho L_{\rm Sob})^{-\alpha} \left[\tau_{\rm max}^{\alpha-1} - \left(\frac{\tau_{\rm max}}{\tau_{\rm max}+1}\right)^{\alpha-1}\right] \frac{,(\alpha)}{\alpha-1} \ ,
\end{aligned}$$

where $\tau_{\rm max} = (\kappa_{\rm max}\, \rho\, L_{\rm Sob})$. Thus, if we follow the pure CAK power law ensemble, with $\kappa_{\rm max} \to \infty$, the first term in the square brackets will be negligibly small, and the second term will approach unity. Then,

$$\mathbf{g}^L_{\rm rad} = \frac{v_{th}}{c^2 \kappa_o^{\alpha-1}} \oint I^C(\Omega) \frac{,(\alpha)}{1-\alpha} \left[\frac{\hat{\mathbf{n}} \cdot \nabla(\hat{\mathbf{n}} \cdot \mathbf{v})}{\rho(\mathbf{r}) v_{th}}\right]^\alpha \hat{\mathbf{n}}\, d\Omega \ . \tag{2.59}$$

Now that the complete Sobolev line force has been derived for a generalized geometry, let us perform the angle integral for certain specific cases. For a radial *point source* of radiation at the origin, the core intensity is given above in eq. (2.39), and the angle integral collapses into the purely radial form,

$$g^L_{\rm rad} = \frac{v_{th}}{c^2 \kappa_o^{\alpha-1}} \frac{L_*}{4\pi r^2} \frac{,(\alpha)}{(1-\alpha)[\rho(r) v_{th}]^\alpha} \left(\frac{\partial v_r}{\partial r}\right)^\alpha \tag{2.60}$$

$$= \frac{\sigma_e^{1-\alpha} L_*}{4\pi c r^2} \frac{k}{[\rho(r) v_{th}]^\alpha} \left(\frac{\partial v_r}{\partial r}\right)^\alpha \ , \tag{2.61}$$

using CAK's force constant k, defined in eq. (2.56). Note that k is sensitively dependent on v_{th}, and most published computations of k and α assume a fiducial hydrogen thermal velocity so that k can be defined independently of the exact composition and abundance of heavy (line driving) ions. Gayley (1995) recasts the CAK line ensemble into a form which clearly separates v_{th} and α from the normalization constant (k or κ_o), but we retain the original CAK notation here because it has become the standard convention.

Also note that the optically thin and thick limits of $\alpha = 0$ and $\alpha = 1$ are apparent in the above line acceleration, and intermediate values of α span this range continuously. This expression can be combined with the approximate thick-line expressions (2.45) and (2.51) to estimate the mean separation between thick lines in the chosen (k, α) distribution,

$$\Delta v \approx \frac{v_{th}^{\alpha}}{k} \left[\frac{1}{\sigma_e \rho} \left(\frac{\partial v_r}{\partial r} \right) \right]^{1-\alpha} \quad , \tag{2.62}$$

and the rough validity of the single-scattering limit can be directly assessed from a given model wind.

2.2.4 The Finite Stellar Disk

For a *spherical star* of finite radius R_*, the wind at a radius r will "see" a finite circular disk of radiation at the origin. Although the continuum force in the radial direction $g_{\rm rad}^C$ will be identical to the corresponding point-source force (due to Gauss' Law for the radiative flux), the line radiation term will be modified by the presence of nonradial rays from the stellar disk. Symmetry allows us to place our observer along the z-axis, and

$$\mathbf{g}_{\rm rad}^L = \frac{\sigma_e^{1-\alpha} k}{c} \oint I^C(\theta', \phi') \left[\frac{\hat{\mathbf{n}} \cdot \nabla(\hat{\mathbf{n}} \cdot \mathbf{v})}{\rho(\mathbf{r}) v_{th}} \right]^{\alpha} \hat{\mathbf{n}} \, \sin\theta' \, d\theta' \, d\phi' \quad , \tag{2.63}$$

where θ' and ϕ' are measured from the observer's position, not the origin. The azimuthal (ϕ') integral can be performed immediately, but the polar integral is less trivial.

Defining $\mu' = \cos\theta'$ and assuming a purely radial velocity field, the velocity gradient can be derived in general (Castor 1974; Koninx 1992), and is given by

$$\hat{\mathbf{n}} \cdot \nabla(\hat{\mathbf{n}} \cdot \mathbf{v}) = \mu'^2 \frac{\partial v_r}{\partial r} + (1 - \mu'^2) \frac{v_r}{r} \quad . \tag{2.64}$$

The bolometric core intensity can be written as

$$I^C(r, \theta', \phi') \; = \; \frac{L_*}{4\pi R_*^2} \, D(\mu', r) \tag{2.65}$$

where $D(\mu', r)$ is a limb darkening function. Often, a uniformly-bright disk is assumed, with

$$D(\mu', r) = \begin{cases} 0, & -1 \le \mu' < \mu_* \\ 1/\pi, & \mu_* < \mu' < +1 \end{cases} \tag{2.66}$$

where

$$\mu_*(r) \equiv \sqrt{1 - \frac{R_*^2}{r^2}} \tag{2.67}$$

defines the stellar limb, and $D(\mu', r)$ is normalized to give the same angle-integrated flux as in the point-star case, via

$$\frac{L_*}{4\pi r^2} = \frac{L_*}{4\pi R_*^2} 2\pi \int_{\mu_*}^{1} D(\mu', r)\, \mu'\, d\mu' \ . \tag{2.68}$$

Note that one could also use simple linear (grey atmosphere) limb darkening, obtained from the Eddington approximation,

$$D(\mu', r) = \begin{cases} 0, & -1 \le \mu' < \mu_* \\ (2 + 3\mu'')/4\pi, & \mu_* < \mu' < +1 \end{cases} \ , \tag{2.69}$$

where $\mu'' = \cos\theta''$, the angle on the star between radius $\mathbf{r}$ and the direction $\hat{\mathbf{n}}$ towards the point in the wind. Plane trigonometry gives this angle in terms of the observer-centered angle μ':

$$\mu'' = \sqrt{1 - \frac{r^2}{R_*^2}(1 - \mu'^2)} = \sqrt{\frac{\mu'^2 - \mu_*^2}{1 - \mu_*^2}} \ , \tag{2.70}$$

and, for completeness, the star-centered angle $\theta_o = \theta'' - \theta'$ is given by

$$\mu_o = \cos\theta_o = \frac{r}{R_*}\left[1 + \mu'\sqrt{\mu'^2 - \mu_*^2} - \mu'^2\right] \ . \tag{2.71}$$

The general radial line radiation force is now given by

$$g_{\rm rad}^L = \frac{2\pi\sigma_e^{1-\alpha}k}{c[\rho(r)v_{th}]^\alpha}\left(\frac{L_*}{4\pi R_*^2}\right)\int_{-1}^{+1} D(\mu', r)\left[\mu'^2\frac{\partial v_r}{\partial r} + (1 - \mu'^2)\frac{v_r}{r}\right]^\alpha \mu'\, d\mu' \ . \tag{2.72}$$

It is common to define and work with a *finite disk factor,* which isolates the finite disk correction to the simple point source model, and is the ratio of respective line accelerations,

$$\boldsymbol{\eta}^{\rm L} \equiv \frac{\mathbf{g}_{\rm rad}^L(\text{finite disk})}{g_{\rm rad}^L(\text{point source})} \tag{2.73}$$

$$= \frac{2\pi}{(1 - \mu_*^2)(dv_r/dr)^\alpha}\int_{-1}^{+1} D(\mu', r)\left[\mu'^2\frac{\partial v_r}{\partial r} + (1 - \mu'^2)\frac{v_r}{r}\right]^\alpha \mu'\, d\mu' \ , \tag{2.74}$$

and is, in general, a vector quantity. The finite disk factor does not depend on the wind density $\rho(\mathbf{r})$ or on the line distribution constant k, but does depend sensitively

on the exponent α. A continuum finite disk factor $\boldsymbol{\eta}^{\rm C}$ can also be defined, but for a spherical star it is purely radial with a magnitude of unity. Note that, if one defines the logarithmic derivative variable (Castor 1970)

$$\sigma = \frac{\partial \ln v_r}{\partial \ln r} - 1 = \frac{r}{v_r}\frac{\partial v_r}{\partial r} - 1 \quad , \tag{2.75}$$

then one can express the projected velocity gradient as

$$\mu'^2 \frac{\partial v_r}{\partial r} + (1-\mu'^2)\frac{v_r}{r} = \left(\frac{1+\sigma\mu'^2}{1+\sigma}\right)\frac{\partial v_r}{\partial r} \quad , \tag{2.76}$$

and the μ'-integral becomes easier to evaluate. This σ variable is a convenient measure of the anisotropy of the local velocity gradient. Very close to the star $\sigma \gg 1$, which implies the radial velocity derivative $\partial v_r/\partial r$ dominates the overall expansion. At an intermediate radius in the wind, σ drops to zero, and the expansion is locally isotropic. In the outer wind, σ asymptotically approaches -1 at large radii, and the spherical geometry, in the term v_r/r, dominates the (now mainly lateral) expansion.

For the uniformly bright disk (Castor 1974; CAK), the μ'-integral can be evaluated analytically using eq. (2.76) for the projected velocity gradient, and the radial component of the finite disk factor is

$$\eta_r^L(\text{uniform}) \equiv \eta_{un} = \frac{2}{(1-\mu_*^2)(1+\sigma)^\alpha}\int_{\mu_*}^1 (1+\sigma\mu'^2)^\alpha \mu'\, d\mu' \tag{2.77}$$

$$= \frac{(1+\sigma)^{1+\alpha} - (1+\sigma\mu_*^2)^{1+\alpha}}{\sigma(1+\alpha)(1+\sigma)^\alpha(1-\mu_*^2)} \quad . \tag{2.78}$$

Kudritzki et al. (1989) and Koninx (1992) define a convenient variable

$$\chi \equiv \frac{R_*^2}{r^2}\left[1 - \frac{v_r}{r(\partial v_r/\partial r)}\right] = (1-\mu_*^2)\left(\frac{\sigma}{\sigma+1}\right) \tag{2.79}$$

and the uniformly bright finite disk factor can be written as a function of this single variable,

$$\eta_{un} = \frac{1-(1-\chi)^{1+\alpha}}{\chi(1+\alpha)} \quad . \tag{2.80}$$

For points extremely far from the star, $r \to \infty$, $\mu_* \to 1$, and $\sigma \to -1$, η_{un} naturally approaches unity, because the star more and more resembles a true "point source." Very close to the stellar surface, however, $\mu_* \to 0$ and $\sigma \gg 1$, and in this limit, $\chi \to 1$, and

$$\eta_{un} \to \frac{1}{1+\alpha} \quad . \tag{2.81}$$

For the linearly limb-darkened disk, the finite disk factor takes the form

$$\eta_{limb} \;=\; \frac{\eta_{un}}{2} + \frac{3}{2(1-\mu_*^2)(1+\sigma)^\alpha}\int_{\mu_*}^{1}(1+\sigma\mu'^2)^\alpha\sqrt{\frac{\mu'^2-\mu_*^2}{1-\mu_*^2}}\mu'\,d\mu' \quad . \tag{2.82}$$

This integral is, in general, analytically intractable. However, for points extremely far from the star, and for the $\sigma = 0$ point, η_{limb} naturally approaches the uniformly bright η_{un} (which is unity at these radii). Very close to the star, when $\mu_* \rightarrow 0$ and $\sigma \gg 1$,

$$\frac{\eta_{limb}}{\eta_{un}} \;\rightarrow\; \frac{1}{2} + \frac{3}{2}\left(\frac{1+\alpha}{3+2\alpha}\right) \quad , \tag{2.83}$$

which only ranges between 1 and 1.1 for all allowed values of the exponent α. For example, when $\alpha = 0.5$, this ratio approaches 1.0625, and when $\alpha = 0.7$, it approaches $\sim$1.0795. Note also that for $\alpha = 0.5$, the above integral can be computed analytically, but the expression is extremely complex, and there is little practical use in transcribing this solution here. Figure 2.1 illustrates the radial dependence of η_{un} (dashed line, computed analytically) and η_{limb} (solid line, computed numerically) for various values of the exponent α, and for various velocity laws characterized by the simple fitting formula

$$v_r(r) \;=\; v_\infty\left(1-\frac{R_*}{r}\right)^\beta \quad . \tag{2.84}$$

Note that the error in assuming a uniformly bright disk is small, only 5–8% near the surface, and much less so further out.

We can assess the dynamical impact of this modified finite disk factor on a one-dimensional spherically symmetric wind by examining the equation of motion of the wind in the highly supersonic, or zero sound speed limit (Kudritzki et al. 1989; Gayley, Owocki, & Cranmer 1995). Near the surface of the star ($\sigma \gg 1$), where the mass loss rate is thought to be determined, the overall effect of any finite disk factor η on the mass loss rate $\dot{M}$ can be approximated by

$$\dot{M} \;\approx\; \eta^{1/\alpha}\,\dot{M}(\text{point source}) \quad , \tag{2.85}$$

where η is evaluated at the dynamical critical point (see Section 2.3.2 below). Thus, if we can assume the surface values of η_{limb}/η_{un} at the critical point, the effect of including limb darkening could result in a relative mass loss increase of $\sim$11% ($\alpha = 0.7$) to $\sim$13% ($\alpha = 0.5$) over the uniformly-bright models.

2.2.5 The Effect of the Ionization Balance

Abbott (1982a) performed an extensive calculation of the radiative line force using a list of bound-bound transitions spanning six stages of ionization and the

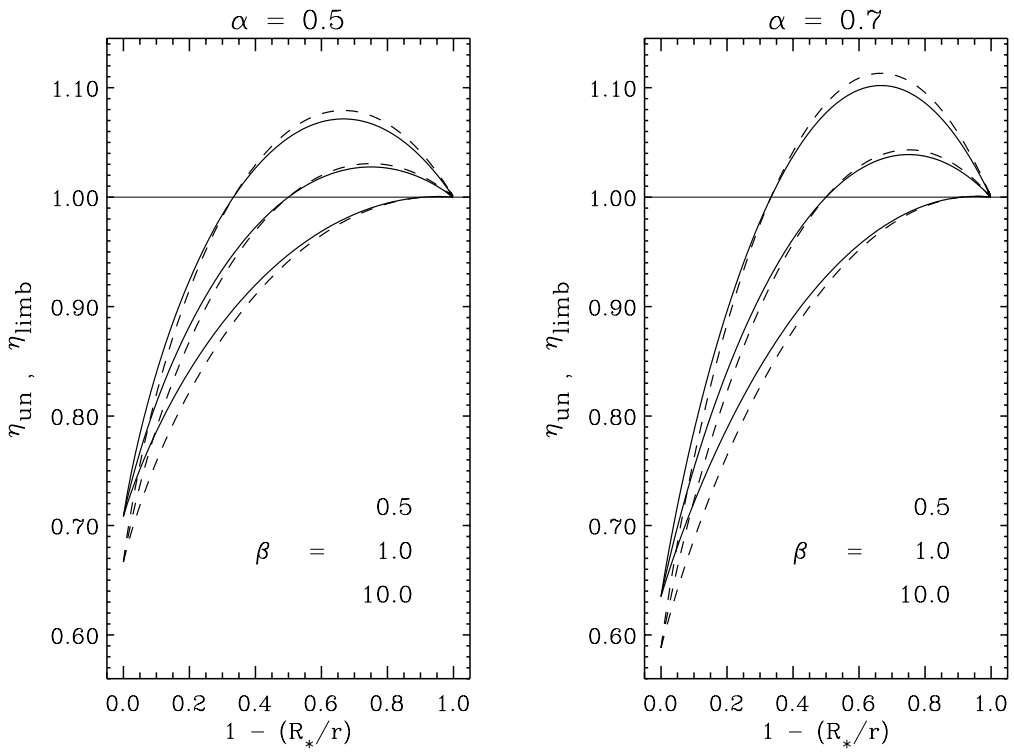

Figure 2.1: The spherical-star finite disk (FD) factor, plotted versus radius in the wind, for various models and assumptions. The dashed lines are the analytic uniformly-bright FD factors, and the solid lines are the numerically-computed FD factors with linear limb darkening. The two plots represent winds with $\alpha = 0.5$ (left) and $\alpha = 0.7$ (right), and the three sets of curves on each plot represent (from top to bottom) velocity laws with $\beta = 0.5$, 1.0, and 10.0.

elements H to Zn. This work confirmed earlier results concerning the dependence of the force on the temperature distribution and chemical composition (through, e.g., the continuum opacity σ_e), but introduced a new dependence on the relative state of ionization of the wind. It was found that, since lower ionization stages contain more lines, the force tends to increase with increasing electron number density n_e, as roughly predicted by the LTE Saha rate equation. However, because the ionization balance remains roughly constant throughout the wind, the force is relatively insensitive to this phenomenon, and is a minor (but necessary) effect. Abbott (1982a) thus assumed a weak power-law dependence on the quantity

$$N_{11} \equiv \frac{n_e}{W} \times 10^{-11}\ \mathrm{cm}^3 \ , \tag{2.86}$$

where the dimensionless "dilution factor" W is defined as the fraction of solid angle Ω_* occupied by the star for an observer at distance r, and for a spherical star,

$$W = \frac{\Omega_*}{4\pi} = \frac{1}{4\pi}\int_{\phi'=0}^{2\pi}\int_{\mu'=\mu_*}^{1} d\mu' d\phi' = \frac{1}{2}(1-\mu_*) \ , \tag{2.87}$$

and it is required to take into account the spherical geometry of the extended envelope around the star. The local radiation density is diluted by this amount as one moves away from the star, and thus affects the photoionization-recombination balance directly. Mihalas (1978, eq. [5-46]) showed that the ionization balance of spherically symmetric winds, via the population ratio (N_j/N_{j+1}), depends linearly on the above factor of (n_e/W).

For a fully-ionized gas, one can write $n_e \approx \rho/\mu m_H$, with the mean molecular weight μ defined as above in eq. (2.12), and the modified fit to the radiation line force can be written

$$g^L_{\mathrm{rad}} \ = \ \frac{GM,}{r^2} k\eta \left(\frac{1}{\sigma_e \rho v_{th}}\frac{\partial v_r}{\partial r}\right)^{\alpha} N_{11}^{\delta} \ . \tag{2.88}$$

The exponent δ typically ranges from 0.02–0.2 in early type stellar winds, and the radiative force thus depends on the density as $\rho^{\delta-\alpha}$. Pauldrach et al. (1990) more recently computed non-LTE models for the line force, using more than 10^5 transitions, and found agreement with Abbott's values of δ at $T_{\mathrm{eff}} > 35,000$ K, but found slightly lower values for cooler temperatures.

2.3 Wind Solutions

2.3.1 Nonlinear Solution Methods

The radiative acceleration derived in Section 2.2 can now be inserted into the radial momentum conservation equation derived in Section 2.1, and this equation

can be solved for the velocity law $v_r(r)$ and mass loss rate $\dot{M}$ of the wind. We proceed in this Section from approximate analytic solutions to successively more sophisticated numerical solutions, and we apply these results to a standard model of the O4f supergiant ζ Puppis (HD 66811) to compare with observations. For this model, we take $M_* = 60 M_\odot$, $R_* = 19 R_\odot$, $L_* = 8 \times 10^5 L_\odot$, and $T_{\rm eff} = 42{,}000\,{\rm K}$ (see, e.g., Howarth & Prinja 1989; Kudritzki et al. 1992). We assume an isothermal wind of temperature $T_{\rm eff}$, corresponding to a sound speed $a = 24\,{\rm km\ s^{-1}}$, and use the line-driving constants $\alpha = 0.60$, $k = 0.15$, and $\delta = 0$. The observed terminal velocity of ζ Puppis is approximately 2200–2500 km s^{-1}, and the mass loss rate, depending on the method of measurement, ranges from 2×10^{-6} to $6 \times 10^{-6}\ M_\odot {\rm yr}^{-1}$ (Prinja et al. 1990; Lamers & Leitherer 1993; Puls et al. 1996).

Using the mass flux constraint (eq. [2.9]) to eliminate the density in the line acceleration, the "CAK equation of motion" can be written in terms of the radius r, radial velocity v, and mass loss rate $\dot{M}$, as

$$\left(v - \frac{a^2}{v}\right)\frac{dv}{dr} + \frac{GM_*(1-\ ,\ )}{r^2} - \frac{2a^2}{r} + \frac{da^2}{dr} - \frac{GM_*,}{r^2} k\eta \left[\frac{4\pi}{\sigma_e v_{th} \dot{M}}\right]^\alpha \left(r^2 v \frac{dv}{dr}\right)^\alpha \ = \ 0 \ , \tag{2.89}$$

where we temporarily neglect the Abbott (1982a) δ-factor. We implement a convenient choice of dimensionless variables,

$$x \equiv \frac{r}{R_*} \quad , \quad u \equiv \frac{v}{a} \quad , \quad w \equiv \frac{r^2 v}{GM_*}\left(\frac{dv}{dr}\right) = \frac{x^2 u}{\Pi}\left(\frac{du}{dx}\right) \quad , \tag{2.90}$$

although for non-isothermal winds, the normalizing value of a must be chosen at a representative radius. Also, the CAK equation is multiplied by an overall factor of r^2/GM_* to scale out the gravitational acceleration. Note that the constant $\Pi \equiv GM_*/a^2 R_*$ is defined as the ratio of the stellar radius R_* to the density scale height $H_\rho = a^2/(GM_*/R_*^2)$ at the stellar surface. Also, Π is the ratio of twice the "Parker radius" $(GM_*/2a^2)$ to the stellar radius R_*, and is a useful constant when working with the dimensionless variables x, u, and w. The left-hand side of the equation of motion, then, is an explicit function F_1 of x, u, and w:

$$F_1(x,u,w) = \left(1 - \frac{1}{u^2}\right) w - H(x) - C\eta w^\alpha = 0 \ , \tag{2.91}$$

where

$$H(x) \ = \ , \ -1 + \frac{2x}{\Pi} + \frac{x^2}{\Pi a^2}\frac{da^2}{dx} \ , \tag{2.92}$$

$$C \ = \ , \ k\left(\frac{4\pi G M_*}{\sigma_e v_{th} \dot{M}}\right)^\alpha \ , \tag{2.93}$$

The equation $F_1 = 0$ thus needs to be solved for u and w as functions of x, the normalized radius, and for the constant $\dot{M}$, which we shall see acts as an eigenvalue of the problem.

It is becoming evident that steady-state solutions to CAK-type equations (see, e.g., Poe, Owocki, & Castor 1990) represent a kind of "attractor," where the mass loss rate $\dot{M}$ is maximized for a given set of initial parameters. However, if $\dot{M}$ is too large, and too much mass is pushed outwards, the radiative force cannot drive the material to infinity, and it falls back down on the star in a time-dependent, usually oscillatory, manner. Thus, steady-state solutions tend to exhibit a unique value of $\dot{M}$, which represents the maximum mass that can be driven to infinity, and thus is the focal point of the attractor.

The wind equation $F_1(x, u, w) = 0$ is a highly non-linear differential equation. The variable w, however, is proportional to du/dx, and if it were possible to solve for w, one could integrate the equation to find the desired velocity law $u(x)$ of the wind. Because there are different regions in the x-u phase space where there are zero, one, or two real solutions for w, one must further specify the *singularity condition*

$$F_2(x, u, w) = \frac{\partial F_1}{\partial w} = 0 \ . \tag{2.94}$$

The solution to the two equations $F_1 = 0$, $F_2 = 0$ forms a curve, the "singular locus," in phase space, which divides a region of no solutions from a region of two solutions (see Cassinelli 1979; Bjorkman 1995). Because the first class of velocity solutions $u(x)$ we wish to consider are the most well-behaved, mathematically (i.e., continuously differentiable functions of x that range from $x = 1$ to $x \to \infty$), we require that these solutions not cross this problematic singular locus.

If the wind equation were *linear* in w or du/dx, i.e., if

$$F_1^* \ = \ A_1(x, u) + \frac{du}{dx} B_1(x, u) \ = \ 0 \ , \tag{2.95}$$

then the singularity condition would demand both $A_1 = 0$ and $B_1 = 0$, and this defines a discrete set of "critical points" $\{x_c, u_c\}$ of the flow. Parker's (1958, 1963) isothermal solar wind solutions have this topology, and the only solutions which satisfy all physical boundary conditions must pass through a transsonic critical point $u_c = 1$. The velocity derivative at the critical point is given by L'Hôpital's rule,

$$\left(\frac{du}{dx}\right)_{\rm crit} \ = \ -\frac{dA_1/dx}{dB_1/dx} \ , \tag{2.96}$$

and Abbott (1980) and Koninx (1992) demonstrate that critical points are also locations where small perturbations in the flow have zero characteristic velocity in

the inertial frame of the star. Of course, solutions which do not pass through critical points are possible (e.g., Chamberlain's [1961] "breeze" solutions), but they can have drastically different boundary properties from those which do pass through critical points.

The general nonlinear form of $F_1(x,u,w)$ in the present hot-star wind analysis has a similar general character to the linear limit above in that there are critical points of the flow, existing on singular loci, which can be located using the above singularity condition and a nonlinear generalization of L'Hôpital's rule, the so-called *regularity condition,*

$$F_3(x,u,w) \equiv \frac{\partial F_1}{\partial x} + \frac{du}{dx}\frac{\partial F_1}{\partial u} \tag{2.97}$$

$$= \frac{\partial F_1}{\partial x} + \left(\frac{\Pi w}{u x^2}\right)\frac{\partial F_1}{\partial u} = 0 \ . \tag{2.98}$$

Non-critical points that lie on singular loci do not connect to analytic (continuously differentiable) solutions, so if a desired steady-state solution must "graze" a singular locus, it must do so at a critical point. Poe, Owocki, & Castor (1990) found that, in the Sobolev approach, the wind solution which carries the maximum mass loss rate to infinity is precisely that which grazes the singular locus at a critical point. (See also Bjorkman 1995 for a discussion of other formal critical points of the CAK equations.)

The three equations, $F_1 = F_2 = F_3 = 0$, almost serve to specify the critical values of x_c, u_c, and w_c, but what thwarts a straightforward solution is the fact that the value of the constant mass loss rate $\dot{M}$ (or equivalently, the constant C in eq. [2.91]) is initially unknown. Thus we have three equations and four unknowns. This problem is solved in practice by guessing a value for the critical radius x_c, and solving the system of equations for u_c, w_c, and C. With this trial critical solution in place, one needs to evaluate whether the velocity law $u(x)$ which passes through it is consistent with the assumed static stellar model. After integrating $u(x)$ from x_c down to the star's surface ($x = 1$), various tests can be performed to evaluate the consistency of the model wind. This "matching" of the core/halo boundary conditions is, in effect, the fourth piece of information required to determine all the variables at the critical point. CAK defined the stellar photosphere as the surface at which the optical depth is unity, and a continuum Sobolev optical depth variable t can be evaluated as a check:

$$t \equiv \frac{\sigma_e \rho v_{th}}{dv/dr} = \left(\frac{\sigma_e v_{th}}{4\pi G M_*}\right)\frac{\dot{M}}{w} \ , \tag{2.99}$$

where w is evaluated at $x = 1$. Note that, although t is not the true optical depth as seen by an observer at infinity, it approaches the true continuum optical depth,

$$\tau_c = \int_{R_*}^{\infty} \sigma_e \rho \, dr \;\approx\; \sigma_e \rho H_\rho \;\approx\; \sigma_e \rho \, \frac{v}{dv/dr} \quad , \tag{2.100}$$

where H_ρ is the density scale height (related to the flow velocity scale height by the mass continuity equation), when $v \approx v_{th}$ as is the case very near the stellar surface. Near the photosphere, the wind velocity grows exceedingly small, and one can begin to assume *hydrostatic* conditions. If the near-isothermality of the gas is maintained, then the density rises (and the velocity falls) exponentially with depth, and differences of a few scale heights do not appreciably affect the overall position of the actual stellar radius (the $x = 1$ point).

Although this implies that the condition $t \approx 1$ can be used to locate the photosphere, and thus utilized to iterate to find the correct value of x_c, the use of the Thomson scattering opacity in t is suspect both in B stars, where bound-free and free-free continuum processes become important, and in Wolf-Rayet stars, where the continuum is optically thick in large regions of the wind. Thus, in practice, the most robust way to "locate the static photosphere" is to integrate downwards from the assumed x_c and evaluate the *velocity* $v(1)$ at $x = 1$ (usually via extrapolation from a numerical grid). The near-hydrostatic region is entered when $v(1) \ll a$, or $u(1) \ll 1$, and a useful condition to define the photosphere is to set a constant fraction of the sound speed, say $u(1) \approx 0.01$. Usually, if the extrapolated value of $u(1)$ is too large, then x_c is too close to the stellar surface, and if the extrapolated $u(1)$ is too small, then x_c is too large. Often, for x_c much too large, the integration may suggest a value of $u(1)$ which is unphysically negative, or there may not be solutions to the wind equation below a certain radius.

Usually, one avoids integrating outward from the critical point until the iteration process outlined above converges on the correct critical point x_c. CAK suggest a further iteration to find the temperature structure, and Pauldrach, Puls, & Kudritzki (1986, hereafter PPK) perform this using non-LTE radiative transfer, but since the wind velocity structure is quite insensitive to the temperature law, we shall consider the imposed $T(r) = T_{\rm eff}$ as correct. Lucy & Abbott (1993), however, derive a clever approximate method for determining $T(r)$ in Wolf-Rayet winds which is worthy of note. One can write the radiative force due the combined effect of continuum and lines in terms of a general "effective" scattering coefficient,

$$(g^C_{\rm rad} + g^L_{\rm rad}) \;=\; \frac{\sigma_{\rm eff}(r)}{c} \frac{L_*}{4\pi r^2} \quad , \tag{2.101}$$

and use the velocity law (obtained via a previous iteration in the temperature structure) to solve for $\sigma_{\rm eff}$ as a function of radius from the equation of motion:

$$\frac{\sigma_{\rm eff}}{\sigma_e} = \frac{1}{,}\left[\left(1-\frac{1}{u^2}\right)w - H(x) + ,\right] \quad . \tag{2.102}$$

This scattering coefficient allows an optical depth variable to be defined,

$$\tilde{\tau} = \int_r^\infty \sigma_{\rm eff}\,\rho\left(\frac{R_*}{r}\right)^2 dr \quad , \tag{2.103}$$

which here assumes an isotropic Eddington factor $f_\nu \equiv K_\nu/J_\nu = 1/3$, as opposed to the radial-streaming value $f_\nu = 1$ assumed in eq. (2.100) above (see Mihalas 1978). This optical depth can be used in a modified Milne-Eddington temperature distribution for a spherically extended gray atmosphere in radiative equilibrium,

$$T(r)^4 = \frac{1}{2}T_{\rm eff}^4\left(2W + \frac{3}{2}\tilde{\tau}\right) \quad , \tag{2.104}$$

where the dilution factor W is given by eq. (2.87). In the optically-thin limit, $T(r)$ depends only on $W^{1/4}$, which varies very slowly with radius. This method of zero-order radiative transfer takes into account "line blanketing" due to the spectral lines that contributed to the line radiation force, but is necessarily limited by the many approximations discussed above.

2.3.2 Analytic Approximations and Empirical Fits

The first analytic solution of the Sobolev wind equations was that of CAK, who ignored the finite disk factor ($\eta = 1$), considered constant values of k and α with radius, and neglected the ionization factor δ. Also, since gas pressure forces play a relatively minor role in driving the highly-supersonic wind, one can neglect these terms ($a \to 0$) in the CAK wind equation (2.89). In fact, the assumption of "zero sound speed" is an approximation of the same order as the use of the Sobolev approximation in both the subsonic and supersonic regions. The wind equation becomes, in the limit $a \to 0$ (or, equivalently, $u \gg 1$),

$$F_1 \approx w + 1 - , \; - Cw^\alpha = 0 \quad , \tag{2.105}$$

and the singularity condition

$$F_2 = \frac{\partial F_1}{\partial w} \approx 1 - \alpha C w^{\alpha-1} = 0 \tag{2.106}$$

allows for the immediate solution of w and C at the critical point,

$$w_c = \frac{\alpha}{1-\alpha}(1 - , \;) \quad , \qquad C = \frac{1}{\alpha^\alpha}\left(\frac{1-,}{1-\alpha}\right)^{1-\alpha} \quad . \tag{2.107}$$

Note, however, that the equation $F_1 = 0$ here does not depend on the radius r. Thus, if one point in the wind satisfies the critical conditions, all points do, and $w \propto r^2 v(dv/dr)$ remains *constant* in the wind. Thus, one can immediately integrate from the stellar radius R_*, and obtain

$$v_{\rm CAK}(r) = v_\infty \left(1 - \frac{R_*}{r}\right)^{1/2} \quad , \tag{2.108}$$

where the asymptotic ("terminal") wind speed is given by

$$v_\infty = \sqrt{\frac{\alpha}{1-\alpha} \frac{2GM_*(1-,)}{R_*}} = \sqrt{\frac{\alpha}{1-\alpha}}\, V_{\rm esc} \quad . \tag{2.109}$$

In addition, the mass loss rate can be found from the definition of the constant C (and, of course, the assumption that k and α remain constant throughout the wind), and

$$\dot{M}_{\rm CAK} = \frac{L_*}{c^2} \left\{ \alpha k^{1/\alpha} \left(\frac{c}{v_{th}}\right) \left[\frac{(1-\alpha),}{1-,}\right]^{(1-\alpha)/\alpha} \right\} \quad . \tag{2.110}$$

For our standard model of ζ Puppis this CAK analysis yields $v_\infty = 1080$ km s^{-1} and $\dot{M} = 5.9 \times 10^{-6}\, M_\odot {\rm yr}^{-1}$, and the terminal velocity v_∞ is quite different from the observed value. The mass loss rate scales with $k^{1/\alpha}$, so modeling a given $\dot{M}$, at least in an *ad hoc* fashion, is not difficult. CAK also computed numerical models with finite gas pressure terms, and found only small variations from the analytic results above. However, these models allowed the computation of a unique critical radius x_c, which CAK found to be approximately 1.5–1.7 times the sonic radius x_s, which is the radius at which $v = a$, and is usually extremely close to the photosphere ($x_s \approx 1$).

The critical radius x_c and velocity u_c can be estimated by applying the regularity condition $F_3 = 0$ to the wind equation (2.91), with no finite disk factor ($\eta = 1$), but *retaining* the small terms proportional to the finite sound speed. Thus,

$$F_3 = \frac{\partial F_1}{\partial x} + \left(\frac{\Pi w}{u x^2}\right) \frac{\partial F_1}{\partial u} = -\frac{2}{\Pi} + \frac{2\Pi w^2}{u^4 x^2} = 0 \quad , \tag{2.111}$$

and we can solve for the critical radius

$$x_c = \frac{\Pi w_c}{u_c^2} \quad . \tag{2.112}$$

Because the addition of a finite sound speed only significantly affects the wind in the subsonic region, one can use the value of w_c derived above in the *zero* sound speed limit, and the associated velocity (evaluated at x_c),

$$u_c = \frac{v_\infty}{a} \sqrt{1 - \frac{1}{x_c}} \quad , \tag{2.113}$$

to find that the critical radius in this approximation is exactly 1.5 times the stellar radius:

$$x_c = 1 + \frac{\Pi w_c}{(v_\infty/a)^2} \;=\; 1 + \frac{1}{2} \;. \tag{2.114}$$

This comes very close to the actual values found by self-consistently integrating the differential equation $F_1 = 0$ and evaluating the optical depth (or velocity) at the stellar surface (CAK).

Strictly speaking, when finite sound speed terms are included in the CAK equation of motion, the velocity never reaches an asymptotic terminal velocity v_∞, and instead grows logarithmically without bound as $r \to \infty$. This occurs because of the sound speed term $2a^2/r$ which dominates the expansion exterior to the "Parker radius" ($R_P = GM_*/2a^2 \gg R_*$). More realistic models with a decreasing wind *temperature,* however, negate the importance of this term at large radii, and a reasonably constant terminal v_∞ is achieved.

Friend and Abbott (1986, hereafter FA), nearly simultaneously with PPK, extended CAK's theoretical framework by including the uniformly-bright *finite disk factor* (see Section 2.2.4), gas pressure terms, and rotation in the equatorial plane. Least squares fits to the numerical results of FA give a similar velocity law,

$$v_{\rm FA}(r) \;=\; v_\infty \left(1 - \frac{R_*}{r}\right)^\beta \;, \tag{2.115}$$

but with $\beta \approx 0.8$, and

$$v_\infty \;\approx\; 2.2\, V_{\rm esc}\, \frac{\alpha}{1-\alpha} \left(\frac{V_{\rm esc}}{10^3 \text{ km s}^{-1}}\right)^{0.2} \left(1 - \frac{V_{\rm eq}}{V_{\rm crit}}\right)^{0.35} \;, \tag{2.116}$$

$$\dot{M}_{\rm FA} \;\approx\; \frac{1}{2} \dot{M}_{\rm CAK} \left(\frac{V_{\rm esc}}{10^3 \text{ km s}^{-1}}\right)^{-0.3} \left(1 - \frac{V_{\rm eq}}{V_{\rm crit}}\right)^{-0.43} \;, \tag{2.117}$$

where the rotational dependence of $\dot{M}_{\rm FA}$ was obtained by Bjorkman and Cassinelli (1993) from FA's Figure 4 (see Chapter 4 for more information on rotating models). The inclusion of the finite disk factor decreases the radiation force near the base of the wind; i.e., $\eta \to 1/(1+\alpha)$ as $r \to R_*$, because there are comparatively fewer radially-directed photons near a source of large "horizontal" extent, but $\eta \to 1$ as $r \to \infty$, because the star looks more like a point source as one recedes from it. The mass loss rate, which is determined in the vicinity of the critical point, is thus reduced. Because less material is accelerated into the outer parts of the wind, where the force becomes close to the point-star force, the terminal velocity increases. The inclusion of the finite disk factor, then, causes roughly no change in the final wind momentum $\dot{M} v_\infty$, but their individual values agree much better

with the observations: for the same assumed α and k constants as above, FA's fit formulae give, for the standard nonrotating ζ Puppis model, $v_\infty = 2850$ km s^{-1} and $\dot{M} = 3.0 \times 10^{-6}\, M_\odot \mathrm{yr}^{-1}$.

In these models, the critical radius also becomes smaller, with $x_c \approx 1.02 - 1.05$, but moves outward with increasing rotation rate. Because x_c is so close to the stellar surface, Gayley, Owocki, & Cranmer (1995) found that it is reasonably safe to assume a constant critical value for the finite disk factor $\eta_c \equiv 1/(1+\alpha)$, and estimate the modified mass loss rate as if η_c were simply a constant multiplying k, i.e.,

$$\dot{M}_{\rm FD} \approx \eta_c^{1/\alpha} \dot{M}_{\rm CAK} \quad . \tag{2.118}$$

For the above model of ζ Puppis, this factor reduces the CAK mass loss rate to $2.7 \times 10^{-6}\, M_\odot \mathrm{yr}^{-1}$.

Note that while the mass loss rate is determined at the critical point, very close to the star, v_∞ is determined effectively at *infinite* radius (because it is "built up" cumulatively, once the mass flux is known that can be driven to infinity). Assuming that the radial velocity obeys a "beta law" at large radii,

$$v_r(r) = v_\infty \left(1 - \frac{R_*}{r}\right)^\beta \quad , \qquad \frac{\partial v_r}{\partial r} = \frac{\beta v_\infty R_*}{r^2} \left(1 - \frac{R_*}{r}\right)^{\beta-1} \quad , \tag{2.119}$$

we can substitute this back into the zero-sound speed equation of motion and take the limit $r \to \infty$. At large radii, we can ignore the finite disk factor (because the star appears as a point source) and write eq. (2.105) in this limit as

$$U^2 + 1 - , \ - C U^{2\alpha} = 0 \quad , \tag{2.120}$$

where $U \equiv (v_\infty / V_{\rm esc})(2\beta)^{1/2}$ and $V_{\rm esc} \equiv (2GM_*/R_*)^{1/2}$. Thus, if $\dot{M}$ is estimated as above, the above algebraic equation can be solved (numerically, if $\alpha \neq 0.5$) for U. The weak dependence in U on the unknown value of β is a minor disadvantage, but it only results in a 10–20% uncertainty in the final value of v_∞.

For α close to 0.5 we can Taylor-expand the slowly-varying function $U^{2\alpha}$ about a constant U_0:

$$U^{2\alpha} = U_0^{2\alpha} + 2\alpha\,(U - U_0)\,U_0^{2\alpha-1} + \cdots \tag{2.121}$$

$$\approx U_0^{2\alpha} \left[(1 - 2\alpha) + 2\alpha\,(U/U_0)\right] \quad . \tag{2.122}$$

If we take $U_0 = 1$,

$$U \approx \alpha C \pm \sqrt{\alpha^2 C^2 - 2\alpha C - 1 + , \ + C} \ \sim \ 2\alpha C \quad , \tag{2.123}$$

and the positive solution is the physically realistic one. Note, however, that the exact solution to the transcendental equation (2.120) is more accurate, and this

Taylor expansion is presented only to illustrate how U is approximately dependent on α and C in this analysis. However, eq. (2.123) does illustrate the fact that, for $\dot{M}$ too large, or C too small, there will be no steady state solutions driven to infinity. In fact, the minimum value of C (found by setting the terms under the square root to zero) is remarkably close (within $\sim 2\%$ for $\alpha = 0.5$–0.7) to the critical point-star value of C found above (eq. [2.107]). For the standard nonrotating ζ Puppis model, eq. (2.120) is solved by $v_\infty = 2688$ km s^{-1} (if we assume $\beta = 0.8$), and the above expansion yields $v_\infty \approx 2374$ km s^{-1}.

More recent sets of semi-analytic models have provided better, but more complex fitting formulae for v_∞, $\dot{M}$, and β of O and B stars. PPK computed grids of models taking into account the finite disk factor, gas pressure terms, and a line force dependent on the state of ionization of the wind. They fit closed-form scaling relations to v_∞ and $\dot{M}$, but the equations are too complex to be reproduced here. Of interest, however, is a fit for the exponent β for models with $T_{\rm eff}$ in the range 20000–50000 K,

$$\beta \approx 0.97\alpha + 0.032 \left(\frac{V_{\rm esc}}{500\,{\rm km\ s^{-1}}} \right) + \frac{0.008}{\delta} \quad , \tag{2.124}$$

where δ is the exponent in the line force modified to take varying stages of ionization into account (see Section 2.2.5). Kudritzki et al. (1989) and Villata (1992) have built up more complex, but more robust expressions for v_∞ and $\dot{M}$. The detailed finite disk and ionization correction factors are modeled approximately as functions of radius only, so that the implicit differential equation of motion can be solved "graphically" (i.e., with numerical root-finding techniques) as an algebraic equation in x, u, and w. Specifically, the Kudritzki et al. (1989) "cooking recipe" gives $v_\infty = 2649$ km s^{-1} and $\dot{M} = 3.8 \times 10^{-6}\, M_\odot {\rm yr}^{-1}$ for the standard ζ Puppis model star.

2.3.3 Numerical Wind Models

The one-dimensional CAK equation of motion (eq. [2.91]) can be solved numerically in several ways. Here we discuss two such solution methods: (1) the "modified CAK" (mCAK) approach, which iteratively locates the critical point and integrates upward and downward from it in radius, and (2) full time-dependent hydrodynamics (using the piecewise parabolic code VH-1) which evolves an approximate initial condition to find possible steady end-states.

The mCAK method first requires the critical values of x_c, u_c, w_c, and C to be found, as discussed above. By starting from an assumed critical radius x_c and, e.g., FA's empirical velocity law fit as an initial guess, we use the Newton-Raphson method of finding roots of the nonlinear system of equations $F_1 = F_2 = F_3 = 0$

to evaluate u_c, w_c, and C. The fact that the wind equation itself ($F_1 = 0$) can be algebraically solved for C allows us to collapse the nonlinear search space from three to two dimensions. After substituting this value of C into the singularity and regularity equations, the Newton-Raphson correction equation

$$\begin{pmatrix} \partial F_2/\partial u & \partial F_2/\partial w \\ \partial F_3/\partial u & \partial F_3/\partial w \end{pmatrix} \begin{pmatrix} \delta u \\ \delta w \end{pmatrix} = \begin{pmatrix} -F_2 \\ -F_3 \end{pmatrix} \tag{2.125}$$

is easily solved for the incremental corrections to u_c and w_c (δu and δw). Various "acceleration" techniques can be used to improve the convergence of this procedure, (see, e.g., Press et al. 1989), but a good starting guess is of primary importance to the rapid convergence of a solution.

With all dynamical variables determined at the critical point, one can integrate inwards and outwards by numerically solving eq. (2.91) for w, and thus du/dx, and stepping up and down in x with a numerical integration routine. In most of the wind, two solution branches for w exist, and the critical point is the place where the wind switches from one branch to the other. For $x < x_c$, the lower of the two values of w ($w < w_c$) is the correct solution, and for $x > x_c$, the higher of the two values of w ($w > w_c$) is the correct solution.

Figure 2.2 shows the resulting mCAK singular locus, critical point, and velocity law for the standard ζ Puppis model star, assuming a uniformly-bright finite disk factor. Only the near-star wind is shown to illustrate the grazing of the singular locus at the critical point. Also shown is the "quasi-static" exponential velocity law which is the limiting case for the deep subsonic wind ($v_r \ll a$). In this region, the radial momentum equation simplifies to the equation of hydrostatic equilibrium

$$\frac{\partial P}{\partial r} \;=\; -\rho\, g_{\rm eff} \;=\; -\rho\, \frac{GM_*(1-,)}{r^2} \quad , \tag{2.126}$$

which is solved for an isothermal medium by the exponentially decreasing density,

$$\rho(r) \;=\; \rho_0 \exp\left[-(r-R_*)/H_\rho\right] \quad , \tag{2.127}$$

where $H_\rho \equiv a^2/g_{\rm eff}$ is the density scale height. The subsonic radial velocity is thus given by the mass continuity equation, and

$$v_r(r) \;=\; \left(\frac{\dot{M}}{4\pi R_*^2 \rho_0}\right) \exp\left[+(r-R_*)/H_\rho\right] \quad . \tag{2.128}$$

Of course, as the wind accelerates past the sonic point, the density no longer drops exponentially, but approaches a $1/r^2$ power law as $v_r \to v_\infty$.

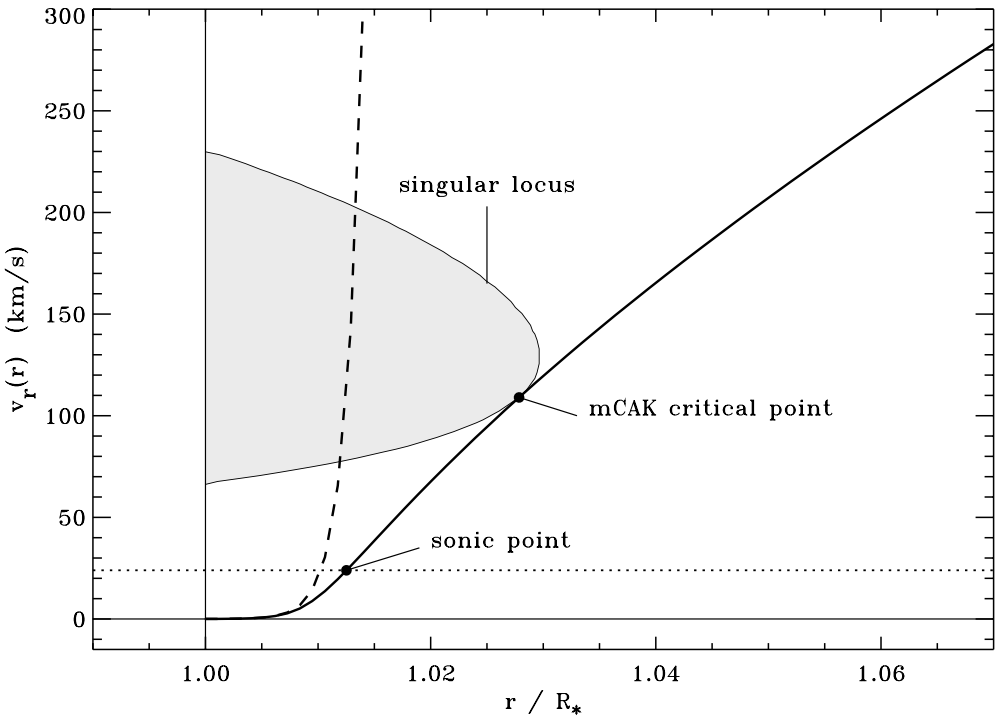

Figure 2.2: Solution topology for the mCAK model of ζ Puppis. The shaded region contains no solutions to the equation of motion, and is bounded by the singular locus of one solution. Also shown are the numerical velocity law (thick solid line), the subsonic exponential approximation for the velocity (dashed line), and the sound speed of the gas (dotted line).

Table 2.1 and Figure 2.3 illustrate the effect of varying the line-driving constants α, k, and δ on the resulting wind solutions. Note that varying k has absolutely no effect on the velocity law $v_r(r)$, but only on the mass loss rate $\dot{M}$. This can be seen in the zero sound speed solutions, and by the fact that the critical value of the constant C (which contains k and $\dot{M}$) itself depends only on α, , , and the assumed finite disk factor. Note also that, as far as the velocity law (v_∞ and $\beta_{\rm eff}$) is concerned, the exponent δ acts as a "negative α," and v_∞ and $\beta_{\rm eff}$ depend mainly on the quantity $\alpha - \delta$ (see Kudritzki et al. 1989). This trend does not extend to $\dot{M}$ and the location of the critical point x_c, however, because the N_{11}^{δ} factor in the radiative force is present in the definition of C as an effective "radially-dependent k."

The effective beta exponent $\beta_{\rm eff}$ listed in Table 2.1 and plotted in Figure 2.3 is defined using the parameterized velocity law (eq. [2.119]) as

$$\beta_{\rm eff}(r) \;=\; \left(\frac{r}{R_*} - 1\right) \frac{r}{v_r} \frac{\partial v_r}{\partial r} \quad , \tag{2.129}$$

and is a convenient measure of the wind's acceleration. We evaluate $\beta_{\rm eff}$ at $r = 2R_*$, which is a canonical median wind location, close to the points where $v_r \approx v_\infty/2$ and $\sigma = 0$ (isotropic expansion) in most wind models. At this point, $\beta_{\rm eff}$ is expressible as

$$\beta_{\rm eff} \;=\; \frac{\log[v_r(r = 2R_*)/v_\infty]}{\log(1/2)} \quad . \tag{2.130}$$

Next we apply a time-dependent numerical hydrodynamics code to the problem of a radiatively driven wind. By including time dependence (in the $\partial/\partial t$ terms previously ignored by the mCAK analysis) we introduce the possibility of finding variable or discontinuous solutions to the wind equations, and we also become able to assess the *stability* of steady-state solutions. The numerical code, VH-1, was developed by J. M. Blondin and colleagues at the University of Virginia, and uses the piecewise parabolic method (PPM) algorithm developed by Collela & Woodward (1984). VH-1 solves the Lagrangian forms of the equations of hydrodynamics in the fluid rest frame, and remaps conserved quantities onto an Eulerian grid at each time step.

In its most general form, VH-1 solves the three-dimensional equations of mass, momentum, and energy conservation (eqs. [2.1]–[2.3]) in an arbitrary coordinate system, but here we examine a one-dimensional spherically symmetric geometry. Also, in all models computed here the energy conservation is dominated by rapid radiative processes, which keep the gas very nearly isothermal with a constant wind temperature T equal to the stellar effective temperature $T_{\rm eff}$. We use a perfect gas law equation of state to evaluate the pressure P. The radiative force due to continuum and line processes is computed as in the mCAK method above, with

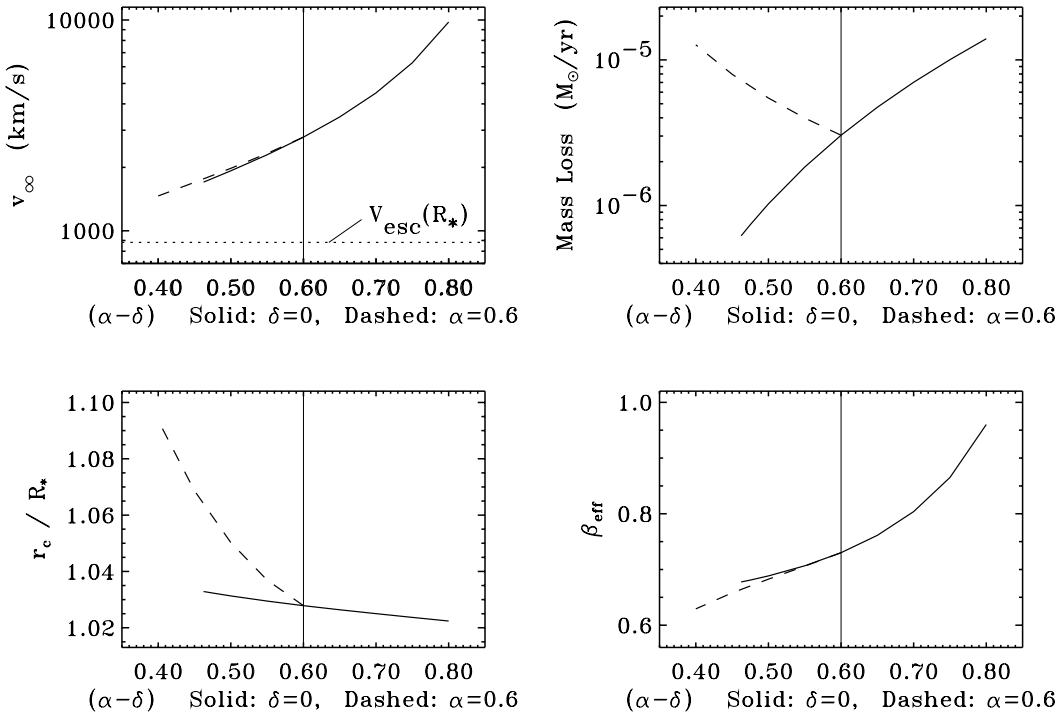

Figure 2.3: Parameter study for various mCAK wind models. Shown are the terminal velocity, mass loss rate, critical radius, and effective beta exponent. The solid line represents models with $\delta = 0$ (thus plotting α as the independent variable), and the dashed line represents models with $\alpha = 0.6$ (thus plotting $[0.6 - \delta]$ as the independent variable).

Table 2.1: Parameter Study for mCAK Standard Model

α	k	δ	v_∞ (km s^{-1})	$\dot{M}$ ($M_\odot$yr^{-1})	x_c	$\beta_{\rm eff}$
			Varying mCAK α			
0.4625	0.15	0.00	1702.74	6.19453 $\times 10^{-7}$	1.032877	0.67761
0.4750	0.15	0.00	1773.16	7.38506 $\times 10^{-7}$	1.032334	0.68101
0.5000	0.15	0.00	1926.19	1.02630 $\times 10^{-6}$	1.031311	0.68847
0.5500	0.15	0.00	2294.36	1.83761 $\times 10^{-6}$	1.029477	0.70658
0.6000	0.15	0.00	2782.85	3.03821 $\times 10^{-6}$	1.027855	0.73009
0.6500	0.15	0.00	3469.08	4.72661 $\times 10^{-6}$	1.026383	0.76123
0.7000	0.15	0.00	4509.55	7.01519 $\times 10^{-6}$	1.025009	0.80386
0.7500	0.15	0.00	6267.86	1.00384 $\times 10^{-5}$	1.023691	0.86517
0.8000	0.15	0.00	9780.13	1.39673 $\times 10^{-5}$	1.022387	0.96012
			Varying mCAK k			
0.6000	0.10	0.00	2782.85	1.54573 $\times 10^{-6}$	1.027855	0.73009
0.6000	0.15	0.00	2782.85	3.03821 $\times 10^{-6}$	1.027855	0.73009
0.6000	0.20	0.00	2782.85	4.90737 $\times 10^{-6}$	1.027855	0.73009
			Varying mCAK δ			
0.6000	0.15	0.00	2782.85	3.03821 $\times 10^{-6}$	1.027855	0.73009
0.6000	0.15	0.05	2328.37	3.98692 $\times 10^{-6}$	1.036940	0.70591
0.6000	0.15	0.10	1978.48	5.46630 $\times 10^{-6}$	1.050246	0.68255
0.6000	0.15	0.15	1698.05	7.96968 $\times 10^{-6}$	1.068636	0.65807
0.6000	0.15	0.20	1463.43	1.26802 $\times 10^{-5}$	1.093625	0.62929

the assumption of a uniformly-bright finite-disk factor and a power law ensemble of spectral lines defined by k, α, and δ.

We specify the boundary conditions in our numerical method in two phantom zones beyond each edge of the grid. At the outer radial boundary, the wind is invariably supersonic outward, and so we set the flow variables in the outer phantom zones by a simple constant-gradient extrapolation. The lower radial boundary of the wind is somewhat more problematic, and we use the boundary conditions described by Owocki et al. (1994): constant-slope extrapolation for v_r, rigid rotation for v_ϕ, and a fixed base density ρ_B. Because the mass loss rates of line-driven winds are determined from the equations of motion alone, we are able to specify an appropriate "photospheric" density that yields a stable, subsonic boundary outflow (see also Owocki, Castor, & Rybicki 1988). For our standard ζ Puppis model star, we choose a subsonic base density $\rho_B = 6 \times 10^{-11}$ g cm^{-3}, and we specify the flow variables on a fixed radial mesh with 200 zones, from R_* to $30R_*$. The zone spacing is concentrated near the stellar base where the flow gradients are largest; at the base, $\Delta r = 0.002R_*$ (which resolves the density scale height $H_\rho \approx [a/V_{\rm esc}]^2 R_*$), and it increases by 3% per zone out to a maximum of $\Delta r = 0.82R_*$ at the outer boundary.

This prescribed model has been implemented for various sets of stellar and wind parameters in this dissertation, and the hydrodynamics usually "settles" rapidly to a steady-state solution that agrees closely with the mCAK analysis. The models are stepped forward explicitly in time at a fixed fraction (0.25) of the Courant-Friedrichs-Lewy time step (see Press et al. 1989). The standard ζ Puppis star was modeled with VH-1, starting from an initial condition given by the mCAK velocity and density described above. The numerical wind solution relaxes to a steady state on a time scale comparable to the dynamical flow time for gas to radially advect across the computational grid,

$$t_d = \int_{r=R_*}^{30R_*} \frac{dr}{v_r(r)} \approx 2 \times 10^5 \, \mathrm{s} \quad . \tag{2.131}$$

Although a rigorous terminal velocity (at $r \to \infty$) cannot be computed for a model on a finite numerical grid, the dynamical variables at the outer radial grid zone are sufficient to compare with similar values from the mCAK analysis. The *ratio* of the VH-1 velocity and density to their corresponding mCAK values, for the ζ Puppis model at $30R_*$, are 1.0191 and 0.9515, respectively. Surprisingly, the major cause of these small differences at large radii probably is due to the slightly different treatments of the subsonic lower boundary.

2.4 An Overview of Non-Sobolev Wind Models

Although the Sobolev approach is used for all multidimensional and time dependent wind models in this dissertation, it is important to understand its limits, and under what circumstances a more rigorous model of the radiation driving becomes necessary. Also, the mCAK approximation of modeling the line ensemble using the (k, α, δ) distribution is another idealization that requires justification and scrutiny. Finally, the *stability* of the steady wind solutions to small perturbations is an important issue to resolve because the consequences of wind instability are potentially observable.

The primary research on extending the Sobolev and mCAK approximations has been undertaken by the Munich stellar astrophysics group in the 1980s and 1990s. PPK compared wind models using the Sobolev approximation to those constructed using a more accurate radiative force computed in the comoving frame of the flow, and found only negligible differences in the velocity laws and mass loss rates of the resulting winds. Even though the Sobolev approximation strongly underestimates the radiative force in the deeply subsonic wind ($v_r \lesssim v_{th}$) because it neglects diffuse radiation, the overall *magnitude* of the radiative force, compared to gas pressure and gravity, is small in this region. The mean end result, then, is insensitive to the force computed there.

The mCAK line ensemble approximation was relaxed by Pauldrach (1987), Pauldrach & Herrero (1988), and Pauldrach et al. (1990), who treated the full multilevel non-LTE problem for tens of thousands of line transitions, as well as a detailed continuum opacity containing bound-free and free-free opacity from dozens of elements. These models resulted in an improved comparison to observations of both the overall v_∞ and $\dot{M}$ values and the detailed profile shapes of individual lines. In most cases, however, the wind dynamics can be characterized well by simply modifying the k, α, and δ force constants in the mCAK model based on this improved radiative transfer. The existence of overlapping lines, and thus the presence of *multiple scattering* of photons, has been treated in both a statistical manner (Friend & Castor 1983; Gayley et al. 1995) and by using detailed line-list and Monte Carlo radiative-transfer computations (Abbott & Lucy 1985; Puls 1987; Lucy & Abbott 1993; Springmann 1994). Although the dynamical properties of winds can be strongly affected when multiple scattering is important (see, e.g., eq. [2.52]), under certain approximations this effect can be treated as a simple "force multiplier" akin to the finite disk factor (Gayley et al. 1995).

Despite the above complications in the radiative transfer, then, a suitably modified version of the Sobolev/mCAK approach seems well-suited to modeling at least the mean dynamical properties of winds around hot stars. However, it

has been suspected since the work of Milne (1926) that the radiative force arising from spectral line opacity may be highly unstable to small perturbations. Lucy & Solomon (1970) noted that because the wind is optically thick in the driving lines, the majority of the force comes from photons within a thermal speed of the blue edge of each line. If a given wind parcel is perturbed slightly to a higher velocity, the blue edge shifts to shorter wavelengths (in the star's frame), where it sees additional *unshadowed* photons which can further accelerate the parcel, thus blueshifting the line profile even more, and so on.

This instability was confirmed by MacGregor, Hartmann, & Raymond (1979) and Carlberg (1980), who performed linear perturbation analyses on the line force and assumed that the most important effect was the Doppler shift associated with the perturbed velocity. This work thus implicitly assumed that perturbations were optically thin, since associated velocity changes in the optical depth (eq. [2.26]) were neglected. However, a similar linearized analysis by Abbott (1980), which applied the Sobolev approximation to both the perturbation and the mean state, came to the opposite conclusion that line-driven winds are *stable* to small perturbations. In fact, Abbott (1980) found that such perturbations propagate as dispersionless "radiative-acoustic waves" at a phase speed which is a function of the mean mCAK-like force (see Chapter 7).

This apparent contradiction was resolved by Owocki & Rybicki (1984), who found that the instability depended sensitively on the length scale of the perturbation, and can be approximated by the "bridging law:"

$$\frac{\delta g_{\rm rad}}{g_{\rm rad,0}} \approx \frac{\delta v}{v_{th}} \left(\frac{ik}{2/L_{\rm Sob} + ik} \right) \quad , \tag{2.132}$$

where $\delta g_{\rm rad}$ is the first order force response to a velocity perturbation of the form $\delta v \propto \exp(ikr)$. In the limit of a large-scale perturbation ($k \ll 1/L_{\rm Sob}$), the Sobolev approximation is valid everywhere, and Abbott's (1980) marginally stable wave result of $\delta g_{\rm rad} \propto i\,\delta v$ applies. In the short-wavelength limit ($k \gg 1/L_{\rm Sob}$), the force and velocity perturbations are proportional, $\delta g_{\rm rad} \propto \delta v$, which is equivalent to the highly unstable optically-thin result of MacGregor et al. (1979) and Carlberg (1980).

Despite a great deal of subsequent research, this central conclusion of instability to small-scale perturbations remains. Lucy (1984) and Owocki & Rybicki (1985) investigated the effect of the *diffuse* radiation field on the instability, and found that it can be greatly reduced or even canceled near the stellar surface, but not in most of the supersonic wind. Rybicki, Owocki, & Castor (1990) extended this analysis into three dimensions and found that horizontal perturbations are more strongly damped than radial perturbations. Owocki & Zank (1991) discussed an effective "radiative viscosity" which arises from asymmetries in the diffuse radiation field, and how this

effect may help to suppress some of the intrinsic wind instability. Indeed, Gayley & Owocki (1995) found that for Wolf-Rayet winds, where the radiation is highly diffuse and photons multiply scatter, the growth rate of the instability is significantly smaller than for O and B stars (but still large enough for small perturbations to grow several orders of magnitude).

Owocki, Castor, & Rybicki (1988, hereafter OCR) performed the first *nonlinear* hydrodynamic calculations of unstable wind structure, and found that small perturbations rapidly grow into reverse shocks which separate high-speed rarefactions from slower, higher-density compressions. These models contained only the direct, pure-absorption radiative force, however. The effect of the scattered radiation field has been included by Owocki (1991, 1992) and Feldmeier (1995) via the "smooth source function" (SSF) approximation, which contains a nonlinear generalization of the Lucy (1984) line-drag and Owocki & Zank (1991) radiative viscosity effects. The SSF method does not compute the diffuse force arising from gradients in the perturbed source function, and Owocki & Puls (1996) have subsequently introduced the "escape integral source function" (EISF) method in order to better model the complex hydrodynamic phenomena which may result from these diffuse forces. The nonlinear structure in the supersonic wind, though, still appears to be dominated by stochastic reverse shocks, and the mean dynamical properties such as v_∞ and $\dot{M}$ appear to be relatively unaffected by the small-scale instability.

Chapter 3

SYNTHETIC OBSERVATIONAL DIAGNOSTICS

Just remember this, my girl,
When you look up in the sky
You can see the stars
And still not see the light,
That's right.

Jack Tempchin & Robb Strandlund, *Already Gone*

In order to compare theoretical models with observations, one must be able to compute the emergent photon distribution from these models and transform such noise-free "data" into a form where a one-to-one comparison with actual data is possible. The presence of hot-star winds has been inferred from radio, infrared, visible, ultraviolet and X-ray observations, but here we concentrate mainly on ultraviolet wavelengths, which are the most luminous for early-type stars. The major goal of this Chapter is to compute the shapes and strengths of P Cygni type spectral lines from an expanding envelope around a star (Section 3.1). Also, in anticipation of subsequent Chapters dealing with highly structured and inhomogeneous winds, a simple form of the continuum polarization from non-spherical and optically thin circumstellar gas distributions is derived (Section 3.2).

3.1 P Cygni Spectral Line Formation

3.1.1 The Source Function of the Radiation Field

Although the source function S_ν was not seen to have a crucial impact on the derivation of the radiation force in Section 2.2, it will be very important when calculating the shapes and strengths of spectral lines formed in the stellar wind.

Let us then evaluate the source function using the "escape probability" formalism of Sobolev (1957) and Castor (1970).

Consider the formal solution to the equation of radiative transfer, given by eq. (2.25),

$$I_\nu(\tau_\nu) = \int_0^{\tau_\nu} S_\nu(t_\nu) e^{-(\tau_\nu - t_\nu)} dt_\nu \; + \; I_\nu^{\rm core} e^{-\tau_\nu} \quad . \tag{3.1}$$

The optical depth is given in the Sobolev approximation by

$$\tau_\nu(\mathbf{r}) = \tau_o(\mathbf{r})\, \Phi(x, \mathbf{r}) \quad , \tag{3.2}$$

where the Sobolev optical depth τ_o and the integrating factor $\Phi(x, \mathbf{r})$ are defined and discussed above in Section 2.2. Note, however, that the same approximations which allowed τ_o to be taken outside the depth integral also allow the source function S_ν to be considered roughly *constant* over a Sobolev length $L_{\rm Sob}$. Thus,

$$I_\nu(\tau_\nu) = S_\nu(\tau_\nu) \left[1 - e^{-\tau_\nu}\right] \; + \; I_\nu^{\rm core} e^{-\tau_\nu} \quad . \tag{3.3}$$

Although the frequency dependence of the intensity and emergent flux will eventually be required to compute line profiles, it is the *frequency averaged* intensity which is needed for the source function to be found. The thermal Doppler motions in the gas, which are dominant in the Sobolev approach, tend to produce complete frequency distribution in the inertial frame. The source function that appears in the radiative transfer will thus be a quantity that is averaged over the line's frequency domain:

$$\bar{S}(\mathbf{r}) \equiv \int_{-\infty}^{+\infty} \phi(x)\, S_\nu(\mathbf{r})\, dx \tag{3.4}$$

(here x is the dimensionless Doppler frequency defined in eq. [2.20]), and the formal solution for the intensity can be similarly averaged over the line,

$$\bar{I} = \bar{S} \left[1 - \left(\frac{1 - e^{-\tau_o}}{\tau_o}\right)\right] + \bar{I}^{\rm core} \left(\frac{1 - e^{-\tau_o}}{\tau_o}\right) \quad , \tag{3.5}$$

using the analytic integral evaluated in eq. (2.38). The quantity in parentheses

$$p(\hat{\mathbf{n}}) = \frac{1 - e^{-\tau_o}}{\tau_o} \tag{3.6}$$

can be considered the probability (dependent on the angle $\hat{\mathbf{n}}$ in the Sobolev optical depth) of escape from the circumstellar region by a locally-scattered line photon.

In addition to the average over line frequency, consider an average (i.e., zeroth moment) of the formal intensity solution over solid angle:

$$4\pi \bar{J} = \oint \bar{I} d\Omega = \bar{S} \left[4\pi - \oint p(\hat{\mathbf{n}})\, d\Omega\right] + \oint \bar{I}^{\rm core}(\hat{\mathbf{n}})\, p(\hat{\mathbf{n}})\, d\Omega \quad . \tag{3.7}$$

This expression allows one to solve explicitly for the angle and frequency independent source function. If isotropic scattering and LTE are assumed, then

$$\bar{S} = \bar{\epsilon}\, B_\nu(T) + (1-\bar{\epsilon})\, \bar{J} \ , \tag{3.8}$$

where $\bar{\epsilon}$ is a line-averaged photon destruction probability per scattering, and the Planck function $B_\nu(T)$ is considered slowly-varying over the line. Note that the probability $\bar{\epsilon}$ (which ranges between 0 and 1) is sometimes replaced by $\bar{\epsilon}'$, the ratio of collisional to radiative deexcitation, where $\bar{\epsilon}' = \bar{\epsilon}/(1-\bar{\epsilon})$ ranges between 0 and $+\infty$, and is proportional to the gas density:

$$\bar{\epsilon}' \ = \ \epsilon_o' \left(\frac{\rho}{\rho_o} \right) \ \ ; \qquad \bar{\epsilon} \ = \ \frac{\epsilon_o(\rho/\rho_o)}{(1-\epsilon_o) + \epsilon_o(\rho/\rho_o)} \ , \tag{3.9}$$

where $\epsilon_o = \epsilon_o'/(1+\epsilon_o')$ is a convenient density-independent probability. Solving the above equation for $\bar{J}$, then, gives the source function in terms of intensity moments and escape probabilities:

$$\bar{S}(\mathbf{r}) = \frac{4\pi\bar{\epsilon}\, B_\nu(T) + (1-\bar{\epsilon}) \oint \bar{I}^{\rm core}(\hat{\mathbf{n}})\, p(\hat{\mathbf{n}})\, d\Omega}{4\pi\bar{\epsilon} + (1-\bar{\epsilon}) \oint p(\hat{\mathbf{n}})\, d\Omega} \ . \tag{3.10}$$

This general expression is often simplified in practice. Most spectral lines observed in winds are pure-scattering resonance lines, so $\bar{\epsilon} \approx 0$. Also, the stellar "core" intensity can be expressed as the product of a constant continuum-like term and a limb-darkening function,

$$\bar{I}^{\rm core}(\hat{\mathbf{n}}) \ \equiv \ I^C D(\hat{\mathbf{n}}) \ , \tag{3.11}$$

and under these two approximations,

$$\bar{S} \ \approx \ \frac{I^C \oint D(\hat{\mathbf{n}})\, p(\hat{\mathbf{n}})\, d\Omega}{\oint p(\hat{\mathbf{n}})\, d\Omega} \ \equiv \ \frac{I^C \beta_c}{\beta} \ , \tag{3.12}$$

where the angle-averaged escape probability is denoted by β, and the probability of a photon escaping the local region and then intercepting the core (the "core penetration probability") is denoted by β_c. If one assumes a perfectly isotropic photon distribution, one can approximate $\beta_c \approx \beta W$, where W is the standard dilution factor (probability of a random ray $\hat{\mathbf{n}}$ intercepting the core).

This escape probability formalism for $\bar{S}$ is a valuable tool, but it has its limits. Recall that the Sobolev approximation requires the velocity to be monotonically varying along all rays pointing away from the star. This, however, is not guaranteed in the multidimensional and time-dependent wind models presented in subsequent Chapters. Winds with nonmonotonic velocity fields have *nonlocal* line forces, since

multiple resonance surfaces can create additional attenuation of the stellar flux (Rybicki & Hummer 1978; Puls, Owocki, & Fullerton 1993, hereafter POF). Multiple resonances can also occur in the presence of line multiplets, but the Sobolev escape probability formalism can be easily modified in this case (see, e.g., Olson 1982). POF compare the use of the local Sobolev method with a self-consistent multiple-resonance technique in structured wind models, and find significant disagreement in the resulting line profiles. However, our hydrodynamical models of large-scale inhomogeneities in winds are much less structured than the one-dimensional instability (small-scale shock) models used by POF, with far fewer zones of nonmonotonic velocity variation in the entire wind. We thus use the escape probability approximation for $\bar{S}$ in all theoretical line profiles in this work, and model the presence of small-scale shocks by *microturbulence* (see Section 3.1.3, below).

3.1.2 The Emergent Intensity and Flux

The radiative flux from a spherical star is a purely radial vector with magnitude

$$\mathcal{F}_\nu \;=\; \int_{\phi'=0}^{2\pi} \int_{\mu'=\mu_*}^{1} I_\nu(\mu',\phi')\,\mu'\,d\mu'\,d\phi' \quad , \tag{3.13}$$

where the angles $\theta' = \cos^{-1}\mu'$ and ϕ' are measured from a position in the wind a distance r from the origin, and

$$\mu_* \;=\; \sqrt{1-\frac{R_*}{r}} \tag{3.14}$$

defines the stellar limb from this position. The local cylindrical coordinate system (p',ϕ',z') is useful to define, with

$$p' \;=\; r\sin\theta' \;=\; r\sqrt{1-\mu'^2} \tag{3.15}$$

$$z' \;=\; r\cos\theta' \;=\; r\mu' \quad , \tag{3.16}$$

and the flux integral, for an observer along the positive z'-axis at an infinite distance from the origin ($r \to \infty$), can be rewritten as

$$\mathcal{F}_\nu \;=\; \frac{1}{r^2}\int_{\phi'=0}^{2\pi} \int_{p'=0}^{R_*} I_\nu(p',\phi',z'\to\infty)\,p'\,dp'\,d\phi' \quad . \tag{3.17}$$

Line profiles are frequently written in terms of a residual flux $\mathcal{R}_\nu \equiv \mathcal{F}_\nu^L/\mathcal{F}_\nu^C$, where the line flux $\mathcal{F}_\nu^L$ uses the full formal solution for I_ν, and the continuum flux $\mathcal{F}_\nu^C$ uses the unattenuated stellar intensity $I_\nu^{\rm core}$.

The flux from a spectral line formed primarily in the *wind,* however, involves more than just an integration over the stellar surface. Formally, the integral over

p' must range from zero to infinity, but in practice we set a maximum radius $R_{\max}$ in all models, beyond which the density and emissivity are negligibly small. Castor (1970), Rybicki & Hummer (1978), and Castor & Lamers (1979) computed P Cygni type line profiles using the Sobolev approximation and a parameterized wind model to compute the intensity and optical depth. The Sobolev intensity in the line is given by eq. (3.3), and for an intrinsic line profile which is much thinner than the expected wind-broadened profile (i.e., for $v_{th} \ll v_\infty$), the integrated profile function is a step function which jumps at the *resonance point,*

$$\Phi(x, \mathbf{r}) \;=\; \begin{cases} 0, & x < \hat{\mathbf{n}} \cdot \mathbf{v}/v_{th} \\ 1, & x \geq \hat{\mathbf{n}} \cdot \mathbf{v}/v_{th} \;\; , \end{cases} \tag{3.18}$$

where here $\hat{\mathbf{n}} = \hat{\mathbf{e}}_{z'}$ because the observer is along the $+z'$ axis.

Note that, since the stellar disk occults the wind for which $0 \leq p' \leq R_*$ and $z' < 0$, there will be rays which intercept the star that will have line frequencies *without* observable resonances. Taking this into account, and assuming that $\mathbf{v}(r = R_*) = 0$ on the stellar surface, the Sobolev line intensity is given by

$$I_\nu(p', \phi', z' \to \infty) \;=\; \begin{cases} I_\nu^{\rm core} \;\; , & 0 \leq p' \leq R_* \, , \; x < 0 \\ I_\nu^{\rm core} e^{-\tau_o^*} + \bar{S}(1 - e^{-\tau_o^*}) \;\; , & 0 \leq p' \leq R_* \, , \; x \geq 0 \\ \bar{S}(1 - e^{-\tau_o^*}) \;\; , & p' > R_* \;\; , \end{cases} \tag{3.19}$$

and τ_o^* is the Sobolev optical depth (eq. [2.35]) evaluated at the resonance point where $x = \hat{\mathbf{n}} \cdot \mathbf{v}/v_{th}$. Castor & Lamers (1979) take into account the underlying photospheric line absorption profile in $I_\nu^{\rm core}$, and find that it can significantly affect the wind profile shape where absorption is appreciable. The major effect is a weakening of the emission component of the overall line, and Castor & Lamers provide an approximate method of estimating this reduction:

$$\mathcal{R}_\nu \;\approx\; qE_\nu + \mathcal{R}_\nu^*(1 - A_\nu) \;\; , \tag{3.20}$$

where $\mathcal{R}_\nu^*$ is the photospheric line residual flux, $(1 - A_\nu)$ and E_ν are the direct ("absorption," from $I_\nu^{\rm core}$) and diffuse ("emission," from $\bar{S}$) components of the wind residual flux, and q is a fractional photospheric dimunition factor defined as

$$q \;\equiv\; \frac{v_{th}}{v_\infty} \int_{x=0}^{v_\infty / v_{th}} \mathcal{R}_\nu^*(x)\, dx \;\; , \tag{3.21}$$

which approaches unity in the limit of no photospheric absorption. Castor & Lamers (1979) find that this dimunition of the emission component of a P Cygni line is the

dominant effect of photospheric absorption, and find much better agreement between a self-consistent solution (with the absorption in $I_\nu^{\rm core}$) and eq. (3.20) than by using the simpler additive approximation of $\mathcal{R}_\nu \approx E_\nu + \mathcal{R}_\nu^* - A_\nu$.

The sign convention used above for the line velocity denotes $x > 0$ as velocities blueshifted toward the observer, and $x < 0$ as velocities redshifted away from the observer. This is opposite to the sign convention often used when dealing with observational data. The above form for the intensity (eq. [3.19]) reveals the existence of the blueshifted absorption trough in P Cygni lines, since blueshifted frequencies experience extra attenuation (in the $I_\nu^{\rm core} e^{-\tau_o^*}$ term) due to line resonances directly in front of the stellar disk. The emission from the diffuse wind-scattered radiation (in the $\bar{S}$ terms) is almost symmetric about line center because it is dominated by the large volume $p' > R_*$, but occultation effects give the red side slightly less emission.

Despite the qualitative success of using the Sobolev approximation to compute line profiles from hot-star winds (e.g., Castor & Lamers 1979), there exist significant quantitative differences between theoretical and observed P Cygni type line profiles. Most notably, strong saturated wind lines, e.g., the C IV $\lambda\lambda$1548, 1551Å doublet, have broad (hundreds of km s^{-1} wide) blueshifted "black troughs," while pure Sobolev theoretical profiles dip down to zero intensity only at one point: the terminal velocity. Lucy (1982, 1983) suggested that this broadening can be caused by multiple scattering between nonmonotonic velocity features in a wind, and this clearly indicates that Sobolev theory is inadequate to treat the radiative transfer in such lines. An alternative and very accurate method of generating wind profiles is to solve the equation of radiative transfer in the comoving frame (CF) of the wind (Mihalas, Kunasz, & Hummer 1975; Hamann 1981). Computationally, however, this method is significantly more expensive than the Sobolev approximation, and thus is impractical for use in interactive spectral analysis.

Lamers, Cerruti-Sola, & Perinotto (1987) have introduced an efficient technique for computing wind line profiles with an accuracy intermediate between the Sobolev approximation and the CF method. Their "Sobolev with Exact Integration" (SEI) algorithm uses the Sobolev escape probability form of the source function $\bar{S}$, but does not assume the simple "step function" solution to the equation of radiative transfer (i.e., it uses eq. [3.1] instead of eq. [3.3]). Hamann (1981) showed that most of the errors incurred in the pure Sobolev approximation come from this integration and not from the source function itself. Thus, the SEI intensity is given by

$$I_\nu(z' \to \infty) = \begin{cases} \int_{z_*}^{+\infty} \left[\kappa_L \, \rho \, \phi \left(x - \hat{\mathbf{n}} \cdot \mathbf{v}/v_{th}\right) \bar{S} \, e^{-\tau_\nu}\right] dz' \; + \; I_\nu^{\rm core} e^{-\tau_\nu} \quad , & p' \le R_* \\ \int_{-\infty}^{+\infty} \left[\kappa_L \, \rho \, \phi \left(x - \hat{\mathbf{n}} \cdot \mathbf{v}/v_{th}\right) \bar{S} \, e^{-\tau_\nu}\right] dz' \quad , & p' > R_* \end{cases} \tag{3.22}$$

where $z_* = (R_*^2 - p'^2)^{1/2}$ is the z' coordinate of the stellar surface. The optical depth must be integrated together with the intensity, and is given by

$$\tau_\nu(z') \;=\; \int_{z'}^{+\infty} \kappa_L \, \rho \, \phi \left(x - \frac{\hat{\mathbf{n}} \cdot \mathbf{v}}{v_{th}} \right) dz'' \;\; . \tag{3.23}$$

Note, however, that in the absence of the nonmonotonic velocities which generate black troughs, the Sobolev, SEI, and CF methods all give virtually identical results, and it is the need to model the complex observations which demands moving beyond pure Sobolev line profiles.

We utilize the SEI method in all models presented here, and we perform the "exact integration" for the line flux using the cylindrical (p', ϕ', z') coordinate system with the observer oriented along the positive z'-axis. The equation of radiative transfer is evaluated in differential form along rays parallel to this axis, and along each ray the optical depth and specific intensity are integrated using second order implicit Euler differencing. The resulting emergent intensities at the outer boundary of the computational grid are then integrated by nested Romberg quadrature in p' and ϕ' to form the flux, and this process is repeated for each frequency point in the total line profile.

3.1.3 Line Broadening and Opacity

The detailed atomic physics of the line transition to be modeled enters the problem in the profile function $\phi(x)$ and the line absorption coefficient κ_L. For simplicity, we assume a Doppler-broadened Gaussian line-profile function of the form

$$\phi(x) \;=\; \frac{\exp(-x^2)}{\sqrt{\pi}} \;\; , \tag{3.24}$$

but for lines with appreciable collisional damping, the normalized Voigt function

$$\phi(x, a) \;=\; \frac{a}{\pi^{3/2}} \int_{-\infty}^{+\infty} \frac{\exp(-y^2)\, dy}{a^2 + (x - y)^2} \tag{3.25}$$

can be used, where the Voigt parameter a is the ratio of the collisional to the Doppler broadening width,

$$a \;=\; \frac{c,}{4\pi\nu_o v_{th}} \;\; , \tag{3.26}$$

and , is the combined damping rate for natural (radiation) and collisional broadening (see Mihalas 1978).

The profile-integrated opacity or strength of a spectral line is given by

$$\chi_L(r) \;\equiv\; \kappa_L(r)\rho(r) \;=\; \frac{\pi e^2}{m_e c} \frac{1}{\Delta\nu_D} (gf)_{\ell u} \left(\frac{n_\ell}{g_\ell} - \frac{n_u}{g_u} \right) \;\; , \tag{3.27}$$

where u and ℓ denote the upper and lower levels of the atomic transition, f is the oscillator strength, and g is the multiplicity of the level. Because of the non-LTE conditions typical in extended atmospheres (and because most of the lines to be modeled are resonance lines), we can assume $n_\ell \gg n_u$ and write

$$(gf)_{\ell u}\left(\frac{n_\ell}{g_\ell} - \frac{n_u}{g_u}\right) \approx f_{\ell u}\, n_\ell = f_{\ell u}\, q_i\, A\, X \frac{\rho}{m_H} \quad , \tag{3.28}$$

where q_i is the fraction of the element in the ith ionization state and A is its elemental abundance (by number) relative to hydrogen. The primary radial variation in χ_L, then, comes from the ionization fraction q_i and the density ρ, and we can write the line absorption coefficient as

$$\kappa_L(r) = \left[\frac{\pi e^2}{m_e c}\,\frac{f_{\ell u} A X}{m_H \Delta\nu_D}\right] q_i(r) \equiv \kappa_0 \left[\frac{q_i(r)}{q_0}\right] \quad , \tag{3.29}$$

where q_0 is the ionization fraction at a specified radius (typically taken where $v_r \approx v_\infty/2$).

Following the notation of POF, let us parameterize the constant coefficient κ_0 by defining a dimensionless line strength

$$k_L \equiv \left(\frac{\dot{M} v_{th}}{4\pi R_* v_\infty^2}\right)\kappa_0 \quad , \tag{3.30}$$

where v_∞ and $\dot{M}$ are taken from a simple one-dimensional steady-state wind model. POF assume $\kappa_L = \kappa_0$, which is valid for some lines of interest in the dominant ionization stage of the wind. However, Bjorkman et al. (1994) discuss various relevant parameterizations for the ionization fraction $q_i(r)$, and use a combined scaling law of the form

$$q_i(r) \propto \left(\frac{\rho}{W}\right)^{-\Delta i}\left(\frac{R_*}{r}\right)^{\gamma} \quad , \tag{3.31}$$

where the first term represents the ionization fraction in a case where the ionization rates are dominated by photoionization and radiative recombination (see Section 2.2.5), and Δi is the difference between the ion stage i and the dominant stage. The second term above results from an empirical opacity fit used by Lamers et al. (1987) and others to model weak lines which lack sharp "edges" in the blueshifted P Cygni absorption troughs.

In order to produce line profiles that best resemble the observations, one additional assumption is often included in the theoretical description of the line profile strength and shape: the presence of "turbulent" velocities. On the smallest scales,

microturbulent velocities can be convolved with the thermal Maxwellian motions of the gas, and an effective Doppler width of the form

$$\Delta\nu_D \;=\; \frac{\nu_o}{c}\sqrt{v_{th}^2 + v_{\rm turb}^2} \tag{3.32}$$

can be assumed. Although most implementations assume a constant microturbulent velocity of the order 50–200 km s^{-1}, better line profile fits have been obtained by assuming that $v_{\rm turb}$ varies in proportion to the mean wind velocity $v_r(r)$ (Haser et al. 1995). Also, for a large sample of B stars, Denissenkov (1994) found that the photospheric microturbulent velocity correlates well with the projected rotation velocity $V_{\rm eq}\sin i$, and this may be useful for empirical models of wind lines from rapidly rotating Be stars.

POF found that a better physical explanation for the effects of "microturbulent broadening" is the presence of stochastic small-scale instability shocks in line-driven winds. Following Lucy's (1982, 1983) conjecture that multiply nonmonotonic shocked velocity laws can explain the broadened black troughs in saturated P Cygni resonance lines, POF computed the nonlocal multiple-resonance source function for a highly structured unstable wind model, and indeed found similar broadening to that produced by ad-hoc microturbulence. However, note that multiple scattering and microturbulence produce black troughs for different reasons. When a non-monotonic velocity structure is present, the increased back-scattering from multiple resonances creates *reduced emission* on the blue side of the line. When microturbulent broadening is present, though, it produces a greater velocity dispersion in the single uncoupled resonance zones, *separating* the redshifted emission from the blueshifted absorption and resulting in a widened line trough. Despite these differences the computed line profiles are morphologically similar, and we apply the simpler microturbulence picture in the line profiles computed in this dissertation.

3.1.4 Examples of SEI P Cygni Line Profiles

We have developed a fully multidimensional code which implements the Sobolev and SEI methods of constructing P Cygni line profiles from expanding winds. Here we present examples of such idealized spectral lines using the one-dimensional ζ Puppis wind model discussed above in Chapter 2. The radial velocity and density, as computed numerically by VH-1, are read into the SEI code, and spherical symmetry is assumed in this case. The "standard" line profile parameters we choose are: $k_L = 1$ (a moderate unsaturated line), $\epsilon_o = 0$ (a pure-scattering resonance line), $v_{\rm turb} = 100\,{\rm km\ s^{-1}}$ (as is required observationally to approximate small-scale instability structure), and $\Delta i = \gamma = 0$ (for a line in the dominant ionization stage of the wind; e.g., as in POF).

Figures 3.1–3.4 show the computed SEI line profiles, plotted versus Doppler line velocity in the star's frame, for variations of the above standard parameters. Figure 3.1 varies the line strength k_L by two orders of magnitude above and below the standard value of unity, while keeping the other parameters fixed. Note that for $k_L \gtrsim 10$ the line is fully saturated, and any extra opacity has a negligible impact on the profile shape. Also, the deepest blueshifted absorption for *weak* lines occurs several hundred km s^{-1} below the maximum model velocity (here, $\sim$2800 km s^{-1}), which implies that observational estimates of v_∞ may be slightly underestimated if *unsaturated* P Cygni absorption troughs are used to determine them. Figure 3.2 shows the standard $k_L = 1$ line, but varies the artificial microturbulent velocity. The sharp profile corresponding to $v_{\rm turb} = 0$ km s^{-1} is virtually identical to the line profile generated by the pure Sobolev method discussed above (see also Lamers et al. 1987). Figure 3.3 also varies $v_{\rm turb}$, but for a strong *saturated* P Cygni line with $k_L = 100$; note the black troughs generated by the increased velocity dispersion.

Following the initial models of Castor (1970), which implied that strong Wolf-Rayet emission lines may be merely the result of thermal emission in an expanding wind, we have varied the collisional probability $\bar{\epsilon}$ according to eq. (3.9). Figure 3.4 shows the result of varying the constant ϵ_o, and allowing the true ratio of collisional to radiative deexcitations ($\bar{\epsilon}'$) to remain proportional to the wind density. We choose the normalizing constant ρ_o in eq. (3.9) to be the maximum (base) density of the model, which implies that rather large values of ϵ_o (close to unity) are required to produce significant emission in the majority of the accelerating wind. Note, however, that many strong Wolf-Rayet lines are recombination, not resonant, transitions, and the line absorption coefficient κ_L depends on the density of the wind because of the need to populate the lower level. The actual line profiles are thus roughly similar to those using an ionization law of the form eq. (3.31), with $\gamma \approx 2$. The profile shapes, then, are "damped out" at high velocities, and often do not show blueshifted P Cygni absorption (see, e.g., Bjorkman et al. 1994).

3.2 Continuum Polarization

Well before Maxwell's theoretical exposition of classical electromagnetism in 1864, the nature of light propagating via transverse waves was generally accepted from empirical evidence. Stokes (1852) showed that any collection of such waves can be characterized by four independent parameters which describe its intensity, geometry, and phase distribution; i.e., the *polarization* state of the wave. If the intensity I of a light beam is measured with respect to a given set of axes, its projected components in two perpendicular planes (their normals also perpendicular to the direction of propagation) can be denoted I_ℓ and I_r. The addition of two or more electric field vectors of the radiation components will, in the most general case,

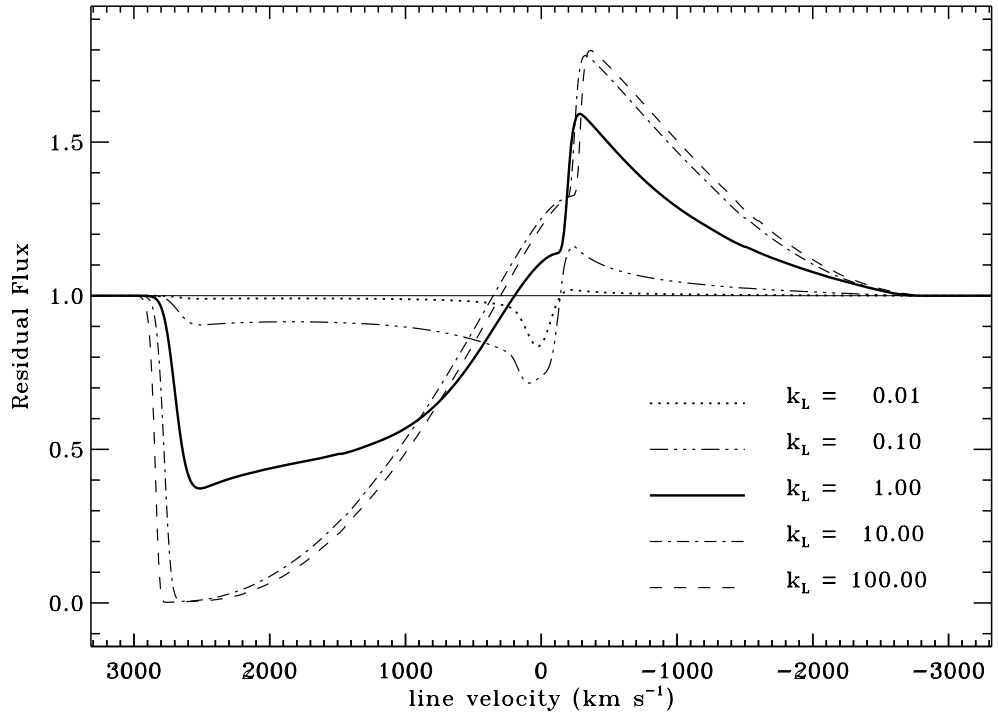

Figure 3.1: P Cygni line profiles, generated by the SEI method, for the standard ζ Puppis model wind. This figure varies the line strength by two orders of magnitude above and below the standard, moderately unsaturated value.

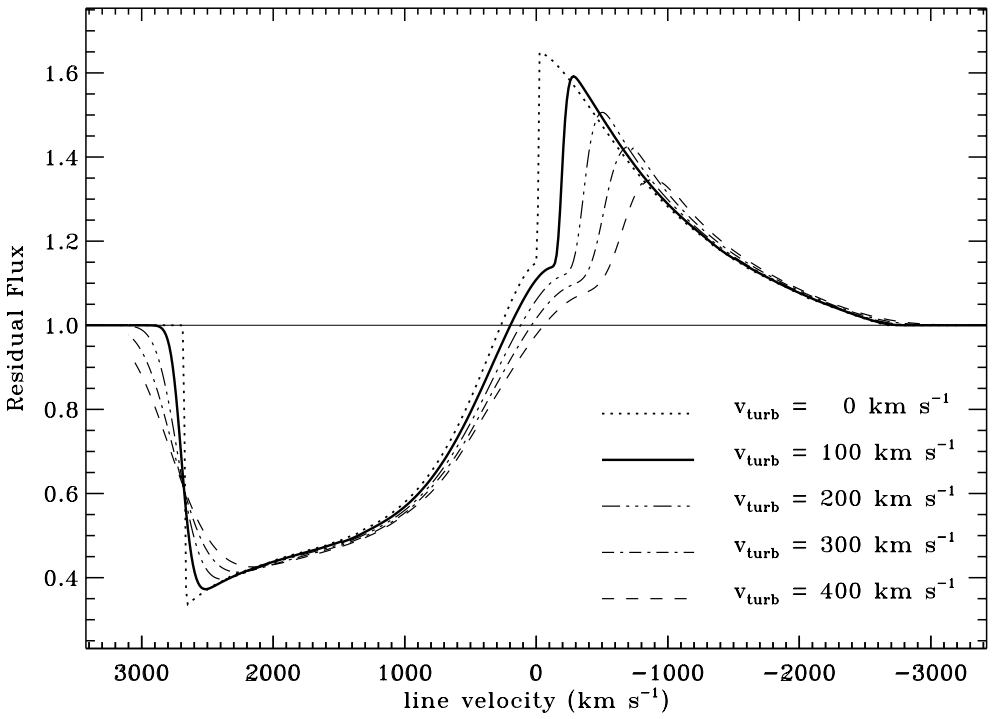

Figure 3.2: P Cygni line profiles, generated by the SEI method, for the standard ζ Puppis model wind. This figure varies the artificial microturbulent velocity above and below the standard value.

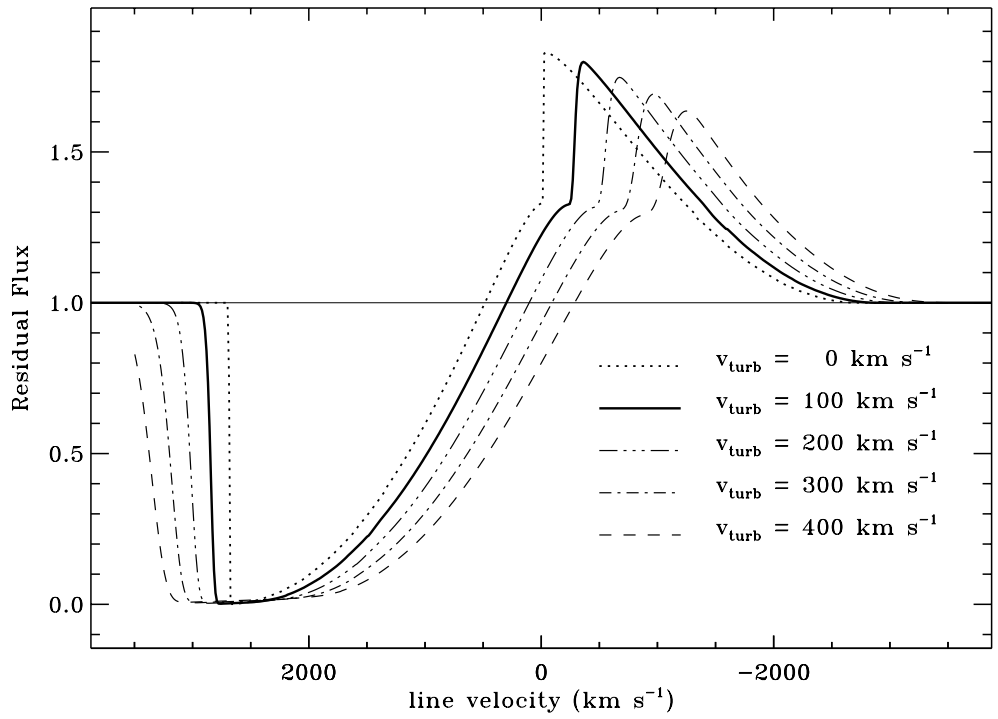

Figure 3.3: P Cygni line profiles, generated by the SEI method, for a strong *saturated* line with 100 times the line strength of the standard model, but using all other standard ζ Puppis parameters. This figure varies the artificial microturbulent velocity above and below the standard value.

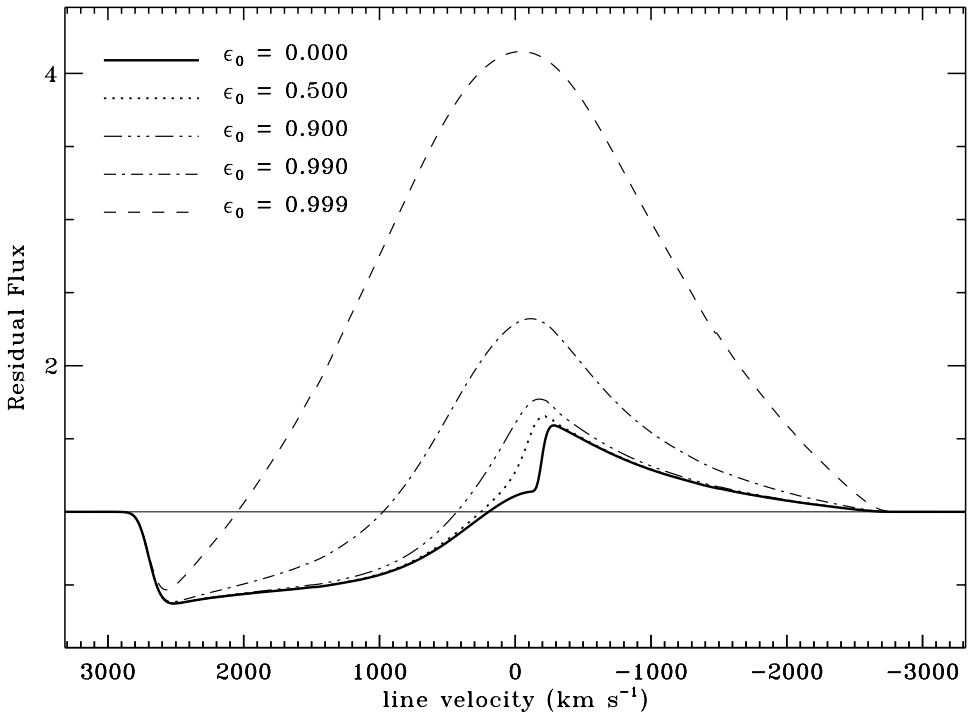

Figure 3.4: P Cygni line profiles, generated by the SEI method, for the standard ζ Puppis model wind. This figure varies the scaled probability of collisional deexcitations, from zero (pure scattering) to values approaching unity (pure thermal emission).

result in a vector whose tip traces out an elliptically helical spiral as it propagates through space. If this ellipse is oriented with an angle θ to the ℓ-reference axis and has an ellipticity (ratio of semiminor to semimajor axes) of $\tan\phi$, the four intensity-like Stokes parameters can be defined as

$$I = (I_\ell + I_r) \tag{3.33}$$
$$Q = (I_\ell - I_r) \tag{3.34}$$
$$U = (I_\ell - I_r)\,\tan 2\theta \tag{3.35}$$
$$V = (I_\ell - I_r)\,\sec 2\theta\,\tan 2\phi \tag{3.36}$$

(see, e.g., Collins 1989). This represents a single *elliptically polarized* and monochromatic beam, expressible most generally as a function of only three independent variables (I, θ, ϕ) since I_ℓ and I_r can be written in terms of each other via

$$\frac{I_\ell}{I_r} = \frac{1 + \cos 2\theta \cos 2\phi}{1 - \cos 2\theta \cos 2\phi} \ . \tag{3.37}$$

For $\phi = \pm\pi/4$ (or $Q = U = 0$) the beam traces out a circular path, and is considered *circularly polarized.* For $\phi = 0$ or $\pm\pi/2$ (or $V = 0$) the beam traces out a one-dimensional, but inclined path, and is considered *linearly polarized.* For all values of θ and ϕ, this "complete" polarization of a monochromatic beam results in $I^2 = Q^2 + U^2 + V^2$.

However, when observing an extended source such as a star, we observe an unresolved collection of many electromagnetic waves, each with its own polarization, convolved together into a single time-averaged intensity. By passing this radiation through, e.g., polarizing filters and quarter-wave plates, we can obtain some information about its overall polarization state. Redefining the above Stokes parameters as the appropriate averages over the incident beams (see Rybicki & Lightman 1979), we obtain the inequality

$$I^2 \geq Q^2 + U^2 + V^2 \ , \tag{3.38}$$

and in the extreme limit of a totally random distribution, $Q = U = V = 0$, and the beam is considered *unpolarized.* Anticipating observations of polarization from stars, let us define the degree of linear polarization P and the position angle Ψ,

$$P \equiv \frac{\sqrt{Q^2 + U^2}}{I} \ , \qquad \tan 2\Psi \equiv \frac{U}{Q} \ , \tag{3.39}$$

and for a completely polarized beam, the position angle Ψ and the ellipse angle θ are equivalent.

Note that the Stokes parameters I and V are invariant under coordinate rotations about the axis of propagation, but Q and U are not. Thus, when computing

the emergent Stokes intensities from a heterogeneous and extended collection of emitters, it becomes necessary to refer the four components due to each emitter to the same set of axes. This is achieved by rotating the vector-like intensity through an angle ψ,

$$\begin{pmatrix} I' \\ Q' \\ U' \\ V' \end{pmatrix} = \begin{pmatrix} 1 & 0 & 0 & 0 \\ 0 & \cos 2\psi & \sin 2\psi & 0 \\ 0 & -\sin 2\psi & \cos 2\psi & 0 \\ 0 & 0 & 0 & 1 \end{pmatrix} \begin{pmatrix} I \\ Q \\ U \\ V \end{pmatrix} , \tag{3.40}$$

where ψ is defined in practice as the angle between the chosen Q-axis for the entire region and the individual normal vectors to the scattering planes which produce the bulk of the polarized radiation.

The observation of polarization from stars is a difficult task. Although Chandrasekhar (1946) predicted that Thomson scattering in stellar atmospheres can give rise to as much as 12% local linear polarization at the limb, this effect averages to zero over a spherical star, for which there is no preferred plane on the sky. It was not until Kemp et al. (1983) observed a phase-dependent variation of polarization from the eclipsing binary Algol that this effect was actually confirmed from individual *portions* of an occulted star. A rapidly rotating star will also exhibit a small degree of atmospheric polarization ($\sim$0.1%) because oblateness and gravity darkening create a preferred plane on the sky (Rucinski 1970; Collins, Truax, & Cranmer 1991). In addition, Collins & Cranmer (1991) predicted that rapidly rotating stars, which produce Doppler-broadened absorption line profiles, should exhibit a slightly stronger variation in linear polarization across these "spatially filtered" lines.

In this work, however, we are mainly concerned with the polarization due to the circumstellar gas, and we will assume the incident light from the star is initially unpolarized. Many classes of hot stars which exhibit emission lines (Be, Of, Wolf-Rayet stars) are also observed to have significant ($\sim$ 1–2%) linear polarization, and this is assumed to come from an asymmetric outer envelope (see, e.g., Zellner & Serkowski 1972; Coyne & McLean 1982; Schmidt 1988). The polarization of Be stars is commonly interpreted as arising from Thomson scattering of photospheric radiation in a rotationally-flattened envelope or disk. Because the circumstellar environments of most O and B stars are *optically thin* to continuum radiation, let us follow Brown et al. (1978) and Wood et al. (1993) in treating this region as a single-scattering medium, thus ignoring absorption, local emission, and multiple-scattering of photons (see, however, Wood et al. 1996). The formal solution to the equation of radiative transfer (eq. [3.1]), in the limit of the scattered radiation dominating the

direct stellar radiation, reduces in the optically thin limit to

$$I_\nu \approx \int_0^{\tau_\nu} S_\nu(t_\nu)\, dt_\nu \approx \int_{-\infty}^{+\infty} \sigma_e\, \rho\, S_\nu\, dz' \quad . \tag{3.41}$$

Representing all intensity-like quantities as four-component Stokes vectors, the flux can be written as

$$\boldsymbol{\mathcal{F}}_\nu = \begin{pmatrix} \mathcal{F}_\nu^I \\ \mathcal{F}_\nu^Q \\ \mathcal{F}_\nu^U \\ \mathcal{F}_\nu^V \end{pmatrix} = \frac{1}{r^2} \int_{\phi'=0}^{2\pi} \int_{p'=0}^{+\infty} \begin{pmatrix} I_\nu^I \\ I_\nu^Q \\ I_\nu^U \\ I_\nu^V \end{pmatrix} p'\, dp'\, d\phi' \quad , \tag{3.42}$$

which is effectively a volume integral over the optically thin scattering envelope,

$$\boldsymbol{\mathcal{F}}_\nu = \frac{1}{D^2} \int_{V_*} \sigma_e\, \rho\, \mathbf{S}_\nu\, dV_* \quad , \tag{3.43}$$

where the distance from the observer to the envelope D is considered much larger than the internal dimensions of the envelope.

The four-component Stokes source function for the Thomson scattering must be evaluated to take into account the geometrical effects of scattering between the ℓ and r polarization planes. Assuming coherent scattering, the source function can be written as

$$\mathbf{S}_\nu(\Omega) = \frac{1}{4\pi} \oint \mathbf{R}(\Omega, \Omega')\, \mathbf{I}_\nu^*(\Omega')\, d\Omega' \quad , \tag{3.44}$$

where the incident intensity is assumed to be unpolarized,

$$\mathbf{I}_\nu^* = \begin{pmatrix} I_\nu^{\text{core}} \\ 0 \\ 0 \\ 0 \end{pmatrix} \tag{3.45}$$

and the 4×4 redistribution matrix $\mathbf{R}$ is the *product* between a Rayleigh phase matrix which takes into account local scattering between the four Stokes components, and the rotation matrix given above (eq. [3.40]) which affixes each scattering into a

single coordinate frame. When this matrix is multiplied by the unpolarized incident intensity vector (see Wood et al. 1993 for details), the source function becomes

$$\mathbf{S}_\nu \;=\; \begin{pmatrix} S_\nu^I \\ S_\nu^Q \\ S_\nu^U \\ S_\nu^V \end{pmatrix} \;=\; \frac{3}{16\pi} \oint I_\nu^{\rm core} \begin{pmatrix} 1+\cos^2\chi \\ \sin^2\chi\,\cos 2\psi \\ -\sin^2\chi\,\sin 2\psi \\ 0 \end{pmatrix} d\Omega' \quad , \tag{3.46}$$

where $\chi = \cos^{-1}(\hat{\mathbf{n}}\cdot\hat{\mathbf{n}}')$ is the scattering angle between the direction of incident radiation $\hat{\mathbf{n}}'$ and the direction pointing to the observer $\hat{\mathbf{n}}$. Note that all V-components are thus zero, implying *linear* polarization of circumstellar envelopes. (Stars with magnetic fields, however, will have a non-zero V polarization due to the Zeeman effect; see Collins 1988.)

For the simple cases of a point source and a spherical, uniformly-bright star at the origin, the angles χ and ψ are evaluated in a straightforward manner, and eq. (3.43) above can be integrated over the source volume V_* and incident solid angles Ω' to determine the emergent Stokes fluxes. The normalized degree of linear polarization and position angle are defined by Wood et al. (1993) as

$$P_\nu \;\equiv\; \frac{\sqrt{(\mathcal{F}_\nu^Q)^2+(\mathcal{F}_\nu^U)^2}}{\mathcal{F}_\nu^I+\mathcal{F}_\nu^{\rm core}} \quad , \qquad \Psi_\nu \;\equiv\; \frac{1}{2}\tan^{-1}\left(\frac{\mathcal{F}_\nu^U}{\mathcal{F}_\nu^Q}\right) \quad , \tag{3.47}$$

where the direct "core" flux is given for a spherical star at the origin by

$$\mathcal{F}_\nu^{\rm core} \;=\; \oint I_\nu^{\rm core}\,\mu'\,d\mu'\,d\phi' \;\approx\; \frac{\pi R_*^2}{D^2}\,I_\nu^{\rm core} \quad . \tag{3.48}$$

Brown et al. (1978), Bjorkman (1992), and Wood et al. (1993) performed the above volume and solid angle integrals for various geometries and derived several useful analytic formulae for P_ν and Ψ_ν for the case of an axisymmetric disk-like density enhancement. Specifically, if one ignores the occultation of material behind the star, one obtains the particularly simple result for such a disk:

$$\mathcal{F}_\nu^Q \;\propto\; \sin^2 i \quad , \qquad \mathcal{F}_\nu^U \;=\; 0 \quad , \tag{3.49}$$

and this potentially allows the separation of such inclination-dependent quantities as $V_{\rm eq}\sin i$. Brown (1994) reviewed various applications of the above theory to observations of Be star disks, axisymmetric and expanding winds, and even time-dependent inhomogeneities in winds such as the small-scale "blobs" inferred from Wolf-Rayet emission lines. In subsequent Chapters we will numerically compute the polarization from winds with large-scale rotational structure, with the eventual goal of comparing these theoretical values with observations.

Chapter 4

RAPID STELLAR ROTATION: CENTRIFUGAL EFFECTS

And the light shone in darkness and
Against the Word the unstilled world still whirled
About the centre of the silent Word.

T. S. Eliot, *Ash Wednesday*

In this Chapter we begin to study the impact of rotation on a star and its wind. Dynamics in a noninertial reference frame requires the consideration of fictitious forces, such as the centrifugal and Coriolis forces for uniform rotation, in order to be able to express, e.g., Newton's laws of classical motion in the standard manner. However, we wish to solve for the stellar wind in the *inertial* (nonrotating) frame, and the centrifugal and Coriolis forces become embedded in the non-Cartesian spherical geometry terms ($\propto v^2/r$) in the momentum conservation equations, eq. (2.5)–(2.7). Before dealing with the effect of these terms on an expanding wind, though, we must assess how the underlying stellar interior and photosphere are affected by rotation (Section 4.1). Only then can we begin to examine the interaction between the now-moving atmosphere and the radiation-driven wind. Expansion in the equatorial plane ($\theta = \pi/2$) is studied in Section 4.2, where we find that steady-state wind solutions may not exist for sufficiently rapid rotation. Finally, the form of the Sobolev line force is re-examined in Section 4.3, and we discuss the possible existence of "shear" wind solutions which can drastically alter the angular momentum of the wind.

4.1 Oblateness and Gravity Darkening

Tassoul (1978) and Smith (1987) review the physics of rotating stellar interiors, and conclude that most normal main sequence and giant stars rotate nearly uniformly. Although evolution may lead to significant differential rotation in the deep interior, observational constraints are still quite ambiguous, and most observations are consistent with uniform or near-uniform rotation. The most obvious effect of rotation on the star is that it becomes flattened, or *oblate*. As opposed to incompressible fluid bodies, centrally-condensed stars do not conserve volume upon increasing their rotation velocity; Papaloizou & Whelan (1973) found the maximum decrease in the polar radius to be only $\sim 3\%$, but the maximum increase in the equatorial radius to be as much as $\sim 50\%$. Let us then assume that a star's polar radius R_p is a constant, and determine how its shape at other latitudes depends on rotation.

The gravitational potential of a uniformly rotating body can be approximated by assuming a pointlike concentration of mass M_* at its center, and superposing a standard "centrifugal" term,

$$\Phi(r,\theta) = -\frac{GM_*}{r} - \tfrac{1}{2}\Omega^2 r^2 \sin^2\theta \quad . \tag{4.1}$$

These are the so-called *Roche equipotentials* (named for the French mathematician Edouard Albert Roche), where Ω is the constant angular velocity of the body. The surface of a rotating star will be confined to equipotential surfaces, and if the polar ($\theta = 0$) radius $r = R_p$ is specified, the potential at the pole can be compared to that at an arbitrary polar angle θ,

$$-\frac{GM_*}{R_p} = -\frac{GM_*}{R_*} - \tfrac{1}{2}\Omega^2 R_*^2 \sin^2\theta \quad , \tag{4.2}$$

and we obtain the shape of the axisymmetric (ϕ-independent) stellar surface $r = R_*(\theta)$ by solving the above cubic equation for R_*. Note that the use of a more self-consistent, e.g., polytropic, mass distribution yields less than a 1% change in the oblate surface radius derived with the Roche model (see Orlov 1961).

In practice, the angular velocity Ω is not always initially known – the actual velocity at the star's equator $V_{\rm eq}$ may be specified in its place. There are thus at least two possible ways to solve for $R_*(\theta)$:

1. **Ω known:** First note that a "critical" or "breakup" angular velocity $\Omega_{\rm crit}$ can be defined, for which $\nabla\Phi$ has zero magnitude at the equator ($\theta = \pi/2$). When $\Omega = \Omega_{\rm crit}$, the radius $R_*(\pi/2) \equiv R_{eq}$ reaches its maximum possible value of

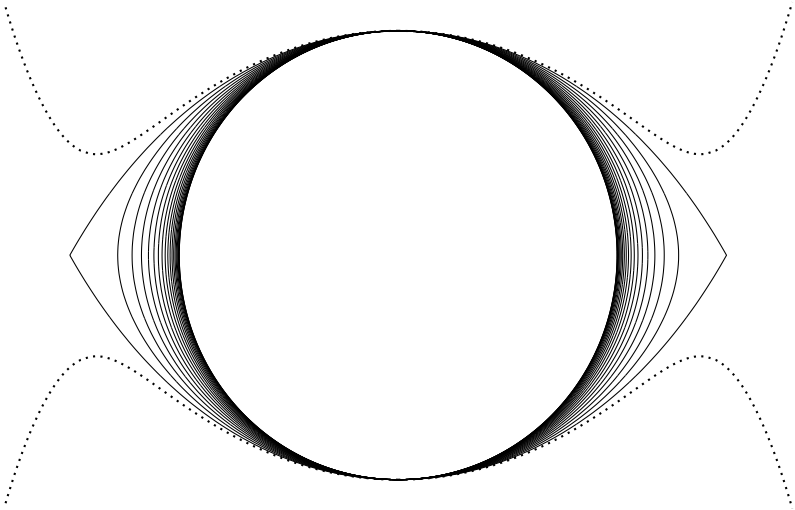

Figure 4.1: Equatorial cross sections of Roche equipotential surfaces, plotted for a uniform distribution of ω values between 0 and 1.05, at increments of 0.05. The dotted curve is a representative post-breakup surface ($\omega = 1.05$).

$R_{eq} = (3/2)R_p$. When $\Omega < \Omega_{\rm crit}$, one can define the fractional angular velocity ω as $\Omega/\Omega_{\rm crit}$, and

$$\Omega = \omega\Omega_{\rm crit} = \omega\sqrt{\frac{GM_*}{R_{eq}^3}} = \omega\sqrt{\frac{8GM_*}{27R_p^3}} \ , \tag{4.3}$$

where $0 \leq \omega \leq 1$ for a closed stellar equipotential. The cubic potential equation (eq. [4.2]) can thus be expressed as

$$\frac{4}{27}\omega^2 x^3 \sin^2\theta - x + 1 = 0 \ , \tag{4.4}$$

where $x = x(\omega,\theta) \equiv R_*(\theta)/R_p$, and solved via trigonometric methods (see Collins 1963; Collins & Harrington 1966) by

$$x(\omega,\theta) = \frac{3}{\omega\sin\theta}\cos\left[\frac{\pi + \cos^{-1}(\omega\sin\theta)}{3}\right] \ . \tag{4.5}$$

Figure 4.1 shows cross sections of these Roche surfaces for a uniformly spaced distribution of ω values between 0 and 1.05, at intervals of 0.05. Note the "cusp" at the equator of a critically-rotating star, where gravity exactly balances the centrifugal force, and the outward equatorial flaring of a model star rotating faster than its breakup velocity.

2. $\boldsymbol{V}_{\rm eq}$ **known:** Since $V_{\rm eq} = \Omega R_{eq}$, the above cubic potential equation can be rewritten as

$$w_o\left(\frac{R_*}{R_{eq}}\right)^2 \sin^2\theta - 1 + \frac{R_p}{R_*} = 0 \ , \tag{4.6}$$

defining $w_o \equiv V_{\rm eq}^2 R_p/2GM_*$. At the equator ($R_* = R_{eq}, \theta = \pi/2$), this equation becomes

$$w_o - 1 + \frac{R_p}{R_{eq}} = 0 \ , \tag{4.7}$$

and $(R_p/R_{eq}) = (1 - w_o)$. The variable w_o ranges from zero ($V_{\rm eq} = 0$) to $\frac{1}{3}$ ($V_{\rm eq} = \Omega_{\rm crit}R_{eq}$), and the general cubic equation becomes

$$w_o(1 - w_o)^2 x^3 \sin^2\theta - x + 1 = 0 \ , \tag{4.8}$$

and, by comparing with eq. (4.4) above, we find that

$$\omega^2 = \frac{27}{4}w_o(1 - w_o)^2 \ , \tag{4.9}$$

and we can use the same trigonometric solution (4.5) to determine the radius $x = R_*/R_p$. Many authors express a star's rotation in terms of a *fractional equatorial velocity,* i.e., $(V_{\rm eq}/V_{\rm crit})$, and this ratio is given by

$$\Upsilon \equiv \frac{V_{\rm eq}}{V_{\rm crit}} = \omega \frac{R_{eq}}{R_{eq,{\rm crit}}} = 2\cos\left(\frac{\pi + \cos^{-1}\omega}{3}\right) \quad . \tag{4.10}$$

Both ω and Υ vary monotonically from 0 to 1, but "median" values of Υ correspond to more "extreme" values of ω (e.g., when $\Upsilon = 0.5$, $\omega = 0.6875$). Thus, despite the more fundamental nature of ω, the fractional velocity Υ more evenly spans the range of oblateness from $x_{eq} = 1$ to 1.5.

Note that the Roche gravitational potential, as defined above, does not include any terms due to radiation pressure or force. As a useful first approximation to the inclusion of such terms, the mass of the star M_* can be replaced by an effective mass term, $M_*(1-,\ )$, where $,$ is the electron scattering Eddington factor introduced in Section 2.2.2. This term is negligible in all but the Wolf-Rayet, O, and earliest B type stars. For the standard ζ Puppis model star of Chapter 2, the Eddington ratio $, = 0.351$, which results in a critical rotation velocity of $V_{\rm crit} = 510.4\,{\rm km\ s^{-1}}$. This is significantly higher than the observed $V_{\rm eq}\sin i$ of 210–230 km s^{-1}, for which the Roche oblateness is only a $\sim$ 6–7% effect at the equator.

In the star's atmosphere one can define radial and latitudinal components of the effective gravity by examining the gradient of the potential Φ:

$$g_r = -\frac{\partial\Phi}{\partial r} = -\frac{GM_*}{r^2} + \Omega^2 r\sin^2\theta = \frac{GM_*}{R_p^2}\left(-\frac{1}{x^2} + \frac{8}{27}x\omega^2\sin^2\theta\right) \quad , \tag{4.11}$$

$$g_\theta = -\frac{1}{r}\frac{\partial\Phi}{\partial\theta} = \Omega^2 r\sin\theta\cos\theta = \frac{GM_*}{R_p^2}\left(\frac{8}{27}x\omega^2\sin\theta\cos\theta\right) \quad . \tag{4.12}$$

Thus, $|\mathbf{g}|^2 = g^2 = g_r^2 + g_\theta^2$, because the azimuthal component of the effective gravity (g_ϕ) is identically zero from meridional symmetry. Note, of course, that this effective gravity applies only on the oblate stellar surface, and not in the wind (which does *not* rotate rigidly). At the equator ($\theta = \pi/2$), the radius at which the effective gravity vanishes is given by $x_{g=0} = 1.5\,\omega^{-2/3}$, and for $\omega = 1$ this occurs precisely at the "cusp" on the surface of the critically-rotating star.

The early work of von Zeipel (1924) and Chandrasekhar (1933) showed that a distorted gaseous star in hydrostatic equilibrium exhibits a change in its net radiative flux which is proportional to the local gravity over its surface. This "gravity darkening" can be qualitatively understood by assuming the condition of *hydrostatic*

equilibrium in the interior of a star, in which the effective gravity $\mathbf{g}$ is derivable from a scalar potential Φ,

$$\nabla P = \rho \mathbf{g} = -\rho \nabla \Phi \quad . \tag{4.13}$$

Because the normals to the surfaces of constant Φ and constant P are anti-parallel, the gas pressure P must be constant on equipotential (constant Φ) surfaces. Thus P must be a function of Φ only, and the density ρ can be expressed as

$$\rho = \frac{|\nabla P(\Phi)|}{|\nabla \Phi|} = -\frac{dP}{d\Phi} \quad , \tag{4.14}$$

assuming the density is monotonically stratified. Thus, in these cases, ρ must be a function of Φ as well. Also, if the atomic abundances (i.e., μ in eqs. [2.11] and [2.12]) are considered constant along equipotentials, the temperature T must also be a function of Φ only. In *radiative equilibrium*, the flux carried outward by photons is given by the conductive term,

$$\boldsymbol{\mathcal{F}} = -\frac{16\,\sigma_B}{3\,\bar{\kappa}\,\rho}\,T^3\,\nabla T \quad , \tag{4.15}$$

where σ_B is the Stefan-Boltzmann constant and $\bar{\kappa}$ is the Rosseland mean absorption coefficient (in cm^2/g), and is a function of the state variables ρ, P, and T. Thus, one can write

$$\nabla T = \frac{dT}{d\Phi}\,\nabla \Phi \tag{4.16}$$

using the chain rule of differentiation, so that the flux can be concisely expressed as

$$\boldsymbol{\mathcal{F}} \;=\; f(\Phi) \nabla \Phi \;=\; -f(\Phi)\,\mathbf{g} \quad , \tag{4.17}$$

where $f(\Phi)$ is constant along an equipotential surface. This expression violates *strict* radiative equilibrium, in which $\nabla \cdot \boldsymbol{\mathcal{F}} = 0$, and thus some non-rotational fluid flow must arise to compensate for the resulting local heating and cooling of gas. However, the time scale of such "meridional circulation" flow (Eddington 1929; Sweet 1950) is usually much too long to significantly affect the validity of the gravity darkening flux derived above.

Slettebak (1949) discussed the variation in effective temperature $T_{\rm eff}$ over the surface of rotationally distorted single stars. Since the total luminosity L_* of the star is equivalent to the flux integrated over its surface, its magnitude is

$$\mathcal{F} = \sigma_B T_{\rm eff}^4(\theta) = K_{vz}\,g(\theta) \quad , \tag{4.18}$$

with von Zeipel's constant K_{vz} given by the constraint that the total integrated flux gives L_*, no matter the degree of rotation, and

$$K_{vz} = \frac{L_*}{\oint g\,dS} \quad , \tag{4.19}$$

where the integral in the denominator is taken over the entire surface of the star. We implicitly assume that the bolometric luminosity L_* remains constant for a given model star rotating at different rates, but this is not strictly true. Because the presence of centrifugal forces weakens the effective gravity in the interior, the central conditions mimic those of a nonrotating star of lower mass. Thus the central temperature and luminosity are lower in rotating stars, but the maximum effects for uniform rotation are quite small; L_* decreases by only 5–10% at the critical rotation velocity (Papaloizou & Whelan 1973).

The evaluation of von Zeipel's constant, though straightforward, involves a complicated integral. The magnitude of the effective gravity g depends on the above solution for the latitudinally-dependent Roche radius $R_*(\theta)$, and the element of surface area is

$$dS = \frac{[R_*(\theta)]^2}{\cos\delta} \sin\theta \, d\theta \, d\phi \quad , \tag{4.20}$$

where δ is the angle between the local gravity and the radius vector ($\cos\delta = -g_r/g$), and takes into account the fore-shortening of the surface area. Note that, in the fully radiative case, the effective temperature is dependent on the gravity raised to the power 0.25. For stars in which convection plays a non-negligible role, however, the variation of flux with gravity is not so simply parameterized. If the exponent (sometimes termed b), which is 0.25 in the radiative case, can take on other values, the gravity darkening is described as

$$\sigma_B T_{\rm eff}^4 = \left(\frac{L_*}{\Sigma_{4b}}\right) g^{4b} \quad , \tag{4.21}$$

where the function Σ_{4b} is given by

$$\Sigma_{4b} \equiv \oint g^{4b} dS = 2\pi \int_0^\pi \frac{g^{4b} R_*^2 \sin\theta \, d\theta}{\cos\delta} \quad , \tag{4.22}$$

and the two limiting cases of $b = 0$ and 0.25 give the surface area of the star (Σ_0) and the surface-weighted gravity (Σ_1), respectively. The values of Σ_0 and Σ_1 have been computed via numerical quadrature, and can be fit via least squares as power series in the fractional angular velocity ω,

$$\begin{aligned} \Sigma_0 &\approx 4\pi R_p^2 \left[1 + 0.19444\,\omega^2 + 0.28053\,\omega^4 - \right. \\ &\quad \left. 1.9014\,\omega^6 + 6.8298\,\omega^8 - 9.5002\,\omega^{10} + 4.6631\,\omega^{12}\right] \qquad (4.23) \\ \Sigma_1 &\approx 4\pi G M_* \left[1 - 0.19696\,\omega^2 - 0.094292\,\omega^4 + \right. \\ &\quad \left. 0.33812\,\omega^6 - 1.3066\,\omega^8 + 1.8286\,\omega^{10} - 0.92714\,\omega^{12}\right] \quad . \qquad (4.24) \end{aligned}$$

Using only even powers of ω gives a much-improved fit over using the same number of free parameters for even and odd powers together. The relative error in these fits

is rather small, but it is slightly dependent on ω. For $\omega < 0.9$, the error is $< 1\%$ for Σ_0 and $< 0.2\%$ for Σ_1. For all ω $(0 < \omega < 1)$, the error is $< 2\%$ for Σ_0 and $< 0.6\%$ for Σ_1.

Lucy (1967) derives $b \simeq 0.08$ for late-type main-sequence stars. Using classical mixing-length computations (Baker & Temesváry 1966), Lucy utilizes the condition that the gradient of the specific entropy vanishes in a fully convective zone to set the limits of state variable structure integrations over the stellar surface. This method is questioned by Anderson & Shu (1977), who find that if flux is carried exclusively by standard mixing-length convection from the deeper layers upward, the photosphere should eventually radiate it away at a constant rate $\sigma_B T_{\rm eff}^4$, independent of the gravitational potential Φ. This implies $b = 0$, and predicts an isothermal effective temperature distribution for main sequence stars later than spectral type $\sim$ F7, but the exponent b can supposedly range from 0 to 0.25 for spectral types $\sim$ F2 to F7. Earlier type stars, however, exhibit the standard radiative $b = 0.25$.

Osaki (1970) treats the problem more generally. The exponent b, in a situation where the radiative and convective contributions to the net flux vary with depth, can be determined numerically, at least to first order, as an eigenvalue of the energy transfer equation in the convective envelope. Zhou & Leung (1990) emphasize the fact that, for systems obeying both hydrostatic and thermal equilibrium, surfaces of constant temperature and pressure do not necessarily coincide. Thermal stability will thus cause convective circumfluence between different latitudes, and Coriolis forces thus play a non-negligible role in the outer layers of such rotating stars. Clearly the present theoretical understanding of *convective* gravity darkening is far from complete, but the von Zeipel result for early-type stars with mainly *radiative* envelopes is definitely on firmer ground.

4.2 Centrifugal Wind Modulation

The wind from a rapidly rotating star will have different properties at different latitudes, and under certain circumstances may vary in all three dimensions and in time. For the present, however, we confine our models to the *equatorial plane,* where rotation has the strongest impact, and where the flow can be constrained to a surface of constant colatitude, $\theta = \pi/2$. (See Pizzo 1982 for discussion of similar approximations in modeling the solar wind.) Thus the θ (latitudinal) component of the momentum conservation equation is assumed satisfied in the equatorial plane by the trivial solution $v_\theta(\theta = \pi/2) = 0$, i.e., no latitudinal flow into or out of the computational domain, with all partial derivatives in the θ direction considered negligible. In this Section we examine two effects which can modulate and redistribute the mass flux from a rotating star: the centrifugal decrease in the effective gravity

(which also causes oblateness) and flux redistribution due to gravity darkening.

4.2.1 Mass Loss Enhancement due to Centrifugal Forces

Following Gerasimovič's (1934) suggestion that the rapid rotation of a star makes it easier for material to be accelerated from the surface, many models of "centrifugally enhanced" winds from hot stars have been constructed (Limber 1964; Friend & Abbott 1986; Pauldrach, Puls, & Kudritzki 1986; Poe 1987; Bjorkman & Cassinelli 1993). Let us review these models and explore the dynamical consequences of this enhanced mass loss on Sobolev mCAK winds. The ϕ (azimuthal) component of the momentum conservation equation is given, in the equatorial plane, by

$$\frac{\partial v_\phi}{\partial t} + v_r \frac{\partial v_\phi}{\partial r} + \frac{v_\phi}{r \sin\theta} \frac{\partial v_\phi}{\partial \phi} = -\frac{v_r v_\phi}{r} - \frac{1}{\rho r \sin\theta} \frac{\partial P}{\partial \phi} \quad , \tag{4.25}$$

but if we assume a time-steady and *azimuthally symmetric* wind (i.e., with vector components such as $v_\phi \neq 0$, but all $\partial/\partial\phi = 0$) only the two terms proportional to v_r survive, and

$$v_r \left(\frac{\partial v_\phi}{\partial r} + \frac{v_\phi}{r} \right) = 0 \quad . \tag{4.26}$$

In the deep photosphere, where $v_r \to 0$, this equation does not necessarily constrain v_ϕ, so we assume $v_\phi(r = R_*) = V_{\rm eq}$ as a lower boundary condition. In the wind, where $v_r \neq 0$, the above equation demands that v_ϕ conserve angular momentum, and that

$$v_\phi(r) = \frac{V_{\rm eq} R_*}{r} = \frac{\Omega R_*^2}{r} \quad . \tag{4.27}$$

To generalize to stellar latitudes other than the equator ($\theta = \pi/2$), one can replace $\Omega \to \Omega \sin\theta$, but keep in mind that two- or three-dimensional effects will dominate the flow at latitudes other than $\theta = 0$ or $\pi/2$, and the inclusion of this one-dimensional centrifugal term then becomes highly suspect (see Chapter 5).

The angular-momentum-conserving rotation of the stellar wind affects the radial momentum equation (eq. [2.5]) by the term proportional to v_ϕ^2/r, and this can be treated as a contribution to the effective gravity,

$$g_{\rm eff} = -\frac{GM_*(1 - ,)}{r^2} + \frac{\Omega^2 R_*^4}{r^3} \quad . \tag{4.28}$$

This rotation term drops off more rapidly in radius than gravity, so that even if it has a strong impact near the star, it can be neglected as $r \to \infty$. Because rotation *reduces* the effective gravity near the surface, it has the ability to induce a greater mass flux. This can be estimated using the methods of Section 2.3.2, where we

assumed a zero sound speed and a critical radius (for finite disk models) extremely close to the surface ($r_c \approx R_*$). Thus, the CAK equation of motion becomes

$$F_1 \approx w + (1-,\ -\Theta) - \frac{C}{1+\alpha} w^{\alpha} = 0 \ , \tag{4.29}$$

where $\Theta \equiv \Omega^2 R_*^3 / GM_* = 8x^3\omega^2(1-,\ )/27$, and the effective gravity term $(1-,\ -\Theta)$ consistently replaces $(1-,\ )$ in the critical point conditions (eq. [2.107]) and the CAK mass loss rate (eq. [2.110]). This approximation for the increase in the mass loss rate compares well with the results of more complex numerical calculations. Note, however, that the local mass flux of the equatorial wind, defined by the equation of continuity (eq. [2.9]), is not equivalent to the *total* mass loss rate of the star, but is expressed as a spherically integrated flux ($4\pi r^2 \rho v$) for convenience.

As the denser wind from a rotating star accelerates outward, the $1/r^3$ term in the effective gravity eventually dies away, and it reverts to its nonrotating value. Because the mCAK radiative force is proportional to the inverse of the density, the acceleration on this higher-$\dot{M}$ material is smaller, and the terminal velocity v_∞ *decreases* for the more rapidly rotating winds. This can be seen heuristically from the infinite-radius v_∞ equations in Section 2.3.2, and especially from the approximate solution, eq. (2.123). Note that here the quantity $(1-,\ )$ is not modified by Θ, because we are at an infinite radius, but C is lower because of the increased mass loss rate. Poe (1987) and Koninx (1992) noted that for a sufficiently high rotation velocity the wind becomes so dense that the line force cannot drive it to infinity, and this corresponds to the imaginary solutions of eq. (2.123) for too-small values of C.

Figure 4.2 shows the velocity laws $v_r(r)$ for numerical mCAK models of the standard ζ Puppis star of Chapter 2, rotating in the equatorial plane at various rotation speeds. For these models, the equatorial radius is kept fixed at R_p, and the effects of gravity darkening on the mass loss rate are ignored. Both the decrease in v_∞ (as originally modeled by Friend & Abbott 1986) and the termination of the steady-state wind at a finite radius r_t (the "Koninx effect") are evident. Koninx (1992) showed that a new singular locus appears at large radii for rotating wind solutions, and the accelerating mCAK velocity laws intersect it non-tangentially. Thus, without the opportunity to *graze* this singular locus, as occurs near the star, the time-steady wind solutions become non-analytic for $r > r_t(V_{\rm eq})$. Note also that as $V_{\rm eq}$ increases, r_t decreases, and the critical radius r_c increases. For a large enough rotation speed, then, the two singular loci merge together, and do not even allow a partially analytic wind.

For the ζ Puppis standard model star, the rotation velocity where r_t drops from infinity to some finite value is $V_{\rm eq} \approx 410\,{\rm km\ s^{-1}}$. This value is apparently

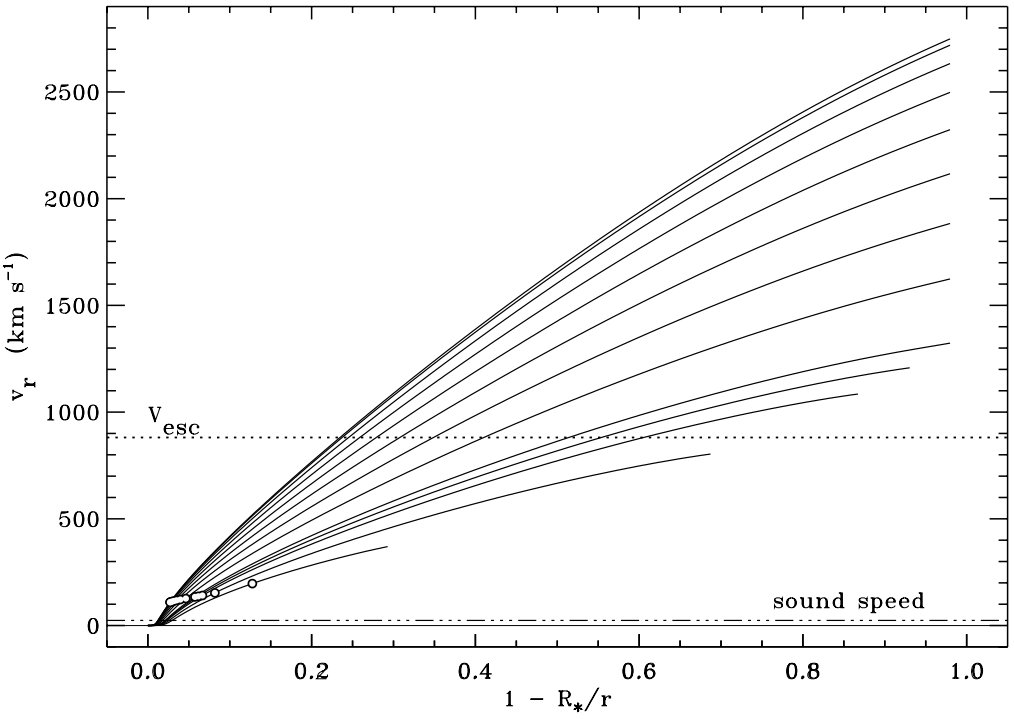

Figure 4.2: Equatorial velocity laws for rotating mCAK models of ζ Puppis. Oblateness and gravity darkening are neglected in these models. From top to bottom, the equatorial rotation velocities are 0, 50, 100, 150, 200, 250, 300, 350, 400, 412.5, 425, 450, 475 km/s. The mCAK critical points for each model are marked by white circles, and the surface escape velocity and sound speed are marked by dashed and dot-dashed lines, respectively. Note the cessation of mCAK wind solutions at *finite radii* for rotation velocities greater than ~410 km/s.

set by the drop in v_∞ to a value just slightly greater than $V_{\rm esc}$, and indeed, for B-stars, where $v_\infty/V_{\rm esc}$ is lower, the rotation speed where r_t becomes finite is also significantly lower. For the ζ Puppis model, the rotation velocity where r_t drops to equal r_c is $V_{\rm eq} \approx 480\,{\rm km\ s^{-1}}$. Numerical VH-1 models for rotation speeds between 410 and 480 km s^{-1} exhibit a well-behaved, time-steady wind for $r < r_t$, and a discontinuity or "kink" in the radial velocity gradient at $r = r_t$. Above this point, no *accelerating* mCAK solutions are available, but a *decelerating* solution is allowed which is extremely close to the pure gravitational "coasting" which would occur if the Sobolev line force were shut off completely. As the rotation velocity of the star increases, the kink-point r_t moves inward, and at some critical value of $V_{\rm eq}$ (still less than $480\,{\rm km\ s^{-1}}$) the decelerating post-kink wind will drop to zero velocity at some $r > r_t$, and the wind will become truly time-dependent. The stalled wind material may fall back down onto the star, and the system would oscillate quasi-stochastically as this limit is reached again and again.

4.2.2 Mass Loss Modulation due to Gravity Darkening

Surprisingly, no models of winds from rotating hot stars have incorporated the effects of gravity darkening. In *radiatively-driven* winds, the surface redistribution of the radiative flux should strongly affect the dynamics of the wind. Cranmer & Owocki (1995, see also Chapter 5) have computed the full vector Sobolev forces from an oblate and gravity-darkened star, but here we use the accuracy of hindsight to examine these effects from a more heuristic, but still reasonably accurate standpoint. As in Section 4.3 below, we present this simplified analysis *before* the full numerical results of Chapter 5 to better familiarize the reader with the various effects in isolation, before seeing them convolved together in the more self-consistent model.

Because of gravity darkening, the continuum radiative flux over the equator decreases as rotation increases, and this has the possibility of reducing the mass loss due to radiative driving, and counteracting the above centrifugal mass loss enhancement. Equations (2.110) and (2.118) can be expressed as a local mass flux per unit area at the stellar surface ($r = R_*$),

$$\dot{m} \equiv \rho v_r = \left\{ \frac{\alpha k^{1/\alpha}}{(1+\alpha) v_{th} c} \left[\frac{(1-\alpha)\sigma_e}{(1+\alpha)c} \right]^{(1-\alpha)/\alpha} \right\} \mathcal{F}^{1/\alpha}\, g_{\rm eff}^{(\alpha-1)/\alpha} \ , \qquad (4.30)$$

and this can be easily extended to the rotating case, where $\mathcal{F}$ and $g_{\rm eff}$ vary with colatitude θ and rotation rate ω. Note that, in general, the line-driving constants α and k vary with temperature (and thus latitude), but for simplicity we assume here they remain fixed. In Section 4.2.1, only the reduction of $g_{\rm eff}$ was taken into account, and it is clear for $\alpha < 1$ that this enhances $\dot{m}$. However, if we assume that the wind "sees" only the *locally* gravity-darkened flux $\mathcal{F}$ at the radius and colatitude

where the local mass loss is determined ($r_c \approx R_*$), we can use the von Zeipel result $\mathcal{F} \propto g_{\rm eff}$ (for $b = 0.25$) to find that

$$\dot{m}(\theta) \propto \mathcal{F}(\theta) \propto g_{\rm eff}(\theta) \ , \tag{4.31}$$

and the pole-to-equator variation of mass flux is independent of α. This implies a *decrease* in mass flux at the equator, where $g_{\rm eff}$ decreases, and an *increase* in mass flux over the poles due to the brighter flux there, compared to a nonrotating star.

For stars exhibiting gravity darkening with an arbitrary von Zeipel exponent b, the variation of mass flux from pole to equator may be increasing *or* decreasing. This can be seen by expressing the local mass flux as

$$\dot{m} \propto \left(K_{vz} g_{\rm eff}^{4b}\right)^{1/\alpha} g_{\rm eff}^{(\alpha-1)/\alpha} \propto g_{\rm eff}^{4(b-b_{crit})/\alpha} \ , \tag{4.32}$$

where $b_{crit} \equiv (1-\alpha)/4$. For $b < b_{crit}$, the mass loss *increases* from pole to equator, as in the non-gravity-darkened case of Section 4.2.1, or $b = 0$. For $b > b_{crit}$, the mass loss *decreases* from pole to equator, as in the fully-radiative case, $b = 0.25$, presented above. For $b = b_{crit}$, (which is equal to 0.1 for $\alpha = 0.6$) the mass flux does not vary with latitude. However, for the early-type O and B stars under consideration here, we expect that $b > b_{crit}$, and that the aforementioned decrease in $\dot{m}$ from pole to equator exists for these stars.

These results are qualitatively different from most other models of winds from rotating stars, which usually predict an equatorial mass loss and density enhancement. Here we find that the bright poles of a rotating hot star eject the densest "plumes" of the wind, and that the equator is both dark and not as dense. Note, however, that the *total* mass loss rate of a rotating star should increase as it spins faster, because, for $b = 0.25$,

$$\dot{M} = \oint \dot{m}\, r^2\, d\Omega \propto K_{vz}^{(1-\alpha)/\alpha} \oint \mathcal{F}\, r^2\, d\Omega \propto K_{vz}^{(1-\alpha)/\alpha} L_* \ , \tag{4.33}$$

and if we assume the bolometric luminosity remains unchanged with rotation, the increase in K_{vz}, or decrease in Σ_1 with increasing ω (see eq. [4.24]) dominates the star-integrated mass loss rate.

Figure 4.3 shows the variation of the mass flux $\dot{m}$ (normalized to the mass flux from a spherical nonrotating star) with colatitude θ and rotation rate ω, for both the pure centrifugal enhancement case of Section 4.2.1 and the von Zeipel ($b = 0.25$) case presented here. In Chapter 5 we compute more rigorously the flux that the wind sees exterior to an oblate and gravity-darkened (uniformly rotating) star, but the approximate results derived above seem to remain qualitatively valid. Thus, in cases where von Zeipel gravity darkening is present, the aforementioned loss of steady-state solutions (the "Koninx effect") should not occur, and the terminal velocity of

the wind may even *increase* over the equator of a rotating star. Of course, if v_∞ remains proportional to $V_{\rm esc}$ (and thus to $g_{\rm eff}$), the trend for the terminal velocity to decrease from pole to equator, and with increasing rotation rate, should remain unchanged.

4.3 Nonradial Radiative Shear Forces

When a radial wind outflow also rotates in the azimuthal direction, the Sobolev line resonances no longer depend only on the *radial* velocity gradient. As derived in Section 2.2.1, the radiative acceleration depends on the projected gradient of the projected velocity component along a given line of sight $\hat{\mathbf{n}}$, which is given by $\hat{\mathbf{n}} \cdot \nabla(\hat{\mathbf{n}} \cdot \mathbf{v})$, and radially asymmetric terms due to rotation can both (1) alter the radial (i.e., mCAK) component of the force, and (2) induce nonradial components of this force. Grinin (1978) first derived the form of these nonradial forces for generalized wind and accretion flows, and MacGregor & Friend (1984) applied them to hot-star winds with magnetic fields. The results of these analyses implied that a non-zero *azimuthal* force can arise in a rotating line-driven wind, but it was not clear if the magnitude of this force would ever be strong enough to significantly affect the radial flow, or in what sense (with or against the direction of rotation) it would act.

Cranmer & Owocki (1995, see also Chapter 5) rederived these general vector radiative forces from a rotating, oblate, and gravity-darkened hot star, but only recently have the dynamical implications of nonradial forces on rotating winds been examined (Owocki, Gayley, & Cranmer 1996). In the spirit of the von Zeipel gravity darkening analysis in the previous Section, here we isolate the azimuthal contribution of the Sobolev nonradial force in the equatorial plane, without considering any other effects of rotation (e.g., oblateness or gravity darkening). Thus, here we outline a simplified theory of radiative driving in a *plane-parallel* (i.e., near-star) environment, and assess the importance of the azimuthal line force which can arise when horizontal "shearing" velocities are present. The original idea for this analysis, and several of the key results herein, are due to K. G. Gayley, and a journal paper on this analysis is currently in preparation.

4.3.1 Plane-Parallel Hydrodynamic Equations

Our goal is to derive analytic relations governing the relative importance of radial and lateral line-driving forces in stellar winds. Because we are concerned mainly with the initial acceleration region of the wind, and thus with radii not too far from the photosphere, we will ignore the *sphericity* of the system, and work in a locally Cartesian frame of reference. (The justification for this approximation

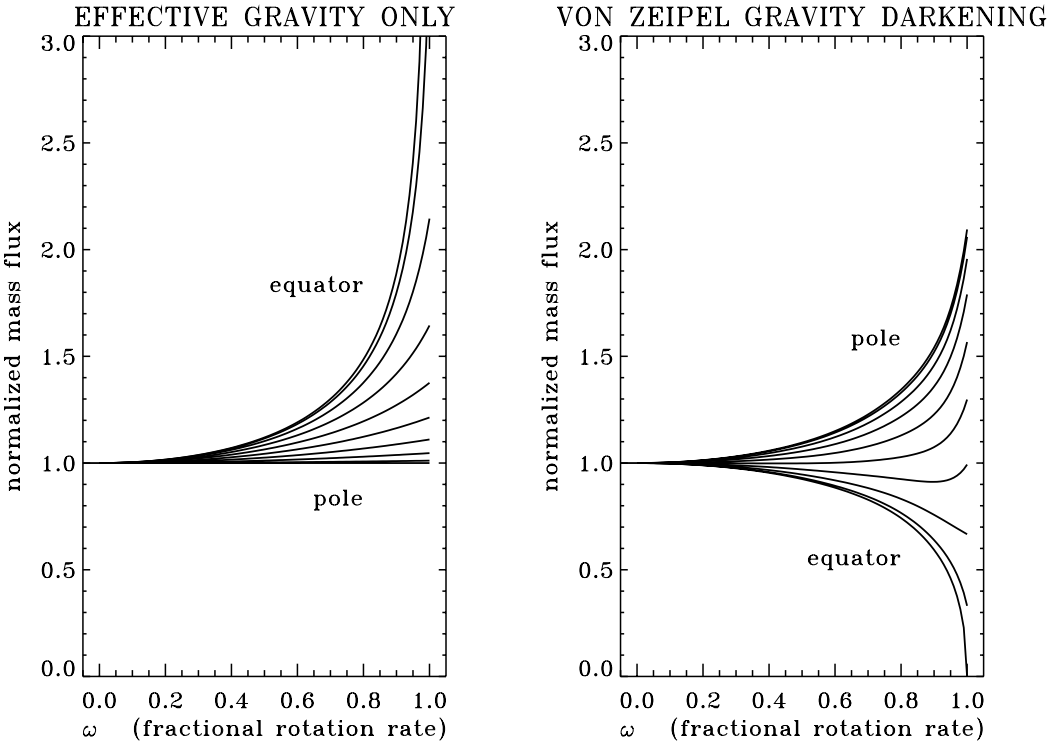

Figure 4.3: Relative mass flux variation with colatitude θ and rotational angular velocity ω, for the pure centrifugal enhancement of Section 4.2.1 (left curves), and the von Zeipel gravity darkening modulation of Section 4.2.2 (right curves). Colatitudes from pole (0 degrees) to equator (90 degrees) are plotted at 10 degree intervals.

will become evident when we determine the radii over which nonradial forces are important.) We define the vertical coordinate z as analogous to radius r, or height $(r - R_*)$, and we define the horizontal coordinate x as analogous to the azimuthal displacement $(r\phi \sin\theta)$, and take specifically $\theta = \pi/2$, or motion in the equatorial plane.

Defining the x and z velocities as u and w, respectively, the equation of mass continuity can be written

$$\frac{\partial \rho}{\partial t} + \frac{\partial}{\partial x}(\rho u) + \frac{\partial}{\partial z}(\rho w) \; = \; 0 \;\; , \tag{4.34}$$

which reduces to the particularly simple form

$$\rho \frac{\partial w}{\partial z} + w \frac{\partial \rho}{\partial z} \; = \; 0 \;\; , \tag{4.35}$$

when we assume time-steady and laterally-symmetric solutions. The assumption of lateral symmetry is equivalent to that of azimuthal symmetry in a rotating spherical system. The mass continuity equation can be integrated to find

$$\rho w \; = \; \dot{m}_0 \;\; , \tag{4.36}$$

which is a planar mass flux in the z direction. This is related to the more common spherical "mass loss rate," $\dot{M} = 4\pi r^2 \dot{m}_0$.

The x and z components of the equation of momentum conservation are

$$\rho \frac{\partial u}{\partial t} + \rho u \frac{\partial u}{\partial x} + \rho w \frac{\partial u}{\partial z} \;\; = \;\; -\frac{\partial P}{\partial x} + \rho g_x^{rad} \tag{4.37}$$

$$\rho \frac{\partial w}{\partial t} + \rho u \frac{\partial w}{\partial x} + \rho w \frac{\partial w}{\partial z} \;\; = \;\; -\frac{\partial P}{\partial z} - \rho g + \rho g_z^{rad} \;\; , \tag{4.38}$$

where g, g_x^{rad}, and g_z^{rad} represent the gravitational and radiative acceleration terms in the x and z directions, respectively. Assuming the above conditions of time-independence and lateral symmetry, together with an isothermal equation of state $(P = \rho a^2)$, these equations simplify to

$$w \frac{\partial u}{\partial z} \;\; = \;\; g_x^{rad} \tag{4.39}$$

$$\left(w - \frac{a^2}{w} \right) \frac{\partial w}{\partial z} \;\; = \;\; g_z^{rad} - g \;\; , \tag{4.40}$$

where eq. (4.35) has been used to eliminate the density gradient in favor of the velocity gradient. The radiative acceleration terms are written in terms of integrals

over the stellar "disk," which in this planar (near-star) limit expands to fill an entire hemisphere. Following the geometrical notation of Cranmer & Owocki (1995),

$$g_z^{rad} = C|w|^\alpha \frac{2}{\pi} \int_{\phi'=0}^{\pi/2} \int_{\mu'=0}^{1} \left(\left| \frac{\partial v_\ell}{\partial \ell} \right|_+^\alpha + \left| \frac{\partial v_\ell}{\partial \ell} \right|_-^\alpha \right) \mu' \, d\mu' \, d\phi' \tag{4.41}$$

$$g_x^{rad} = C|w|^\alpha \frac{2}{\pi} \int_{\phi'=0}^{\pi/2} \int_{\mu'=0}^{1} \left(\left| \frac{\partial v_\ell}{\partial \ell} \right|_+^\alpha - \left| \frac{\partial v_\ell}{\partial \ell} \right|_-^\alpha \right) \sqrt{1-\mu'^2} \, d\mu' \, \sin\phi' \, d\phi' \,, \tag{4.42}$$

with the constant C defined in the plane-parallel limit as

$$C \equiv \frac{GM_*, \; k}{R_*^2} \left(\frac{1}{\dot{m}_0 \, \sigma_e v_{th}} \right)^\alpha \tag{4.43}$$

and the line-of-sight velocity gradient, $\hat{\mathbf{n}} \cdot \nabla(\hat{\mathbf{n}} \cdot \mathbf{v})$, is written here as

$$\left(\frac{\partial v_\ell}{\partial \ell} \right)_\pm = \mu'^2 \left(\frac{\partial w}{\partial z} \right) \pm \mu' \sqrt{1-\mu'^2} \, \sin\phi' \left(\frac{\partial u}{\partial z} \right) \quad . \tag{4.44}$$

4.3.2 Zero-Order Solutions

First, consider solutions to the equations of motion without any radiative acceleration terms. For a nontrivial wind solution ($w \neq 0$), eq. (4.39) implies that the horizontal velocity u must be constant in z. The z-momentum equation, eq. (4.40), similarly implies the implicit Parker-like solution for $w(z)$:

$$a^2 \ln\left(\frac{w}{w_0} \right) - \frac{1}{2} \left(w^2 - w_0^2 \right) = gz \quad , \tag{4.45}$$

with the assumptions that g is constant in the near-star region of interest, and that $w(z=0) \equiv w_0$. In the supersonic ($w \gg a$) limit, the sound-speed-dependent term in the equation of motion can be neglected, and

$$w(z) \approx \sqrt{w_0^2 - 2gz} \quad . \tag{4.46}$$

In the extremely subsonic ($w \ll a$) limit, the inertial term in the equation of motion, proportional to $w(\partial w/\partial z)$, can be neglected, and

$$w(z) \approx w_0 \exp(z/H) \quad , \tag{4.47}$$

where the isothermal scale height $H \equiv a^2/g$.

The standard analysis of radiatively-driven stellar winds usually assumes that the horizontal radiative force g_x^{rad} is negligible when compared to the radial radiative

force g_z^{rad}. In our plane-parallel approximation, this is equivalent to assuming that $\partial u/\partial z = 0$. Note that the horizontal velocity itself (u) does not appear in any of the equations of motion, so it can be set to an arbitrary constant. Although we will eventually be concerned with "steep" shearing solutions (i.e., *large* values of $|\partial u/\partial z|$), the behavior of solutions in the limit of small horizontal gradients will be instructive to decide whether large solutions are even *possible* (see Figure 4.4).

The radial radiative force, in the limit of a vanishing horizontal velocity gradient, can be reduced to the particularly simple form:

$$g_z^{rad} = C \left| w \frac{\partial w}{\partial z} \right|^{\alpha} \frac{2}{\pi} \int_{\phi'=0}^{\pi/2} \int_{\mu'=0}^{1} |2\mu'|^{\alpha} \, \mu' \, d\mu' \, d\phi' \tag{4.48}$$

$$= C \left| w \frac{\partial w}{\partial z} \right|^{\alpha} \left(\frac{1}{1+\alpha} \right) \quad . \tag{4.49}$$

Using this, one can write the CAK equation of motion (eq. [4.40]) as

$$F_1 \equiv \left(1 - \frac{a^2}{w^2} \right) y + g - \frac{C}{1+\alpha} |y|^{\alpha} = 0 \quad , \tag{4.50}$$

with $y \equiv w(\partial w/\partial z)$. Since the CAK critical point is often seen to occur in the supersonic portion of the wind, we can analyze this equation in the limit of *zero-sound-speed,* and write the singularity condition,

$$\frac{\partial F_1}{\partial y} = 1 - \frac{\alpha C}{1+\alpha} |y|^{\alpha - 1} = 0 \quad , \tag{4.51}$$

and these two equations can be solved uniquely for C, which is related to the mass loss rate, and y_c, the critical value of the radial velocity gradient. Thus,

$$y_c = g \left(\frac{\alpha}{1-\alpha} \right) \quad , \qquad C |y_c|^{\alpha} = g \left(\frac{1+\alpha}{1-\alpha} \right) \quad . \tag{4.52}$$

In the region of z-values of interest, $y = y_c$ is *constant,* and the definition of y can be integrated to find

$$w(z) \approx \sqrt{w_0^2 + 2 \left(\frac{\alpha}{1-\alpha} \right) g z} \quad , \tag{4.53}$$

which is very similar to the above eq. (4.46), with the radiative acceleration counteracting gravity. Thus, in the spirit of the approximations in eqs. (4.46) and (4.47), we can *fit* the entire run of $w(z)$ from subsonic to supersonic velocities by the implicit solution of

$$a^2 \ln \left(\frac{w}{a} \right) + \frac{1-\alpha}{2\alpha} \left(w^2 - a^2 \right) = g z \quad , \tag{4.54}$$

where we have set $w_0 = a$.

4.3.3 Taylor Series Shear Analysis

The horizontal radiative acceleration is identically zero in the limit $\partial u/\partial z = 0$, but it will be instructive to determine the quantity $\partial g_x^{rad}/\partial(\partial u/\partial z)$, which is the *slope* of this force, in the limit of small horizontal velocity gradients. Figure 4.4 shows a relatively strong and weak horizontal radiative acceleration, plotted along with the inertial term (the left side of eq. [4.39]), both versus $\partial u/\partial z$. When the slope of g_x^{rad} – in the vicinity of the origin – is smaller than that of the straight line, the only solution available is the trivial one, $\partial u/\partial z = 0$. However, when the slope of g_x^{rad} is larger than that of the straight line, other "steep" shearing solutions become available. It is our goal to determine when these solutions are allowed in a line-driven wind.

The horizontal equation of momentum conservation can be written in terms of a new variable $\Psi \equiv (\partial u/\partial z)/(\partial w/\partial z)$, as

$$\Psi \;=\; C|y|^{\alpha-1}\,\frac{2}{\pi}\int_{\phi'=0}^{\pi/2}\int_{\mu'=0}^{1}\left(F_+ - F_-\right)\,\sqrt{1-\mu'^2}\;d\mu'\,\sin\phi'\,d\phi' \quad , \tag{4.55}$$

where here the line-of-sight velocity gradient terms have been scaled to

$$F_\pm \;\equiv\; \left|\mu'^2 \pm \Psi\,\mu'\sqrt{1-\mu'^2}\,\sin\phi'\right|^\alpha \quad . \tag{4.56}$$

Expanding to first order about $\Psi = 0$,

$$F_\pm(\Psi) \;=\; F_\pm(0) \;+\; \Psi\left(\frac{\partial F_\pm}{\partial \Psi}\right)_{\Psi=0} \;+\; \cdots \tag{4.57}$$

$$\approx\; \mu'^{2\alpha} \;\pm\; \alpha\Psi\mu'^{2\alpha-1}\sqrt{1-\mu'^2}\,\sin\phi' \quad . \tag{4.58}$$

The horizontal momentum conservation equation becomes, upon substituting $y = y_c$ from above,

$$\Psi \;=\; C|y_c|^{\alpha-1}\,\frac{4\alpha\Psi}{\pi}\int_{\phi'=0}^{\pi/2}\sin^2\phi'\,d\phi'\int_{\mu'=0}^{1}\left(\mu'^{2\alpha-1}-\mu'^{2\alpha+1}\right)\,d\mu' \tag{4.59}$$

$$=\; \left(\frac{1+\alpha}{\alpha}\right)\left(\frac{\Psi}{2(1+\alpha)}\right) \;=\; \frac{\Psi}{2\alpha} \quad , \tag{4.60}$$

which implies that, to obtain steep solutions in Figure 4.4, we require $\alpha < (1/2)$. This is a stringent limit which applies in the *supersonic* wind, and for realistic values of α, no shear solutions should be possible in the majority of the wind.

Note that the above analysis assumed a radial velocity gradient $y = y_c$ as given by the supersonic critical point analysis. In the *subsonic* region of the wind,

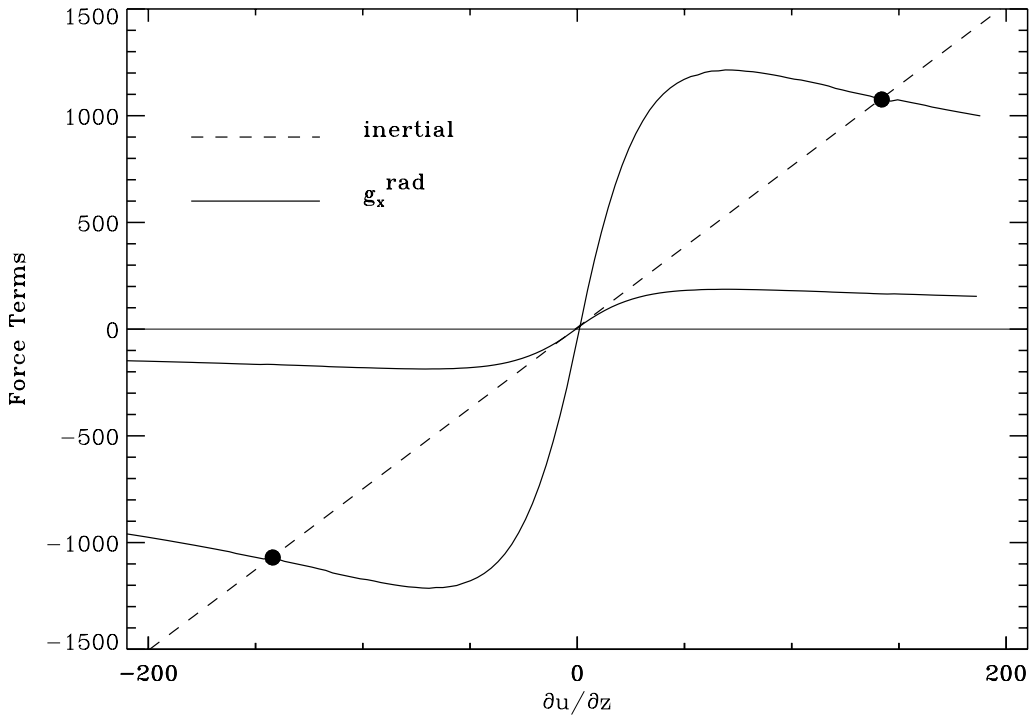

Figure 4.4: Horizontal radiative acceleration (solid lines) and inertial acceleration $w\,\partial u/\partial z$ (dashed line), plotted as a function of the vertical gradient of the horizontal velocity. A weak horizontal acceleration only satisfies the equations of motion for $\partial u/\partial z = 0$, but a strong horizontal acceleration also has "steep" shear solutions (filled circles) for large values of $|\partial u/\partial z|$.

this does not apply, and we can assume the radial velocity law given by eq. (4.47), implying that

$$y = \frac{w^2}{H} = \frac{w_0^2}{H}\exp(2z/H) \quad . \tag{4.61}$$

However, let us still assume that the mass-loss constant C is still given by the supersonic critical point analysis, since the mass flux is thought to be determined at that point. If we define $w_0 = a$, then, for negative z-values,

$$\Psi = C|y_c|^{\alpha-1}\left|\frac{y}{y_c}\right|^{\alpha-1}\left(\frac{\Psi}{2(1+\alpha)}\right) \tag{4.62}$$

$$= \Psi\left(\frac{\alpha}{1-\alpha}\right)^{1-\alpha}\frac{1}{2\alpha}\exp\left[-\frac{2z}{H}(1-\alpha)\right] \tag{4.63}$$

$$= \frac{\Psi}{2\alpha}\left[\left(\frac{\alpha}{1-\alpha}\right)^{1-\alpha}\left(\frac{w}{a}\right)^{2\alpha-2}\right] \equiv \frac{\Psi}{2\alpha}\zeta(\alpha,w) \quad . \tag{4.64}$$

For example, if $\alpha = 0.5$, the condition for steep solutions is simply $w < a$, but if $\alpha = 0.7$, the condition reduces to $w \lesssim 0.872\,a$. Clearly if $w \approx a$ the subsonic approximation breaks down, but these results conclusively show that extremely subsonic winds have a steep shear solution available for $\partial u/\partial z$. Unfortunately the magnitudes of *all* radiative forces are small in the deeply subsonic wind, and it is not clear how important these solutions will be at this depth.

4.3.4 Higher Order Shear Estimates

The above first-order Taylor series analysis tells us only if steep shearing solutions are or are not present. By going to higher order, we can model the "concavity" of $g_x^{rad}(\Psi)$ sufficiently well to actually solve for the steep value of Ψ. To simplify matters somewhat, note that the z-component of the radiative acceleration, $g_z^{rad}(\Psi)$ is an *even* function in powers of Ψ, and the x-component is an *odd* function in powers of Ψ. Thus, the scaled line-of-sight velocity gradient $F_\pm$ (eq. [4.56]) needs to be expanded at least to *third* order, to take into account the next highest order terms in both g_x^{rad} and g_z^{rad}:

$$F_\pm(\Psi) = F_\pm(0) + \Psi\left(\frac{\partial F_\pm}{\partial\Psi}\right)_0 + \frac{1}{2}\Psi^2\left(\frac{\partial^2 F_\pm}{\partial\Psi^2}\right)_0 + \frac{1}{6}\Psi^3\left(\frac{\partial^3 F_\pm}{\partial\Psi^3}\right)_0 + \cdots \tag{4.65}$$

$$\approx \mu'^{2\alpha} \pm \alpha\Psi\mu'^{2\alpha-1}\sqrt{1-\mu'^2}\,\sin\phi' \tag{4.66}$$

$$+ \frac{1}{2}\alpha(\alpha-1)\Psi^2\mu'^{2\alpha-2}(1-\mu'^2)\,\sin^2\phi' \tag{4.67}$$

$$\pm \frac{1}{6}\alpha(\alpha-1)(\alpha-2)\Psi^3\mu'^{2\alpha-3}(1-\mu'^2)^{3/2}\,\sin^3\phi' \quad . \tag{4.68}$$

Performing the angle integrations yields, for both components of the radiative acceleration,

$$g_z^{rad} \approx \frac{C}{1+\alpha}|y|^{\alpha}\left[1-\frac{1}{4}\Psi^2(1-\alpha)\right] \tag{4.69}$$

$$g_x^{rad} \approx \frac{C}{1+\alpha}|y|^{\alpha}\left(\frac{\Psi}{2}\right)\left[1-\frac{1}{4}\Psi^2(2-\alpha)\right] \quad . \tag{4.70}$$

Note that the critical-point solution to the vertical momentum conservation equation implies

$$C|y_c|^{\alpha-1} = \left(\frac{1+\alpha}{\alpha}\right)\frac{1}{1-\Psi^2(1-\alpha)/4} \quad , \tag{4.71}$$

with y_c defined as before, and the horizontal momentum conservation equation becomes (compare to eq. [4.62])

$$\Psi = \frac{\Psi}{2\alpha}\left[\frac{1-\Psi^2(2-\alpha)/4}{1-\Psi^2(1-\alpha)/4}\right]\left|\frac{y}{y_c}\right|^{\alpha-1} \tag{4.72}$$

$$= \frac{\Psi}{2\alpha}\left[\frac{1-\Psi^2(2-\alpha)/4}{1-\Psi^2(1-\alpha)/4}\right]\zeta(\alpha,w) \quad , \tag{4.73}$$

generalizing the notation defined for the *subsonic* wind in eq. (4.64). This last equation can be solved for the steep (nontrivial) solution,

$$\Psi = \sqrt{\frac{4(\zeta-2\alpha)}{2\alpha^2-(2+\zeta)\alpha+2\zeta}} \quad , \tag{4.74}$$

where $\zeta = 1$ if we assume $y = y_c$ in the supersonic wind. Figure 4.5 shows solutions for $w(z)$, from eq. (4.54), and $(\partial u/\partial z)$, as given above, for the specified $(\partial w/\partial z)$ and various values of α. Note that there is a relatively small and *finite* range of z-values for which there exists a significant horizontal shear for realistic ($\alpha > 0.5$) CAK winds, and the plane-parallel approximation in this Section is reasonably justified.

4.3.5 Stability of Shear Flows

The steep shear solutions derived above, which emerge from the photosphere with appreciable vertical gradients in both the u and w velocities, may or may not be stable to small perturbations. Let us review the conditions necessary for horizontal velocities to cause a convective instability in a plane-parallel atmosphere (see, e.g., Moss & Smith 1981). Consider a static and stratified medium which is convectively *stable,* i.e., with a Brunt-Väisälä oscillation frequency,

$$\omega_{BV}^2 = \frac{g}{\rho}\left[\left(\frac{\partial\rho}{\partial z}\right)_{ad} - \left(\frac{\partial\rho}{\partial z}\right)\right] \tag{4.75}$$

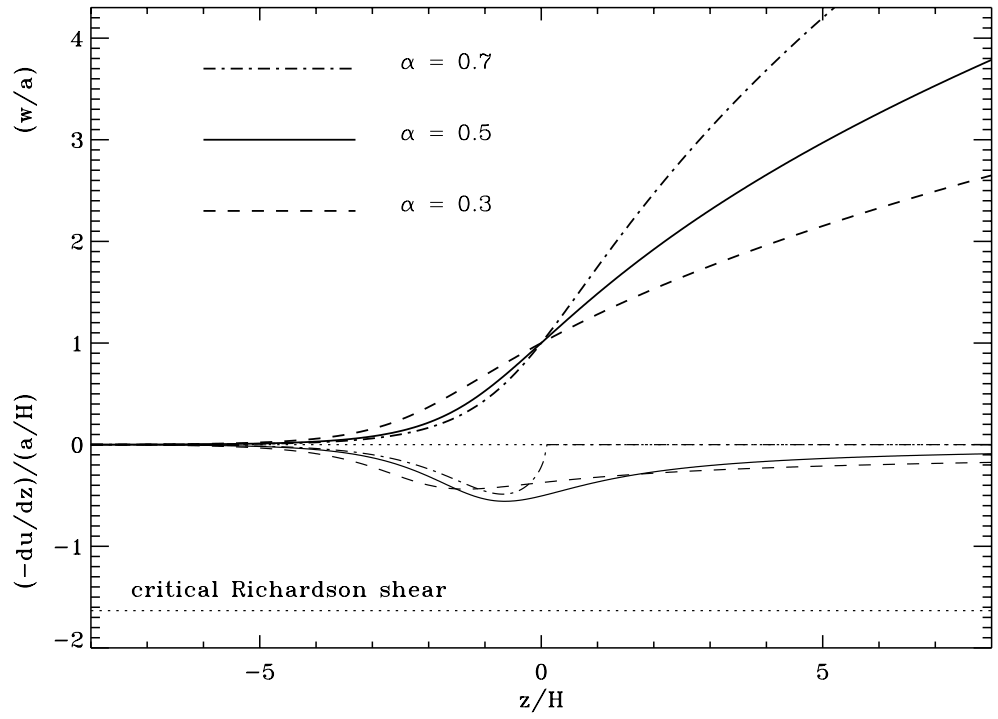

Figure 4.5: Upper curves: vertical velocity laws $w(z)$ for different mCAK α exponents, plotted versus height z, which is taken to be zero at the sonic point. **Lower curves:** dimensionless "steep" shear solutions from the third-order Taylor expansion of Ψ. The integrated "buildup" in u can be estimated by inspection to be limited only to a few sound speeds.

$$= \frac{g^2}{a^2}(\gamma - 1) > 0 \ , \tag{4.76}$$

where here the sound speed a is the *adiabatic* sound speed $(\gamma P/\rho)^{1/2}$, and eq. (4.76) is the Brunt-Väisälä frequency for an *isothermal* stratified atmosphere (see Chapter 7). The average force per unit volume felt by an oscillating parcel of gas, during a complete cycle of displacement, is approximately equal to

$$\Delta f \approx \frac{1}{2}\omega_{BV}^2 \rho \Delta z \ , \tag{4.77}$$

where the blob moves a mean distance Δz in one half-period of motion. The work (per unit mass) required to *interchange* two similar blobs, initially at heights z and $z + \Delta z$, is given by

$$\Delta W \approx \frac{2\Delta f}{\rho}\Delta z \approx \omega_{BV}^2 (\Delta z)^2 \ . \tag{4.78}$$

If we consider the possibility that *shear forces* can provide the work necessary to overturn these otherwise convectively *stable* parcels, we can express this work in terms of the kinetic energy stored in the relative horizontal motion of different layers. Assuming our two "stacked" blobs have horizontal speeds u and $u + \Delta u$, and also assuming that their *mixing* eventually yields a mean speed $u + \Delta u/2$, the difference in kinetic energies (per unit mass) between the initial and final states is

$$\Delta K = \frac{1}{2}u^2 + \frac{1}{2}(u + \Delta u)^2 - \frac{1}{2}\left[2\left(u + \frac{1}{2}\Delta u\right)^2\right] \tag{4.79}$$

$$= \frac{1}{4}(\Delta u)^2 \ , \tag{4.80}$$

indicating that the addition of shear in *any* horizontal direction produces extra positive kinetic energy which can drive a Kelvin-Helmholz instability. However, in our stratified medium, we only have instability if this kinetic energy outweighs the work needed to disrupt the convective stability, or

$$\Delta K > \Delta W \ . \tag{4.81}$$

This condition can be written in terms of the dimensionless *Richardson number,*

$$\mathrm{Ri} \equiv \frac{\Delta W}{4\,\Delta K} = \frac{\omega_{BV}^2 (\Delta z)^2}{(\Delta u)^2} \approx \frac{\omega_{BV}^2}{(\partial u/\partial z)^2} \ , \tag{4.82}$$

and the medium is stable when $\mathrm{Ri} \gtrsim (1/4)$ and unstable when $\mathrm{Ri} \lesssim (1/4)$. For an isothermal atmosphere, we can derive a critical value of the vertical gradient of the horizontal velocity, using $\mathrm{Ri} = 1/4$, and

$$\left(\frac{\partial u}{\partial z}\right)_{\mathrm{crit}} = \frac{2g}{a}\sqrt{\gamma - 1} \approx 1.63\left(\frac{a}{H}\right) \ , \tag{4.83}$$

for $\gamma = 5/3$. Note from Figure 4.5 that the magnitude of the "steep" shear solutions of $\partial u/\partial z$ are well *below* this critical value, implying their stability to shear-induced convective mixing.

The present plane-parallel analysis does not distinguish between steep *spin-up* azimuthal velocities ($\partial u/\partial z > 0$) and steep *spin-down* azimuthal velocities ($\partial u/\partial z < 0$). This degeneracy is lifted in the fully three-dimensional models in spherical coordinates presented in Chapter 5. A test point in the wind over a spherical star sees a distinct difference between the approaching and receding limbs of the rotating stellar disk, and the different Doppler shifts of stellar photons cause a definite bias toward azimuthal forces in the *opposite* direction to the rotation. Spin-down solutions are almost always favored in winds which rotate slower than the rigid body of the star, and this rapid decrease in $v_\phi(r)$ is able to rob the wind of a fraction of its angular momentum.

Chapter 5

RAPID STELLAR ROTATION: WIND COMPRESSED DISKS

It was forged in mills where the winter
Beats incessant; ten winters the disc
Unremitting endured the cold hammer.

William Blake, *The Book of Ahania*

In the previous Chapter we studied the effects of stellar rotation on the line-driven wind from a hot star, mainly by confining ourselves to the plane of the equator ($\theta = \pi/2$) and assuming azimuthal symmetry. In this Chapter we relax the former assumption and examine wind dynamics in the full meridional plane, while still retaining symmetry about the rotation axis. Stellar rotation influences the wind outflow through centrifugal and Coriolis forces that enforce angular momentum conservation, generally tending to deflect material toward the equatorial plane and thus enhancing the density and mass outflow there. Bjorkman & Cassinelli (1993; hereafter BC) have proposed this simple and powerful "wind compressed disk" (WCD) paradigm for explaining how rotation can deflect wind flow streamlines toward the equatorial plane to possibly form shocked disks. Owocki, Cranmer, & Blondin (1994; hereafter OCB) generally confirmed BC's kinematic picture using a numerical hydrodynamics code, but found several quantitative differences from BC's original analytic model.

Section 5.1 outlines BC's original idea of wind compression, and also discusses several subsequent refinements and insights into the general phenomenon. Section 5.2 examines in detail how oblateness and gravity darkening of the underlying star alters the radiative driving of the wind, and describes initial attempts to model how this affects the wind outflow itself. This Section incorporates results

from Cranmer & Owocki (1995) and Owocki, Gayley, & Cranmer (1996). Section 5.3 displays computed theoretical P Cygni line profiles and continuum polarization from hydrodynamical models of rapidly-rotating winds, but this modeling is still in progress. Finally, Section 5.4 presents a preliminary analysis of the dynamics of the thin shocked disk which occurs in some rapidly rotating WCD models.

5.1 The Basic Wind Compression Effect

The original model of BC contained two relatively independent components: (i) the *wind compression* that arises from the overall equatorial deflection of the wind, and (ii) the *shocked disk* which can form if compression streamlines attempt to cross the plane of the equator. OCB has shown that the approximations BC used to compute the wind compression, with several minor modifications, are essentially valid, while their model of the disk itself is less reliable. Thus, in the present analysis, we will concentrate only on extensions to the analytic wind compression, and momentarily ignore the consequences of the presence of a shocked disk.

The analytic models of BC are essentially kinematic, in that the radial wind velocity is specified as a function of radius r and colatitude θ, and centrifugal and Coriolis forces then deflect these radial streamlines toward the plane of the equator. The essential assumption of a supersonic wind (thus allowing "fluid particles" to be treated as pressureless and non-interacting Newtonian tracers) is reasonably valid, as long as the wind is assumed to be rigidly-rotating with the star below the sonic point. Thus, the particle streamlines are determined solely by the external forces: gravity and radiative acceleration. Angular momentum conservation confines these trajectories to an "orbital plane" perpendicular to the initial angular momentum vector. Although BC model the radial velocity as a "beta law" (eq. [2.119]), with v_∞ a function of the stream's initial colatitude θ_i, we can generalize to the case of arbitrary velocity laws at the pole and the equator (external to any disks). At all latitudes, we thus define

$$v_r(r/R_*, \theta_i) \;=\; v_r^{\rm pole}(r/R_p)\,[1-\Theta(\theta_i)] + v_r^{\rm eq}(r/R_{\rm eq})\,\Theta(\theta_i) \;\;, \tag{5.1}$$

where we define the "latitude interpolation" function $\Theta(\theta_i)$. This form is meant to be a generalization of BC's radial velocity fits, and indeed reduces to their model when: (1) the radial velocities are assumed to follow a beta-law, and (2) the star is spherical. This function is given by

$$\Theta(\theta_i) \;\equiv\; \frac{[1-(R_*(\theta_i)/R_{eq})\,\omega\sin\theta_i]^\gamma - 1}{(1-\omega)^\gamma - 1} \;\;. \tag{5.2}$$

The exponent γ was found, through fits to Friend & Abbott's (1986) equatorial wind models (with rotation and a uniformly bright finite disk), to be $\gamma \approx 0.35$. However,

the results of Poe (1987) indicate that for O-stars, $\gamma \approx 0.5$ (see also Ignace et al. 1996). BC and OCB specify the latitude-dependent mass flux $\dot{M}(\theta_i)$ from similar fits to Friend & Abbott's (1986) models. We have similarly generalized this formalism, given polar and equatorial values for $\dot{M}$, in order to compute the local density $\rho(r, \theta)$:

$$\dot{M}(\theta_i) \; = \; \dot{M}_{\rm pole} \left[1 - \frac{R_*(\theta_i)}{R_{eq}} \omega \sin\theta_i \right]^{\xi} \quad , \tag{5.3}$$

where $\xi \approx -0.43$ from Friend & Abbott's models, but is uniquely determined, from $\xi \; \equiv \; \log(\dot{M}_{\rm eq}/\dot{M}_{\rm pole})/\log(1-\omega)$, given the polar and equatorial values. Note, however, that strict mass conservation along streamlines demands that

$$\dot{M}(\theta_i) d(\cos\theta_i) \; = \; 4\pi \rho(r,\theta) v_r(r,\theta) r^2 d(\cos\theta) \quad , \tag{5.4}$$

and this expression is used to determine the local density $\rho(r, \theta)$. (BC; Ignace et al. 1996).

The motion in the orbital plane around an inclined azimuthal angle ϕ_i is specified by the local conservation of angular momentum, and

$$v_{\phi_i}(r, \theta_i) \; = \; \frac{\Omega R_*(\theta_i)^2 \sin\theta_i}{r} \quad . \tag{5.5}$$

Note that BC's factor of $V_{rot} \equiv V_{\rm eq} \sin\theta_i$ has been consistently replaced with $V_{rot} \equiv \Omega R_*(\theta_i) \sin\theta_i$, which is not strictly equivalent for an oblate star, but more accurately takes the whole star's rigid rotation into account. The specification of v_r and v_{ϕ_i} allows orbital trajectories to be computed, and the resulting equation of motion, found from the ratio of these two velocities, is integrated from the sonic point R_s to obtain the value of the inclined azimuthal angle traversed by the streamline,

$$\phi_i(r, \theta_i) \; = \; \int_{r'=R_s}^{r} \frac{v_{\phi_i}(r', \theta_i)}{r' v_r(r', \theta_i)} dr' \quad . \tag{5.6}$$

BC and Ignace et al. (1996) use a kinematic beta law for v_r, and are able to evaluate this integral analytically. Given these trajectories, one can determine the velocity vector field in the wind, $\mathbf{v} = v_r \hat{r} + v_\theta \hat{\theta} + v_\phi \hat{\phi}$, and the density scalar field ρ, using the geometrical relations derived by BC. Specifically,

$$v_\theta \; = \; v_{\phi_i}(\cos\theta_i \, \sin\phi) \tag{5.7}$$

$$v_\phi \; = \; v_{\phi_i}(\cos\theta_i \, \cos\theta \, \cos\phi \, + \, \sin\theta \, \sin\theta_i) \quad , \tag{5.8}$$

where $\cos\phi = \tan\theta_i / \tan\theta$, and

$$\rho \; = \; \frac{\dot{M}(\theta_i)}{4\pi r^2 v_r} \left[\cos\phi_i + \frac{\cos^2\theta_i}{\sin\theta_i} \frac{d\phi_i}{d(\sin\theta_i)} \sin\phi_i \right]^{-1} \quad . \tag{5.9}$$

Note that, in order to specify $\mathbf{v}$ and ρ for an arbitrary "grid" point (r, θ), one must first solve for the initial colatitude θ_i of the streamline which passes through the given point in the wind, and this usually involves numerically finding the root of the trajectory equation (5.6) that also satisfies BC's geometrical transformation, $\cos\theta = \cos\theta_i \cos\phi_i$.

At high latitudes, rapid rotation causes wind streamlines to deflect away from the poles and toward the equatorial plane. These fluid streamlines are diverging faster than r^2 (spherical expansion), and this affects the conservation of mass which in turn impacts on the equation of motion. Kopp & Holzer (1976) and MacGregor (1988) investigate this effect in the context of magnetically enforced non-spherical expansion, and MacGregor finds (for point-star CAK winds) that although the mass loss rate is seldom strongly affected, the asymptotic wind velocity can be enhanced in regions of rapid flow divergence. Let us derive the appropriate non-spherical expansion factor for wind over the poles of a rapidly rotating star.

Consider a small initial streamline colatitude θ_i, assuming $\sin\theta_i \approx \theta_i$ and $\cos\theta_i \approx 1 - \theta_i^2/2$. The divergence of this streamline, always infinitesimally close to the pole (thus $R_*(\theta_i) \approx R_p$), will provide the necessary non-spherical divergence factor required in the mass continuity equation. We can approximate the motion in the inclined orbital plane by

$$v_{\phi_i}(r, \theta_i) \approx \frac{\Omega R_p^2 \, \theta_i}{r} \quad , \tag{5.10}$$

and the inclined azimuthal angle ϕ_i (eq. [5.6]) is then given by

$$\phi_i(r, \theta_i) \approx \Omega R_p^2 \, \theta_i \int_{r'=R_s}^{r} \frac{dr'}{r'^2 \, v_r(r')} \quad . \tag{5.11}$$

What is needed, however, is the angle θ of the streamline itself as a function of radius. Using one of BC's geometrical transformations, and realizing that all angles are small,

$$\begin{aligned} \cos\theta &= \cos\theta_i \cos\phi_i \\ \left(1 - \theta^2/2\right) &\approx \left(1 - \theta_i^2/2\right)\left(1 - \phi_i^2/2\right) \quad . \end{aligned} \tag{5.12}$$

Neglecting fourth order terms, we find that

$$\theta(r) \approx \theta_i \sqrt{1 + (\phi_i/\theta_i)^2} \quad . \tag{5.13}$$

Note that (ϕ_i/θ_i) depends only on the radius r (eq. [5.11]), and can be computed analytically if a beta-law is assumed for the radial velocity (BC; Ignace et al. 1996).

To be able to write the mass continuity equation, we must parameterize the area of a given polar (or near-polar) flux tube. Assuming azimuthal symmetry,

$$A(r) \;=\; 2\pi \int_0^{\theta(r)} r^2 \sin\theta' \, d\theta' \;=\; 2\pi r^2 \left[1 - \cos\theta(r)\right] \quad . \tag{5.14}$$

Thus, following Kopp & Holzer (1976), this area can be written as the product of the area at the stellar surface A_* with the spherical and non-spherical factors of expansion,

$$A(r) \;=\; A_* \left(\frac{r}{R_*}\right)^2 f(r) \quad , \tag{5.15}$$

where

$$f(r) \;=\; \frac{1 - \cos\theta(r)}{1 - \cos\theta_i} \;\approx\; \frac{\theta(r)^2}{\theta_i^2} \;\approx\; 1 + \left(\frac{\phi_i}{\theta_i}\right)^2 \quad . \tag{5.16}$$

It is this non-spherical factor $f(r)$ which is inserted into the mCAK equation of motion, and which can strongly affect the wind dynamics over the pole of a rotating star (see MacGregor 1988 and Section 5.2.5, below).

5.2 The Oblate Finite Disk Factor

This Section begins the process of eliminating certain approximations used in computing the radiative acceleration on the wind. Although OCB formulated the two-dimensional (2D) wind dynamics exterior to an *oblate* stellar surface in order to properly define the centrifugally distorted hydrostatic boundary, they assumed a purely radially-directed radiation force from a spherical, non-rotating star. In order to produce more self-consistent and accurate models, we present here the theoretical formalism for including the effects of stellar oblateness, limb darkening, and gravity darkening on the radiation force. In addition, we subsequently estimate the dynamical impact of such phenomena on the winds and WCDs around B stars. The actual inclusion of such forces in the time-dependent hydrodynamics is deferred to subsequent work, however, because of their inherent complexity and the increased computational expense.

Without actually computing these complex multidimensional forces, it is difficult to assess even the sense of their effect on the resulting wind dynamics. While oblateness and gravity darkening over the equator could lead to an overall decrease in the acceleration (due to the reduced flux), the higher radiative flux emanating from the poles could in turn "pinch" the force toward the equator, thus increasing the tendency to form a disk. By computing the fully oblate and gravity-darkened vector force, we thus begin to disentangle these various competing effects from each other, as well as evaluate their relative importance in the wind and disk dynamics.

5.2.1 Geometrical Considerations

Let us set up the geometrical formalism required to compute the general radiative acceleration integrals. Consider an azimuthally-symmetric oblate star centered on an origin, with its surface denoted by spherical polar coordinates $R_*(\theta)$, θ, and ϕ, and a field point in the wind, a distance r_o from the origin, inclined an angle θ_o from the z axis, and in the x-z plane (i.e. $\phi_o = 0$). Define a new, "wind-centered" coordinate system by rotating the y axis by an angle θ_o and translating the origin to the position of the field point. Thus, the new z' axis points away from the center of the star, in the $\hat{\mathbf{r}}_o$ direction, the new x' axis points in the $\hat{\boldsymbol{\theta}}_o$ direction, and the new y' axis is parallel with the old y axis (see Figure 5.1). Using Cartesian coordinates, the transformation between the two systems is given by

$$\begin{aligned} x' &= x\cos\theta_o - z\sin\theta_o \\ y' &= y \\ z' - r_o &= x\sin\theta_o + z\cos\theta_o \ . \end{aligned} \tag{5.17}$$

To evaluate the radiative acceleration integrals, both the direct stellar intensity and the projected velocity gradient must be evaluated for arbitrary rays $\hat{\mathbf{n}}$, directed from points on the stellar surface to the field point at the transformed origin. The necessary angular integrations are thus most conveniently expressed in terms of the transformed spherical polar coordinates r', θ', and ϕ'.

Before being able to evaluate the stellar intensity $I^C(\hat{\mathbf{n}})$, it is necessary to know at what point the ray $\hat{\mathbf{n}}$ intercepts the stellar surface. For a spherical star with no limb or gravity darkening, this information is never needed, but the position-dependent effective temperature $T_{\rm eff}(\theta)$ is required in the present case to compute the stellar intensity. For a given ray $\hat{\mathbf{n}}$, specified by wind-centered angles θ' and ϕ', there are, in general, either zero, one, or two possible values of r' which intercept the stellar surface, corresponding to rays lying outside, on, or inside the limb of the star, respectively. In the case of two solutions, of course, the smaller of the two values for r' corresponds to the more physically relevant (nearer) point on the oblate surface. We find these solutions numerically by transforming the point referenced by wind-centered coordinates (r', θ', ϕ') into star-centered coordinates (r, θ, ϕ), and computing the corresponding surface radius $R_*(\theta)$. If $r = R_*$ for the given value of r', then the ray $\hat{\mathbf{n}}$ exactly intercepts the stellar surface, and the star-centered angle θ can be used to compute the gravity-darkened effective temperature, and thus the intensity.

For arbitrary locations in the wind, the direct specific intensity from points on the star is given by

$$I^C(\mathbf{r}, \hat{\mathbf{n}}) \ = \ \sigma_B T_{\rm eff}^4 \, D(\mathbf{r}, \hat{\mathbf{n}}) \ , \tag{5.18}$$

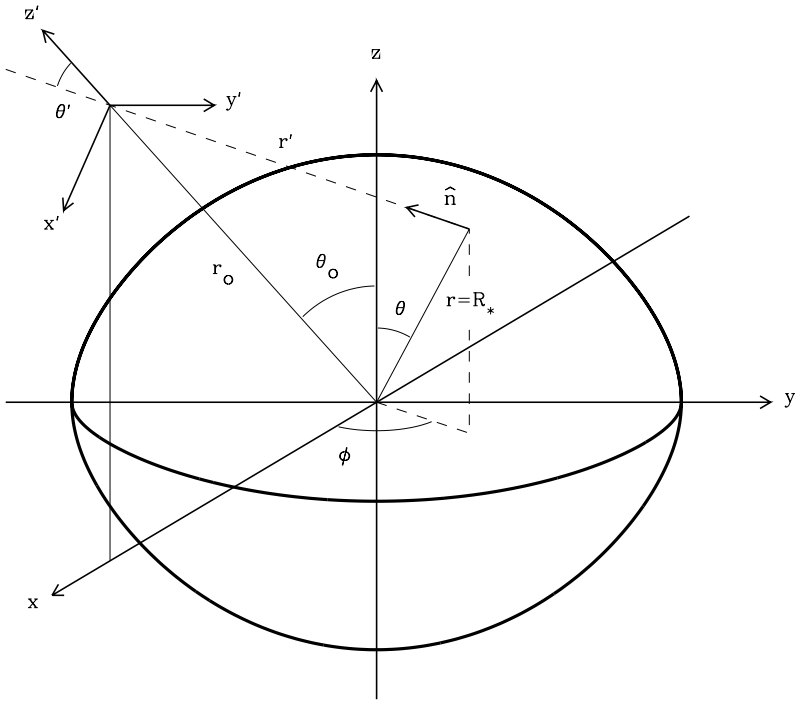

Figure 5.1: Coordinate geometry for the computation of the oblate finite disk (OFD) factor. The star-centered (un-primed) and wind-centered (primed) coordinate systems are shown, related by the position of the field point.

where the effective temperature is evaluated on the point at which the ray $\hat{\mathbf{n}}$ intercepts the oblate stellar surface. The linear limb darkening function is similar to that used for a spherical star,

$$D(\mathbf{r},\hat{\mathbf{n}}) = \begin{cases} 0, & \text{outside the limb,} \\ (2+3\mu'')/4\pi, & \text{inside the limb,} \end{cases} \tag{5.19}$$

but μ'', the cosine of the angle between the local normal to the surface (opposite the local gravity) and the ray angle $\hat{\mathbf{n}}$, must be specified more precisely by

$$\mu'' = -\frac{\mathbf{g}\cdot\hat{\mathbf{n}}}{|\mathbf{g}|} \ . \tag{5.20}$$

Note from, e.g., Figure 2 of Cranmer & Owocki (1995), that it is only for nearly equator-on views that limb darkening has a large qualitative impact on the appearance of a gravity darkened star.

The projected velocity gradient $\hat{\mathbf{n}}\cdot\nabla(\hat{\mathbf{n}}\cdot\mathbf{v})$, which resembles the rate-of-strain tensor in fluid dynamics, has been derived for a general 3D geometry by Batchelor (1967) and Koninx (1992). The assumption of azimuthal symmetry in this work somewhat simplifies this complex expression:

$$\hat{\mathbf{n}}\cdot\nabla(\hat{\mathbf{n}}\cdot\mathbf{v}) = \left(\frac{\partial v_r}{\partial r}\right)a_1^2 + \left(\frac{1}{r}\frac{\partial v_\theta}{\partial\theta}+\frac{v_r}{r}\right)a_2^2 + \left(\frac{v_r}{r}+\frac{v_\theta\cot\theta_o}{r}\right)a_3^2 + \left(\frac{\partial v_\theta}{\partial r} - \frac{v_\theta}{r}+\frac{1}{r}\frac{\partial v_r}{\partial\theta}\right)a_1a_2 + \left(\frac{\partial v_\phi}{\partial r}\right)a_1a_3 + \left(\frac{1}{r}\frac{\partial v_\phi}{\partial\theta}\right)a_2a_3 + \left(\frac{v_\phi}{r\sin\theta_o}\right)a_3a_4 \ , \tag{5.21}$$

with trigonometric factors defined by

$$\begin{aligned} a_1 &= n_r &&= n_{z'} &&= \mu' \\ a_2 &= n_\theta &&= n_{x'} &&= \sqrt{1-\mu'^2}\cos\phi' \\ a_3 &= n_\phi &&= n_{y'} &&= \sqrt{1-\mu'^2}\sin\phi' \\ a_4 &= \partial n_\phi/\partial\phi &&= -n_x &&= -\mu'\sin\theta_o - \sqrt{1-\mu'^2}\cos\phi'\cos\theta_o \end{aligned} \tag{5.22}$$

and using the standard notation $\mu' = \cos\theta'$.

Finally, we can explicitly write the oblate finite disk (OFD) factors in terms of the transformed coordinates, and following eq. (2.73),

$$\boldsymbol{\eta}^{\rm C} = \frac{4\pi r_o^2}{L_*}\oint \sigma_B T_{\rm eff}^4(\theta)\, D(\mathbf{r},\hat{\mathbf{n}})\ \hat{\mathbf{n}}\, d\mu' d\phi' \tag{5.23}$$

$$\boldsymbol{\eta}^{\rm L} = \frac{4\pi r_o^2}{L_*(\partial v_r/\partial r)^\alpha}\oint \sigma_B T_{\rm eff}^4(\theta)\, D(\mathbf{r},\hat{\mathbf{n}})\,[\hat{\mathbf{n}}\cdot\nabla(\hat{\mathbf{n}}\cdot\mathbf{v})]^\alpha\ \hat{\mathbf{n}}\, d\mu' d\phi' \ . \tag{5.24}$$

We can use the r, θ, and ϕ components of $\hat{\mathbf{n}}$ (found from the trigonometric factors a_1, a_2, and a_3 above) to obtain the respective components of $\boldsymbol{\eta}^{\rm C}$ and $\boldsymbol{\eta}^{\rm L}$. Note that η_ϕ^C is identically zero because of symmetry about the x'-z' plane in the flux. The corresponding line factor η_ϕ^L, however, is *not* zero, because the v_ϕ-component of the wind flow breaks this symmetry.

Although the OFD integrals require numerical evaluation in the most general case, the continuum OFD factor $\boldsymbol{\eta}^{\rm C}$ has a rather simple limit as the field point approaches the surface of the star (i.e. $r_o = R_*$). On the surface, the emergent vector flux is given wholly by the effect of von Zeipel gravity darkening (see Section 4.1), and depends only on the inclination colatitude θ_o,

$$\boldsymbol{\eta}^{\rm C}(r = R_*) = \frac{4\pi r^2}{L_*}\boldsymbol{\mathcal{F}} = -\frac{4\pi R_*^2(\theta_o)}{\Sigma_1}\,\mathbf{g}(\theta_o) \ . \tag{5.25}$$

Thus, using the expression for the r and θ components of the effective gravity from Section 4.1,

$$\eta_r^C(r = R_*) = \frac{4\pi GM_*}{\Sigma_1}\left[1 - \frac{8}{27}\left(\frac{R_*(\theta_o)}{R_p}\right)^3 \omega^2 \sin^2\theta_o\right] \tag{5.26}$$

$$\eta_\theta^C(r = R_*) = \frac{4\pi GM_*}{\Sigma_1}\left[-\frac{8}{27}\left(\frac{R_*(\theta_o)}{R_p}\right)^3 \omega^2 \sin\theta_o\cos\theta_o\right] \ . \tag{5.27}$$

Note that, as expected, the radial force points outward, and the equatorward (θ) force points toward the *poles*, indicating that as the star becomes more flattened, the local normal vectors to the stellar surface point more and more toward the $\pm z$ directions. The fact that $\eta_\phi^C = 0$ is evident, at least at the stellar surface, because g_ϕ is identically zero.

5.2.2 Representative B Star Model

Our basic B-star model is the standard S-350 model of OCB, a B2.5 main sequence star, chosen because it lies near the middle of the nominal range of spectral types for the Be phenomenon. Specifically, we take $M_* = 7.5M_\odot$, $R_p = 4R_\odot$, $L_* = 2310L_\odot$, and $T_{\rm eff} = 20000$ K. An equatorial rotation velocity of 350 km s^{-1} is used, because it exhibits a moderate degree of oblateness, gravity darkening, and wind compression, and it corresponds to a fractional angular velocity of $\omega = 0.89325$. We assume an isothermal wind of temperature $T_{\rm eff}$, corresponding to a sound speed of 16.53 km s^{-1}, and use the line-driving constants $\alpha = 0.51$, $k = 0.609$, and $\delta = 0.166$ (BC, OCB). In the most general case, these constants probably vary with latitude and distance from the star, but for simplicity we assume they remain fixed throughout the wind.

Table 5.1: Oblate Finite Disk Wind Models

	S-350	A	A1
$r_{\rm crit}(0°)/R_p$	—	1.06910	1.05547
$r_{\rm crit}(90°)/R_p$	—	1.35253	1.35253
$v_r(6R_p, 0°)$ (km/s)	1221.54	1098.05	1304.39
$v_r(6R_p, 90°)$ (km/s)	489.07	559.23	559.23
$\beta_{\rm eff}(2R_p, 0°)$	0.65050	0.71712	0.77445
$\beta_{\rm eff}(2R_p, 90°)$	1.41291	1.04191	1.04191
$\dot{M}(0°)$ ($10^{-10}\,M_\odot$/yr)	3.158	5.926	6.269
$\dot{M}(90°)$ ($10^{-10}\,M_\odot$/yr)	16.96	12.32	12.32
$\rho(2R_p, 90°)/\rho(2R_p, 0°)$	14.3948	8.66475	9.07238
$\max(v_\theta)$ (km/s)	74.593	60.168	58.637

Table 5.2: Oblate Finite Disk Wind Models, continued

	B	C	D	E
$r_{\rm crit}(0°)/R_p$	1.03328	1.03548	1.03614	1.03557
$r_{\rm crit}(90°)/R_p$	1.35443	1.35177	1.35153	1.35160
$v_r(6R_p, 0°)$ (km/s)	2145.33	1987.36	2001.96	2000.94
$v_r(6R_p, 90°)$ (km/s)	817.54	797.02	799.07	798.86
$\beta_{\rm eff}(2R_p, 0°)$	0.92815	0.90088	0.90325	0.90305
$\beta_{\rm eff}(2R_p, 90°)$	1.31931	1.29759	1.29928	1.29905
$\dot{M}(0°)$ ($10^{-10}\,M_\odot$/yr)	5.775	5.723	5.729	5.726
$\dot{M}(90°)$ ($10^{-10}\,M_\odot$/yr)	3.086	3.093	3.096	3.096
$\rho(2R_p, 90°)/\rho(2R_p, 0°)$	2.98853	2.84927	2.86214	2.86212
$\max(v_\theta)$ (km/s)	53.862	54.408	54.353	54.344

The wind from this model star can be specified either using the semi-analytic WCD compression paradigm or by numerically modeling the 2D wind hydrodynamics. Tables 5.1 and 5.2 show several characteristic wind quantities for the various wind models to be discussed. The standard OCB numerical model S-350, and a corresponding semi-analytic model A, are computed using the uniformly-bright spherical finite disk factor η_{un} (eq. [2.78]), evaluated using the polar value of the stellar radius at all latitudes. The polar and equatorial values of $v_r(r)$ and $\dot{M}$ for model A were computed in one dimension (1D) using a modified CAK (mCAK) code, with centrifugal forces and arbitrary finite disk factors included, and which performs the standard critical point analysis and solves the radial momentum conservation equation (see Friend & Abbott 1986; Pauldrach, Puls, & Kudritzki 1986). Abbott's (1982a) correction term for the radiative acceleration, proportional to $(\rho/W)^\delta$, is included in these models, but the standard 1D form of the dilution factor W is assumed, using the value of the stellar radius corresponding to the colatitude of the field points (i.e. either 0° or 90°). The other wind models in Tables 5.1 and 5.2 all assume the semi-analytic wind compression formalism of Section 5.1, use successive approximations to the OFD factors derived above, and will be discussed further below. The exponent $\beta_{\rm eff}$ is defined as in eq. (2.129), and the tabulated "equatorial" values from the 2D hydrodynamics code are taken at $\theta \approx 87.1°$, outside the shocked disk, in order to more clearly compare with the pure wind-compression models.

5.2.3 The Continuum Oblate Finite Disk Factor

Let us first examine the continuum OFD factor $\boldsymbol{\eta}^{\rm C}$, which depends only on the stellar intensity and not the wind. Although the continuum acceleration in O and B stellar winds is a relatively unimportant piece of the dynamical problem (because often, , $\ll 1$), we will find that, to zero order, $\boldsymbol{\eta}^{\rm C}$ and $\boldsymbol{\eta}^{\rm L}$ behave in similar ways. Thus, an understanding of the oblateness and gravity darkening effects in the former is essential for understanding the latter.

Figures 5.2 and 5.3 display the radial and latitudinal components of the continuum OFD factor, η_r^C and η_θ^C, for our representative model. Note that the dominant effect in both components follows the sense of the "sub-stellar" surface gravity darkening derived above (eq. [5.26] and [5.27]). This implies that, for an arbitrary point in the wind, most of the star's flux appears to come from an effective temperature corresponding to the point on the star nearest to the field point, where the limb darkening function is a maximum. Thus, η_r^C varies roughly monotonically, from a maximum at the bright poles to a minimum at the darker equatorial plane, and η_θ^C is negligibly small at the poles and equator, where the normal to the stellar surface is radial, and reaches a negative (poleward) maximum in the mid-latitudes.

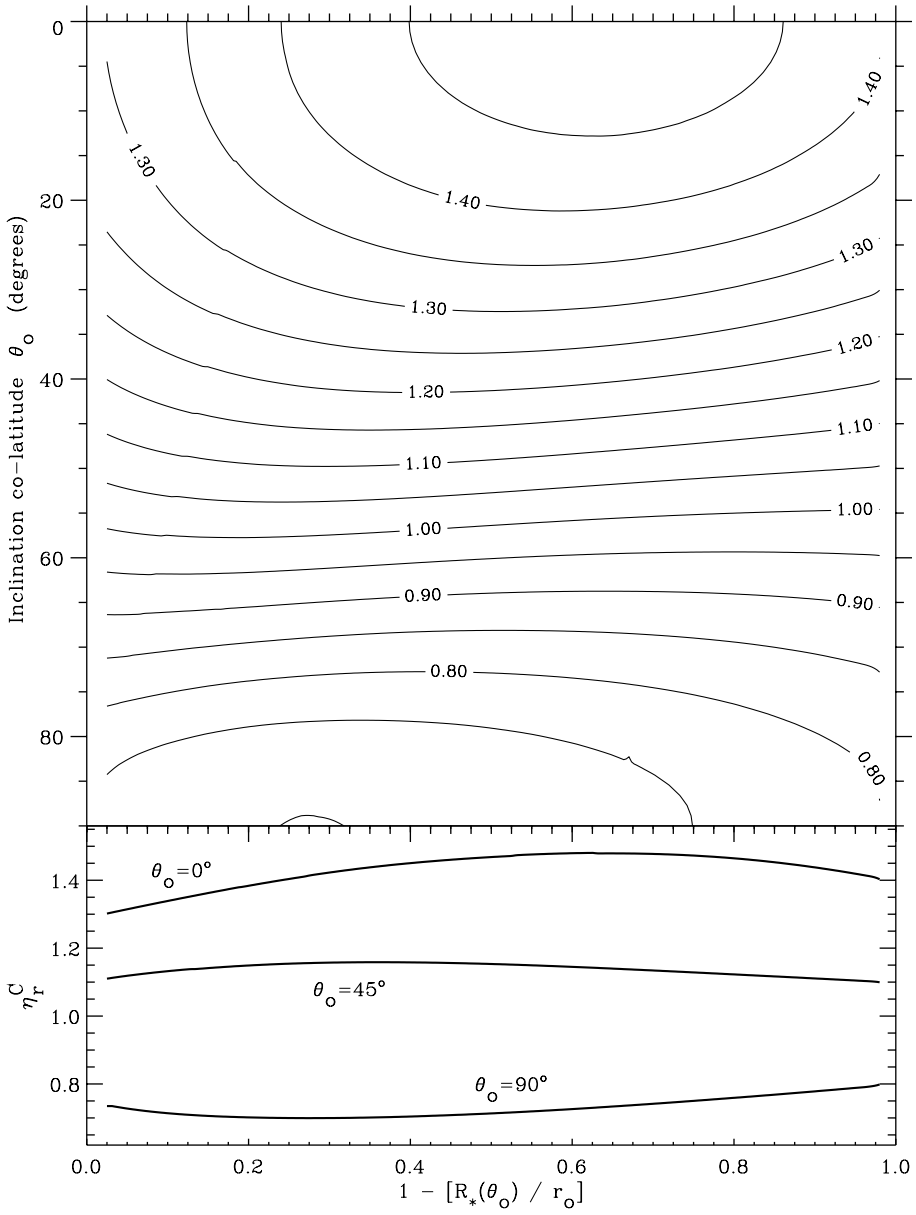

Figure 5.2: Combined contour and line plots of the **radial** (r) continuum OFD factor for the standard oblate B-star model. The line plots at the bottom of each panel illustrate the variation with radius for field points at inclinations of 0 (pole-on), 45, and 90 degrees (equator-on). The radial coordinate varies from 0 at the latitude-dependent stellar surface to 1 at infinity.

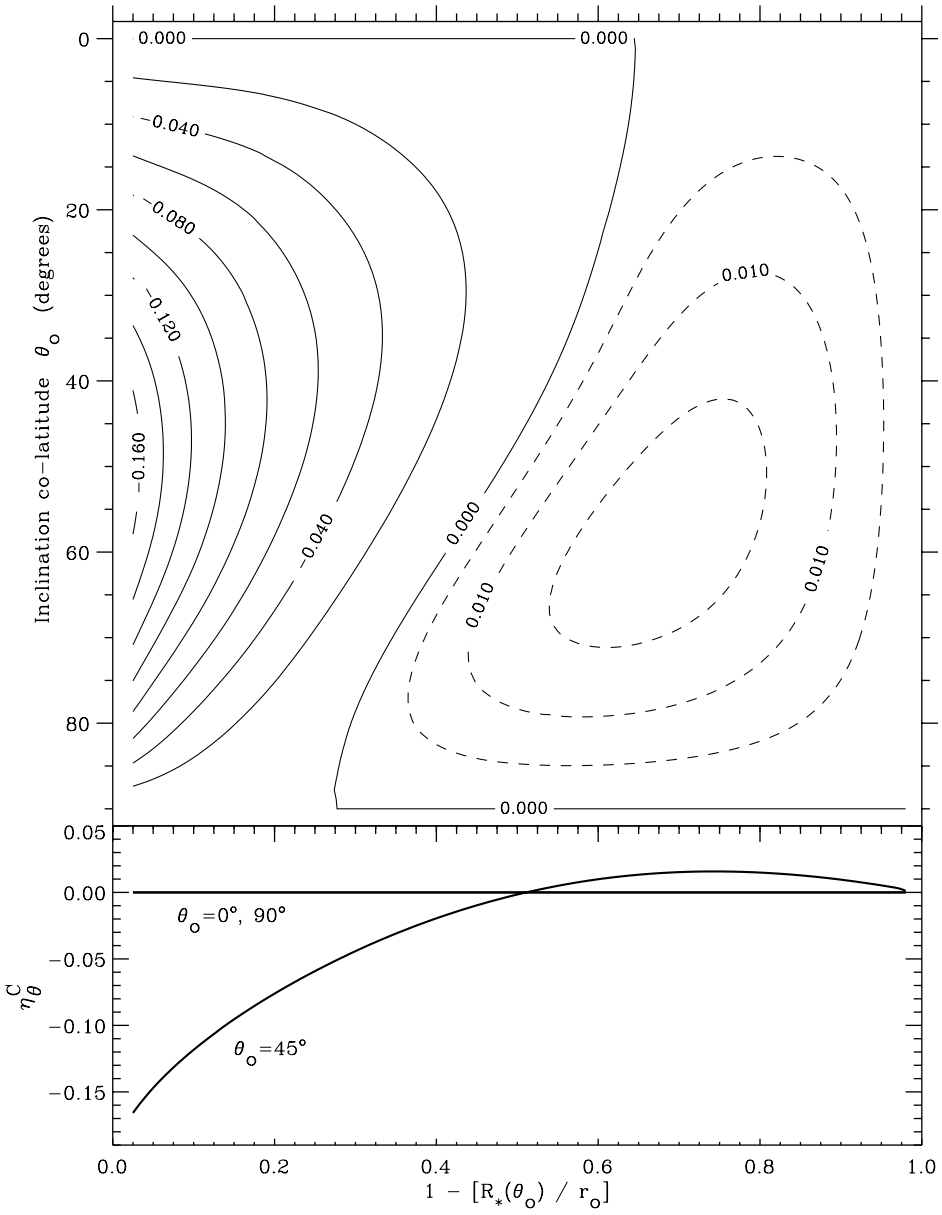

Figure 5.3: Combined contour and line plots of the **latitudinal** (θ) continuum OFD factor for the standard oblate B-star model. The line plots at the bottom of each panel illustrate the variation with radius for field points at inclinations of 0 (pole-on), 45, and 90 degrees (equator-on). The radial coordinate varies from 0 at the latitude-dependent stellar surface to 1 at infinity.

This sub-stellar gravity darkening, although dominant near the surface, is modulated by three other important effects in the circumstellar regions. First, as one moves away from the star, a larger fraction of the stellar surface, and thus a wider range of effective temperatures, is seen and integrated over. Points over the poles will see more and more of the darker equator, and points near the equatorial plane will see more of the bright poles. This effect is easily seen in η_r^C as $r_o \to \infty$, which begins to decrease near the poles and increase near the equatorial plane, and in η_θ^C, which becomes positive as $r_o \to \infty$, indicating a small degree of bright-to-dark equatorward acceleration. The second effect, which also becomes important at large distances from the star, is that the flux vector in the wind becomes more and more radial in direction, and the star appears more like a point source of flux. This primarily affects η_θ^C, driving it to zero as $r_o \to \infty$, and only weakly affecting η_r^C because the flux vector is always nearly radial.

The third effect on $\boldsymbol{\eta}^{\mathrm{C}}$ is somewhat more subtle, and has an impact at all distances from the star, but is relatively small in magnitude. The oblateness of the star causes a purely geometrical change in the continuum OFD factor, which is the ratio of the flux from an oblate surface to that from a perfect inverse-square point or spherical source. As the field point moves from the stellar surface ($r_o = R_*$) into the wind, the surface seen is either larger (over the poles) or smaller (over the equator) than is expected for a corresponding sphere extending out from the initial surface point. For example, over the pole ($\theta_o = 0$), an observer at $r_o \to \infty$ sees a circular disk with area πR_{eq}^2, but the spherical point-flux "Gaussian surface" over the poles would have radius R_p and an observed surface area πR_p^2. The ratio of the observed to the expected areas provides a rough magnitude for this effect on the OFD factors, and can be seen in η_r^C for small r_o as a slight increase near the pole and a slight decrease near the equator.

Before examining the more dynamically important line OFD factor, one final, and initially surprising feature of $\boldsymbol{\eta}^{\mathrm{C}}$ should be discussed. OCB anticipated that the inclusion of gravity darkening could lead to a "pinching" effect in the acceleration, with the force from the bright poles confining and diverting an increased acceleration toward the equatorial plane. This gravity-darkening effect is indeed seen in the limit of large r_o, but is always of negligible magnitude and dominated by the sub-stellar gravity darkening, $T_{\mathrm{eff}}(\theta_o)$. The fact that η_θ^C is negative at mid-latitudes near the star indicates that, not only is pinching toward the equator unimportant, but the flux is usually directed *away* from the equator toward the poles. Geometrically, this should come as no surprise, because the ultimate extreme of an oblate star is a flat disk, with normal vectors pointed solely in the $\pm z$ directions, away from the equator. Thus, if an enhanced equatorward force is desired for the production of stronger WCDs, it will not be found from oblateness and gravity darkening alone.

5.2.4 The Line Oblate Finite Disk Factor

The line OFD factor $\boldsymbol{\eta}^{\mathrm{L}}$ is shown in Figures 5.4, 5.5, and 5.6, and was computed using the wind velocity from the initial semi-analytic model A. The small-scale numerical noise in these figures comes mainly from the discrete computation of the velocity derivatives in the r and θ directions. To zero order, the radial factors η_r^C and η_r^L behave very similarly. Roughly, the factor η_r^L can be considered as a "convolution" of the angle integral over the oblate and gravity darkened intensity, η_r^C, and the angle integral over the projected velocity gradient term. This latter integral is given in the spherical limit by η_{un} or η_{limb}, and, to an overall accuracy of $\sim 15\%$, one can indeed model $\eta_r^L \approx \eta_r^C \eta_{un}$, where η_{un} is evaluated using the stellar polar radius. Differences between this approximation and the true value of η_r^L stem from the absence of nonradial velocity components in η_{un}, and of course from the fact that one cannot rigorously split up the integration over a product into the product of two integrals.

The latitudinal component of the line factor η_θ^L also resembles the corresponding continuum factor η_θ^C, but does not exhibit as large a range of positive values for large field point radii. Also, near the stellar surface η_θ^L approaches zero because the dominant terms in the projected velocity gradient term $\hat{\mathbf{n}} \cdot \nabla(\hat{\mathbf{n}} \cdot \mathbf{v})$ grow negligibly small for small radii. The latitudinal velocity v_θ, as well as the gradients $\partial v_\theta / \partial r$ and $\partial v_r / \partial \theta$, contribute most strongly to the latitudinal OFD factor. Near and below the sonic point, these three terms all grow small when compared to the radial gradient $\partial v_r / \partial r$ which normally dominates the finite disk factor near the stellar surface.

The line OFD factor in the azimuthal direction η_ϕ^L has no continuum counterpart, and should be understood solely in terms of the projected velocity gradient term $\hat{\mathbf{n}} \cdot \nabla(\hat{\mathbf{n}} \cdot \mathbf{v})$. Note from Figure 5.6 that this factor is always negative, and thus directed in the opposite direction from the star's rotation. The surface magnitude of η_ϕ^L implies that the wind could be significantly "spun down" from its angular momentum conserving azimuthal velocity. This fact, combined with the similarly negative sense of η_θ^L, seems to indicate that the overall effect of both nonradial OFD factors can be modeled to zero order by simply decreasing the star's equatorial rotation velocity V_{eq}. In the WCD paradigm, both v_θ and v_ϕ in the wind are most strongly influenced by the azimuthal orbital-plane velocity v_{ϕ_i}, which depends directly on V_{eq}.

The negative sense of η_ϕ^L can be understood by examining the projected velocity gradient term, equation (5.21), and noting that the only terms to produce a variation in the ϕ-component of the integrand (and thus non-cancellation when multiplied by n_ϕ) are those dependent on v_ϕ and $\partial v_\phi / \partial r$. For an outward ray $\hat{\mathbf{n}}$ tilted in the positive ϕ, or prograde direction, the projected component of v_ϕ decreases

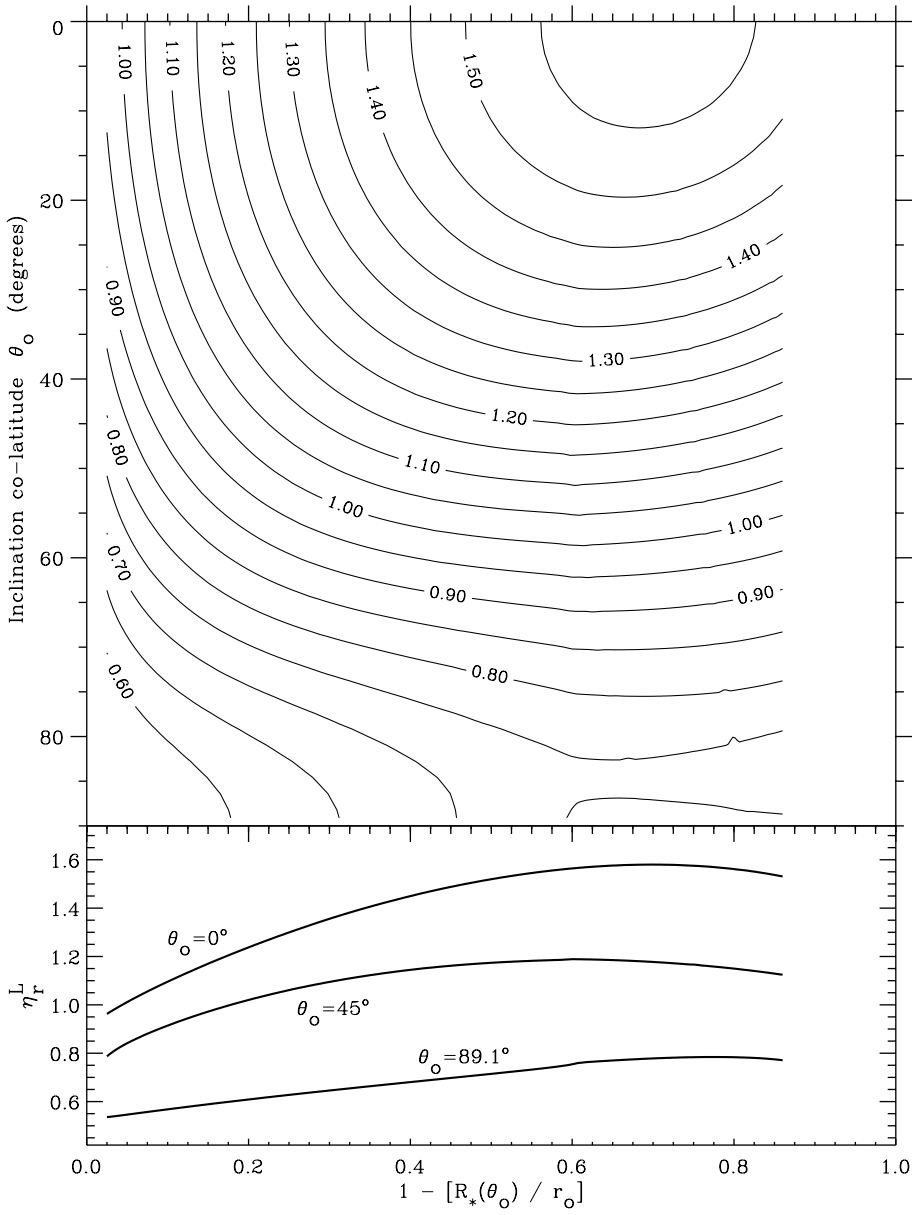

Figure 5.4: Combined contour and line plots of the **radial** (r) line OFD factor for the standard oblate B-star model, with wind specified by the semi-analytic model A. The line plots at the bottom of each panel illustrate the variation with radius for field points at inclinations of 0 (pole-on), 45, and 90 degrees (equator-on). The radial coordinate varies from 0 at the latitude-dependent stellar surface to 1 at infinity.

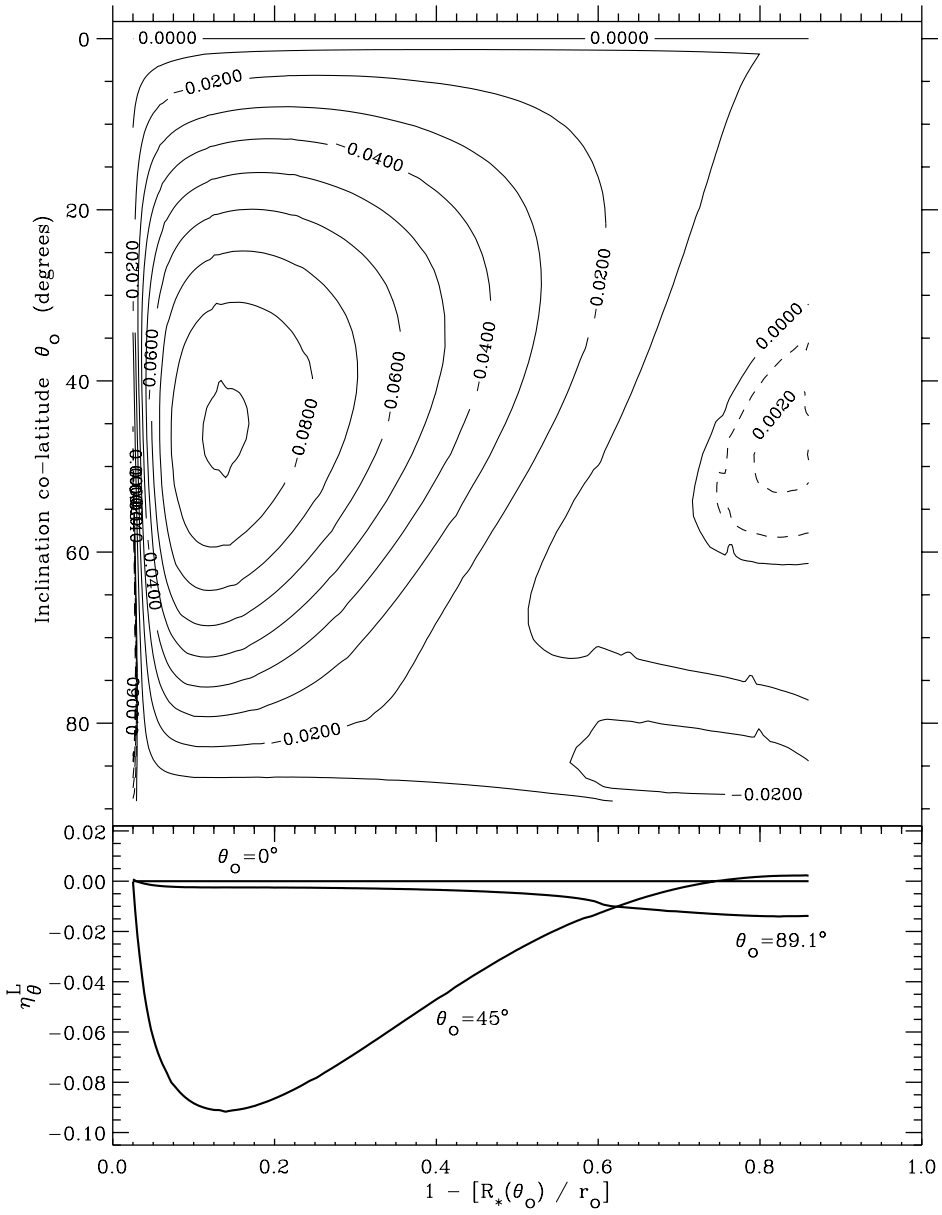

Figure 5.5: Combined contour and line plots of the **latitudinal** (θ) line OFD factor for the standard oblate B-star model, with wind specified by the semi-analytic model A. The line plots at the bottom of each panel illustrate the variation with radius for field points at inclinations of 0 (pole-on), 45, and 90 degrees (equator-on). The radial coordinate varies from 0 at the latitude-dependent stellar surface to 1 at infinity.

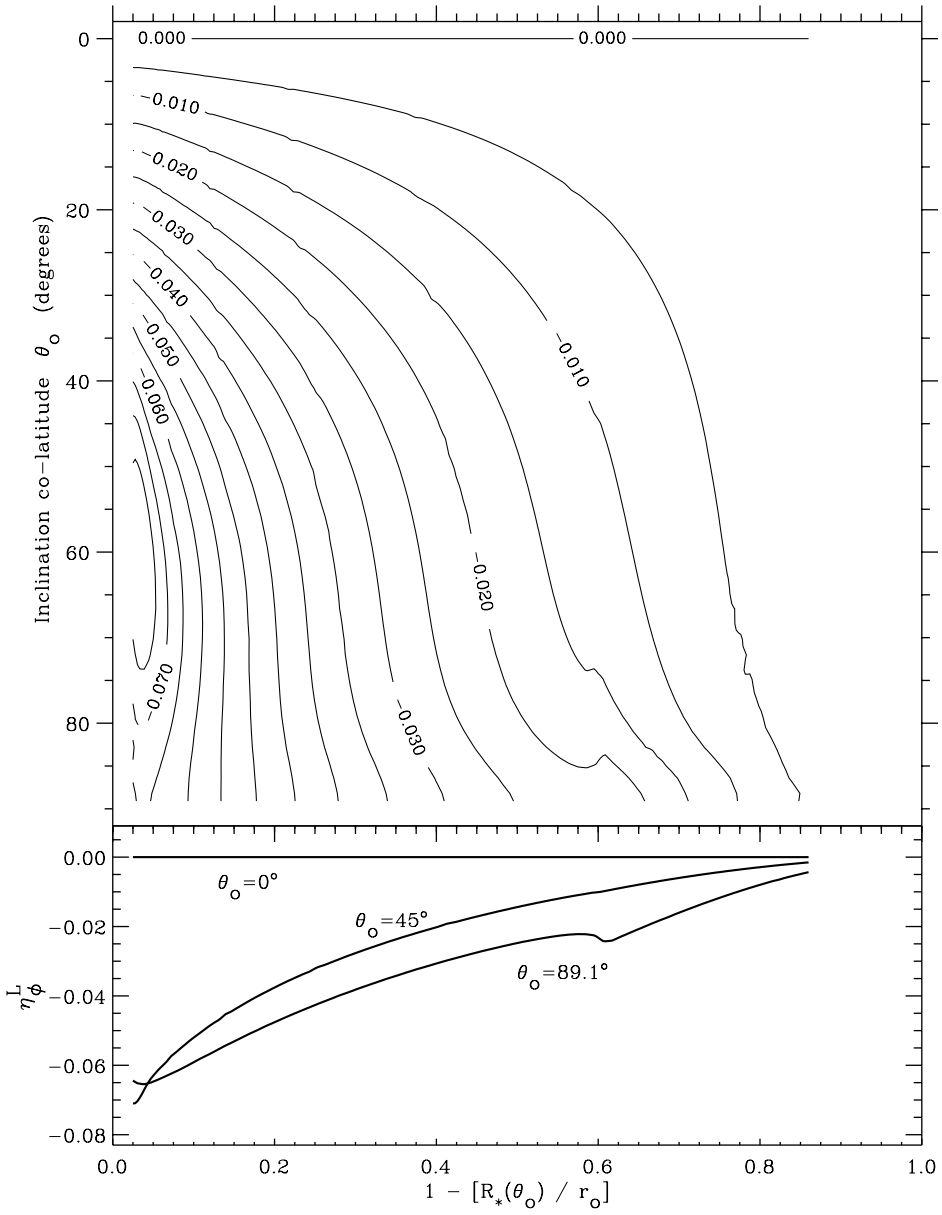

Figure 5.6: Combined contour and line plots of the **azimuthal** (ϕ) line OFD factor for the standard oblate B-star model, with wind specified by the semi-analytic model A. The line plots at the bottom of each panel illustrate the variation with radius for field points at inclinations of 0 (pole-on), 45, and 90 degrees (equator-on). The radial coordinate varies from 0 at the latitude-dependent stellar surface to 1 at infinity.

as one moves outward. However, for an outward ray $\hat{\mathbf{n}}$ tilted in the negative ϕ, or retrograde direction, the component of v_ϕ along the ray is negative, and increases (grows less negative) as one moves outward. Thus, when summed with the other, usually positive gradient terms in equation (5.21), rays in the retrograde direction have a stronger contribution to the integrand. The net effect is the "retrograde shear" (discussed in Section 4.3) that directs η_ϕ^L away from the direction of stellar rotation.

The semi-analytic model A, which provides the wind velocity field for the computation of the line OFD factor, contains only wind compression, and no shocked equatorial disk. If the velocity field of the numerical model S-350 were to be used in the computation of $\boldsymbol{\eta}^{\mathrm{L}}$, however, the presence of a disk would strongly affect the values of the line OFD factor near the plane of the equator. Although this calculation is beyond the scope of this work, its general impact should be considered. The equatorial disks found by OCB contain a drastic reduction in both the radial and latitudinal velocities, while the azimuthal velocities remain roughly continuous with the exterior wind. The gradients of v_r and v_θ, however, are maximum at the edges of the disk, where strong compression (and also high temperatures and "superionization") is thought to occur. The magnitudes of the OFD factors η_r^L and η_θ^L should be significantly enhanced in these regions, then possibly return to nearly their exterior wind values once well inside the disk. Although this enhancement provides a possible mechanism for depositing added density in the equatorial regions (through stronger latitudinal forces), definitive results will have to wait until a more self-consistent dynamical calculation is performed.

5.2.5 Effect on a Radiation Driven Wind

Once the OFD factors have been computed, we can implement them in the solution of the dynamical equations of motion and examine their overall impact on the 2D wind. However, the numerical evaluation of the OFD integrals, equations (5.23) and (5.24), is quite computationally expensive, and until recently it has been impractical to include this velocity-dependent quadrature into the time-dependent hydrodynamics. It is still possible, though, to anticipate some of the effects of oblateness and gravity darkening. First of all, because electron scattering is only a relatively minor effect in the winds of late O and early B stars (, $\ll 1$), we may ignore the impact of the continuum OFD factor $\boldsymbol{\eta}^{\mathrm{C}}$ on the dynamics of the wind. Also, in order to allow approximate 1D solutions of the equations of motion, let us consider only the impact of the radial component of the line OFD factor η_r^L on the wind over the poles and the equator. We can employ the same 1D mCAK method used for model A to find solutions for $v_r(r)$ and $\dot{M}$ along these two loci of wind points, but with the radial OFD factors used instead of the spherical finite disk

factor η_{un}. This defines the first step in an iterative process, designed to find a quasi-self-consistent wind solution:

1. Compute polar and equatorial $v_r(r)$ and $\dot{M}$ using 1D mCAK code.
2. Determine wind compression velocities in r, θ, and ϕ directions, using modified BC semi-analytic model (see Section 5.1).
3. Use this velocity field to re-integrate the OFD factor η_r^L for points over the poles and equator.
4. Repeat steps 1 to 3 until solutions settle to consistent values.

Note that, although this procedure disregards the effects of the nonradial OFD factors at all latitudes, and only estimates the radial OFD factor at mid-latitudes, it can provide a first estimate of how the overall wind compression will be affected by the presence of pole-to-equator variations in the radiative acceleration.

Before actually carrying out this iterative process, let us consider one additional, and possibly important, 2D effect: the polar streamline divergence derived above in Section 5.1. Model A1 in Table 5.1 was computed using this polar non-spherical divergence, and its polar terminal velocity (represented by the radial velocity at 6 polar radii) and its equator-to-pole density contrast agree slightly better with OCB's numerical model S-350, which naturally contains this 2D effect. In the equatorial regions there would seem to be the opposite effect – streamline convergence – but pressure forces, ignored in the simple wind compression picture of Section 5.1, act to redirect the flow into a nearly radially outflowing disk.

Starting with the original initial model A, models B through E in Table 5.2 were computed using the above iterative process and polar non-spherical divergence. Self-consistency seems to have been reached in the four iterations shown. The overall effect of the polar and equatorial radial OFD factors is a general weakening of the BC wind compression, as shown by the equator-to-pole density contrast, which is only $\sim 30\%$ of its original (non-OFD) value. Note that this density ratio does not include the shocked disk expected to form at the equator, but the strength of the disk in part depends on the amount of wind compression immediately exterior to it. The polar and equatorial wind terminal velocities are both increased by factors of 1.5 to 2, and the velocity laws using the OFD factors accelerate toward their terminal values over a longer distance (i.e., they are less "steep"). The local mass flux over the pole is virtually unchanged, while the mass flux over the equator has decreased by a factor of four. This can be understood at the pole by the competition between the generally larger OFD factor and the non-spherical divergence factor, while at the equator the generally smaller OFD factor (due to gravity darkening)

acts alone to decrease the radiation force, and thus the local amount of mass loss (see eq. [4.31]).

We caution that, although this dynamical analysis contains much of the physics derived for the OFD factors above, it ignores all nonradial force components in the OFD factor, and only treats the radial components approximately. Indeed, preliminary 2D hydrodynamical models which incorporate these OFD forces evolve to qualitatively different solutions than predicted above. Owocki, Gayley, & Cranmer (1996) show that the small *poleward* and *retrograde* forces in the θ and ϕ directions actually result in the complete inhibition of the BC equatorial wind compression effect. This conspires with the net *decrease* in $\dot{M}$ over the equator due to gravity darkening (see Section 4.2) to further decrease the predicted equatorial density enhancement. In the most rapidly rotating models there is even a density *minimum* at the equator, and bipolar higher-density "lobes" around the poles. The apparent contradiction between these (seemingly robust) theoretical results and the inferred detection of WCDs around O and B stars in several cases (e.g., Bjorkman et al. 1994; Harries & Howarth 1996) is currently being examined. Of course, as Ignace et al. (1996) have indicated, in systems where line driving and gravity darkening are not expected to occur, the BC wind compression paradigm is still likely to represent an important dynamical component of the circumstellar matter around rotating stars.

5.3 Line Profiles and Polarization

The SEI line synthesis method discussed in Chapter 3 can be extended to winds without spherical symmetry, and in this Section we present P Cygni line profiles from a representative two-dimensional axisymmetric WCD model. The oblate stellar "boundary" is taken into account numerically, and the wind's velocity and density variations in r and θ are transformed into an arbitrary observer-centered coordinate system. Figure 5.7 shows P Cygni line profiles of the A1 model wind presented in Section 5.2 above, for observers at various inclinations. The "standard" line parameters of Section 3.1.4 are used: $k_L = 1$, $\epsilon_o = 0$, $v_{\rm turb} = 100\,{\rm km\ s^{-1}}$, and $\Delta i = \gamma = 0$.

The most evident inclination-dependent variations are due to the decreasing terminal velocity and increasing mass flux from pole to equator. Note that this wind compression model does not contain a shocked disk, and thus the line profiles do not show the strong low-velocity "shelf" feature found by Bjorkman et al. (1994) in theoretical P Cygni profiles of stars with equatorial disks. More complete multi-dimensional hydrodynamical models, such as those of Owocki, Gayley, & Cranmer (1996), do not contain strong WCDs, and in fact exhibit a *decreasing* mass flux

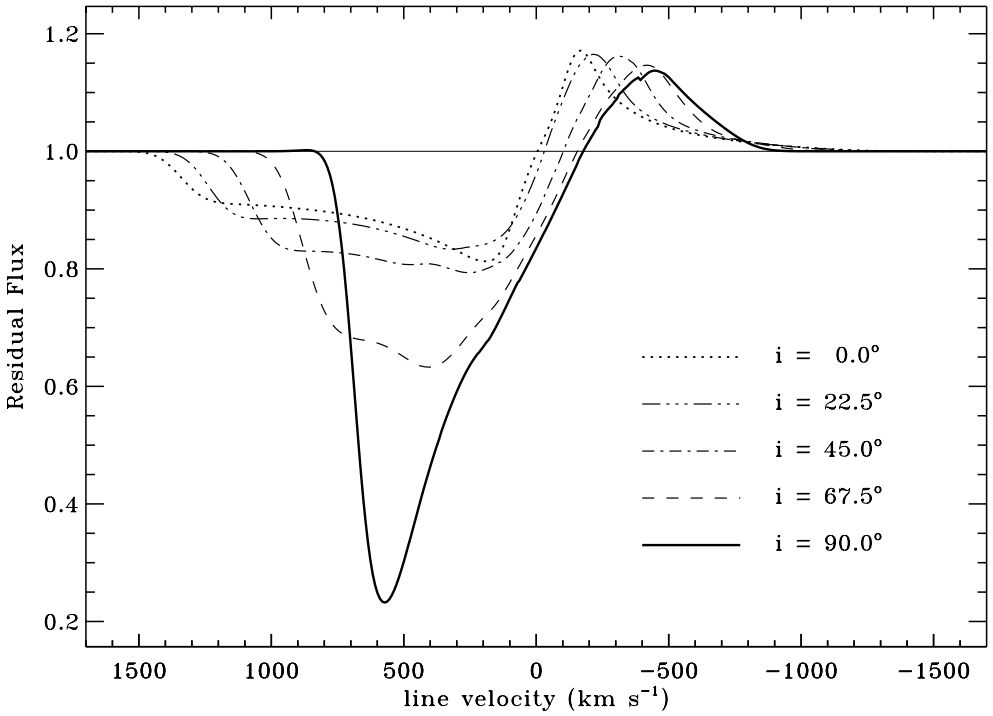

Figure 5.7: Theoretical (SEI) P Cygni line profiles for the A1 analytic wind compression model wind. Observers at $i = 0, 22.5, 45, 67.5$, and 90 degrees are shown.

from pole to equator. Preliminary computations of P Cygni line profiles and photospheric diagnostics such as Hα (see, e.g., Petrenz & Puls 1996) show significant differences between these paradigms, and this promises to aid in identifying the actual circumstellar distributions of matter around rotating O and B stars.

Figure 5.8 shows the continuum electron-scattering polarization for both the A1 wind compression model and the S-350 hydrodynamical WCD model computed by OCB. The code written to calculate this polarization integrates over the wind volume exterior to the oblate star, but performs the solid-angle integration (in, e.g., eq. [3.46]) over a non-gravity-darkened spherical surface of radius R_p. The overall approximate dependence on $\sin^2 i$, as discussed in Section 3.2 for an axisymmetric non-occulted envelope, is evident, and deviations from $\sin^2 i$ arise from the occultation of material behind the star. Note the difference in magnitude between the models with and without a shocked wind compressed disk; the polarization increases by a factor of 20 when the thin WCD is included, and its presence seems necessary to generate an observable amount of polarization in the weak winds of B stars. However, in the much denser winds of O stars, even modest wind compression without a disk can generate a significant continuum polarization ($\sim$0.3% for ζ Puppis; see Harries & Howarth 1996).

5.4 An Idealized 1D Model of the Shocked Disk

For hot stars where equatorial wind compression is present, OCB found that the dynamics *within* the shocked disk is markedly different from the predictions of Bjorkman & Cassinelli (1993). Because the Sobolev line driving scales inversely with the gas density, the material in the disk is not accelerated as strongly as the remainder of the wind, and this results in a net *inflow* of matter onto the star beneath a "stagnation point" r_o, which moves outward with increasing rotation velocity. Because of the sharp contrast between the rapid equatorial wind flow exterior to the disk and the slow pressure-confined flow interior to the disk, it may be possible to model the dynamics of the disk in one dimension, and treat the "input" of mass and momentum from the wind as an external boundary condition. Bjorkman (1992) began to construct such a model, but assumed the detached-disk paradigm of BC. In this Section we outline some of the key equations in a 1D model of a shocked disk with a stagnation point. Note, however, that this analysis is still at a preliminary stage of development, and the main purpose of this Section is to document these initial steps in the problem.

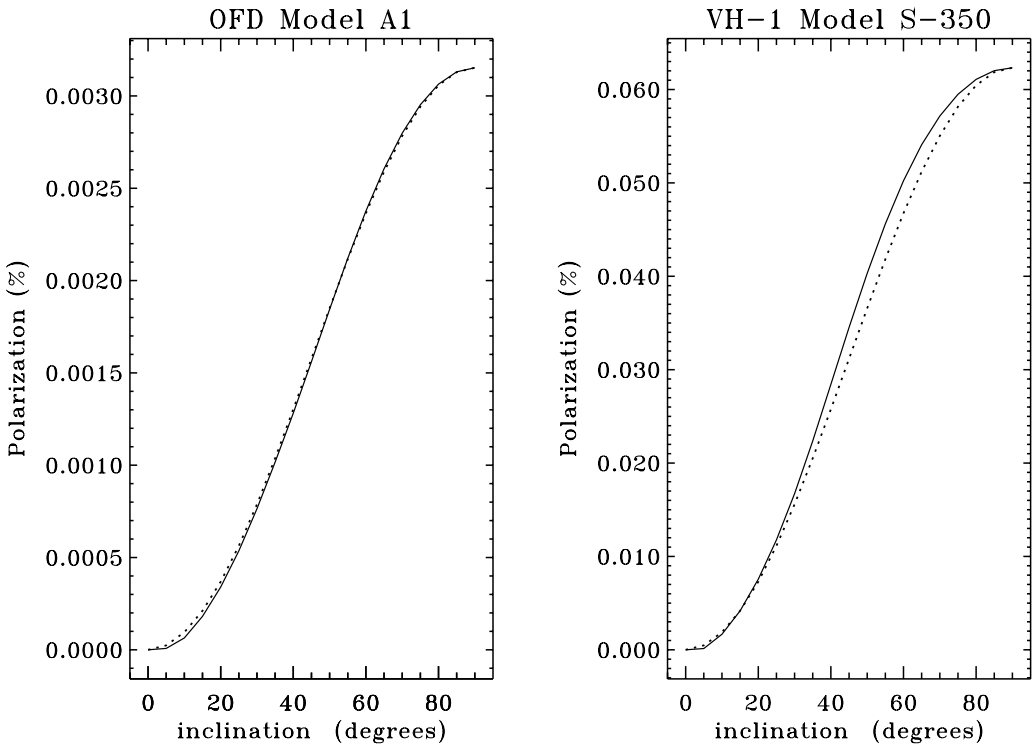

Figure 5.8: Optically-thin electron scattering polarization for the A1 analytic wind compression model (left curves), and for the S-350 numerical hydrodynamics wind model (right curves). Solid lines show the numerically-computed polarization variations with inclination, and dashed lines show the square of the sine of the inclination, normalized to the equatorial polarization.

5.4.1 Equations of Motion

In order to model the interior of a shocked equatorial wind compressed disk (WCD), several assumptions must be made. First, because numerical models have shown that the disk is extremely thin, let us consider it to be ideally *planar,* and replace the 3D volume mass density ρ with a 2D surface density σ, expressed as mass per unit area in the disk. Second, because of the relative success of the analytic wind compression model (Bjorkman & Cassinelli 1993; Owocki, Cranmer, & Blondin 1994; Cranmer & Owocki 1995), we can consider the input of mass and momentum into the disk as known, and thus write the fluid equations with "source terms" of mass and momentum deposited from the exterior wind.

In general, the 2D fluid equations of mass and momentum conservation can be written in conservative form as

$$\frac{\partial \sigma}{\partial t} + \nabla \cdot (\sigma \mathbf{v}) \; = \; j_o \tag{5.28}$$

$$\frac{\partial}{\partial t}(\sigma v_r) + \nabla \cdot (\sigma \mathbf{v} v_r) + \frac{\partial P_{\rm eff}}{\partial r} - \sigma g_r \; = \; j_r \tag{5.29}$$

$$\frac{\partial}{\partial t}(\sigma v_\phi) + \nabla \cdot (\sigma \mathbf{v} v_\phi) + \frac{1}{r}\frac{\partial P_{\rm eff}}{\partial \phi} - \sigma g_\phi \; = \; j_\phi \;\; , \tag{5.30}$$

where j_o, j_r, and j_ϕ are the source terms of mass and linear momentum in the radial (r) and azimuthal (ϕ) cylindrical-coordinate directions, respectively, and the vector $\mathbf{g}$ represents a general external acceleration. Note that the divergence operation is taken in the 2D equatorial plane only, and the effective "pressure" $P_{\rm eff}$ here has units of force per unit length.

The source terms can be written in terms of the actual mass density and flow velocity of the wind, denoted by ρ_w and $\mathbf{w}$, exterior to the disk. Consider an infinitesimally small volume δV embedded in the equatorial disk. The volume δV can be written

$$\delta V \; = \; \delta z \; \delta A \; = \; (w_z \, \delta t) \; \delta A \;\; , \tag{5.31}$$

with δA being the projected area of the volume in the equatorial plane, and δt being an infinitesimal time interval over which the wind flows through the vertical (z) extent of the volume. The vertical velocity w_z of the wind entering from above is given by $w_z = w_\theta \sin\theta - w_r \cos\theta$, but is approximately equal to w_θ itself near the equatorial plane. Although we are utilizing a continuum description of the fluid, let us momentarily define a number N of fluid particles (each of mass m) in the volume δV, and $N = \rho_w \, \delta V \, / m$. Thus, the "creation rate" of particles in the disk, per unit area per unit time, is defined as

$$\mathcal{S} \; \equiv \; \frac{N}{\delta A \; \delta t} \; = \; \frac{\rho_w}{m} \, w_z \;\; , \tag{5.32}$$

and the source terms of mass and linear momentum are given simply by

$$j_o = m\mathcal{S} \ , \quad j_r = mw_r\mathcal{S} \ , \quad j_\phi = mw_\phi\mathcal{S} \ . \tag{5.33}$$

These terms are similar to the "mass loading" sources in energetic solar-wind plasmas, where conservation of individual ionic species is violated by ionization and charge-exchange processes (see, e.g., Story 1996). Note that the wind density ρ_w and velocity $\mathbf{w}$ are functions of position, given by the Bjorkman and Cassinelli (1993) analytic wind compression model, and thus the source terms can be considered known as well.

With the derived source terms, and the assumptions of azimuthal symmetry and steady state, the fluid conservation equations in the equatorial plane become

$$\frac{1}{r}\frac{\partial}{\partial r}(r\sigma v_r) \ = \ j_o \tag{5.34}$$

$$\frac{1}{r}\frac{\partial}{\partial r}(r\sigma v_r^2) - \frac{\sigma v_\phi^2}{r} \ = \ -\frac{\partial P_{\rm eff}}{\partial r} + \sigma g_r + j_o w_r \tag{5.35}$$

$$\frac{1}{r}\frac{\partial}{\partial r}(r\sigma v_r v_\phi) + \frac{\sigma v_r v_\phi}{r} \ = \ \sigma g_\phi + j_o w_\phi \ . \tag{5.36}$$

By expressing divergences as cylindrical "slab-like" derivatives we implicitly assume a flat disk, with a constant scale height h. Later, however, we will be able to use a relationship between σ and the volume density ρ to estimate how h may vary with radius. The two above momentum equations can be simplified by appropriately separating the products in the differentiations on the left-hand side, and using the mass continuity equation. These two equations thus simplify to

$$v_r\frac{\partial v_r}{\partial r} - \frac{v_\phi^2}{r} \ = \ -\frac{1}{\sigma}\frac{\partial P_{\rm eff}}{\partial r} + g_r + \frac{j_o(w_r - v_r)}{\sigma} \tag{5.37}$$

$$v_r\frac{\partial v_\phi}{\partial r} + \frac{v_r v_\phi}{r} \ = \ g_\phi + \frac{j_o(w_\phi - v_\phi)}{\sigma} \ . \tag{5.38}$$

The quantity j_o/σ has units of inverse time, and can be considered a kind of "mass injection rate" which sets the scale for the r and ϕ accelerations.

For the present, let us leave the azimuthal momentum equation, and assume v_ϕ to be known (usually, $v_\phi \sim 1/r$, which conserves angular momentum). Note that we cannot immediately neglect the pressure gradient term in the radial momentum equation, because the wind velocity inside the disk can become arbitrarily small. If an isothermal wind is assumed, with sound speed a, and an idealized 2D equation of state $P_{\rm eff} = \sigma a^2$ is applied, the radial equation of motion can be written in terms of a mass flux variable $J \equiv \sigma v_r r$, and the two governing differential equations become

$$\frac{dJ}{dr} \ = \ j \tag{5.39}$$

$$\left(v_r - \frac{a^2}{v_r}\right)\frac{dv_r}{dr} = g_r + \frac{v_\phi^2}{r} + \frac{a^2}{r} + \frac{j_o r}{J}\left[v_r(w_r - v_r) - a^2\right] \quad , \tag{5.40}$$

defining $j \equiv j_o r = \rho_w w_z r$ as a "linear" mass flux into the disk.

The external acceleration term g_r in general contains both gravity and the effects of radiative driving:

$$g_r = -\frac{GM(1-,)}{r^2} + \frac{GM,}{r^2} k\eta\,(r, v_r, dv_r/dr)\left(\frac{1}{\sigma_e \rho v_{th}}\frac{dv_r}{dr}\right)^\alpha \left[\frac{n_e}{(10^{11}\,\mathrm{cm}^{-3})W}\right]^\delta \tag{5.41}$$

(see CAK; Abbott 1982a; Friend & Abbott 1986). In the remainder of this analysis, however, we will consider a simplified form of the radiative driving, neglecting Abbott's (1982a) ionization correction ($\delta = 0$), and assuming a point source of radiation ($\eta = 1$). Note, however, the presence of the 3D mass density ρ in the line acceleration. This can be dealt with in the present 2D model in one of two ways: (1) replace ρ by the quantity σ/h, where h is a representative radially-dependent disk scale height, or (2) use the simple ram pressure balance given by BC for an ideally flat disk,

$$\rho \approx \rho_w \left(1 + \frac{w_z^2}{a^2}\right) \quad . \tag{5.42}$$

In the following, we will use the latter assumption, and assume ρ to be a known function of radius. This implies that once we solve for $\sigma(r)$, we automatically have $h(r)$, and we can evaluate the validity of the above thin-slab approximation directly. As an aside, if we *assume* h to have a given value, this allows us to estimate σ and turn the equation of motion into a purely algebraic equation for $v(r)$. This method, though, is unreliable because of the extremely sensitive dependence on this choice for h. Finally, then, we can express the *effective* external acceleration as

$$\left(g_r + \frac{v_\phi^2}{r} + \frac{a^2}{r}\right) \equiv -g(r) + k(r)\left(\frac{dv_r}{dr}\right)^\alpha \quad , \tag{5.43}$$

with both $g(r)$ and $k(r)$ being known positive quantities.

The unknown mass flux $J(r)$ can be easily integrated, given an initial condition from which to integrate. A convenient radius to choose is the "stagnation point" r_o, at which $v_r \equiv v = 0$. Numerical studies have shown that there is an inner disk inflow ($v < 0$) below this radius, and outflow ($v > 0$) above it. Figure 5.9 shows the functions $j(r)$ and $J(r)$ for the S-350 model of OCB. Because the location of the stagnation point is not known *a priori*, $J(r)$ is known only relative to an unknown additive constant, and three representative choices are shown. Note, however, that the mass-supply function $j(r)$ is sharply peaked in radius, rapidly approaching zero both as $r \to R_*$ and as $r \to \infty$. This implies that J, its integral, varies most rapidly

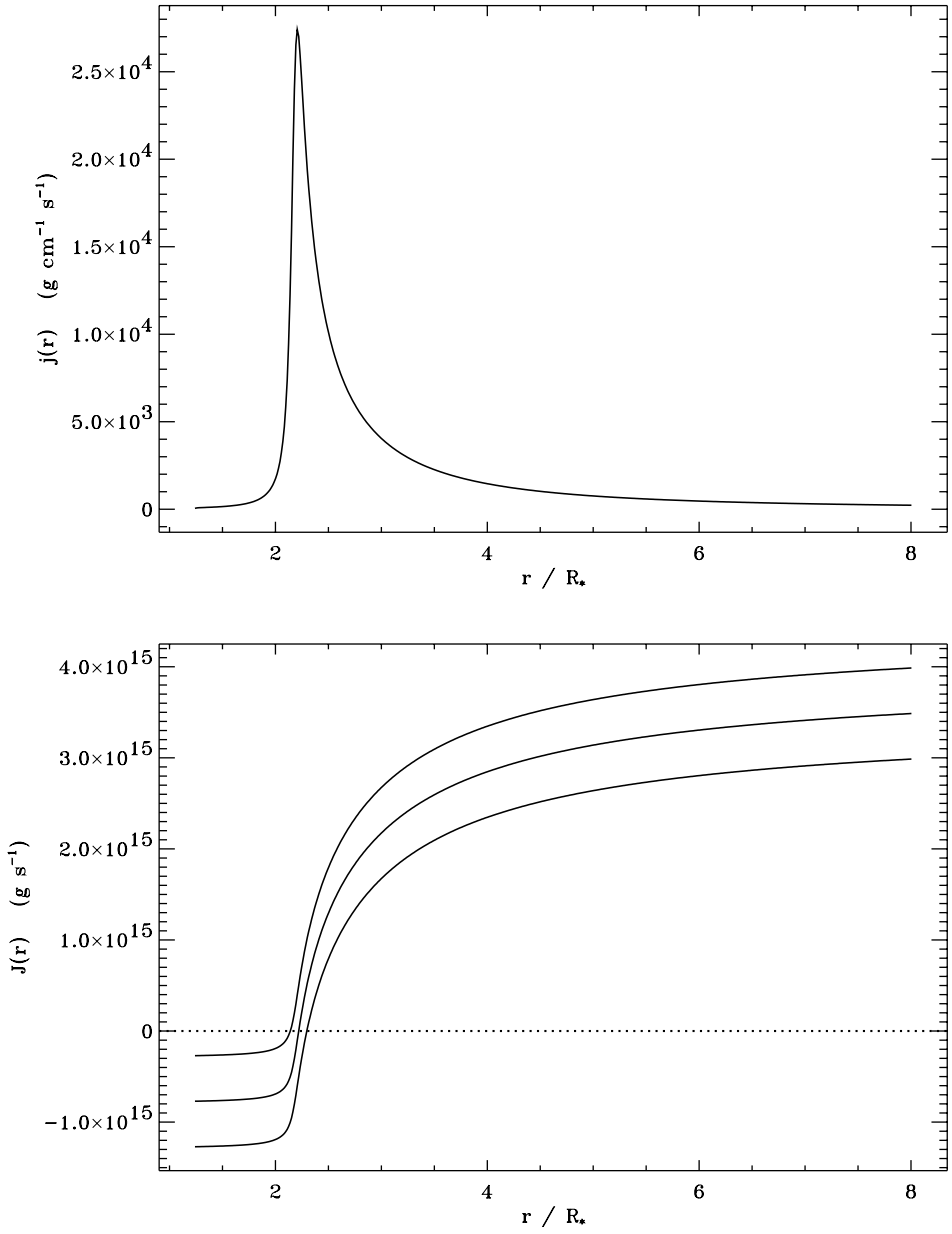

Figure 5.9: Upper curve: Mass-loading source term $j(r)$, which is sharply peaked near the stagnation point. **Lower curve:** Integrated source of mass flux $J(r)$, unknown to within an additive constant. $J(r)$ crosses zero at the stagnation point.

where j is at its peak, and should cross zero very near this point. The actual position of the stagnation point for the S-350 numerical model is $r_o = 2.03R_p$, which is close to the peak of $j(r)$ at $\sim 2.2R_p$.

We can represent the equation of motion as

$$F_1\left(r, v, \frac{dv}{dr}\right) = \left(v - \frac{a^2}{v}\right)\frac{dv}{dr} + g - k\left(\frac{dv}{dr}\right)^{\alpha} - \frac{j}{J}\left[v(w_r - v) - a^2\right] = 0 \quad . \quad (5.44)$$

If we choose $\alpha = 1/2$, it becomes possible to solve for the velocity gradient quadratically, and

$$\frac{dv}{dr} = \left[\frac{kv}{2(v^2 - a^2)} \pm \sqrt{\frac{v}{v^2 - a^2}}\sqrt{\frac{k^2 v}{4(v^2 - a^2)} - g + \frac{j}{J}\left[v(w_r - v) - a^2\right]}\right]^2 \quad . \quad (5.45)$$

5.4.2 Stagnation Point Analysis

At the stagnation point, $v = 0$, several terms in the equation of motion grow without bound. The equation here becomes dominated by the two sound-speed terms in this limit:

$$F_1 \approx -\frac{a^2}{v}\left(\frac{dv}{dr}\right)_o + \frac{ja^2}{J} = 0 \quad , \quad (5.46)$$

but this is just an expression of L'Hôpital's rule, because, as $v \to 0$, $J \to 0$, and

$$\frac{j(r)v(r)}{J(r)} \to \frac{j(r)(dv/dr) + v(r)(dj/dr)}{dJ/dr} \to \frac{dv}{dr} \quad . \quad (5.47)$$

Although this implies that solutions passing through the stagnation point may be non-unique, this *exact* cancellation of the sound-speed terms is fortuitous because it allows us to ignore these terms in the analysis of the overall disk dynamics. This is analogous to the zero-sound-speed approximation in the standard CAK analysis (Section 2.3.2), which is valid in most of the wind.

To better obtain a physical understanding of the "mass loading" source term in the radial momentum equation, let us also momentarily ignore the *radiative forces* and the effects of rotation. Although the use of this assumption would not reproduce full numerical models of wind compressed disks (i.e., OCB), we find that the solution topology of these one-dimensional disk winds is quite complex even without radiation forces and rotation. It is important to first understand the effects of the source terms in isolation before considering the full problem. The equation of motion, then, is approximated by

$$v\frac{dv}{dr} + g - \frac{jv(w_r - v)}{J} = 0 \quad , \quad (5.48)$$

where here $g = GM_*/r^2$. If we demand a finite acceleration through the stagnation point r_o, L'Hôpital's rule provides the value of the velocity gradient and surface density there:

$$\left(\frac{dv}{dr}\right)_o = \frac{g(r_o)}{w_r(r_o)} \quad , \qquad \sigma_o = \frac{j_o(r_o)\, w_r(r_o)}{g(r_o)} \quad . \tag{5.49}$$

The only unknown quantity here is the value of r_o itself, but a reasonably good approximate value is given by the peak of $j(r)$ in, e.g., Figure 5.9.

Let us examine the solution topology of the above differential equation by writing it in dimensionless form; i.e., by defining the variables

$$x \equiv 1 - \frac{r_o}{r} \quad , \qquad y \equiv \frac{v}{\sqrt{GM_*/r_o}} \quad , \qquad \tilde{w} \equiv \frac{w_r}{\sqrt{GM_*/r_o}} \tag{5.50}$$

where x ranges from a negative constant $(1 - r_o/R_*)$ at the stellar surface, through zero at the stagnation point, to unity as $r \to \infty$. The variables y and $\tilde{w}$ are scaled to an escape-speed-like quantity at the stagnation point. For simplicity let us also assume that j and $\tilde{w}$ are *constants* in the wind, implying that $J \approx j(r_o)(r - r_o)$ in the vicinity of the stagnation point. The equation of motion is then given by

$$y\frac{dy}{dx} = -1 + \frac{y(\tilde{w} - y)}{x(1-x)} \quad , \tag{5.51}$$

or in a more standard form for nonlinear differential equations,

$$\frac{dy}{dx} = \frac{x(x-1) + y(\tilde{w} - y)}{xy(1-x)} \quad . \tag{5.52}$$

There are four *singular points* of this equation, where both the numerator and denominator approach zero:

1. $(x = 0, y = 0)$: This is the stagnation point, where L'Hôpital's rule gives the finite velocity gradient

$$\frac{dy}{dx} = \frac{1}{\tilde{w}} \quad , \tag{5.53}$$

which agrees with eq. (5.49) above. However, solutions of infinite slope are also formally possible at this point, implying that the stagnation point is a "nodal" type singular point with a very pathological nature (see, e.g., Holzer 1977).

2. $(x = 1, y = 0)$: This is a threshold point at which the wind *decelerates* to zero velocity at $r \to \infty$, and the finite velocity gradient is a mirror image of the above:

$$\frac{dy}{dx} = -\frac{1}{\tilde{w}} \quad . \tag{5.54}$$

This nodal point also admits infinite-slope solutions.

3. $(x = 0, y = \tilde{w})$: This solution is uninteresting in the present analysis because it implies full "entrainment" of the disk velocity at the *external* wind velocity at the stagnation radius, and this is not expected to occur.

4. $(x = 1, y = \tilde{w})$: This "attractor"-like point represents full entrainment as $r \rightarrow \infty$, which is a realistic assumption for winds that actually are propelled to infinity by the external wind source terms.

Figure 5.10 shows the solution topology for this simplified form of the equation of motion for two values of $\tilde{w}$ on opposite sides of unity. The dotted lines are loci of *zero slope* solutions (i.e., when the numerator of eq. [5.52] vanishes), and the four singular points are also intercepted by these loci. Solutions which pass through the stagnation point ($x = 0$, $y = 0$) attempt to stay on the finite-slope solution $dy/dx = 1/\tilde{w}$, but any infinitesimal perturbation makes them switch to near-infinite slope solutions, branching off in an unstable way. Solutions which *decelerate* from the finite-slope line receive a slight enhancement in the surface density σ, and this eventually amplifies into an over-dense solution that must decelerate to zero velocity (and possibly "crash" back down in a time-dependent manner). Solutions which *accelerate* from the finite-slope line grow less dense, and thus may be able to accelerate out to infinity if there is sufficient added momentum from the source term. This multiplicity of possible solutions is a direct result of the nonlinearities in the governing ODE, and when more realistic physics is incorporated, this degeneracy may be lifted.

Note that for the $\tilde{w} = 0.8$ topology there is insufficient momentum being added to the wind to accelerate any solutions to infinity, and all velocity laws $y(x)$ which pass through the stagnation point eventually decelerate to zero velocity. For the $\tilde{w} = 1.2$ topology, however, some solutions have enough momentum to counteract gravity and accelerate to the "entrainment" velocity $y = \tilde{w}$ at $x = 1$. The fact that $\tilde{w}$ is scaled to the *escape speed* at r_o provides the physical justification of only $\tilde{w} \gtrsim 1$ solutions being able to entrain disk solutions to infinity.

Radii beneath the stagnation point, for which we assume the velocity is directed inwards toward the star (i.e., $x < 0$, $y < 0$) exhibit different types of solutions from the above. Despite the existence of infinite-slope solutions immediately below the stagnation radius, a stable and convergent decelerating solution appears to exist when integrating *downward* from $x = 0$. Because the majority of the mass-loading occurs around the stagnation point, the solutions at lower x values are causally determined from higher radii, and the stability of this part of the velocity law seems assured.

The obvious next step in this analysis would be to consider the radiative driving and centrifugal terms in the equation of motion, but at this preliminary stage

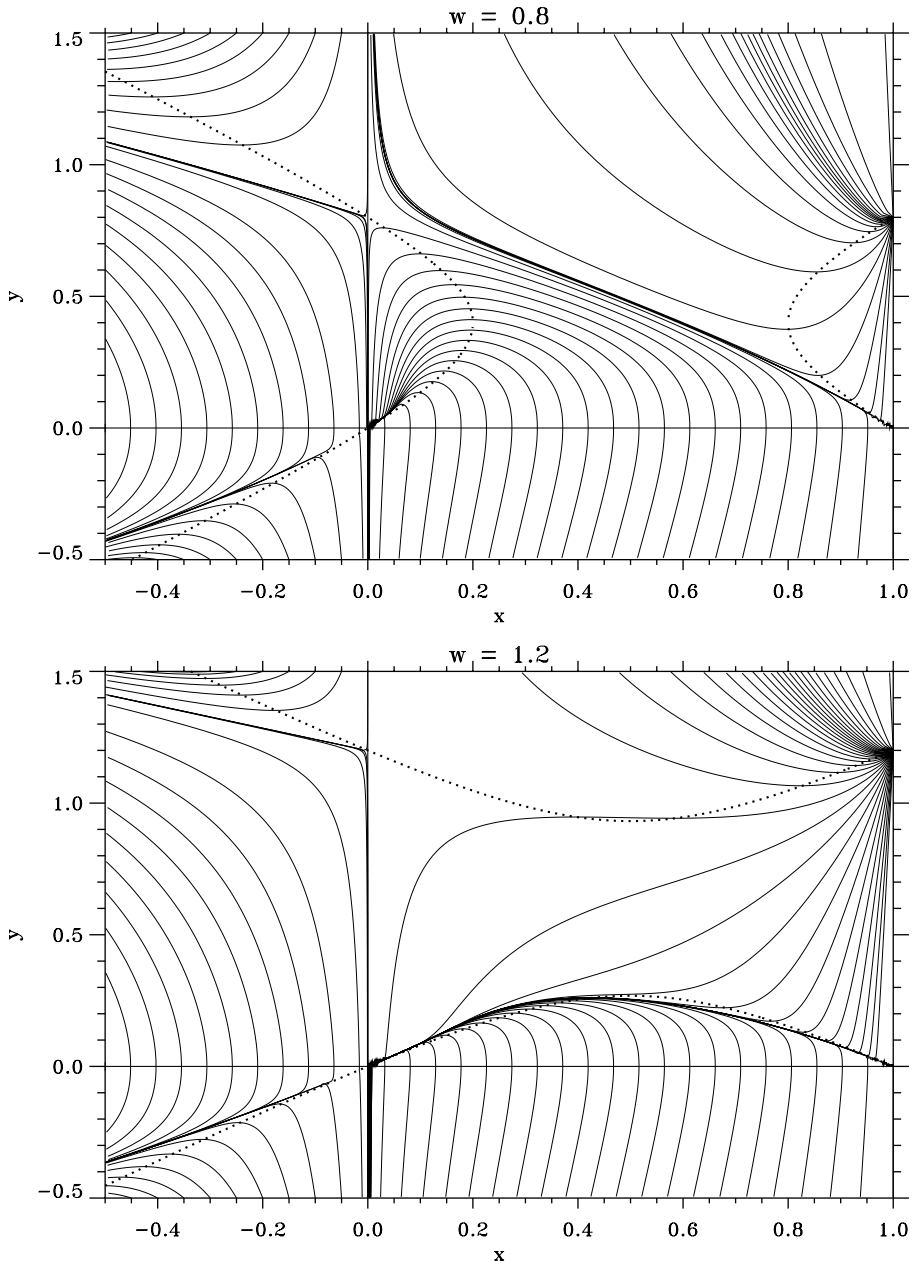

Figure 5.10: Solution topology to the dimensionless 1D wind compressed disk equation of motion, without radiation or centrifugal forces. The upper curve shows a *small* value of the external wind velocity (0.8); a situation where not enough momentum is provided to propel the wind to infinity. The lower curve shows a *large* value of the external wind velocity (1.2); a situation where the wind can be propelled to infinity, but some decelerating solutions are still possible.

we have not yet explored these effects. To zero order, we expect that radiative forces should not be extremely important in very *dense* wind compressed disks (because of the $\rho^{-\alpha}$ dependence in the Sobolev line force). However, for observed B-star rotation rates, OCB found that actual WCDs are only enhanced in density by factors of 10–100 over the polar wind, and radiative forces in the disk may be significant. Certainly the presence of another outward force would help the radial velocity in WCDs to accelerate out to infinity, and possibly may lift the solution degeneracy around the stagnation point.

Finally, then, the utility of this one-dimensional model of a disk must be critically examined. The two-dimensional numerical hydrodynamics solutions show the disk velocity laws to be quite stable and well-behaved. Thus, if the extreme instability and degeneracy of the 1D solutions persists when all relevant physics has been included, then the only remaining difference between the methods is the treatment of the *latitudinal* direction. It may be the case that the only accurate way to study the phenomenon of WCD formation is in two dimensions, with the "source terms" modeled self-consistently, together with the disk. This would represent the failure of the present 1D formalism, but no matter the outcome, we will have learned a great deal about the physics of wind-fed disks around rotating stars from this attempt.

Chapter 6

DYNAMICAL MODELS OF COROTATING WIND STRUCTURE

In spiral routes by long detours,
(As a much-tacking ship upon the sea,)
For it the partial to the permanent flowing,
For it the real to the ideal tends.

Walt Whitman, *Song of the Universal*

The ubiquitous temporal and structural variability of hot-star winds has been reviewed in Section 1.2.3 above, and in this Chapter we begin to construct hydrodynamical models designed to produce discrete absorption components (DACs) in P Cygni line profiles. As opposed to earlier *kinematic* models of corotating wind structure, the principal goal of this Chapter is to model the *dynamical* effect of radiative driving on the formation of CIRs in a hot star wind, and to compute synthetic observational diagnostics to see if, e.g., slow DAC-like signatures can be theoretically produced. Our computational approach is to apply a reasonable parameterization for a localized "star spot" perturbation in the radiation force near the stellar surface, and allow the wind to respond consistently. Although the actual photospheric structure perturbing the base of the wind is likely to be different, we suspect the characteristic response of a radiatively-driven medium will be insensitive to the details of this physical mechanism, and mainly depend on base changes in the fluid velocity and density.

The remainder of this Chapter is organized as follows (see Cranmer & Owocki 1996). We first (Section 6.1) describe the azimuthally-dependent force enhancement that is utilized to induce nonaxisymmetric structure in the equatorial plane. Next (Section 6.2) we present results for a series of O star models with varying rotation

rates and wind parameters, and discuss the emergent corotating structure. We then (Section 6.3) compute synthetic ultraviolet P Cygni line profile time series for the various models in our parameter study. We also present a representative calculation of the continuum polarization variations for one of these models with time and observer-inclination. Finally, a discussion and conclusion section (Section 6.4) summarizes our results and outlines directions for future work.

6.1 The Local Radiative Force Enhancement

We induce azimuthal structure in our models by varying the Sobolev line force over a localized "star spot" in the lower wind. Since this force is directly proportional to the stellar flux ($L_*/4\pi r^2$), increasing or decreasing $g_r^{\rm lines}$ over a small area is operationally equivalent to assuming a bright or dark region of the photosphere. Note, however, that by modulating the radiative force in this manner we do *not* mean to literally propose the existence of strong flux-varying spots on early-type stars. We merely use this simple method to perturb the wind in lieu of more definite knowledge about the physical cause(s) of surface inhomogeneities. Because the line driving grows weaker as one moves deeper into the subsonic wind and photosphere, the force enhancement is essentially confined to the transonic and supersonic wind, obviating the need to model a perturbed stellar atmosphere.

The induced variation in the line force is assumed to have a specified radial and azimuthal dependence which remains fixed to the stellar surface, and thus rotates through the computational domain with the star. The force enhancement is a function of radius r and a corotating azimuthal angle ψ,

$$\psi \;=\; \phi - \Omega t \quad , \tag{6.1}$$

with $\Omega \equiv V_{\rm eq}/R_*$ the star's constant rotational angular velocity. The perturbed line force has the form

$$\begin{aligned} g_r^{\rm lines}(r,\psi) &= g_0(r) + \delta g(r,\psi) \\ &= g_0(r)\left\{1 + A\,\gamma(r)\exp\left[-\left(\psi-\psi_0\right)^2/\sigma^2\right]\right\} \quad , \end{aligned} \tag{6.2}$$

where g_0 is the unperturbed Sobolev force (eq. [2.88]), ψ_0 is the azimuthal position of the center of the spot, and A is its dimensionless amplitude. We will refer to "dark spots" as those with $-1 < A < 0$ and "bright spots" as those with $A > 0$. The azimuthal variation of the force is here assumed to be Gaussian about ψ_0, with full width at half maximum (FWHM) given by $\Phi \equiv 2\sigma\sqrt{\ln 2}$. The radial modulation $\gamma(r)$ is constrained by the geometrical extent of the spot. Close to the star, the spot is all that can be seen, and so $\gamma(r \to R_*) \to 1$; far from the star, the spot only represents a fraction of the observed stellar disk, and so $\gamma(r)$ approaches a small, but constant value as $r \to \infty$.

For a field point directly over ($\psi = \psi_0$) a *circular* flux enhancement with angular diameter Φ, the radial function $\gamma(r)$ can be derived analytically from the the normalized residual flux,

$$\frac{\mathcal{F} - \mathcal{F}_0}{\mathcal{F}_0} \;=\; A\frac{r^2}{R_*^2}\int\!\!\int D(r,\mu',\phi')\,\mu' d\mu' d\phi' \;=\; A\gamma(r) \quad , \tag{6.3}$$

where $\mathcal{F}$ and $\mathcal{F}_0$ are the total and unperturbed fluxes. The amplitude A takes into account the relative magnitude of the spot's "residual effective temperature," and is equivalent to $(T_{\rm spot}^4 - T_0^4)/T_0^4$. The area integral is taken over a solid angle centered about the z-axis, with angles $\theta' = \cos^{-1}\mu'$ and ϕ' measured from the field point in the wind at radius r, and the residual limb darkening function D set to zero for rays not intercepting the spot. Thus, for simple linear limb darkening,

$$\gamma(r) \;=\; \frac{2\pi r^2}{R_*^2}\int_{\mu_0(r)}^1 \frac{1}{4\pi}\left(2 + 3\sqrt{\frac{\mu'^2 - \mu_*^2}{1-\mu_*^2}}\right)\mu' d\mu' \quad , \tag{6.4}$$

where $\mu_* \equiv [1 - (R_*^2/r^2)]^{1/2}$ defines the stellar limb, and

$$\mu_0(r) \;=\; \begin{cases} \mu_*, & r\cos(\Phi/2) \le R_* \\ \sqrt{1 - R_*^2\sin^2(\Phi/2)/S^2}, & r\cos(\Phi/2) > R_* \end{cases} \tag{6.5}$$

defines the visible edge of the spot. The distance S from the field point to the edge of the spot is $[r^2 + R_*^2 - 2rR_*\cos(\Phi/2)]^{1/2}$. We thus adopt the radial modulation function given by the analytic integral of (6.4),

$$\gamma(r) \;=\; \frac{1}{2}\left[1 + \left(\frac{1-\mu_0^2}{1-\mu_*^2}\right) - \left(\frac{\mu_0^2 - \mu_*^2}{1-\mu_*^2}\right)^{3/2}\right] \quad , \tag{6.6}$$

which approaches unity as $r \to R_*$ and approaches a constant value of $[1+\sin^2(\Phi/2) - \cos^3(\Phi/2)]/2$ as $r \to \infty$. Although this residual flux integral is also able to provide oblique ($\psi \neq \psi_0$) and nonradial components of the flux enhancement of a star spot, we restrict our present models to the explicit *radial* perturbation given by equations (6.2) and (6.6).

Again we emphasize that we do not intend here to propose that bright or dark spots are necessarily the specific mechanism for inducing corotating stream structure in hot-star winds. (Indeed, we intend our results to provide a more generic representation of the wind response to a large variety of base perturbations, including, e.g., magnetic fields, nonradial pulsations, or mass ejections.) Taken literally, the standard spot models here, with $A = \pm 0.5$ and $\Phi = 20°$, should produce observable photometric variations at the 1–2% level. But other weaker and smaller spot

models we have computed (see Figures 6.16 and 6.17) can also yield visible DAC wind structure with a much lower, perhaps undetectable, photometric signature.

Figure 6.1 shows contours of the force enhancement in the equatorial plane for a spot with $\Phi = 20°$, as well as wind "streaklines" for various stellar rotation speeds, as discussed further below (Section 6.2.3). Note that the spot significantly affects only a relatively small area of the wind: an azimuthal extent of $\sim 2\Phi$ and a radial extent of about a stellar radius. This allows several spots to be superposed on the stellar surface without any appreciable overlap in their force enhancements. Following the empirical arguments of Kaper & Henrichs (1994), who suggest a variable dipole magnetic field as the seed of large-scale wind structure, we place *two* spots separated by 180° on our model stars.

Before examining how a rotating wind responds to the localized force enhancement, it is instructive to see how a non-rotating wind is affected. Figure 6.2 shows the radial velocity and density (directly over the spot) at a reference radius of $10R_*$, well beyond the region of significant direct force enhancement, as a function of amplitude A. The general trend is for a "bright" spot to increase the local mass loss and thus increase the density of the wind near the star. Further out in the wind, where the effect of the spot drops off, the radiative force cannot accelerate the higher density material as strongly, so it approaches a *lower* terminal speed than in the unperturbed wind. Conversely, "dark" spots decrease the mass loss in the surrounding wind and thus allow the less dense material to be accelerated more strongly, leading to a much *higher* terminal speed. The three sets of data in Figure 6.2 correspond to: (1) one-dimensional, finite-disk, "modified CAK" (mCAK) solutions with a realistic critical point analysis (solid lines), (2) numerical two-dimensional hydrodynamical models using VH-1 (filled circles), and (3) a simple analytic fit to the data (dashed lines). The one-dimensional mCAK models contain the radial spot modulation $\gamma(r)$, but no information about neighboring streamline divergence or convergence. For spots with $A \gtrsim 0.6$, the one-dimensional models cease to have steady-state solutions that reach to infinity because too much mass is driven off the star to be accelerated beyond its gravitational escape velocity. The two-dimensional models can drive more mass to infinity because the density is reduced by a slight azimuthal expansion, which leads to a faster-than-radial divergence of flow tubes (see, e.g., MacGregor 1988).

The simple fit to the velocity and density variation in Figure 6.2 depends on only one free parameter, and makes use of the approximate dependence of the CAK mass loss rate on an arbitrary force multiplier (see Cranmer & Owocki 1995, eq. [24]). Directly over the spot,

$$\dot{M} \approx \dot{M}^{(0)}(1+A)^{1/\alpha} \ , \tag{6.7}$$

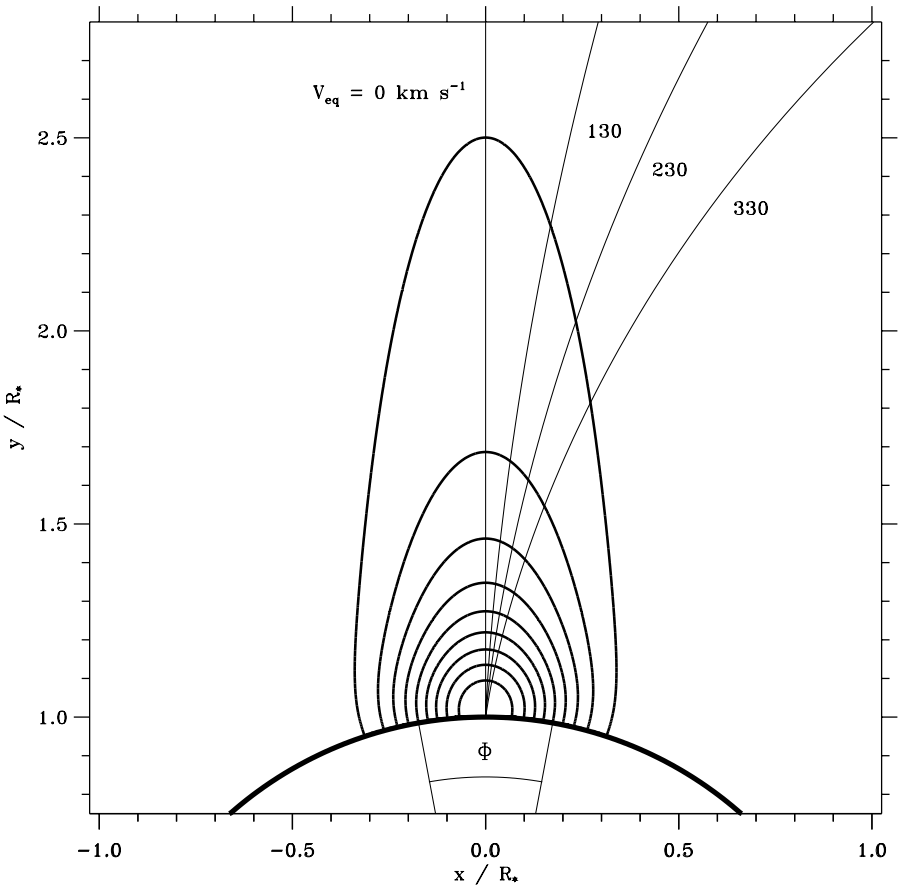

Figure 6.1: Contours of the star-spot force enhancement for a spot with full width at half maximum $\Phi = 20$ degrees. The contour levels shown range from $0.1A$ to $0.9A$ in intervals of $0.1A$. Overplotted are streaklines of unperturbed wind models from stars rotating at 0, 130, 230, and 330 km/s.

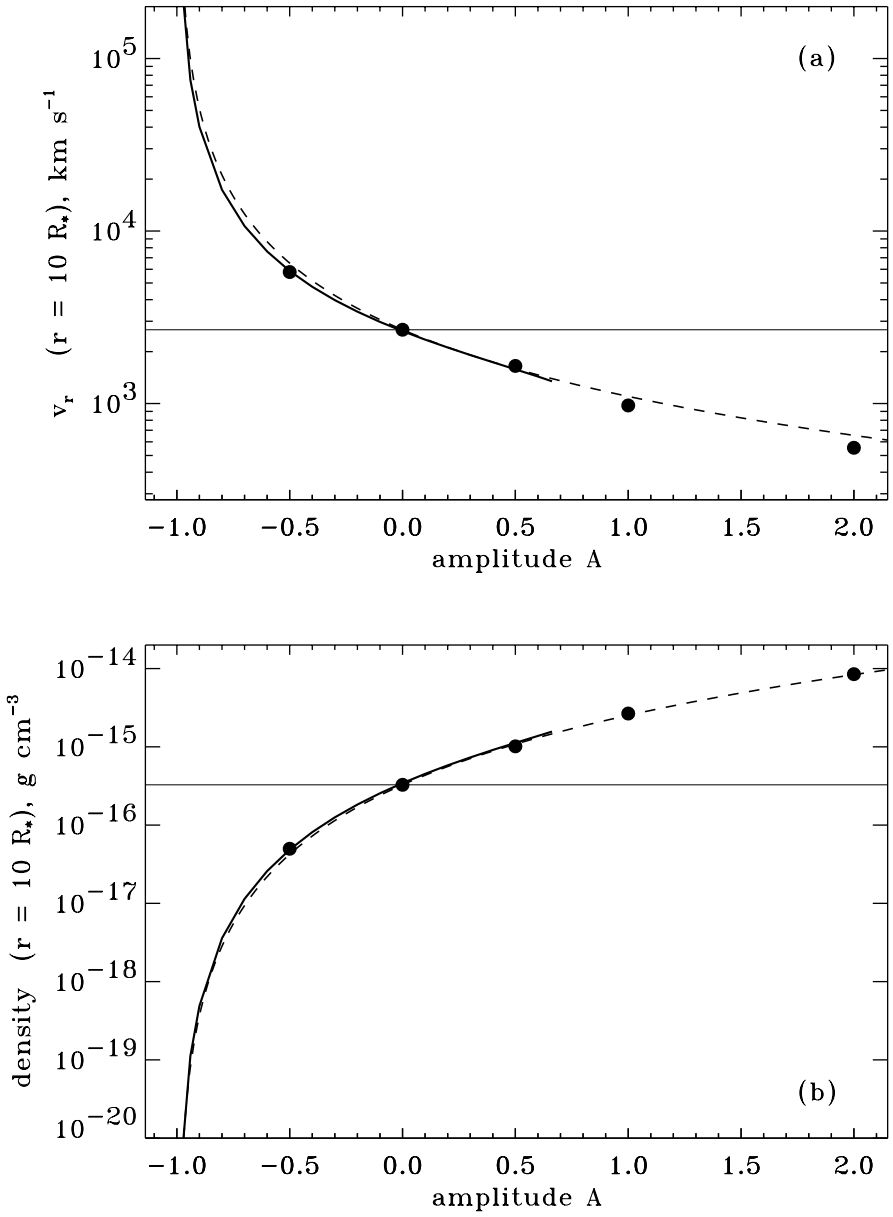

Figure 6.2: Variation with spot amplitude (for $\Phi = 20$ degrees) of (a) radial velocity and (b) density at a radius of 10 stellar radii, for non-rotating winds. Solid lines show one-dimensional mCAK solutions, filled circles show two-dimensional hydrodynamical solutions, and dashed lines show a simple one-parameter fit to both sets of data.

where $\dot{M}^{(0)}$ is the unperturbed mass loss rate, and we assume that the CAK critical point r_c, where the mass flux is determined, is close enough to the star that $\gamma(r_c) \approx 1$. In a one-dimensional steady state, the mass conservation equation is integrated in the usual way to obtain $\dot{M} = 4\pi\rho v_r r^2$, and this provides a relation between the velocity and density at a given radius. We thus define fitting functions which obey this multiplicative constraint:

$$\rho \approx \rho^{(0)}(1+A)^{s/\alpha} \quad , \tag{6.8}$$

$$v_r \approx v_r^{(0)}(1+A)^{(1-s)/\alpha} \quad , \tag{6.9}$$

where we have found the best fit value of $s = 1.77$ for our dashed-line fits in Figure 6.2.

6.2 Numerical Results

Because the DAC phenomenon is primarily observed in O-star winds, we choose to center our study on a standard model of the O4f supergiant ζ Puppis. Specifically, we take $M_* = 60 M_\odot$, $R_* = 19 R_\odot$, $L_* = 8 \times 10^5 L_\odot$, and $T_{\rm eff} = 42,000\,{\rm K}$ (see, e.g., Howarth & Prinja 1989; Kudritzki et al. 1992). The measured rotational $V_{\rm eq} \sin i$ for ζ Puppis is 230 km s^{-1}, which we take for the equatorial rotation velocity of our standard model. We neglect the small ($\sim$7%) oblateness induced by this degree of rotation, which corresponds to a Roche equipotential surface rotating at 63% of its critical angular velocity. We assume an isothermal wind of temperature $T_{\rm eff}$, corresponding to a sound speed $a = 24\,{\rm km\ s^{-1}}$, and use the line-driving constants $\alpha = 0.60$ and $k = 0.15$ (see eq. [2.88]). In one-dimensional mCAK models, these result in a terminal velocity $v_\infty = 2580\,{\rm km\ s^{-1}}$ and a mass flux $\dot{M} = 3.28 \times 10^{-6}\, M_\odot/{\rm yr}$. We use the VH-1 hydrodynamics code described above in Section 2.3.3, and model the wind in the equatorial plane, varying r (from R_* $30R_*$) and ϕ (from 0° to 180°) on the two-dimensional computational grid (Cranmer & Owocki 1996).

The Sobolev approximation assumes a monotonically accelerating velocity field, but this is not guaranteed in the time-dependent simulations presented below. Winds with nonmonotonic velocities have *nonlocal* line forces, since multiple resonance surfaces can create additional attenuation of the stellar flux (Rybicki & Hummer 1978; POF). We do not treat this nonlocal coupling directly, but we have compared CIR models using an upper limit (unattenuated) and a lower limit (strongly attenuated) for the line force in multiply-resonant regions of the wind. The lower limit assumes decelerating flows ($\partial v_r/\partial r < 0$) receive the same small force contribution from nonradial rays as a flow that is not accelerating at all ($\partial v_r/\partial r = 0$). The upper limit uses the absolute value of the radial velocity gradient $|\partial v_r/\partial r|$ in equation (2.88) and in the finite disk factor f. In practice, we find the overall wind

dynamics to be qualitatively similar in both limits, but have standardized on the upper limit method for all the results presented here.

The localized "star spot" radiative force enhancement described above depends primarily on two quantities: the amplitude A and the azimuthal full width Φ. These, together with the equatorial rotation velocity $V_{\rm eq}$, are the three free parameters we vary in our study of non-axisymmetric structure formation. Table 6.1 outlines the input parameters and several output quantities (to be discussed below) for the models we computed. Models 1 and 2 are standard "bright" and "dark" spot models, with $A = +0.5$ and -0.5, and they represent a basis to explain the general hydrodynamical phenomenon of stream interaction. The subsequent models in Table 6.1 are intended to confirm our understanding of the physics of CIR formation, and are discussed below in a more limited fashion. In Table 6.1 we also define Δv_r as the maximum absolute velocity perturbation $(v_r - v_r^{(0)})$ in the model, either positive or negative, and the other variables are discussed further below. All velocities in Table 6.1 are expressed in km s^{-1}.

6.2.1 Standard Bright Spot: Model 1

Figure 6.3 shows gray-scale plots for the density, radial velocity, azimuthal velocity, and radial Sobolev optical depth in Model 1, *normalized to the unperturbed wind*. To ease comparison with other models, the azimuthal coordinates here have been incremented by a constant factor to align the peak of the spot (ψ_0) with the center-line or x-axis of the diagram. Note the expected tendency for a bright spot to create higher density and lower radial velocity. However, the *azimuthal* velocity only differs by a small subsonic amount from the unperturbed angular-momentum-conserving form $v_\phi^{(0)}(r) = V_{\rm eq} R_*/r$. This demonstrates the almost purely *radial* effect of the spot enhancement.

Most of the corotating structure from the spot settles onto nearly constant spiral "streaklines" in the wind. In the present models, streaklines are equivalent to flow streamlines in the star's rotating frame of reference. Figure 6.4 compares streamlines and streaklines computed for Model 1. By numerically integrating the kinematic relation

$$\frac{r\, d\phi}{dr} = \frac{v_\phi(r,\phi) - r\Omega_F}{v_r(r,\phi)} \quad , \tag{6.10}$$

from a locus of points on the stellar surface spaced evenly in ϕ, one can alternatively compute either streamlines in the inertial reference frame, with $\Omega_F = 0$, or streaklines in the rotating reference frame, with $\Omega_F = \Omega$. Areas with a higher (lower) concentration of streaklines correspond to regions of relative compression (rarefaction), though not all density variations are reflected in the streaklines. The dashed lines in Figure 6.4 show the streamline and streakline originating directly over the

Table 6.1: Summary of CIR Parameter Study

Model	A	Φ	$V_{\rm eq}$	$(\rho/\rho^0)_{\rm max}$	Δv_r	r_L/R_*	r_{NL}/R_*	r_i/R_*
1	+0.50	20°	230	3.747	–629.2	1.607	6.417	6.736
2	–0.50	20°	230	5.071	+2272.	2.188	—	7.646
3A	+0.01	20°	230	1.023	–29.30	8.169	6.005	306.0
3B	+0.10	20°	230	1.243	–193.0	2.782	6.157	31.10
3C	+2.50	20°	230	39.95	–1285.	1.210	6.157	1.981
4A	+0.50	10°	230	2.840	–598.3	1.163	3.736	3.868
4B	+0.50	40°	230	2.206	–493.3	2.526	10.38	12.47
4C	+0.50	80°	230	1.977	–238.8	4.383	>30	23.94
5A	+0.50	20°	130	3.969	–783.4	1.892	9.324	11.90
5B	+0.50	20°	330	2.485	–482.9	1.492	4.934	4.556

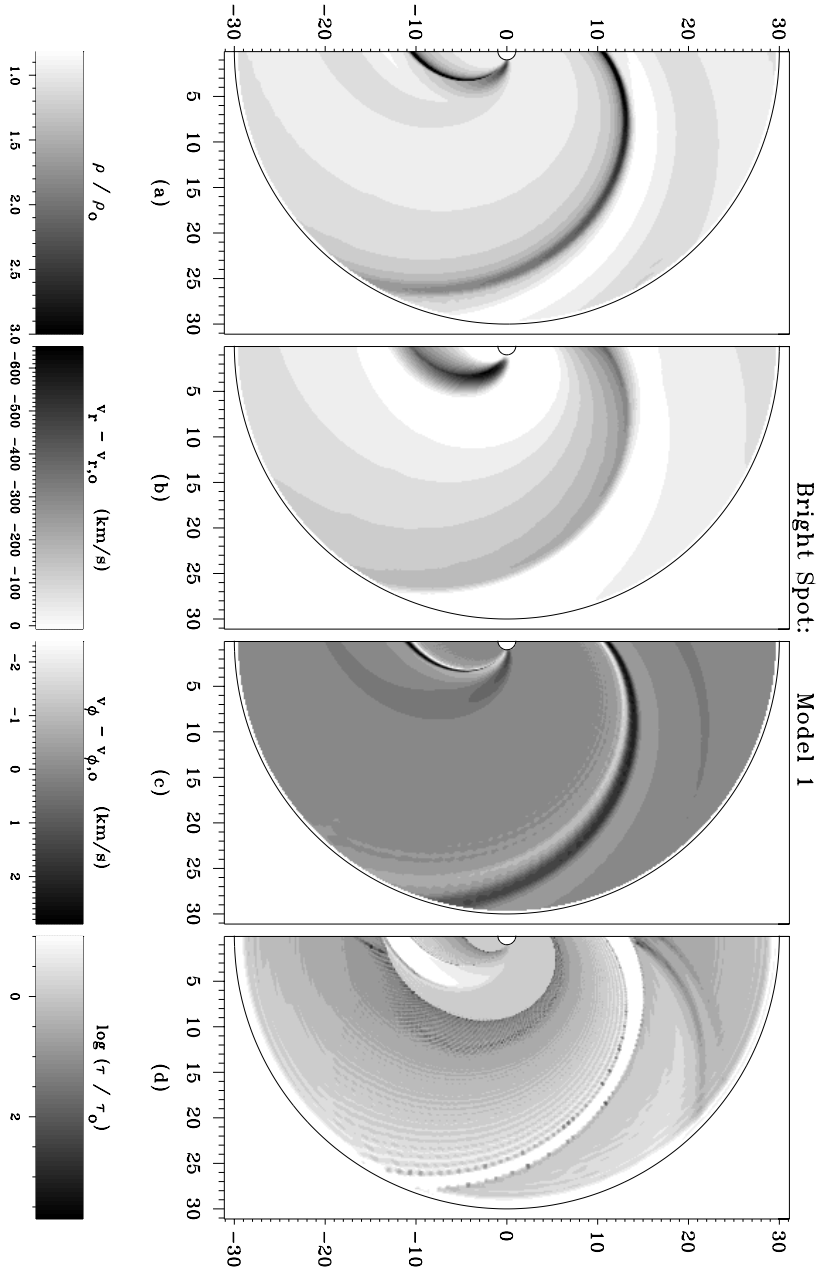

Figure 6.3: CIR structure for Model 1, settled to a steady state. Shown are the (a) density, (b) radial velocity, (c) azimuthal velocity, and (d) radial Sobolev optical depth, all normalized to the unperturbed wind initial condition.

spot. The streamline appears nearly radial, but careful inspection shows that it has a modest (18°) prograde deflection, resulting from corotation of the relatively slow wind outflow near the surface. Through most of the wind, however, the streamlines are close to radial, and this allows one to qualitatively interpret the azimuthal coordinate as a *time* dimension. For any streamline at a fixed value of ϕ, which is intercepted by different streaklines as the (corotating steady state) system sweeps by, the two-dimensional hydrodynamics becomes effectively one-dimensional, but now truly time dependent. This concept allows us to understand the "spread out" CIR structure in terms of a simpler model of radial wave or shock propagation. Hundhausen (1973) modeled solar-wind CIR formation and evolution in one dimension using this approximation.

We can disentangle the actual patterns of high density, low velocity, and more optically thick CIR structure by examining several causally-connected regions of this model:

I. **Direct Enhancement:** Close to the stellar surface, the Gaussian-shaped spot increases the mass flux and wind density over a limited ($r \lesssim 2R_*$) region near the star. This enhanced-density patch is slightly deformed by rotation from the contours shown in Figure 6.1, but is essentially equivalent. The density increases over the spot by a maximum factor of ~2.6, only slightly smaller than that predicted by the non-rotating analysis (see eq. [6.8]). This region also shows considerable azimuthal spreading in v_ϕ as the wind begins to adjust to the presence of the spot.

II. **Prograde Precursor:** Just ahead of the spot ($\psi > \psi_0$), a small fraction of the enhanced higher-density wind is able to "leak out" azimuthally and settle onto a set of relatively unperturbed streaklines. The density in this feature is only enhanced by a factor of ~1.2, indicating that it comes from material in the prograde tail of the Gaussian distribution. It becomes isolated from the direct spot enhancement at a relatively large distance from the star ($r \approx 6.4R_*$) after the CIR rarefaction (IV) has appeared between it and the CIR shock (III).

III. **CIR Compression:** The low radial velocity wind from the center of the spot curls around on more tightly-wound streaklines than the surrounding unperturbed wind, and these streams begin to interact at a finite radius from the star ($r \approx 1.6R_*$). Alternately, in the above one-dimensional interpretation, the slow stream can be considered equivalent to a radially-extended Gaussian "wave packet" which nonlinearly steepens as the fast mean wind begins to overtake it. The result of this collision of fast and slow streams is a corotating weak shock compression (the CIR) which, because it is driven by ram pressure from the mainly unperturbed wind, propagates out at very near the

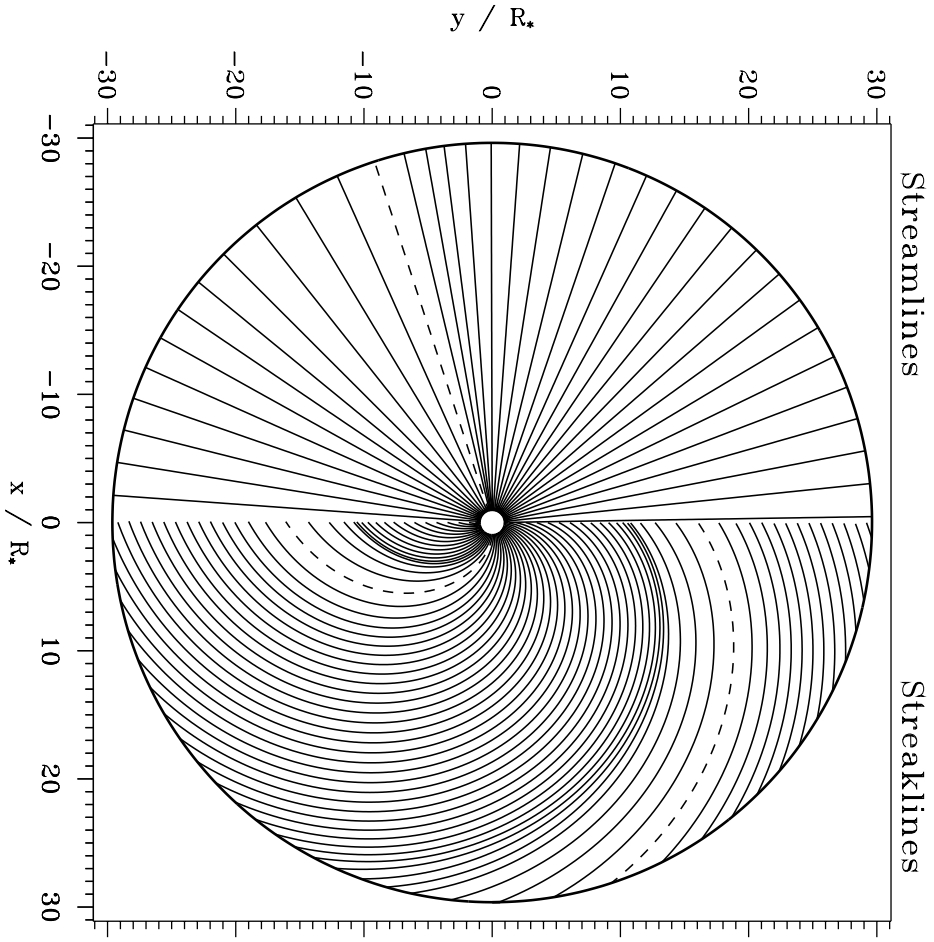

Figure 6.4: Streamlines (left) and streaklines (right) for Model 1, integrated from 72 equally-spaced points on the star, separated by 5 degree intervals. Dashed lines indicate initial points situated at the center of the spot enhancement.

unperturbed wind velocity. Because the flow is isothermal, we do not see a separation into a distinct forward and reverse shock pair, as is observed in the more nearly adiabatic solar wind.

IV. **CIR Rarefaction:** Ahead of the nonlinear shock the streaklines fan out and form a lower-density rarefied region. The formation of this rarefaction is mandated by mass flux conservation, and the radial velocity correspondingly peaks slightly above its unperturbed value here. Because the density in this feature never dips too far below the unperturbed density ($\min[\rho/\rho^{(0)}] \approx 0.82$), the rarefaction propagates out at nearly the same velocity as the CIR compression.

V. **Radiative-Acoustic "Kink:"** In a purely hydrodynamical wind, the radial CIR shock structure is the sole result of the nonlinear steepening of the initial enhancement. Any nondissipative signals propagating in the rest frame of the wind (at characteristic speeds $\pm a$) are limited to the relatively undisturbed lateral (nonradial) direction. In a line-driven wind, however, Abbott (1980) and Rybicki et al. (1990) found that large spatial-scale linear perturbations propagate in the radial direction at modified "radiative-acoustic" characteristic speeds. Abbott (1980) derived

$$C_{\pm} \;=\; -\tfrac{1}{2}U \pm \sqrt{\left(\tfrac{1}{2}U\right)^2 + a^2} \tag{6.11}$$

for radial modes, where $U \equiv \partial(g_r^{\rm lines})/\partial(\partial v_r/\partial r)$ and $C_{\pm}$ reduces to the purely acoustic case if $U = 0$ (see Section 7.2.7 for a full derivation). In most of the wind, though, $U \gg a$, and the outward (positive root) solutions are subsonic, and the inward (negative root) solutions are supersonic. In Model 1 we see both an acoustic lateral mode (spreading in v_ϕ at large radii; Figure 6.3c) and a nonlinear analog of the inward radiative-acoustic mode, which propagates slowly outward in the star's frame ($0 < v_r + C_- < v_r$) as a weak discontinuity, or "kink," in the radial velocity gradient. Because of its slow propagation (more tightly-wound streaklines) this feature eventually collides with the CIR rarefaction from the other spot at a radius of $\sim$13.5 R_* and ceases to exist.

We trace these five features in Figure 6.5, which is a close-up of the density gray-scale shown in Figure 6.3a. Unique tracks were found by searching for local extrema (in radius) of various quantities, and following contiguous patterns around in azimuth. The direct spot enhancement (I) appears at the stellar surface as a local maximum in the normalized density $\rho/\rho^{(0)}$, and collides with the CIR/kink pair of features (III and V) at a radius of $\sim 3.9 R_*$. These "bifurcated" extrema are found by tracking local minima and maxima in the radial velocity, as shown in Figure 6.6 below. They appear at a relatively small radius r_L (see Table 6.1),

where the spot perturbation is still linear. The remaining precursor/rarefaction pair of features (II and IV) correspond to other local minima and maxima in the normalized density, and they appear further out (at a larger radius r_{NL}) where the disturbance has definitely steepened into a nonlinear shock. It is interesting that the CIR compression and rarefaction do not form together at the same point, but this is understandable, since the latter can be considered an effect or response of the former.

To estimate which wind structures should yield the most prominent signatures in observed line profile variations, let us examine the radial Sobolev optical depth,

$$\tau_r(r,\phi) \equiv \frac{\kappa_L \, \rho(r,\phi) \, v_{\rm th}}{|\partial v_r(r,\phi)/\partial r|} \quad . \tag{6.12}$$

The gray-scale plot in Figure 6.3d shows the changes in the optical depth relative to the mean, unperturbed wind. Since both the line absorption coefficient κ_L and the ion thermal speed $v_{\rm th}$ are assumed to have the same constant values in both the mean and perturbed flow, all variations here stem from changes in the ratio of density to velocity gradient. Somewhat surprisingly, the regions of strongest optical depth enhancement occur not within the dense CIR compression (feature III), but rather within the relatively shallow velocity gradient region after the Abbott kink (feature V).

Figure 6.6 plots the radial variation of velocity and density from selected slices of constant azimuthal angle ϕ. For this corotating steady state, the changing features in these line plots also indicate the time evolution of structure at fixed azimuths. This allows us to follow the outward propagation of both the CIR density enhancement (local minima in velocity) and the trailing radiative-acoustic kink (local maxima in velocity). In the high-density CIR, the wind is either strongly accelerating or decelerating, so both the numerator and the denominator in the Sobolev optical depth (eq. [6.12]) are enhanced, resulting in very little net increase. Just outward from the kink, however, the density is nearly unperturbed, while the velocity gradient is much shallower, implying a large increase in the Sobolev optical depth. In synthetic line profiles (see Section 6.3.2 and Figure 6.13), this near plateau produces a distinct absorption feature quite similar to slowly evolving DACs. As the (corotating) steady-state structure rotates in front of the observer's line of sight, material flowing *through* the kink appears at the velocities of the local maxima in Figure 6.6, but the evolution of the feature is governed by the radiative-acoustic mode propagation, which leads to an apparent acceleration that is much slower than the actual acceleration of the wind material.

Ahead of the CIR, between the compressive density maximum and the rarefied minimum, there is a region of high acceleration that arises from the prograde

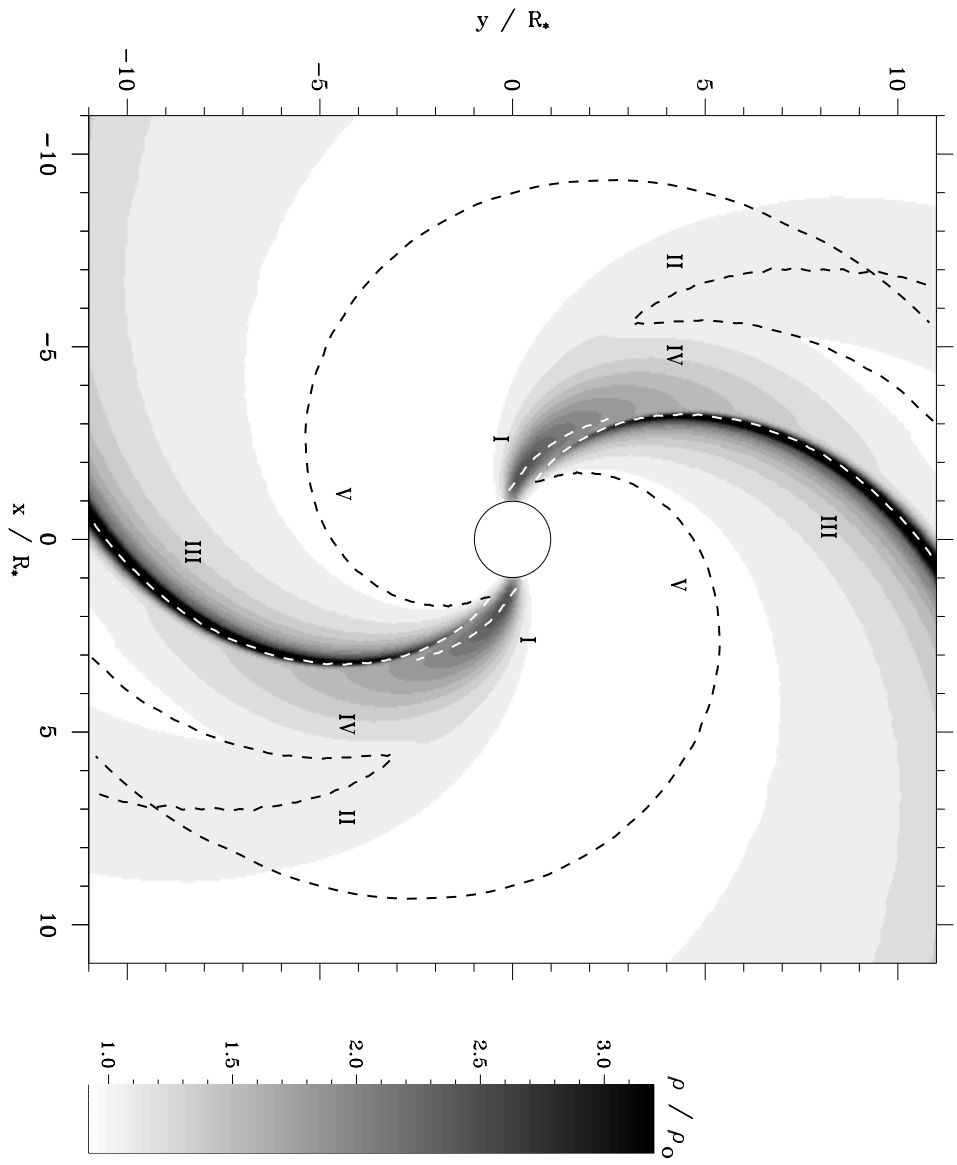

Figure 6.5: Normalized density gray-scale for Model 1, as in Figure 6.3a. Overplotted are dashed lines which trace the: (I) direct spot enhancement, (II) prograde precursor, (III) CIR compression, (IV) CIR rarefaction, and (V) radiative-acoustic Abbott kink.

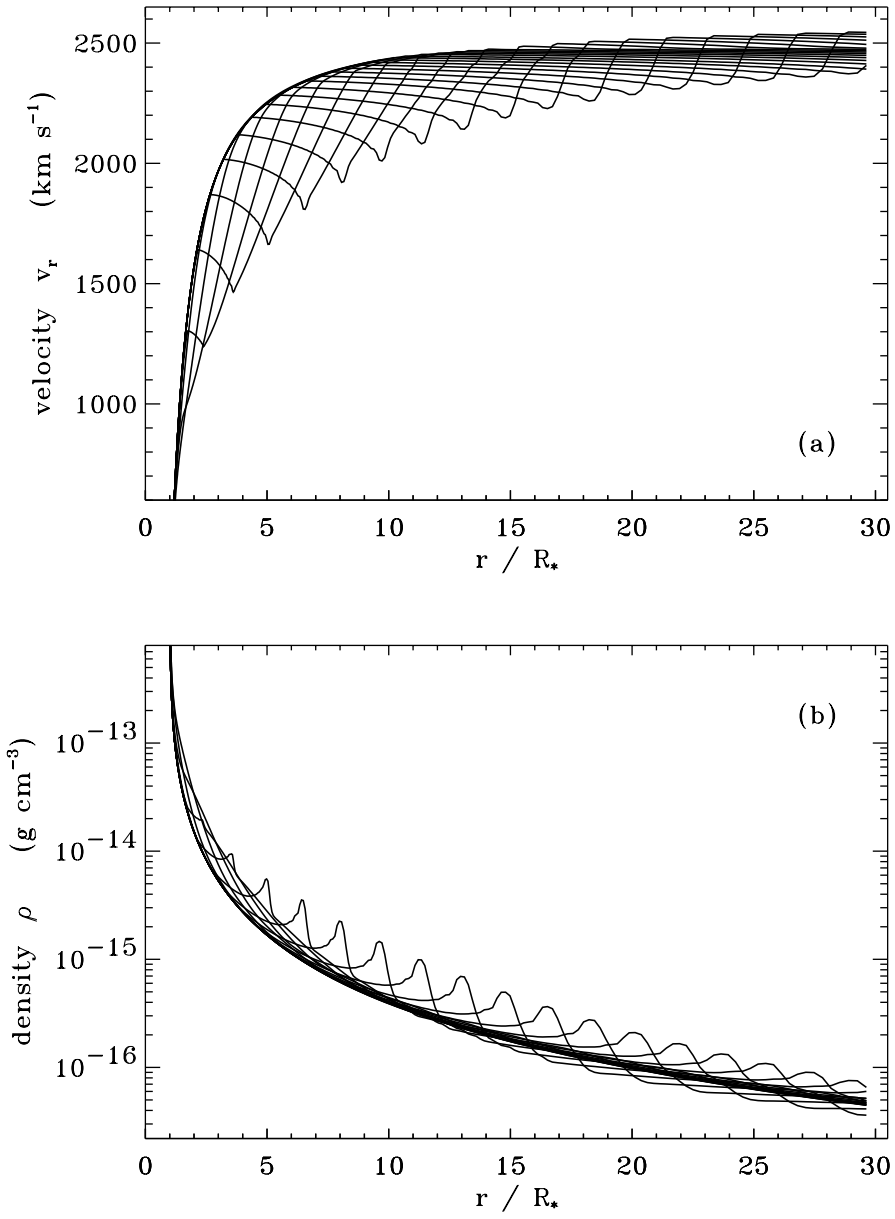

Figure 6.6: Line plots for Model 1 of the radial variation of (a) radial velocity and (b) density in the equatorial plane at 16 equally-spaced azimuthal angles, 11.25 degrees apart.

edge ($\psi > \psi_0$) of the Gaussian spot, which steepens into a monotonic sawtooth structure connecting the shock with the lower-density unperturbed wind. This region contains a lower net optical depth than the unperturbed wind, implying a relative *lack* of absorption in synthetic line profiles. This effect is only slightly weaker than the enhanced absorption due to the plateau, suggesting that isolated patches of extra absorption (DACs) may be difficult to model theoretically without a corresponding lower optical depth feature (with apparent relative "emission").

6.2.2 Standard Dark Spot: Model 2

A wind perturbed by a locally decreased radiative force ($A = -0.5$) produces a lower-density, high-speed stream, and thus settles to a steady state on the computational grid faster than a model with slow streams. Figure 6.7 shows gray-scale plots for the density, radial velocity, azimuthal velocity, and radial Sobolev optical depth for Model 2, normalized in the same way as in Figure 6.3. Although the dark spot produces an extremely rarefied wind, a high-density CIR forms (on the leading edge of the perturbation) where the high velocity stream collides with the slower unperturbed wind. The corotating structure present in Model 2 is qualitatively simpler than that in Model 1. The CIR/kink pair of features initially appears at $r_L \approx 2.2R_*$, and advects smoothly throughout the wind. There is no analog to the second pair of features (starting further out at r_{NL}) in this model.

For slices of constant ϕ, Figure 6.8 plots the radial dependence of the velocity and density. The contrast with the slow structure in Figure 6.6 is apparent. Note that the back-propagating radiative-acoustic kink is also present in this model, comprising the left edge of the flat-topped velocity peaks. However, since the kink here is a reaction to the forward-steepened shock, it forms within the fast and rarefied upstream region, and thus does not contribute strongly to the Sobolev optical depth of the corotating feature. The high density CIR also does not have an enhanced opacity because of the steep velocity gradients near the shock, as in Model 1. Indeed, Figure 6.7d shows that most of the highest optical depth material comes from the unperturbed wind, and that the high-speed CIR should be mainly a source of *decreased* absorption. The isolated "clumps" of highest optical depth in Figure 6.7d (and in Figure 6.3d) are artifacts of the finite differencing used to compute the radial velocity gradient, and do not significantly affect the volume-integrated quantities used in constructing line profile diagnostics.

The CIR structure in Model 2 appears very similar to that seen in hydrodynamic models of the solar wind, e.g., note the resemblance between Figure 6.8 and Figures 2 and 3 of Hundhausen (1973). The two major differences between solar

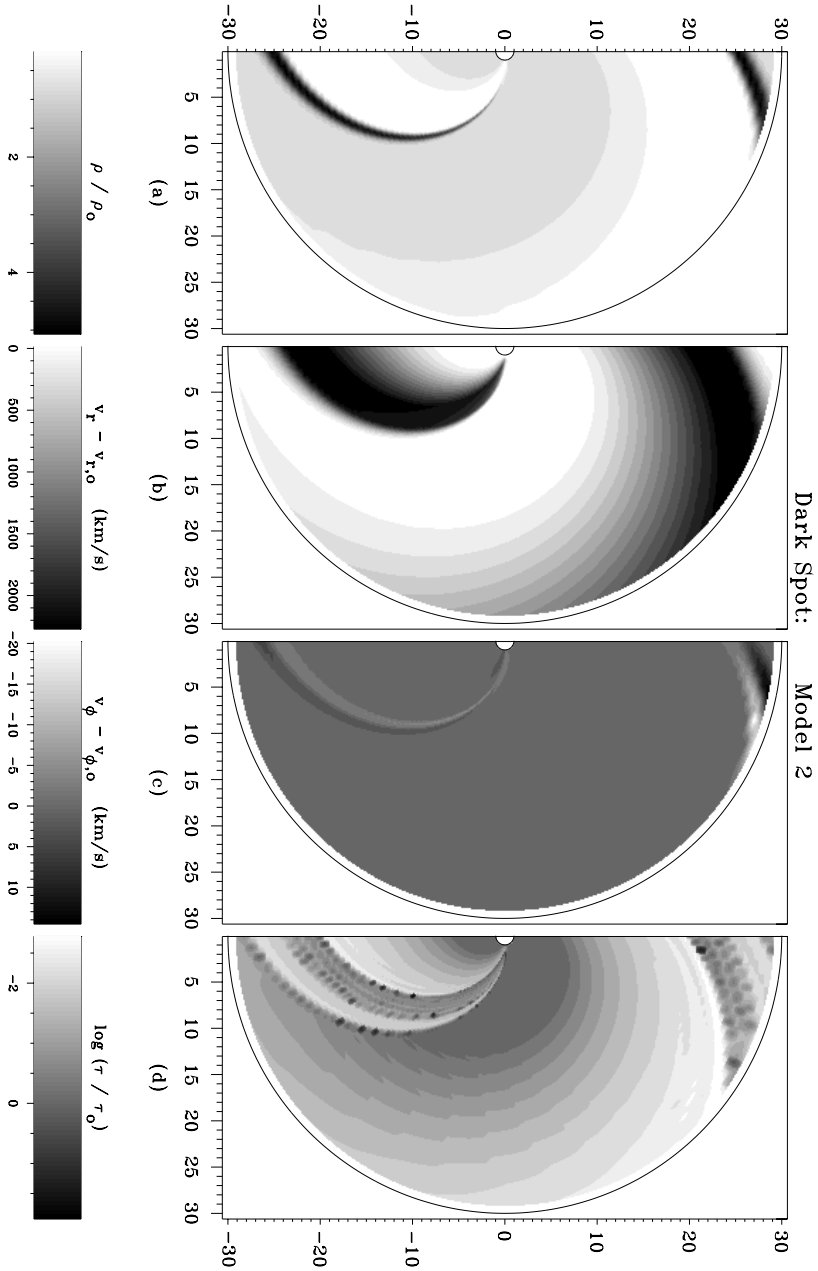

Figure 6.7: As in Figure 6.3, except for Model 2.

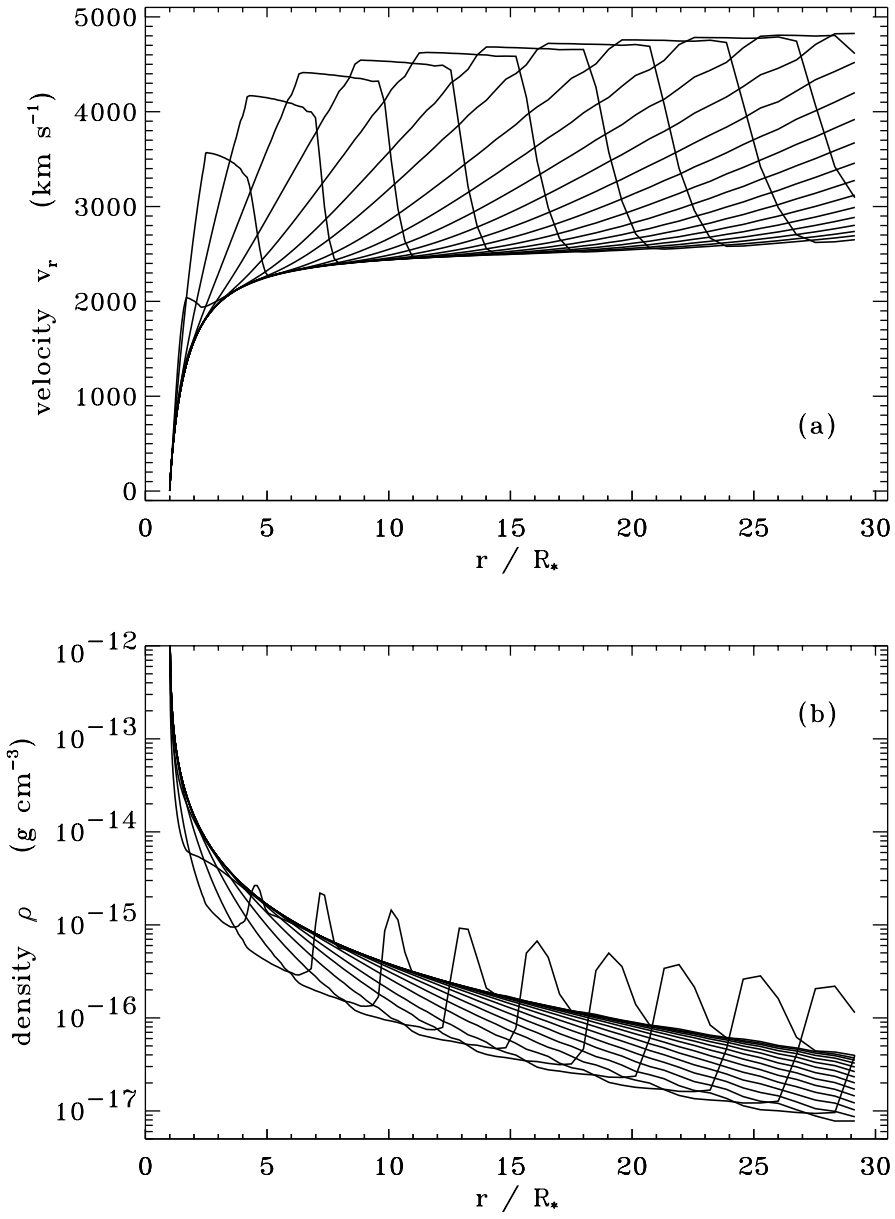

Figure 6.8: As in Figure 6.6, except for Model 2.

wind high-speed streams and those in our model are: (1) the distinct forward and reverse adiabatic shocks in the former and (2) the back-propagating radiative-acoustic kink in the latter. Despite this similarity, all subsequent models in our parameter study use the bright spot of Model 1, which promises to simulate better the slow DACs in early-type stellar winds.

6.2.3 Variation of Spot Amplitude, Width, and Stellar Rotation Velocity

Let us now examine the effect of changing various spot and wind parameters. To provide a basis for understanding the full hydrodynamical calculations, we can estimate the expected effects in terms of a simple wind streakline picture (see Figure 6.4). Note that the shape of these streaklines can be well approximated by neglecting both the wind's acceleration and the angular-momentum-conserving azimuthal velocity, which nearly "cancel each other out" when computing streakline deflection. Thus, the angular deflection is given in this approximation by the Archimedean spiral relation,

$$\phi - \phi_0 \approx -\frac{\Omega}{v_\infty}(r - r_0) \quad . \tag{6.13}$$

Mullan (1984a) used this to estimate the interaction radius r_i between a fast and slow stream initially set apart on the stellar surface by a given azimuthal separation $\Delta\phi$,

$$\frac{r_i}{R_*} = 1 + \frac{\Delta\phi}{V_{\rm eq}}\left(\frac{v_\infty^{(f)} v_\infty^{(s)}}{v_\infty^{(f)} - v_\infty^{(s)}}\right) \quad . \tag{6.14}$$

Here $v_\infty^{(f)}$ and $v_\infty^{(s)}$ are the terminal velocities of the fast and slow streams. Table 6.1 contains this simple prediction for r_i for all the hydrodynamical models in our parameter study. We assume $\Delta\phi = \Phi$, and for bright-spot models, we take the fast stream to be the unperturbed wind, and the slow stream to have $v_\infty^{(s)}$ given by equation (6.9). Conversely, for the dark-spot model the fast stream is given by equation (6.9) and the slow stream is unperturbed wind.

Models 3A, 3B, and 3C vary the spot amplitude A, and thus the direct enhancement in density and velocity over the spot (see Table 6.1). The resulting structure looks qualitatively similar to that of Model 1, but the fast/slow stream interaction takes place at different radii. Figure 6.9 traces the corresponding CIR compression and radiative-acoustic kink features for these models. As expected, CIRs form further out when there is a smaller discrepancy between the fast and slow stream speeds, but the linear minima and maxima in velocity first appear (at r_L) much closer to the star than the simple interaction analysis above predicts. The "nonlinear" radius r_{NL}, where the CIR rarefaction branches off from the prograde

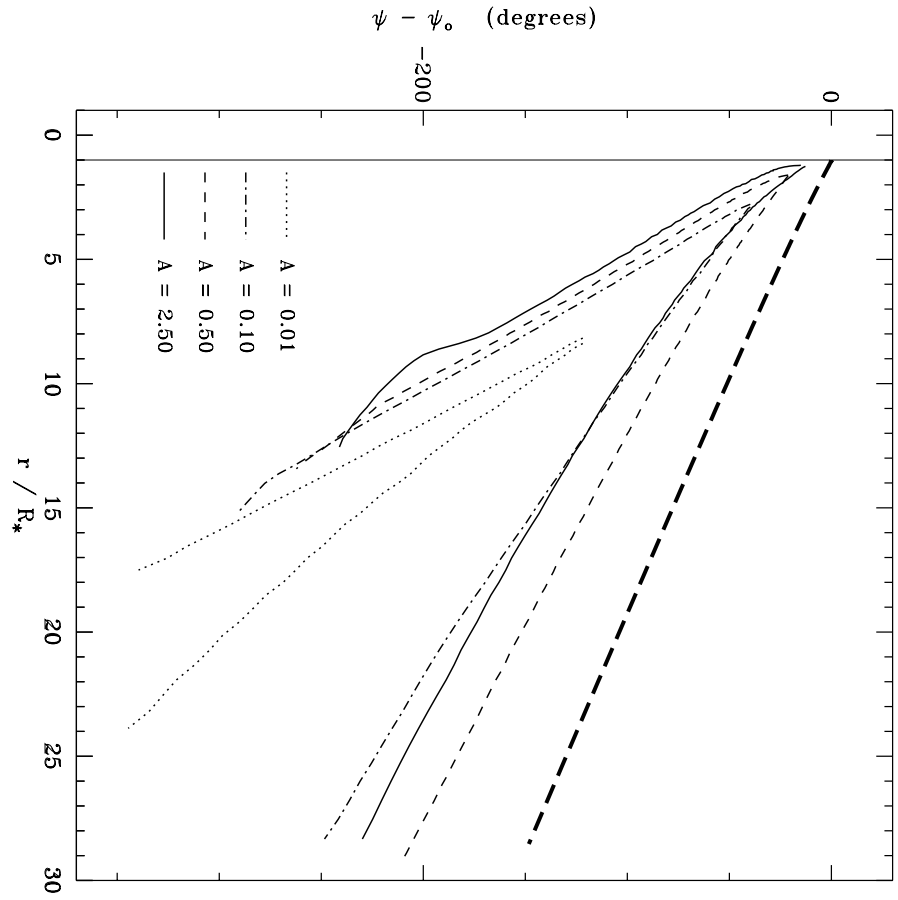

Figure 6.9: Velocity minima and maxima corresponding to CIR compression and radiative-acoustic kink features, shown for Model 1 and variable amplitude Models 3A, 3B, 3C. The heavy dashed line is the streakline for the unperturbed one-dimensional standard model wind.

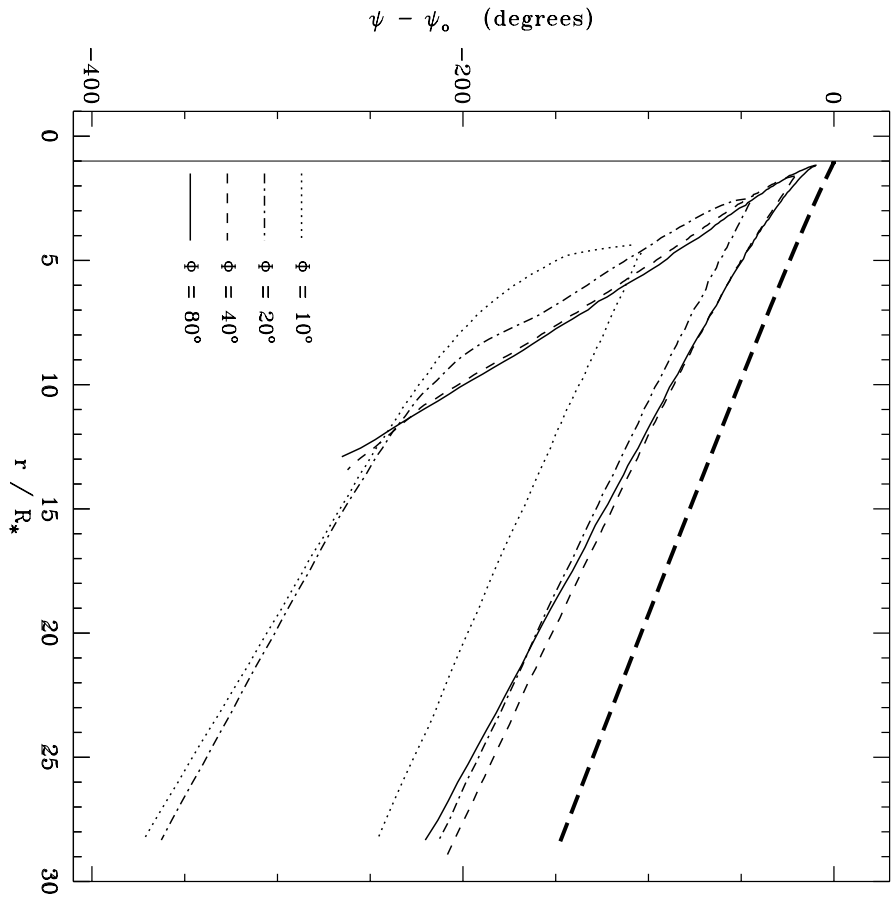

Figure 6.10: As in Figure 6.9, except for Model 1 and variable spot-width Models 4A, 4B, 4C.

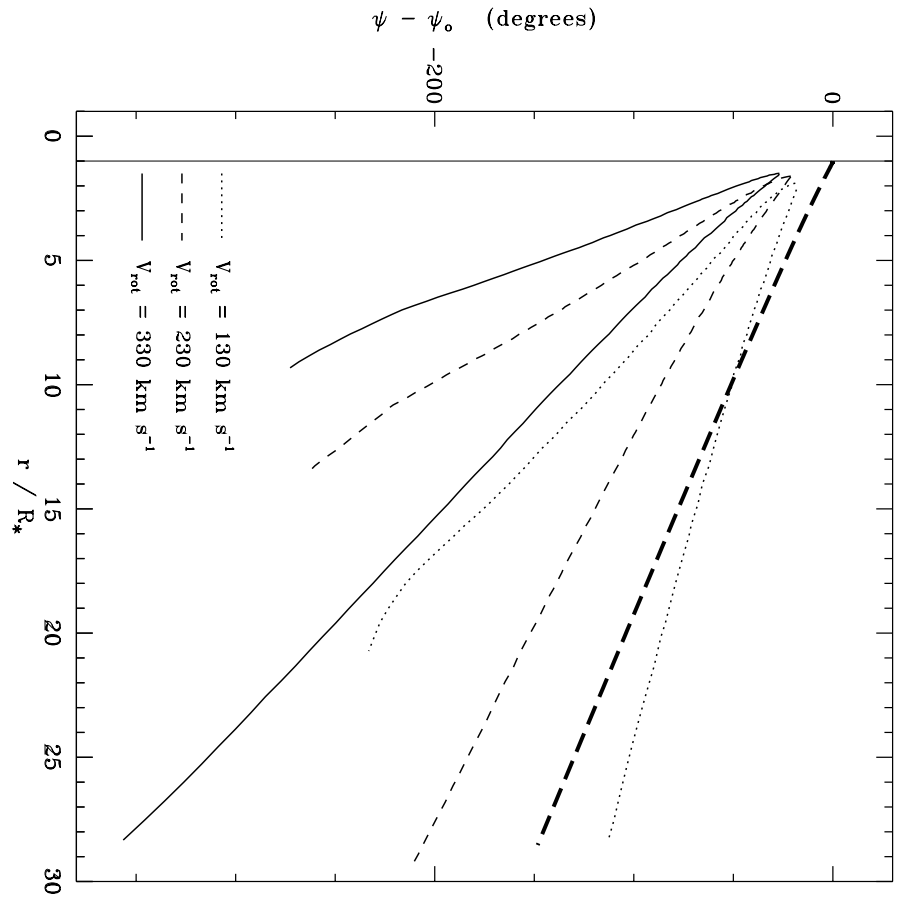

Figure 6.11: As in Figure 6.9, except for Model 1 and variable rotation Models 5A, 5B.

dense precursor, is relatively *constant* with A, indicating a qualitatively different formation mechanism from the compression/kink features.

Figure 6.12 shows how the velocity law of the kink and CIR shock varies with spot amplitude, with each model rotated in azimuth to line up similar features. For the smallest values of A (0.01, 0.1), no shock has yet formed, so both features appear "kink-like," propagating nearer to the slow radiative-acoustic mode speed than to the mean wind speed (see Figure 6.9). The shock steepening is evident for larger values of A, and the most extreme model ($A = 2.50$) shows considerable slowing of the dense CIR resulting from the inverse dependence of the radiative force with density (e.g., eq. [2.88]). Our canonical Model 1 CIR, then, seems just on the verge between both "slowing" mechanisms, as well as having a shape between the low-A weak discontinuities and the high-A shocks. In all cases, however, the decelerating plateau-region ahead of the kink has the same characteristic (negative) acceleration, indicating that the enhanced optical depth at this radius may not vary strongly with spot amplitude.

Models 4A, 4B, and 4C vary the azimuthal spot width Φ, and Figure 6.10 shows their CIR compression and kink features. Increasing or decreasing the full-width Φ simply alters the spatial scale of the interactions, and, in the limit of very small spots (where the star's sphericity can be neglected) the CIR structures seem self-similar with respect to an overall expansion factor. Table 6.1 indicates an inverse relationship between Φ and the maximum CIR density, and this can be understood heuristically by the fact that when a given spot amplitude is spread over a larger area, the collision of fast and slow streams is more diluted, and the resulting shocks are not as strong. Model 4A, with the smallest width $\Phi = 10°$, shows an apparent reversal in this trend, and we suspect that some of the detailed shock structure is under-sampled in our relatively coarse (in this case) azimuthal grid. Note that Mullan's (1984a) interaction radius r_i agrees well with the location of the nonlinear rarefaction/precursor feature r_{NL} for these models.

Observations (Prinja 1988; Henrichs et al. 1988) suggest that the recurrence and acceleration times of DACs tend to vary inversely with the projected equatorial rotation speed, $V_{\rm eq} \sin i$. To examine how well our dynamical models might reproduce these observed trends, Models 5A and 5B vary the equatorial stellar rotation velocity $V_{\rm eq}$. Figure 6.11 shows their CIR compression and kink features. The dominant effects are the overall variation of the spiral streaklines (see, e.g., eq. [6.13]), and the inverse centrifugal dependence of v_∞ on the rotation rate (Friend & Abbott 1986). The strength of the CIR shock decreases for more slowly rotating stars, and we believe that this results from the variation of the streaklines with respect to the star-spot enhancement (Figure 6.1). Perturbed gas which rapidly advects out of the region of direct enhancement receives less of a "boost" of extra density, and thus

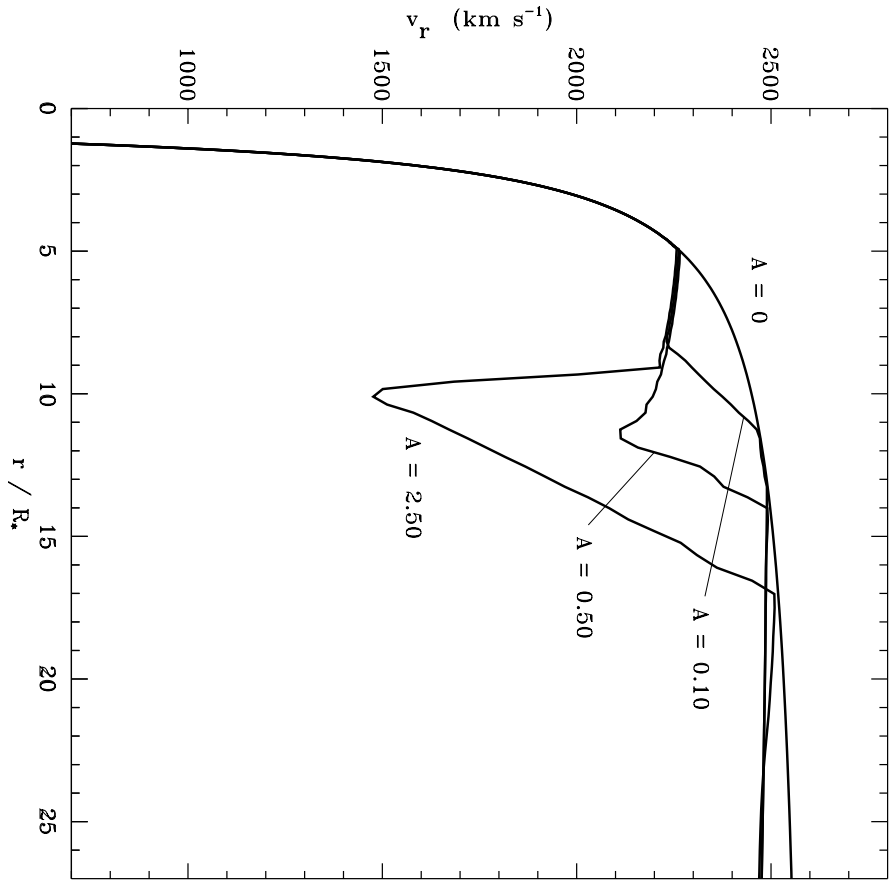

Figure 6.12: Radial velocity showing the radiative-acoustic kink and CIR shock for models with varying spot amplitude. Each ϕ slice was chosen independently to align the initial kink deceleration at the same radius.

does not form as strong a compression when interacting with the ambient wind.

6.3 Synthetic Observational Diagnostics

6.3.1 SEI Line Profile Construction

Ultraviolet P Cygni lines are sensitive probes of the wind structure of hot luminous stars, and it is important to model accurately observed variations in their profile shape. Here we use a multidimensional extension of the SEI (Sobolev with Exact Integration) method of Lamers, Cerruti-Sola, & Perinotto (1987), discussed in Chapter 3, to compute synthetic line profiles. In this method, the source function is calculated locally in the wind using the Sobolev escape probability approximation, and the emergent flux profile is computed by numerically integrating the formal solution to the transfer equation. Bjorkman et al. (1994) discuss a two-dimensional extension of the basic SEI algorithm, and our computational approach is similar in that we do not yet treat the general case of nonlocal (or line doublet) resonance coupling. Our method, however, efficiently computes line profiles from an arbitrary three-dimensional distribution of density and velocity, for observers at arbitrary vantage points.

Following the notation of POF, we parameterize the opacity of a model pure-scattering resonance line by defining a dimensionless line-strength

$$k_L \equiv \left(\frac{\dot{M} v_{\rm th}}{4\pi R_* v_\infty^2} \right) \kappa_L \ , \tag{6.15}$$

where v_∞ and $\dot{M}$ are taken from the unperturbed model wind. We assume the mass absorption coefficient κ_L is constant in radius, which is valid for lines of interest in the dominant ionization stage of the wind, and at least allows qualitative comparison for other lines. We consider two representative cases: a moderate unsaturated line ($k_L = 1$) and a strong saturated line ($k_L = 100$).

The local two-dimensional (solid angle) integrals required to obtain the escape probability and core-penetration probability for the Sobolev source function are computed using Romberg's successive refinement algorithm. The explicit form of these integrals is found in Lamers et al. (1987). POF compare the use of the local Sobolev formalism with a self-consistent multiple-resonance technique in structured wind models, and find significant disagreement in the resulting line profiles. However, our CIR model winds are much less structured than the one-dimensional instability models used by POF, with at most only two zones of nonmonotonic velocity variation in the entire wind. Further, here we concentrate on *residual* line profile variability, which should be less susceptible to consistency errors in the source function than the actual line profile shape.

We perform the "exact integration" for the line flux using a cylindrical (p', ϕ', z') coordinate system with the observer oriented along the positive z'-axis at an infinite distance from the origin. The equation of radiative transfer is evaluated in differential form along rays parallel to this axis, and along each ray the specific intensity is integrated using second order implicit Euler differencing. The resulting emergent intensities at the outer boundary of the computational grid are then integrated by nested Romberg quadrature in p' and ϕ' to form the flux, and this process is repeated for each frequency point in the total line profile. We refer the reader to Lamers et al. (1987) and POF, who summarize these integrals, but only apply them in the spherically symmetric (ϕ' independent) case.

We make two major approximations in our line profile construction technique:

1. The three-dimensional wind structure is formed by interpolating in latitude between the two-dimensional equatorial plane models and the one-dimensional unperturbed polar wind. For simplicity we assume the same Gaussian structure of the "star spots" in latitude as in longitude, and apply it to the entire wind:

$$\begin{aligned} \rho(r,\theta,\phi) &= \rho^{(0)}(r)\,[1 - E(\theta)] + \rho^{(2\mathrm{D})}(r,\phi)\,E(\theta) \\ v_r(r,\theta,\phi) &= v_r^{(0)}(r)\,[1 - E(\theta)] + v_r^{(2\mathrm{D})}(r,\phi)\,E(\theta) \\ v_\phi(r,\theta,\phi) &= v_\phi^{(0)}(r)\,[1 - E(\theta)]\,\sin\theta + v_r^{(2\mathrm{D})}(r,\phi)\,E(\theta)\,\sin\theta \quad , \end{aligned} \tag{6.16}$$

   where $E(\theta) \equiv \exp[-(\pi/2 - \theta)^2/\sigma^2]$ (see eq. [6.2]). As in the two-dimensional models, we retain our assumption that $v_\theta = 0$. Note that the azimuthal velocity has an extra factor of $\sin\theta$ included to preserve angular momentum conservation out of the equatorial plane, and this provides a latitudinal wind variation even for *unperturbed* models.

2. The total Doppler width of the Gaussian line profile contains both thermal and microturbulent contributions,

$$v_D \equiv \sqrt{v_{\mathrm{th}}^2 + v_{\mathrm{turb}}^2} \quad , \tag{6.17}$$

   with the thermal speed set by $v_{\mathrm{th}} = 0.28a$, as appropriate for CNO driving ions. For simplicity, we assume a constant microturbulent velocity $v_{\mathrm{turb}} = 100\,\mathrm{km\ s^{-1}}$, though better line-profile fits have been obtained by assuming this varies in proportion to the mean wind velocity (Haser et al. 1995). Though phenomenological, this use of a microturbulent velocity allows realistic line-profile synthesis with a minimum of free parameters. It also compensates for the suppression here of the small-scale instability, which one-dimensional, nonlocal simulations have shown to result in many of the same observational signatures as microturbulence (POF; Owocki 1994).

6.3.2 Time Variability in Dynamical Models

We produce time-variable P Cygni line spectra by positioning an "observer" in the equatorial plane ($i = 90°$) at successive azimuthal angles ϕ with respect to the two-dimensional models. For the standard rotation velocity used in Models 1, 2, 3, and 4, the line profile variability repeats with a period

$$\Pi = \frac{\pi R_*}{V_{\rm eq}} = 2.091\,{\rm days} \quad . \tag{6.18}$$

Of course, since spiral streakline structures in the models often subtend more then 180° of azimuth, continuous DAC-like signatures can exist for times longer than this period. We arbitrarily define $t = 0$ when the observer is positioned directly over the center of one of the photospheric spot perturbations.

As emphasized by Lamers (1994), we find that most of the line profile variability occurs in the absorption column of the wind ($0 \leq p' \leq R_*$), with comparatively little variation in the larger emission volume ($p' > R_*$). Because the flux integration over this emission volume dominates the CPU time in our SEI line-profile synthesis, we only computed full, variable emission-volume profiles for a few selected test cases, namely for observers at four equally-spaced azimuthal angles ($\phi = 0°, 45°, 90°, 135°$) for Model 1, as well as at one arbitrary azimuthal angle for an unperturbed ϕ-independent wind model. For an unsaturated ($k_L = 1$) line, we found that the perturbations in the absorption-column flux reach as high as 47% of the continuum level, whereas those in emission-volume flux never exceed 1.9%. Since these latter variations would only be marginally observable with IUE signal-to-noise ratios of 20 to 40, we neglect the perturbed emission volume when computing subsequent line profiles on a finer time- and velocity-sampled grid.

Figures 6.13 and 6.14 show the absorption-column line profile variability for Model 1, repeated over three data periods (1.5 rotation periods) to emphasize the rotationally-modulated structure. Following the standard observational convention, the gray-scale is normalized by a "minimum absorption" (maximum flux) template, constructed independently at each line velocity. This choice contains the implicit bias that the variability takes the form of extra *absorption,* which is only partly appropriate for Model 1. The unsaturated ($k_L = 1$) line exhibits definite DACs that apparently accelerate through the profile on ~3.9-day time scales, even though their recurrence time is shorter. The saturated ($k_L = 100$) line exhibits blue-edge variability on the same time scale (see below). Figures 6.13 and 6.14 also contain the time-averaged line profiles for Model 1 and the minimum and maximum absorption templates, which show the extent of the absorption variability at each velocity. We also plot the standard deviation of the data, allowing a qualitative comparison to observed temporal variance spectra.

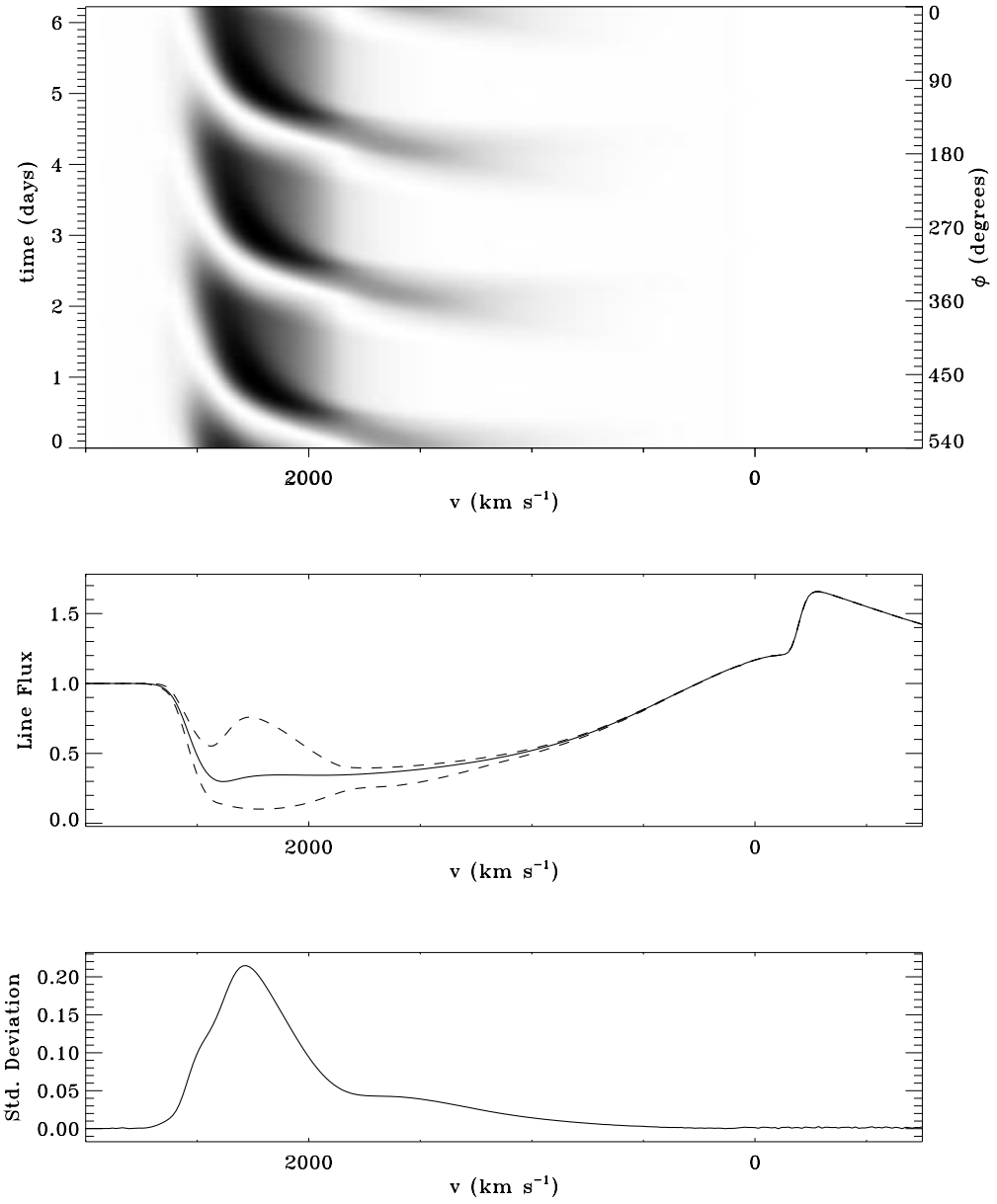

Figure 6.13: SEI absorption-column line variability for Model 1, computed for an unsaturated line. The gray-scale values range from white (maximum flux) to black (minimum flux), measured relative to the dashed-line templates in the middle panel. The solid lines show the time-averaged line profile, in the middle panel, and the standard deviation, or square root of the variance, in the bottom panel.

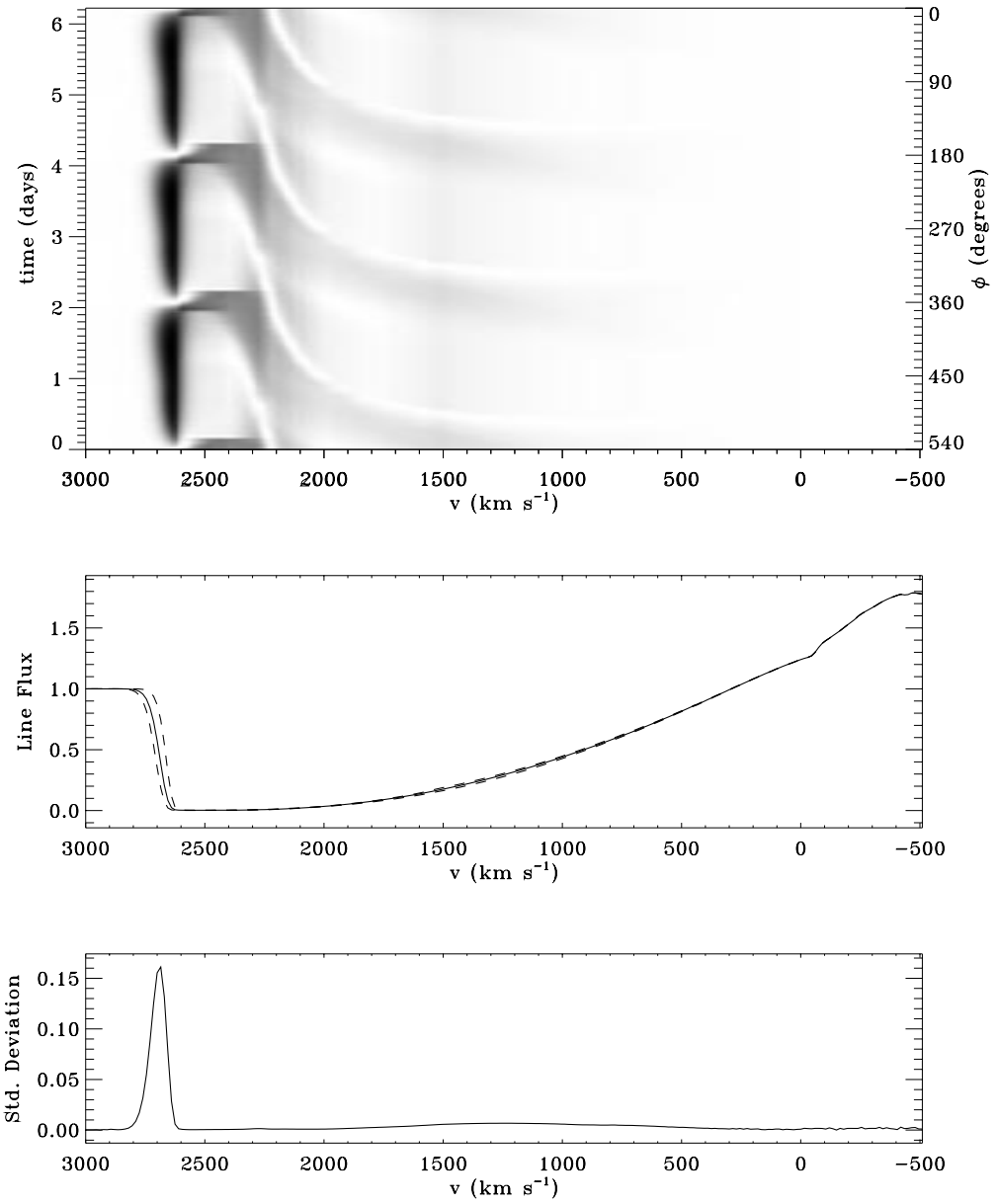

Figure 6.14: As in Figure 6.13, except for a strong saturated line. The gray-scale variability between 1000 and 2550 km/s is deceiving (there is actually *negligible* variability) because of the observational convention of *dividing* by the minimum absorption flux, which here approaches zero.

Figure 6.15 shows the absorption-column line profile variability for Model 2. The accelerating features in this unsaturated ($k_L = 1$) line differ from those in Figure 6.13 in two apparent ways. First, because of the high-velocity stream induced by the dark spot, the variability extends out to nearly 5000 km s^{-1}, almost twice the unperturbed wind terminal speed. Second, the enhanced absorption at lower line velocities ($v \lesssim 2000\,\mathrm{km\ s^{-1}}$) represents the mean state, and the isolated accelerating features appear as a lack of absorption. Although we anticipated this trend in Section 6.2.2, it is surprising to note the overall *similarity* between the bright and dark spot profiles at higher line velocities ($2000\,\mathrm{km\ s^{-1}} \lesssim v \lesssim 2400\,\mathrm{km\ s^{-1}}$). The primary difference here is that the strongest absorption feature trails, in Model 1, and leads, in Model 2, the overall region of enhanced absorption. Far from the star, the near-terminal-speed wind is beginning to laterally homogenize the bright or dark spot perturbations into a simpler pattern of alternating large-scale compressions and rarefactions.

The extreme blue edges of saturated ultraviolet wind lines from hot stars are observed to fluctuate in position and strength (Prinja et al. 1992; Henrichs et al. 1994; Kaper 1993, Chapter 6; Kaper et al. 1996), indicating that variable amounts of rarefied gas exist at velocities in excess of the terminal velocity. In dynamical models of structure in line-driven winds, such high speed rarefactions arise quite naturally from the tendency of the line acceleration to scale inversely with the flow density. One extreme example is the very rarefied, high-speed flows that form from the small-scale instability intrinsic to the line-driving (see, e.g., Owocki et al. 1988; Owocki 1994; Feldmeier 1995). But this also holds for the large-scale structure arising from both the dark and bright spot models computed here. In the case of the dark spot, Model 2, the variation at high velocity is quite extreme, greater than ever observed, and this provides a strong argument against such large-scale dark spots and their associated rarefied high-speed streams in hot-star winds. For the bright-spot models, the blue-edge modulation is more moderate, and generally consistent with the observed variability.

However, observations generally indicate that the velocity of saturated absorption ("v_{black}") remains relatively constant, with most of the variation attributed to changes in the steepness of the blue-edge rise to the continuum (Prinja et al. 1992; also Kaper 1993); in contrast, in the model here, the black velocity exhibits nearly the same variation as the overall edge. This model further predicts a quite distinctive phase correspondence between the maximum extent of the blue edge of saturated lines (Figure 6.14) and the blueward asymptotic extension of DACs in unsaturated lines (Figure 6.13). This seems in qualitative agreement with some of the observational trends noted by Kaper et al. (1996), though in general the relationship among the various types of line-profile variability can be quite complex (Prinja et al. 1992). In particular, the blue-edge, high-velocity variation sometimes

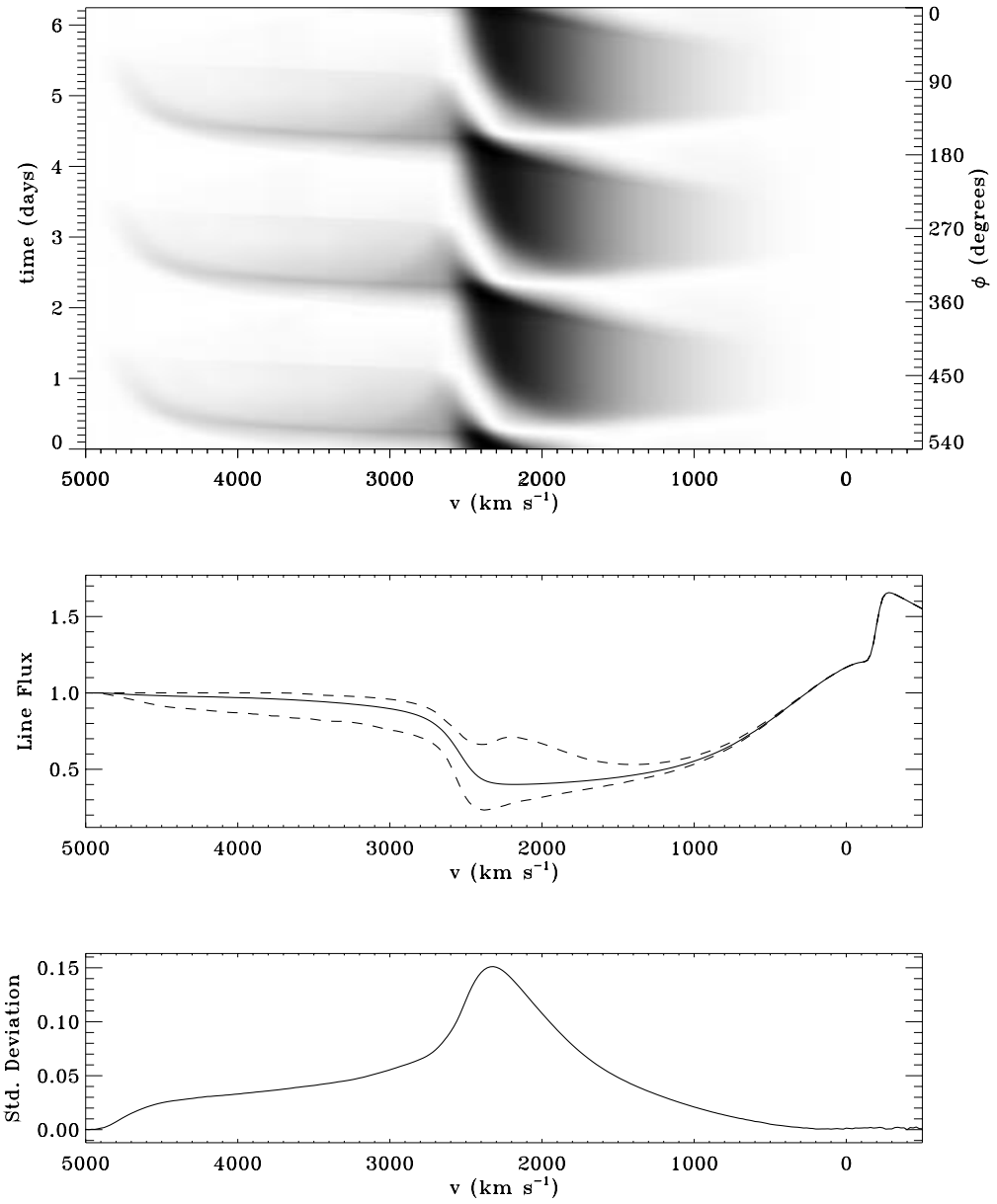

Figure 6.15: As in Figure 6.13, except for Model 2.

shows strikingly close correspondence to the behavior in *low-velocity* line diagnostics (e.g., He II λ4686, Kaper 1993, Chapter 6), and such behavior does not appear to have a clear explanation in the context of the simple CIR models presented here.

In order to interpret more clearly the evolution of DACs in our models, we utilize the observational fitting technique of Henrichs et al. (1983) and Kaper (1993), which represents the DACs as dense, plane-parallel slabs of gas in the observer's line of sight. For each component, the dependence of the quotient flux (normalized by the minimum absorption template) on the line-of-sight velocity v is fit by

$$I(v) \;=\; \exp\left\{-\tau_c \exp\left[-\left(\frac{v - v_c}{v_t}\right)^2\right]\right\} \quad , \tag{6.19}$$

where τ_c is a representative central optical depth, v_c is the line velocity of the center of the DAC, and v_t is related to its width in velocity space. These three parameters are varied and fit to each feature in the time series using Marquardt's χ^2 method (Bevington 1969). Although many of our synthetic DACs are asymmetric about v_c, with slightly more absorption on the low-velocity side of the feature, the fits always reproduce well the overall line shape. One additional useful quantity, the column density of the DAC, is given for our model lines by

$$N_{col} \;=\; \frac{\sqrt{\pi}}{\kappa_L v_{\rm th} \langle m \rangle} \frac{\tau_c v_t}{(1 + v_c/c)} \quad , \tag{6.20}$$

where $\langle m \rangle$ is the mean mass of gas atoms and ions (see POF and Kaper 1993).

In Figures 6.16, 6.17, and 6.18 we plot the resulting fit parameters (v_c, v_t, N_{col}) as a function of time for the bright-spot, unsaturated-line models in the parameter study. The inherent "overlap" in the time series (i.e., multiple DACs at a given time) has been removed to more clearly show the evolution of the individual DAC. As is often seen in observed line profile variability, the feature accelerates through the line profile while growing progressively narrower, its column density increasing to a maximum value, then decreasing as the DAC nears its terminal velocity. In our models, v_c often reaches or exceeds the wind's unperturbed v_∞, but the rapidly dropping values of N_{col} (which also is related to the equivalent width of the DAC) might preclude actual observation of this final period of evolution. In fact, most of the DACs we track seem to approach an initial "pseudo terminal speed" ($\sim$ 0.8-0.9 v_∞) while the column density is at its peak, then accelerate further to the wind's terminal speed as the column density decreases.

As expected, the DACs produced by radiative-acoustic kinks accelerate quite slowly. Figure 6.18 compares the acceleration of DACs from Models 1, 5A, and

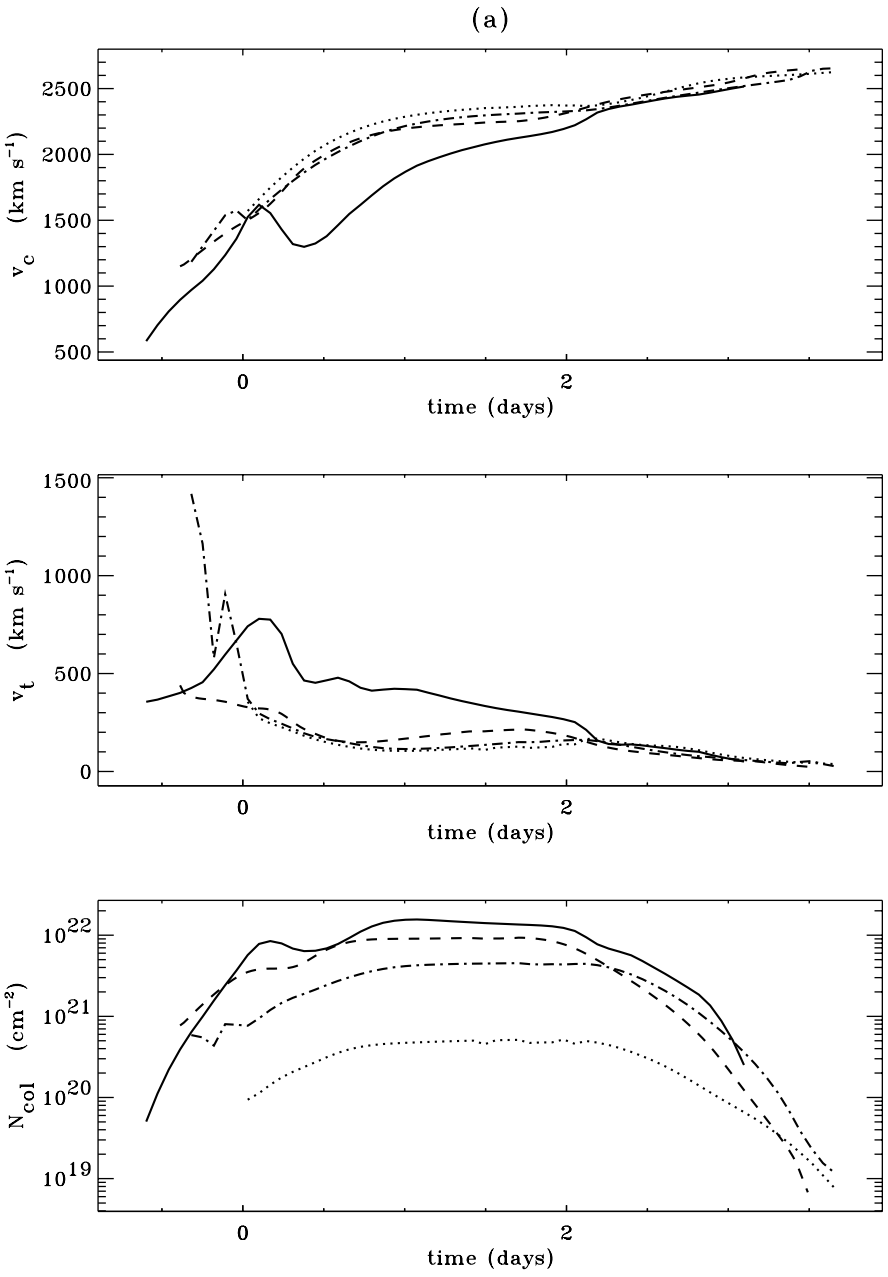

Figure 6.16: Best-fit DAC features: central line velocity, characteristic width, and slab-model column depth, shown for Model 1 and variable amplitude Models 3A, 3B, 3C. Here we plot the DAC from only a *single* stream structure, so as not to clutter the plot with multiple DACs at a given time. The line styles for each set of models are identical to those in Figure 6.9.

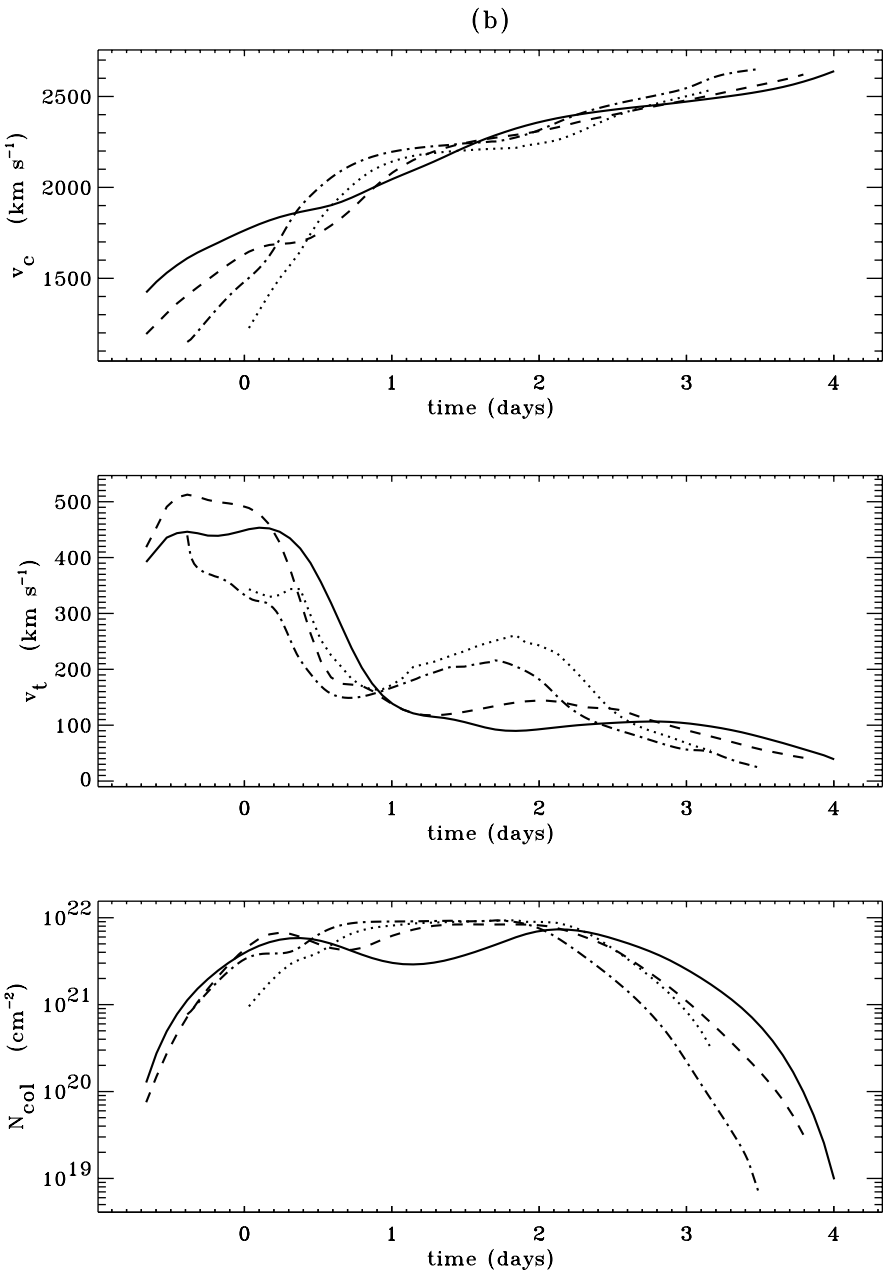

Figure 6.17: As in Figure 6.16, except for Model 1 and variable spot-width Models 4A, 4B, 4C. The line styles correspond to those in Figure 6.10.

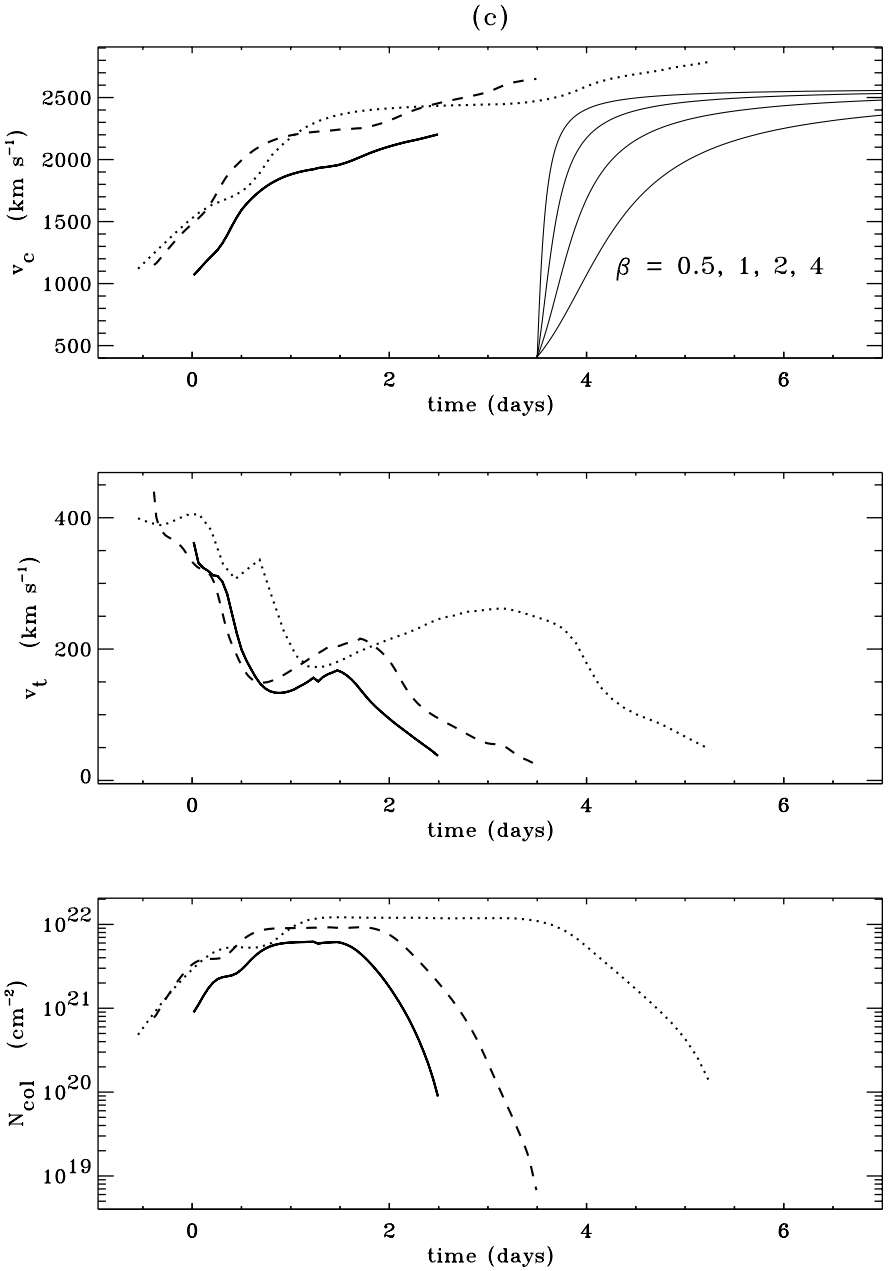

Figure 6.18: As in Figure 6.16, except for Model 1 and variable rotation Models 5A, 5B. The line styles correspond to those in Figure 6.11.

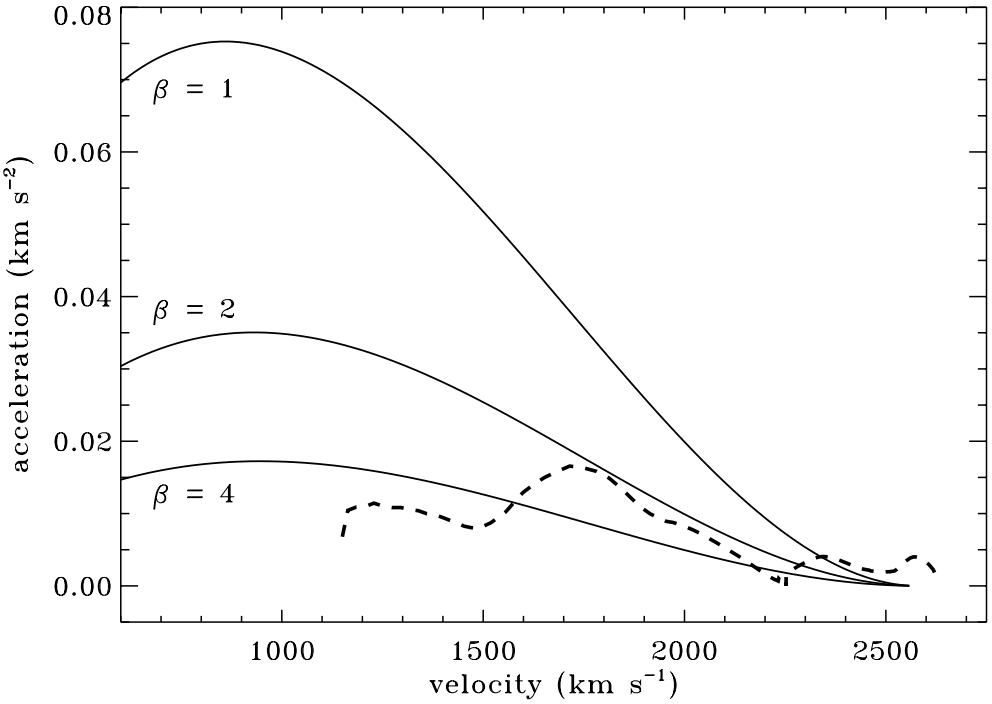

Figure 6.19: DAC acceleration versus velocity for Model 1 (dashed line) and analytic "beta" velocity laws (solid lines).

5B with several analytic "beta" velocity laws. We compute $v(t)$ by numerically integrating the kinematic relation

$$t = t(r[v]) = \int_{R_*}^{r} \frac{dr'}{v_0 + (v_\infty - v_0)(1 - R_*/r')^\beta} \ , \tag{6.21}$$

where we take $v_0 = a$ and $v_\infty = 2580\,\mathrm{km\ s^{-1}}$. The slow acceleration of the DACs is equivalent to $\beta \approx 2 - 4$, which agrees with the observations of Prinja et al. (1992) and Prinja (1994). Note, however, that an estimation of a single characteristic β for a DAC is problematic, since (1) its terminal speed is not clearly defined, and (2) $v_c(t)$ experiences several minor acceleration and deceleration episodes superimposed on the overall DAC acceleration. Figure 6.19 plots acceleration versus velocity for the DAC of Model 1, and compares it to the beta laws defined above. The small-scale irregularity at velocities greater than about $2200\,\mathrm{km\ s^{-1}}$ is likely due to numerical errors in computing the acceleration $\partial v_c/\partial t$ from velocities on a finite grid of "observation times." The nonmonotonicity in Figure 6.19 at velocities less than $2200\,\mathrm{km\ s^{-1}}$ reflect the fact that the kink structures are dynamically quite complicated, with varying line-of-sight velocity behavior at different radii and viewing angles. Thus the apparent acceleration of DACs is not fit very well with simple "beta" velocity law. Indeed, in both magnitude and nonmonotonic character, the apparent accelerations here are actually quite similar to those in actual DAC observations, e.g., those found by Prinja et al. (1992) in the wind of ζ Puppis.

6.3.3 Continuum Polarization Variations

Figure 6.20 shows optically-thin electron-scattering polarization from the standard (bright spot) Model 1, computed by integrating over the solid angle subtended by a uniformly-bright (non-spotted) spherical star. The equatorial density variations have been extended to other latitudes as described in eq. (6.16) above, and the polarization for observers at different latitudes (i.e., inclinations) and longitudes (i.e., phases) has been calculated. As in previous plots, time decreases as phase increases. For equator-on ($i = 90°$) views, all polarization is in the Q-plane, and the variation in magnitude is nearly sinusoidal. The extrema occur when the bases of the CIR density compressions, not the direct spot enhancements, are facing the observer (minima in P) and are in the plane of the sky (maxima in P). Fore pole-on ($i = 0°$) views, the magnitude of the polarization does not vary in time, but a circular pattern in the Q-U plane is traversed twice per rotation period. The reasonably strong ($\sim$0.1%) polarization from CIRs here may be conflated with polarization from other sources, e.g., wind compressed disks (see Harries & Howarth 1996). However, most stars exhibiting DACs are thought to be viewed nearly equator-on, and the strongly time-variable polarization computed here can be easily separated from a persistent and non-variable rotational component.

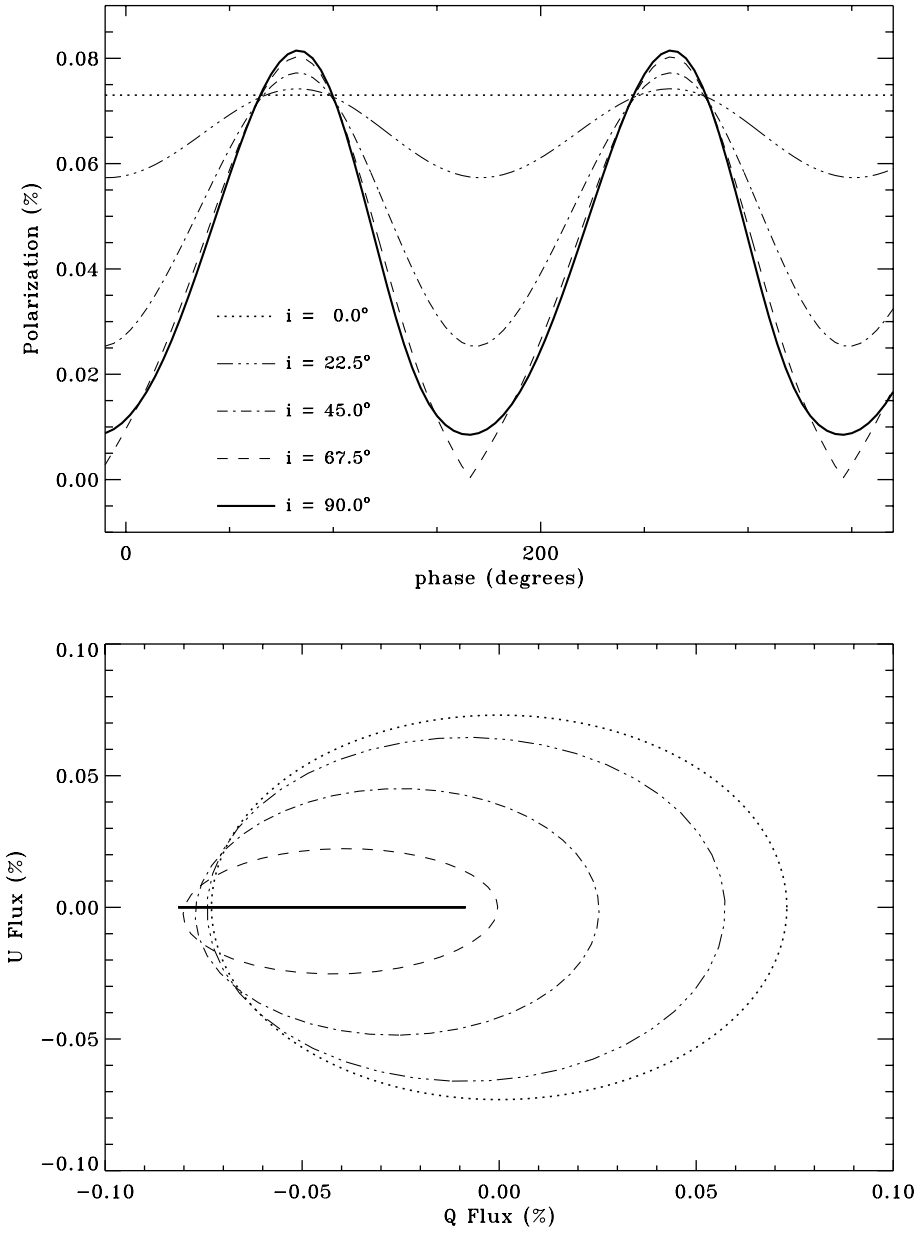

Figure 6.20: The upper plot shows the magnitude of polarization P varying with azimuthal phase, for observers at $i = 0, 22.5, 45, 67.5$, and 90 degrees. The lower plot shows the individual Q and U variations over one full cycle, or 180 degrees of phase.

6.4 Summary, Conclusions, and Future Work

We have carried out two-dimensional hydrodynamical simulations of an azimuthally inhomogeneous radiation-driven wind from a rotating O star. The wind responds to a photospheric radiative force enhancement by forming large-scale corotating structures extending far beyond the region of direct perturbation. Although classical CIR compressions and rarefactions are often seen, the most important structures observationally are slowly-propagating radiative-acoustic kinks or plateaus which have a large Sobolev optical depth. These plateaus show up as strong DACs when formed behind streams resulting from *enhanced mass loss,* and they accelerate at a slower rate than the wind passes through them. Although further calculations will be needed, it seems likely that most possible wind perturbation mechanisms (e.g., localized magnetic "helmet streamers" or steepened nonradial gravo-acoustic oscillations from the photosphere) would also involve similar strong variations in mass flux. Thus, while the spot models computed here may be of limited direct applicability, they provide a useful first basis for analyzing the dynamical and observational characteristics of any such large-scale wind structure associated with mass flux modulations.

Preliminary P Cygni line profile synthesis has shown several important trends in the emergent DACs from these model structures:

1. The slow acceleration of DAC features is fit reasonably well by $\beta \approx 2 - 4$, and we find no significant correlation between their acceleration time scale and the star's rotation velocity. Of course, since the CIRs in our models are linked to the rotating surface, there is a definite correlation between the *recurrence* time scale of DACs and $V_{\rm eq}$.

2. Despite minor variations, the DAC parameters v_c and v_t do not depend strongly on the amplitude A or full width Φ of the model spot perturbation. The primary exception is the high-amplitude Model 3C ($A = 2.50$) which accelerates much more slowly due to the higher density in the CIR shock.

3. The optical depth τ_c and column density N_{col} seem to be sensitive probes of the amplitude of the initial surface perturbation (see Figure 6.16, bottom panel). The concavity of N_{col} during the strongest period of DAC evolution may be able to provide information about the azimuthal size of the perturbation, but this is not as clearly observable an effect (see Figure 6.17, bottom panel).

Let us now compare our model results with actual observations of large-scale wind structure. In many cases both (1) slow and quasi-episodic DACs and (2) faster periodic modulations are seen simultaneously in OB-star winds (Kaper 1993; Massa

et al. 1995). As seen above, the first type of variation can be readily reproduced by the CIR and radiative-acoustic plateau that results from an azimuthally localized mass-loss enhancement. Though our models assume strict rotational periodicity, such DACs could also be readily caused by *transient* CIRs for which the surface mass loss "eruption" lasts long enough to make structure that covers a substantial portion of the stellar disk. The second type of structure observed in OB winds (fast, near-sinusoidal flux variations accelerating *with* the wind) is more difficult to produce with a CIR model, because the required optical depth or density variations disrupt the mean wind velocity streaklines. To explain these faster modulations, we intend to investigate models in which wind structure is induced by nonradial pulsation (NRP) of the underlying star (Owocki, Cranmer, & Fullerton 1995).

The success here in reproducing realistic DACs suggests that the CIR model warrants further study and development. One important extension will be to use a more complete radiative force that incorporates the line-driven instability. The resulting stochastic variations may disrupt the large-scale CIR structure, but slowly evolving kink-like plateaus have been seen to survive and propagate in various one-dimensional instability simulations (Fullerton & Owocki 1992; Owocki, Fullerton, & Puls 1994). In addition, extending the present models to three dimensions may shed light on the variability of wind-compressed disks and other latitudinally-varying structures in, e.g., Be-star winds. Finally, it will be important to develop techniques to synthesize other observational diagnostics, such as subordinate-level ultraviolet and optical lines, infrared photometry, and continuum and line polarization, which will allow further constraints on models of wind variability. The resulting phenomenological "atlas" would provide a solid basis for interpreting the great diversity of OB-star wind variability observations in terms of fundamental, dynamical models of time-dependent wind structure.

Chapter 7

PULSATIONS, WAVES, AND DISCONTINUITIES IN STELLAR WINDS

Wave after wave
Will flow with the tide
And bury the world as it does
Tide after tide
Will flow and recede
Leaving life to go on
As it was.

Neil Peart, *Natural Science*

Hot luminous stars (spectral types O, B, Wolf-Rayet) are observed to have strong stellar winds which exhibit variability on time scales ranging from hours to years. Many classes of these stars are also seen, via photospheric line-profile or photometric variability, to pulsate radially or nonradially. It has been suspected for some time that these oscillations can induce periodic modulations in the surrounding stellar wind and produce observational signatures in, e.g., ultraviolet P Cygni line profiles. This Chapter outlines a dynamical foundation for understanding the propagation of stellar pulsations into an accelerating wind, and presents initial observational predictions and constraints for various types of stars.

Section 7.1 contains an overview of the theory of nonradial pulsations (NRPs) of stars, with a description of how the *discrete* spectrum of small-amplitude oscillation modes ("standing waves") may be observable from the photosphere. Section 7.2 presents a parallel derivation of linear wave theory, with emphasis on the *continuous*

spectrum of possible oscillations ("traveling waves") in the photosphere and accelerating wind. This work represents a preliminary attempt to bridge the gap between interior pulsations and propagating wind structure. Finally, Section 7.3 examines the nonlinear steepening of finite-amplitude waves and the resulting discontinuities and "kinks" that may develop in stellar winds.

7.1 Global Stellar Pulsation

There exist several classes of early-type stars which are inferred to pulsate strongly enough to be detected either photometrically or via line profile variations. The β Cep variables (spectral types $\sim$ B0 to B3) and the "slowly pulsating B stars" (SPBs) or 53 Per variables (spectral types $\sim$ B3 to B9) have recently been explained in terms of the standard Cepheid opacity instability mechanism (Dziembowski 1994), which leads to strong spontaneous pulsation. Many classical Be stars have been observed to pulsate, and Kambe et al. (1993) has found a correlation between circumstellar emission episodes and increased NRP amplitudes. O and B supergiants exhibit complex variability on many time scales, and it is difficult to isolate clear signatures of pulsation, rotational modulation, or intrinsic wind activity (Fullerton 1990; Kaper 1993; Fullerton, Gies, & Bolton 1996). Let us begin to disentangle these effects by examining the theory of NRP in stellar interiors, and hopefully the mass motions of the underlying star can act as a "seed" for photospheric and wind variability.

7.1.1 Linearized Hydrodynamic Equations

For the equilibrium state, let us assume a spherical non-rotating star, with density ρ_o, pressure P_o, and temperature T_o functions of radius only. Also, let us take the equilibrium fluid velocity $\mathbf{v}_o$ to be identically zero everywhere inside the star. Following Cox (1980) and Unno et al. (1979), we can define the Lagrangian displacement vector

$$\boldsymbol{\xi} \equiv \delta\mathbf{r} = \mathbf{r}(t) - \mathbf{r}_o = (\delta r)\hat{\mathbf{e}}_r + (r\,\delta\theta)\hat{\mathbf{e}}_\theta + (r\sin\theta\,\delta\phi)\hat{\mathbf{e}}_\phi \ , \tag{7.1}$$

as the instantaneous spatial departure from equilibrium. Let us denote equilibrium quantities as f_o, their Eulerian (fixed in space) variations as f', and their Lagrangian (moving with the fluid) variations as δf. To first order accuracy, the Lagrangian and Eulerian perturbations in *velocity* are equivalent, and

$$\mathbf{v}' = \delta\mathbf{v} = \mathbf{v}(t) - \mathbf{v}_o = \mathbf{v}(t) = \frac{d\boldsymbol{\xi}}{dt} = \frac{\partial\boldsymbol{\xi}}{\partial t} \ . \tag{7.2}$$

For other fluid quantities, however, the Lagrangian and Eulerian variations are not equivalent. To first order, for a scalar quantity f,

$$\delta f \;=\; f' + \boldsymbol{\xi}\cdot\nabla f_o \;\;. \tag{7.3}$$

The linearly perturbed equations of hydrodynamics can be written as follows. (See Section 7.2 for a more in-depth explanation of the linearization of the fluid equations.) In Eulerian form, the linearized mass continuity equation (noting that $\mathbf{v}' = \delta\mathbf{v} = \mathbf{v}$) is

$$\frac{\partial\rho'}{\partial t} + \nabla\cdot(\rho_o\mathbf{v}) \;=\; 0 \;\;. \tag{7.4}$$

However, using equations (7.2) and (7.3) above, integrating with respect to time, and expressing the result in Lagrangian form, we obtain the more useful form

$$\delta\rho + \rho_o\nabla\cdot\boldsymbol{\xi} \;=\; 0 \;\;. \tag{7.5}$$

The vector momentum equation is given in Eulerian form as

$$\frac{\partial\mathbf{v}}{\partial t} \;=\; \frac{\rho'}{\rho_o^2}\nabla P_o - \frac{1}{\rho_o}\nabla P' + \mathbf{g}' \;\;, \tag{7.6}$$

and in Lagrangian form as

$$\frac{d^2\boldsymbol{\xi}}{dt^2} \;=\; -\delta\left(\frac{\nabla P}{\rho}\right) + \delta\mathbf{g} \;\;, \tag{7.7}$$

where $\mathbf{g}$ is the general external acceleration (often assumed due to gravity only). Both forms of the momentum equation will be useful later.

Because we will eventually be concerned with only *adiabatic* (isentropic) variations, the equation of energy conservation can be solved by two particularly simple solutions which express, e.g., the pressure and temperature perturbations in terms of the density perturbation. Defining the adiabatic exponents,

$$\Gamma_1 \equiv \left(\frac{d\ln P}{d\ln\rho}\right)_{ad} \;\;, \qquad \Gamma_3 - 1 \equiv \left(\frac{d\ln T}{d\ln\rho}\right)_{ad} \;\;, \tag{7.8}$$

$$\frac{\Gamma_2 - 1}{\Gamma_2} \equiv \left(\frac{d\ln T}{d\ln P}\right)_{ad} = \frac{\Gamma_3 - 1}{\Gamma_1} = \nabla_{ad} \;\;, \tag{7.9}$$

the adiabatic energy relations can be expressed in terms of the thermodynamic identities,

$$\frac{\delta P}{P_o} \;=\; \Gamma_1\frac{\delta\rho}{\rho_o} \;\;, \qquad \frac{\delta T}{T_o} \;=\; (\Gamma_3 - 1)\frac{\delta\rho}{\rho_o} \;\;, \tag{7.10}$$

where the adiabatic exponents $,_1$ and $,_3$ are assumed unperturbed. Isothermal variations can be modeled by setting $,_1 = ,_2 = ,_3 = 1$, but this is not applicable in the stellar interior (see Section 7.2 for the differences between an isothermal *mean state* and isothermal *variations*).

Finally, the Eulerian momentum equation can be re-written in terms of a smaller number of perturbed variables (which will be useful when finding solutions). Cox (1980) derives the following form, using equations (7.5) and (7.10):

$$\frac{d^2\boldsymbol{\xi}}{dt^2} \;=\; -\nabla\chi + \mathbf{A}\frac{,_1 P_o}{\rho_o}\left(\nabla\cdot\boldsymbol{\xi}\right) \quad , \tag{7.11}$$

where

$$\chi \;\equiv\; \frac{P'}{\rho_o} + \psi' \;, \qquad \mathbf{A} \;\equiv\; \frac{\nabla\rho_o}{\rho_o} - \frac{\nabla P_o}{,_1 P_o} \;, \tag{7.12}$$

and ψ' is the perturbed gravitational potential ($\mathbf{g} = -\nabla\psi$). Cox mentions that the above momentum equation is true for a spherical equilibrium condition, but it is also valid for any equilibrium configuration which obeys

$$\left(\boldsymbol{\xi}\cdot\nabla\rho_o\right)\nabla P_o \;=\; \left(\boldsymbol{\xi}\cdot\nabla P_o\right)\nabla\rho_o \;. \tag{7.13}$$

In some cases of rotating *barotropic* stars, where $\mathbf{g}$ is derivable from a potential and the pressure and density surfaces coincide, this relation can hold as well.

The vector $\mathbf{A}$, sometimes called the "Schwarzschild discriminant," has only a radial component $A_r\hat{\mathbf{e}}_r$ for a spherical equilibrium model. This variable represents a convective stability criterion, because the effective buoyant force (per unit volume) of a small density parcel in a radially stratified fluid is

$$f_B \;=\; -g\Delta\rho(r) \;=\; -\rho_o g A_r \delta r \;, \tag{7.14}$$

where $\Delta\rho$ is the difference between the parcel density and the density of its surroundings. Thus, if $A > 0$, the fluid is convectively *unstable*, and if $A < 0$, the fluid is convectively *stable*, and oscillates with the Brunt-Väisälä frequency ω_{BV} (see Section 7.2.5), where

$$\omega_{BV}^2 \;=\; -A_r g \;. \tag{7.15}$$

7.1.2 Simple Oscillatory Solutions

If we make the standard assumption that all perturbation variables vary in time only sinusoidally, as $e^{i\omega t}$, the three components of the momentum equation can be expressed as

$$\omega^2\xi_r \;=\; \frac{\partial\chi}{\partial r} + A_r\frac{,_1 P_o}{\rho_o}\left(\frac{\delta\rho}{\rho_o}\right) \tag{7.16}$$

$$\omega^2 \xi_\theta = \frac{1}{r}\frac{\partial \chi}{\partial \theta} \tag{7.17}$$

$$\omega^2 \xi_\phi = \frac{1}{r \sin\theta}\frac{\partial \chi}{\partial \phi} \ . \tag{7.18}$$

Using the expressions for ξ_θ and ξ_ϕ, the divergence of $\boldsymbol{\xi}$ can be easily represented as

$$\nabla \cdot \boldsymbol{\xi} = \frac{1}{r^2}\frac{\partial}{\partial r}\left(r^2 \xi_r\right) - \frac{1}{\omega^2 r^2}\mathcal{L}^2 \chi \ , \tag{7.19}$$

where the operator $\mathcal{L}^2$ is defined by Cox (1980) to be

$$\mathcal{L}^2 \equiv -\frac{1}{\sin\theta}\frac{\partial}{\partial \theta}\left(\sin\theta \frac{\partial}{\partial \theta}\right) - \frac{1}{\sin^2\theta}\frac{\partial^2}{\partial \phi^2} \ . \tag{7.20}$$

This operator is a familiar one: its eigenfunctions are the spherical harmonics $Y_{\ell m}$, and its eigenvalue equation is

$$\mathcal{L}^2 Y_{\ell m}(\theta, \phi) = \ell(\ell+1) Y_{\ell m}(\theta, \phi) \ , \tag{7.21}$$

where $\ell = 0, 1, 2, \ldots$; $m = -\ell, -\ell+1, \ldots, \ell-1, \ell$. The azimuthal mode number, m, denotes the number of pulsational minima or maxima around a chosen equator, while the meridional degree, ℓ, describes the latitudinal variation of the pulsational amplitude. Specifically, there are $(\ell - |m|)$ nodes between the north and south poles of a star, and the poles are always nodes. We will assume that all perturbation variables can be *separated* into a product of a radial eigenfunction and a spherical harmonic function. The frequency ω thus becomes an eigenvalue of the problem, with each solution for ω corresponding to a solution for the radial eigenfunction.

In general, there are two classes of oscillatory solutions to the linearly perturbed momentum equation. These can be seen by examining the r-component of the curl of the momentum equation (i.e., the "vorticity" equation)

$$\omega^2 \left(\nabla \times \boldsymbol{\xi}\right)_r = 0 \tag{7.22}$$

(the $\mathbf{g}'$ term vanished because it can be written as a gradient of a scalar potential). Thus, if $\omega^2 = 0$, we can solve for the so-called *"toroidal"* modes, and if $(\nabla \times \boldsymbol{\xi})_r = 0$, we can solve for the *"spheroidal"* modes. Both types of modes, taken together, make up the complete set of solutions to the momentum equation. For spherical, non-rotating stars, the toroidal modes are obviously non-oscillatory, but in rotating stars they have non-vanishing frequencies (see Section 7.1.5, below). For **spheroidal** modes,

$$\left(\nabla \times \boldsymbol{\xi}\right)_r = \frac{\partial}{\partial \theta}\left(r \sin\theta \, \xi_\phi\right) - \frac{\partial}{\partial \phi}\left(r \xi_\theta\right) = 0 \ , \tag{7.23}$$

and this will provide a constraint on the angular variation of ξ_θ and ξ_ϕ. The Lagrangian displacement $\boldsymbol{\xi}$ can be separated into "vertical" (radial) and "horizontal" (tangential) components, each separable into radial and spherical harmonic eigenfunctions:

$$\boldsymbol{\xi} \;=\; \xi_r \hat{\mathbf{e}}_r + \xi_h \hat{\mathbf{e}}_h \;\;, \tag{7.24}$$

where

$$\xi_r(r,\theta,\phi) \;=\; \frac{u_\ell(r)}{r^2} Y_{\ell m}(\theta,\phi) \tag{7.25}$$

$$\xi_h(r,\theta,\phi) \;=\; \frac{v_\ell(r)}{r} Y_{\ell m}(\theta,\phi) \;\;, \tag{7.26}$$

and the radial eigenfunctions u_ℓ and v_ℓ are also dependent on the eigenvalue ω. In order to separate ξ_h into its horizontal components in the θ and ϕ directions, we note that $\boldsymbol{\xi}$ is the sum of a gradient of a scalar (χ) and a purely radial vector. In this case, ξ_θ and ξ_ϕ are given simply by angular derivatives of ξ_h, and Cox gives

$$\xi_\theta \;=\; \frac{\partial \xi_h}{\partial \theta} \;\;, \qquad \xi_\phi \;=\; \frac{1}{\sin\theta} \frac{\partial \xi_h}{\partial \phi} \;\;, \tag{7.27}$$

and the tangential (non-unit) direction vector is given by

$$\hat{\mathbf{e}}_h \;=\; \left(\frac{1}{Y_{\ell m}} \frac{\partial Y_{\ell m}}{\partial \theta} \right) \hat{\mathbf{e}}_\theta + \left(\frac{1}{Y_{\ell m} \sin\theta} \frac{\partial Y_{\ell m}}{\partial \phi} \right) \hat{\mathbf{e}}_\phi \;\;. \tag{7.28}$$

Note that ξ_θ and ξ_ϕ uniquely satisfy the spheroidal mode constraint given above in equation (7.23).

In addition, we can also now write

$$\nabla \cdot \boldsymbol{\xi} \;=\; \frac{1}{r^2} \frac{\partial}{\partial r} \left(r^2 \xi_r \right) - \frac{\ell(\ell+1)}{r} \xi_h \;\;, \tag{7.29}$$

and comparison with equation (7.19) provides the useful relation

$$\xi_h \;=\; \frac{\chi}{\omega^2 r} \;\;, \tag{7.30}$$

which will be utilized below when we attempt to constrain $u_\ell(r)$, $v_\ell(r)$, and the pressure perturbation δP, all in terms of one (unfortunately arbitrary) surface amplitude.

Correspondingly, the **toroidal** set of solutions, with $\omega^2 = 0$ and $\xi_r = 0$ for non-rotating systems, are given by the alternate set of angular derivatives of a horizontal displacement,

$$\xi_\theta \;=\; \frac{T_{\ell m}(r)}{r \sin\theta} \frac{\partial Y_{\ell m}}{\partial \phi} \tag{7.31}$$

$$\xi_\phi \;=\; -\frac{T_{\ell m}(r)}{r} \frac{\partial Y_{\ell m}}{\partial \theta} \;\;, \tag{7.32}$$

but $(\nabla \times \boldsymbol{\xi})_r \neq 0$ for these modes, as allowed by the vorticity equation in this case. The radial eigenfunctions $T_{\ell m}$ ideally depend on the frequency ω, but in the present case ($\omega^2 = 0$), all toroidal solutions are degenerate and uninteresting.

7.1.3 Surface Constraints

Being primarily interested only in the photospheric and wind manifestation of nonradial pulsations (NRPs), we now focus on the surface ($r = R_*$) boundary condition in the solution for the radial eigenfunctions. The assumption that the Lagrangian pressure variation δP vanishes at the surface,

$$\delta P \;=\; P' + \xi_r \frac{\partial P_o}{\partial r} \;=\; 0 \tag{7.33}$$

(a "mechanical" boundary condition) is useful in deriving a relation between the radial and tangential displacements. Using the equilibrium condition of hydrostatic equilibrium ($\partial P_o/\partial r = -\rho_o g$), we can solve equation (7.33) for

$$\frac{\xi_r}{H_p} \;=\; \frac{P'}{P_o} \;, \tag{7.34}$$

where H_p is the pressure scale height, $P_o/\rho_o g$. Thus, using equation (7.30), we can define the ratio of horizontal to vertical motions,

$$K \;\equiv\; \frac{\xi_h(R_*)}{\xi_r(R_*)} \;=\; \frac{g(R_*)}{\omega^2 R_*}\left(1 + \frac{\psi'}{P'/\rho_o}\right) \tag{7.35}$$

$$\approx\; \frac{GM_*}{\omega^2 R_*^3} \;, \tag{7.36}$$

using Cowling's (1941) approximation, which neglects the perturbation of the gravitational potential ψ. As is often done when considering observations of the surfaces of pulsating stars, we can define a "radial velocity amplitude,"

$$V_p \;\equiv\; \frac{u_\ell(R_*)}{R_*^2}\omega \;, \tag{7.37}$$

and, given V_p and ω (or V_p and K), together with the angular eigenvalues ℓ and m, the value of the displacement vector $\boldsymbol{\xi}$ at the surface of the star is uniquely specified.

Although the simple analysis above provides an adequate surface constraint on the Lagrangian displacement, it does not allow for the full computation of the pressure and density variation on the stellar surface. In the theory of stellar interiors, it is often assumed that the pressure P_o and the density ρ_o vanish at the surface, and this implies

$$\delta P \;=\; P' \;=\; 0 \;. \tag{7.38}$$

The quantity $(\delta P/P_o)$, however, should remain finite at all radii, and the adiabatic energy conditions (eq. [7.10]) allow the corresponding density and temperature ratios $(\delta\rho/\rho_o)$ and $(\delta T/T_o)$ to be computed. Dziembowski (1971) and Cox (1980) derive a surface relation for $(\delta P/P_o)$ by solving the radial component of the Lagrangian momentum equation (7.7) for

$$\frac{\partial}{\partial r}\left(\frac{\delta P}{P_o}\right) = \frac{1}{H_p}\left[\frac{\delta P}{P_o} + \frac{\omega^2}{g}\xi_r + \frac{1}{r^2}\frac{\partial}{\partial r}\left(r^2\xi_r\right) - \frac{\ell(\ell+1)}{r}\xi_h - \frac{1}{g}\frac{\partial\psi'}{\partial r}\right] \quad . \tag{7.39}$$

Under the assumptions that: (i) $H_p \ll R_*$ near the surface, and (ii) the quantities $(\delta P/P_o)$ and (ξ_r/R_*) do not vary appreciably over the uppermost scale height H_p of the star, the quantity in square brackets above can be set to zero because $(\delta P/P_o)$ must remain finite. This quantity can then be used to solve for $(\delta P/P_o)$. This can be combined with the surface boundary condition for the perturbed gravitational potential – where ψ' and g are assumed continuous across the perturbed stellar surface – to obtain the final surface relation

$$\frac{\delta P}{P_o} = \left[\ell(\ell+1)K - 4 - \frac{1}{K}\right]\frac{\xi_r}{R_*} + \left[\ell(\ell+1)K - (\ell+1)\right]\frac{\psi'}{gR_*} \quad . \tag{7.40}$$

In the Cowling (1941) approximation, only the first term in square brackets, proportional to (ξ_r/R_*), remains, and it can be clearly seen that the Lagrangian pressure variations can either be in phase or 180° out of phase with the perturbation displacements themselves, depending on the values of ℓ and K.

Buta & Smith (1979) derive in detail the light variations from a linear and adiabatic nonradial pulsator. Note that, for a black body, the frequency-integrated intensity variation from the star can be given by

$$\frac{\delta I}{I_o} = 4\frac{\delta T}{T_o} \quad . \tag{7.41}$$

They find three competing factors which produce variability: (i) the purely thermodynamic change $(\delta T/T_o)$ derivable from equation (7.40), (ii) a "surface normal" (limb darkening) effect due to the changing direction of the local normal to points on the star, and (iii) a "surface area" effect due to the changing projected area of surface elements. More sophisticated treatments have included non-adiabatic effects (see, e.g., Stamford & Watson 1981), rapid rotation (Lee & Saio 1990; Aerts 1993; Townsend 1996), and extended atmospheres (Gouttebroze & Toutain 1994). For stellar wind dynamics, however, we need to derive the light (i.e., incident flux) variations for an "observer" at a *finite* distance from the star – not an infinite distance as is often assumed in the works cited above.

7.1.4 Discrete Frequency Eigenvalues

Because stars are bound systems with the majority of their constituent gas within a finite volume, only a *discrete* set of eigenfrequencies ω arises. This is analogous to simpler physical systems, such as a string fixed at both ends exhibiting a discrete set of vibrational overtone frequencies. Clement (1994), however, discusses the case of *local* instabilities inside stars (e.g., in convective zones) which excite a continuous spectrum of frequencies. These arise because no firm "boundaries" exist to limit the solutions in these regions. Here we will examine stars that are *globally* stable, and have only discrete eigenfrequencies. For realistic stellar models, these modes separate into several natural groupings, and it will be useful to analyze a simple model of a stellar interior in order to classify and understand these different solutions.

The classical illustrative model in stellar pulsation theory is the "homogeneous compressible" sphere, which has a constant equilibrium density throughout its volume, but allows first-order density fluctuations to exist. This model is equivalent to a so-called *polytrope* of index $n_p = 0$; a polytrope is an idealized stellar configuration with a quasi-adiabatic equation of state, $P \propto \rho^{1+(1/n_p)}$. For $n_p = 0$, of course, this implies that the zero-order density is completely insensitive to changes in pressure, and the equation of hydrostatic equilibrium can be integrated in this case to obtain

$$\rho(r) \;=\; \rho_o \;, \qquad P(r) \;=\; \tfrac{2}{3}\pi G \rho_o^2 (R_*^2 - r^2) \;. \tag{7.42}$$

Although unrealistic, the discrete eigenfrequencies which arise in this model have exact counterparts in more centrally-condensed (and realistic) fluids. Pekeris (1938) and Ledoux & Walraven (1958) derived a second-order differential equation for the parameter $\alpha \equiv \nabla \cdot \boldsymbol{\xi} = -\delta\rho/\rho_o$, using Cowling's (1941) approximation ($\psi' = 0$) and equations (7.10), (7.16), and (7.19). This equation for α becomes decoupled from the equation of motion (for ξ_r), and can be expressed, defining $x \equiv r/R_*$, as

$$\left(1 - x^2\right) \frac{\partial^2 \alpha}{\partial x^2} + \left(\frac{2 - 6x^2}{x}\right) \frac{\partial \alpha}{\partial x} + f(x, \ell, K, , _1)\, \alpha \;=\; 0 \;, \tag{7.43}$$

where

$$f(x, \ell, K, , _1) \;\equiv\; \frac{2}{, _1} \left[\frac{1}{K} + 4 - \ell(\ell+1)K\right] - \ell(\ell+1)\left(\frac{1 - x^2}{x^2}\right) - 6 \;. \tag{7.44}$$

Note that the stellar surface ($x = 1$) is a regular singular point of this equation, and a power series solution of the form

$$\alpha_{n\ell} \;=\; x^\ell \sum_{i=0}^{n} C_{2i}\, x^{2i} \tag{7.45}$$

provides a recursion relation for the coefficients C_{2i} when substituted back into equation (7.43). In order to have finite solutions in the domain $0 \leq x \leq 1$, the series must terminate at a finite n, and this constraint (setting the numerator in the recursion relation to zero for a given n) provides the discrete spectrum of solutions which satisfy the equation

$$\frac{1}{K} - \ell(\ell+1)K \;=\; {}_{,1}\left[n(2n+2\ell+5)+2\ell+3\right] - 4 \;\equiv\; 2D_{n\ell} \;, \tag{7.46}$$

where $n = 0, 1, 2, \ldots$ is the radial *order* of the solution. In most models, the radial eigenfunctions $u_\ell(r)$ and $v_\ell(r)$ exhibit n nodes or roots between the center and surface. Note that the quantity $1/K$ is a dimensionless squared frequency, which we can denote as $\hat{\omega}^2$, and the above equation is a quadratic which can be solved for

$$\hat{\omega}^2 \;=\; D_{n\ell} \pm \sqrt{D_{n\ell}^2 + \ell(\ell+1)} \;. \tag{7.47}$$

The positive roots are denoted p-modes, or pressure modes, and the negative roots (which in general models do not always result in $\hat{\omega}^2 < 0$, as they do above) are denoted g-modes, or gravity modes. The physical meaning behind these labels will be discussed below. Note that these solutions are degenerate for the $2\ell+1$ possible values of the azimuthal parameter m, but this degeneracy will be lifted when rotation is introduced.

One additional set of discrete modes is possible, and these correspond to the purely solenoidal (zero divergence) displacements of a homogeneous *incompressible* fluid sphere. In these modes, $\delta P = \delta\rho = 0$, and thus $\alpha = 0$. Chandrasekhar (1964) derived the associated eigenfrequencies for the homogeneous compressible model, and

$$\hat{\omega}^2 \;=\; \frac{2\ell(\ell-1)}{2\ell+1} \;. \tag{7.48}$$

These frequencies, originally identified in the incompressible case by Kelvin, are called f-modes, or fundamental modes. There is no oscillation for $\ell = 0$ or $\ell = 1$, and there is only one radial order, $n = 0$, with frequencies usually between those for the p-mode and g-mode $n = 0$ orders. Kelvin's incompressible f-modes have the unique property of possessing analytic solutions for the radial eigenfunctions:

$$\boldsymbol{\xi} \;\propto\; \nabla\left[r^\ell Y_{\ell m}(\theta,\phi)\right] \;, \qquad \text{hence,} \qquad u_\ell(r) \;\propto\; \ell r^{\ell+1} \;, \quad v_\ell(r) \;\propto\; r^\ell \;. \tag{7.49}$$

For general, centrally-condensed stellar models, the f-modes need not have zero divergence (i.e., constant volume), and in numerical computations the p, g, and f-modes all appear together in the solutions.

In general, the different classes of discrete modes can be described for the complete set of spheroidal (p, g, f) and toroidal solutions, as follows:

1. **f-modes:** The unique "pseudo-Kelvin" fundamental mode is characterized by the simplest radial eigenfunctions $\xi_r(r)$ and $\xi_h(r)$, usually with the fewest possible number of extrema. The f-mode frequency occurs at the unique value when the Brunt-Väisälä frequency ω_{BV} equals the horizontal acoustic, or "Lamb" frequency S_ℓ,

$$S_\ell^2 \equiv \frac{\ell(\ell+1)}{r^2}\frac{, {}_1P_o}{\rho_o} = k_H^2 a^2 \ , \tag{7.50}$$

   at the same point in the stellar interior. Because ω_{BV}^{-1} and S_ℓ^{-1} are the characteristic times a wave takes to move radially and horizontally (respectively) one oscillation wavelength, f-modes occur when these motions are the most comparable to each other.

2. **p-modes:** Because their motion is primarily radial, and only weakly horizontal ($K \lesssim 1$), the strong Eulerian variations in pressure and density create longitudinal acoustic waves, with pressure as the dominant restoring force. The p-mode frequencies are generally higher than those for f-modes, and $\hat{\omega}^2$ grows without bound for large n or ℓ. For $\ell = 0$, the p_n modes correspond to the purely *radial* oscillations exhibited by such stars as Cepheid and Mira type variables.

3. **g-modes:** These oscillations are primarily horizontal ($K \gtrsim 1$), and show only small Eulerian variations in pressure and density. The dominant restoring force in this case is gravity, and these oscillations can be likened to the "bobbing" of an object floating in water exhibiting transverse wave motion. The g-mode frequencies are generally lower than those for f-modes, and $\hat{\omega}^2 \rightarrow 0$ for a given ℓ as $n \rightarrow \infty$. In many stellar models, there exist both positive (g^+) and negative (g^-) modes, the former corresponding to oscillations and the latter corresponding to convective instability, with growth rate $-\hat{\omega}^2$.

4. **r-modes:** Also called "t" (toroidal) modes, these oscillations were described in detail by Papaloizou & Pringle (1978), and appear only for rotating stars. The motions are almost exclusively horizontal, and the inertial centrifugal and Coriolis forces are the dominant restoring forces. In this manner they are comparable to the Rossby waves which provide zonal motions in planetary atmospheres and oceans.

Figure 7.1 illustrates the discrete spheroidal (p, g, f) oscillation modes for an idealized nonrotating star. Solid lines link modes of the same radial order n, and the gray hatched regions represent waves which can *propagate* in the photosphere (see Section 7.2.5 below). The model star is a B supergiant, with $M_* = 20M_\odot$ and $R_* = 22R_\odot$, but the stellar interior has been scaled in radius from a zero-age main sequence

(ZAMS) configuration computed by the code of Hansen & Kawaler (1994). This, together with the simple Cowling-approximation pulsation code used to compute the eigenperiods (also from Hansen & Kawaler 1994), implies that these periods are only useful in an illustrative sense and should not be assumed quantitatively accurate.

Smeyers (1984) reviews several *asymptotic* treatments of adiabatic spheroidal modes, and presents the following useful approximations for high-order p- and g-modes. For the p-mode displaying $n \gg 1$ nodes in the radial displacement,

$$\omega_p \approx \frac{\pi}{2}\left(2n + \ell + n_p + \frac{1}{2}\right)\left[\int_0^{R_*} \frac{dr}{\sqrt{\,_1P_o/\rho_o}}\right]^{-1} , \tag{7.51}$$

where n_p is a characteristic polytropic index of the photosphere. For high-order g-modes,

$$\omega_g \approx \frac{2}{\pi}\left(2n + \ell + n_p + \frac{5}{2}\right)^{-1}\sqrt{\ell(\ell+1)}\int_0^{R_*} |\omega_{BV}|\frac{dr}{r} . \tag{7.52}$$

These approximate formulae have been derived by assuming a *wavelike* behavior of the radially dependent functions $u_\ell(r)$ and $v_\ell(r)$, and the above expressions are extensions of local wave dispersion relations to the global modes of the star.

Finally, we can note that the observationally-derived "period-mean density" relation,

$$Q = \Pi\sqrt{\bar{\rho}/\bar{\rho}_\odot} \tag{7.53}$$

can be understood in terms of the dimensionless frequency $\hat{\omega}$. The period of the oscillations is $\Pi = 2\pi/\omega$, the mean density of a spherical star is given by

$$\bar{\rho} = \frac{M_*}{V_*} = \frac{3M_*}{4\pi R_*^3} , \tag{7.54}$$

and $\bar{\rho}_\odot$ is the mean density of the sun. Thus, the "pulsation constant" Q can be written

$$Q = \frac{2\pi}{\hat{\omega}}\sqrt{\frac{R_\odot^3}{GM_\odot}} \approx \frac{0.1159 \text{ days}}{\hat{\omega}} . \tag{7.55}$$

If a class of stars, over a wide range of spectral types (and radii and masses), all exhibit nearly the same oscillatory modes, then $\hat{\omega}$, and thus Q, will remain nearly constant.

7.1.5 The Effects of Rotation

Let us now consider a uniformly rotating star. By writing the equations of hydrodynamics in the corotating frame, we can preserve the condition of zero

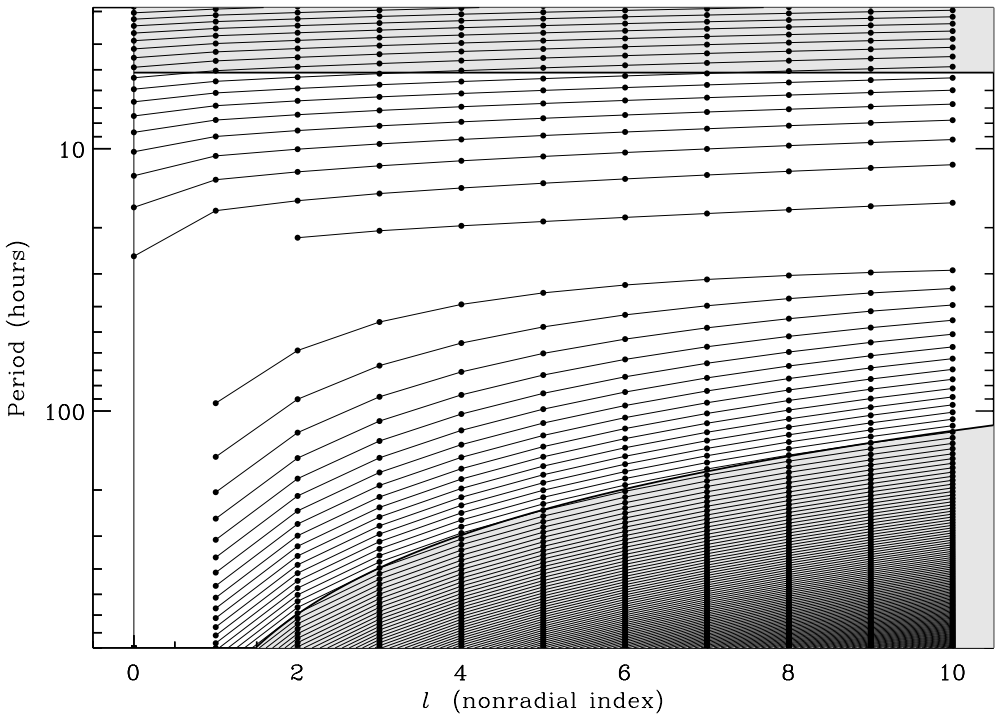

Figure 7.1: Discrete NRP eigenperiods (filled circles) for an idealized B supergiant model. For $\ell = 0$, only the short-period p-modes exist, and for $\ell = 1$, only the p and g-modes are present. The f-modes, with periods between the two, begin at $\ell = 2$. The gray hatched regions denote periods and horizontal wavenumbers ($k \approx \ell/R$) which can propagate radially in an isothermal photosphere.

equilibrium velocity ($\mathbf{v}_o = 0$). The equation of mass continuity is unchanged, while the momentum conservation equation contains two new terms (e.g., on the left side of eq. [7.6]), representing the non-inertial centrifugal force,

$$-\tfrac{1}{2}\nabla|\boldsymbol{\Omega}\times\boldsymbol{\xi}|^2 \tag{7.56}$$

and the Coriolis force,

$$2\boldsymbol{\Omega}\times\mathbf{v}\ , \tag{7.57}$$

where $\boldsymbol{\Omega} = \Omega\hat{\mathbf{e}}_z$ is the angular velocity of rotation. Most analyses of the effects of rotation on NRPs assume sufficiently *slow* rotation so that the $\mathcal{O}(\Omega^2)$ centrifugal term can be neglected, and that all rotational effects come from the $\mathcal{O}(\Omega)$ Coriolis term. Although we will often apply this approximation below, it is by no means universally applicable, even for modes with $(\Omega/\omega) < 1$. Fortunately, however, the primary effect of the centrifugal force is to affect the *equilibrium* state by means of oblateness and gravity darkening, and it has only negligible impact on small perturbations (Unno et al. 1989). The complete (centrifugal + Coriolis) problem is quite complicated, and the use of spherical harmonic eigenfunctions and distinct p, g, f, and r modes becomes less exact for rapidly rotating stars (Lee & Saio 1990; Clement 1994; Townsend 1996).

Using the above slow-rotation approximation, then, the oscillatory equation of motion can be written as

$$\omega^2\boldsymbol{\xi} - 2i\omega(\boldsymbol{\Omega}\times\boldsymbol{\xi}) \;=\; \nabla\chi + \mathbf{A}\frac{{}_{,1}P_o}{\rho_o}\left(\frac{\delta\rho}{\rho_o}\right)\ , \tag{7.58}$$

and, to first order (and for a star still assumed to be *spherical*), we can make use of the same separation of variables used in Section 7.1.2 to find solutions. Note, however, that the vorticity equation (eq. [7.22]) is now

$$\omega^2\left(\nabla\times\boldsymbol{\xi}\right)_r \;=\; \frac{2i\omega\Omega}{r\sin\theta}\left[\frac{\partial}{\partial\theta}\left(\xi_r\sin^2\theta + \xi_\theta\sin\theta\cos\theta\right) + \cos\theta\frac{\partial\xi_\phi}{\partial\phi}\right]\ , \tag{7.59}$$

and it is no longer a simple matter to separate the spherical and toroidal type solutions from one another.

Aerts (1993) finds that the standard spheroidal modes (derived in Sections 7.1.2 and 7.1.4) are rotationally perturbed by the addition of Ω-dependent spheroidal terms with the same ℓ and m as the non-rotating mode, and two toroidal modes with the same m, but $\ell \pm 1$. These first order perturbations are proportional to (Ω/ω). The toroidal terms can be derived from the rotational vorticity equation (7.59), and written in terms of the zero order (non-rotating) eigenfunctions $u_\ell^{(0)}$ and $v_\ell^{(0)}$. Lee & Saio (1990) and Townsend (1996) discuss the procedure of constructing a new set

of basis eigenfunctions for an arbitrarily rotating system, and in general, an infinite sum of toroidal and spheroidal modes proportional to $Y_{\ell m}$ (for $|m| \leq \ell < \infty$) is required to express *each* rotating mode. These higher order terms have a stronger impact on the mainly horizontal g and r modes, and little impact on the p-modes.

Along with the rotational perturbation in the eigenfunctions, the eigenvalues ω are similarly affected. Ledoux (1951) first derived the general rotational "splitting" of the $2\ell + 1$ frequency degeneracy for different values of m. Expanding equation (7.58) in terms of a non-rotating solution $\boldsymbol{\xi}^{(0)}$ and a small rotational perturbation $\boldsymbol{\xi}^{(1)}$, Ledoux noted that the right-hand side of equation (7.58) vanishes when the equation is dotted into the complex conjugate $\boldsymbol{\xi}^{*(0)}$ and integrated over the entire mass of the star, and the two terms that remain are

$$2\omega^{(0)}\omega^{(1)} \int_0^{R_*} \left(\boldsymbol{\xi}^{(0)} \cdot \boldsymbol{\xi}^{*(0)}\right) 4\pi r^2 dr - 2i\omega^{(0)} \int_0^{R_*} \left[\left(\boldsymbol{\Omega} \times \boldsymbol{\xi}^{(0)}\right) \cdot \boldsymbol{\xi}^{*(0)}\right] 4\pi r^2 dr \; = \; 0 \quad . \tag{7.60}$$

Using the terminology introduced in Section 7.1.2, we can solve for the rotationally perturbed part of the frequency,

$$\omega^{(1)} \; = \; m\Omega \frac{\int_0^{R_*} \left[2u_\ell(r)v_\ell(r)/r + v_\ell^2(r)\right] \rho(r) dr}{\int_0^{R_*} \left[2u_\ell^2(r)/r^2 + \ell(\ell+1)v_\ell^2(r)\right] \rho(r) dr} \; \equiv \; m\Omega \, C_{n\ell} \quad . \tag{7.61}$$

For the homogeneous compressible model of Section 7.1.4,

$$C_{n\ell} \; \approx \; \frac{K(2+K)}{1 + \ell(\ell+1)K^2} \quad , \tag{7.62}$$

but Ledoux finds that for more realistic polytropic indices, and specifically for low-order f and g-modes, $C_{n\ell}$ is typically of the order 0.1–0.2. Papaloizou & Pringle (1978) derive, for r-modes,

$$C_{n\ell} \; \approx \; \frac{2}{\ell(\ell+1)} \quad , \tag{7.63}$$

and in this case we have the unusual situation where $\omega^{(1)} > 0$, but $\omega^{(0)} = 0$.

Finally, we can now determine the overall effect that (sufficiently slow) rotation will have on a given intrinsic NRP frequency $\omega^{(0)}$. Because the spherical harmonics are defined in the rotating frame of the star, the *observed* inertial-frame frequency is found by making the transformation

$$\phi \; = \; \phi_{\rm inertial} - \Omega t \quad , \tag{7.64}$$

so the overall dependence of any perturbed quantity will be

$$\begin{aligned} f \; &\propto \; \exp(im\phi + i\omega t) \\ &\propto \; \exp\left[im(\phi_{\rm inertial} - \Omega t) + i(\omega^{(0)} + \omega^{(1)})t\right] \quad , \end{aligned} \tag{7.65}$$

and, effectively,

$$\omega_{\rm observed} = \omega^{(0)} - m\Omega(1 - C_{n\ell}) \quad . \tag{7.66}$$

Thus, the convention is to call $m < 0$ modes "prograde" and $m > 0$ modes "retrograde" because of their effect on the apparent frequency of features propagating across the stellar disk. In general, it is not a trivial matter to observationally identify rotationally-split pulsation modes of this kind. Although some well-sampled objects, such as the Sun and some white dwarf stars, exhibit the full $2\ell + 1$ splitting for many neighboring (n, ℓ) modes, early-type main sequence and supergiant stars usually only show one or two NRP periods at one epoch. Thus, the variables $\omega_{\rm observed}$ and Ω are known reasonably well (the latter from $V_{\rm eq} \sin i$), but $\omega^{(0)}$, m, and $C_{n\ell}$ are all virtually unconstrained. Even if an accurate theoretical NRP mode spectrum exists, eq. (7.66) allows many combinations of, e.g., ω and m to satisfy given observational values of $\omega_{\rm observed}$ and Ω.

7.2 Wave Propagation in Winds

The discrete spectrum of NRP "standing waves" derived above depends on the stellar interior being a *bounded* system. However, we are interested in the transition between the stellar interior and the "exterior" – i.e., the photosphere and accelerating wind. In order to ascertain whether this surrounding medium is significantly affected by underlying global oscillations we need to examine the physics of *wave dispersion* in a stratified and radiatively-accelerated gas. In this Section the linearized (first order perturbation) equations of mass, momentum, and energy conservation are described, and solved for wavelike variations of the density, pressure, and velocity in various circumstances. Although most low-order NRP modes are evanescent, or exponentially damped in the photosphere, we find that the presence of an accelerating stellar wind allows these modes to propagate radially in the transsonic and supersonic regions of the wind.

7.2.1 Basic Hydrodynamic Equations

Our goal is to derive linear analytic relations governing the propagation of modified acoustic waves in an accelerating stellar wind. For simplicity we will treat only the *two-dimensional* problem of the equatorial plane ($\theta = \pi/2$) around a star, with radius r and azimuthal angle ϕ being the two spatial independent variables. Thus, we assume no flow into or out of this plane, and that all latitudinal gradients vanish there.

Let us define the velocity components $v_r \equiv w$, $v_\theta \equiv v$, and $v_\phi \equiv u$. This choice is motivated by the correspondence we will draw below between spherical

polar variables r, θ, ϕ and Cartesian variables z, y, x, respectively. Thus, we can write the equation of mass continuity,

$$\frac{\partial \rho}{\partial t} + w\frac{\partial \rho}{\partial r} + \rho\frac{\partial w}{\partial r} + \frac{2\rho w}{r} + \frac{u}{r}\frac{\partial \rho}{\partial \phi} + \frac{\rho}{r}\frac{\partial u}{\partial \phi} \;=\; 0 \;\; . \tag{7.67}$$

The r and ϕ components of the equation of momentum conservation are

$$\rho\frac{\partial w}{\partial t} + \rho w\frac{\partial w}{\partial r} + \frac{\rho u}{r}\frac{\partial w}{\partial \phi} - \frac{\rho u^2}{r} \;=\; -\frac{\partial P}{\partial r} - \rho\,(g - g_{\rm rad}) \tag{7.68}$$

$$\rho\frac{\partial u}{\partial t} + \rho w\frac{\partial u}{\partial r} + \frac{\rho u}{r}\frac{\partial u}{\partial \phi} + \frac{\rho u w}{r} \;=\; -\frac{1}{r}\frac{\partial P}{\partial \phi} \;\; , \tag{7.69}$$

where g and $g_{\rm rad}$ represent the gravitational and radiative acceleration terms. Let us assume an ideal gas equation of state,

$$P \;=\; \frac{\rho k_B T}{\bar{m}} \;=\; (\gamma - 1)\rho e \;\; , \tag{7.70}$$

where k_B is Boltzmann's constant, $\bar{m}$ is the mean molecular mass of gas particles, γ is the ratio of specific heats c_P/c_V (usually 5/3 for a monatomic gas), and e is the specific internal energy of the gas.

This system of equations is closed by an equation of internal energy conservation, given by

$$\frac{DP}{Dt} - \left(\frac{\gamma P}{\rho}\right)\frac{D\rho}{Dt} \;=\; H(T) \;\; , \tag{7.71}$$

where the Lagrangian total derivative is defined here as

$$\frac{D}{Dt} \;\equiv\; \frac{\partial}{\partial t} + \mathbf{v}\cdot\nabla \;\; . \tag{7.72}$$

The function H is a temperature-dependent rate of net heating or cooling, and is most generally a function of ρ, P, and T. For simplicity, however, we restrict ourselves to only examine its behavior with temperature (see Mihalas & Mihalas 1984). Thus, the energy conservation equation is

$$\rho\frac{\partial P}{\partial t} + \rho w\frac{\partial P}{\partial r} + \frac{\rho u}{r}\frac{\partial P}{\partial \phi} - \gamma P\frac{\partial \rho}{\partial t} - \gamma P w\frac{\partial \rho}{\partial r} - \frac{\gamma P u}{r}\frac{\partial \rho}{\partial \phi} \;=\; \rho H \;\; . \tag{7.73}$$

7.2.2 Linearization

Let us assume the dynamical variables in the fluid equations can be separated into an equilibrium state (zero order) and a small-amplitude perturbation (first order):

$$u \;\equiv\; u_0(r) + u_1(r,\phi,t) \tag{7.74}$$

$$w \equiv w_0(r) + w_1(r,\phi,t) \tag{7.75}$$
$$\rho \equiv \rho_0(r) + \rho_1(r,\phi,t) \tag{7.76}$$
$$P \equiv P_0(r) + P_1(r,\phi,t) \tag{7.77}$$
$$T \equiv T_0(r) + T_1(r,\phi,t) \ . \tag{7.78}$$

The gravitational acceleration g is assumed to be a zero-order function of r only, but the radiative acceleration $g_{\rm rad}$ is more complicated. In the most general radiation hydrodynamical formulation (Mihalas & Mihalas 1984), $g_{\rm rad}$ and H depend on angle-moments of the radiation field specific intensity I_ν, which is specified by the equation of radiative transfer. However, here we assume the circumstellar radiation field is dominated by the (known) "core" stellar intensity, that the radiative acceleration is given by the standard analytic Sobolev form, and that the wavelengths of perturbations are larger than the Sobolev length $L_{\rm Sob}$ (Owocki & Rybicki 1984, hereafter OR-I). Thus, $g_{\rm rad}$ depends on r, the radial velocity w, and the density ρ (as well as the velocity gradient $\partial w/\partial r$, but this is formally a function of w and r). Expanding to first order in a Taylor series,

$$\begin{aligned} g_{\rm rad} &\equiv g_{\rm rad,0} + g_{\rm rad,1} \\ &= g_{\rm rad}(w_0,\rho_0) + \left\{ (w-w_0) \left.\frac{\partial g_{\rm rad}}{\partial w}\right|_{w_0} + (\rho-\rho_0) \left.\frac{\partial g_{\rm rad}}{\partial \rho}\right|_{\rho_0} \right\} \ . \end{aligned} \tag{7.79}$$

Thus we can define

$$g_{\rm rad,1} = \left\{ w_1 \left.\frac{\partial g_{\rm rad}}{\partial w}\right|_{w_0} + \rho_1 \left.\frac{\partial g_{\rm rad}}{\partial \rho}\right|_{\rho_0} \right\} \equiv w_1 F_1 + \rho_1 F_3 \ . \tag{7.80}$$

Similarly, the heating/cooling rate H is expressed as the sum

$$H \equiv H_0 + H_1 = H(T_0) + T_1 \left.\frac{\partial H}{\partial T}\right|_{T_0} \equiv H_0 - \frac{C\rho_0 k_B T_1}{\bar{m}} \ , \tag{7.81}$$

where C is defined as a cooling relaxation time-constant (see OR-I, eq. [58]). The variables C, F_1, and F_3 are considered to be zero-order functions of radius only, and are *not* the same as the variables of the same name in Chapter 2. Note that we leave room for a variable "F_2," but defer to Section 7.2.7 to define it formally.

Substituting in these expansions yields, in general, terms of zero through third order. Let us assume that the zero-order solutions for u_0, w_0, ρ_0, P_0, and T_0 are *known* functions of r, so that the zero-order terms in the fluid equations can be canceled exactly when writing any higher-order equations. The zero-order equation of mass continuity,

$$w_0 \frac{\partial \rho_0}{\partial r} + \rho_0 \frac{\partial w_0}{\partial r} + \frac{2\rho_0 w_0}{r} = 0 \ , \tag{7.82}$$

provides a constraint linking the zero-order density and radial velocity gradients. The zero-order equations of momentum conservation reduce to

$$w_0 \frac{\partial w_0}{\partial r} - \frac{u_0^2}{r} + \frac{1}{\rho_0}\frac{\partial P_0}{\partial r} + (g - g_{\rm rad,0}) \;=\; 0 \tag{7.83}$$

$$\frac{\partial u_0}{\partial r} + \frac{u_0}{r} \;=\; 0 \;\;, \tag{7.84}$$

which allows us to solve for the radial variation of the azimuthal velocity, $u_0(r) = V_{\rm rot} R_* / r$, as well as eliminate the zero-order net radial force $(g - g_{\rm rad,0})$. Similarly, the zero-order heating rate can be eliminated via the zero-order energy equation,

$$H_0 \;=\; w_0 \frac{\partial P_0}{\partial r} - w_0 \left(\frac{\gamma P_0}{\rho_0} \right) \frac{\partial \rho_0}{\partial r} \;\;. \tag{7.85}$$

Finally, we can write the *first order* fluid equations, neglecting second and third order terms because they are small when compared to those of first order. Thus, taking care to use the above zero-order constraints to simplify, the continuity equation becomes

$$\frac{\partial \rho_1}{\partial t} + w_1 \frac{\partial \rho_0}{\partial r} + w_0 \frac{\partial \rho_1}{\partial r} + \rho_1 \frac{\partial w_0}{\partial r} + \rho_0 \frac{\partial w_1}{\partial r} + \frac{2\rho_0 w_1}{r} + \frac{2\rho_1 w_0}{r} + \frac{u_0}{r}\frac{\partial \rho_1}{\partial \phi} + \frac{\rho_0}{r}\frac{\partial u_1}{\partial \phi} \;=\; 0 \;\;, \tag{7.86}$$

and the momentum equation components become

$$\rho_0 \frac{\partial w_1}{\partial t} + \rho_0 w_0 \frac{\partial w_1}{\partial r} + \rho_0 w_1 \frac{\partial w_0}{\partial r} - \frac{\rho_1}{\rho_0}\frac{\partial P_0}{\partial r} + \frac{\rho_0 u_0}{r}\frac{\partial w_1}{\partial \phi} - \frac{2\rho_0 u_0 u_1}{r}$$

$$+ \frac{\partial P_1}{\partial r} - \rho_0 w_1 F_1 - \rho_0 \rho_1 F_3 \;=\; 0 \tag{7.87}$$

$$\rho_0 \frac{\partial u_1}{\partial t} + \rho_0 w_0 \frac{\partial u_1}{\partial r} + \frac{\rho_0 u_0}{r}\frac{\partial u_1}{\partial \phi} + \frac{\rho_0 w_0 u_1}{r} + \frac{1}{r}\frac{\partial P_1}{\partial \phi} \;=\; 0 \;\;. \tag{7.88}$$

The ideal gas equation of state can be expressed in first order as

$$\frac{P_1}{P_0} \;=\; \frac{\rho_1}{\rho_0} + \frac{T_1}{T_0} \tag{7.89}$$

and the energy equation can be expanded to obtain

$$\rho_0 \frac{\partial P_1}{\partial t} + \rho_0 w_0 \frac{\partial P_1}{\partial r} + \rho_0 w_1 \frac{\partial P_0}{\partial r} + \frac{\rho_0 u_0}{r}\frac{\partial P_1}{\partial \phi} - \gamma P_0 \frac{\partial \rho_1}{\partial t} - \gamma P_0 w_0 \frac{\partial \rho_1}{\partial r} - \gamma P_0 w_1 \frac{\partial \rho_0}{\partial r}$$

$$- \frac{\gamma P_0 u_0}{r}\frac{\partial \rho_1}{\partial \phi} - \gamma P_1 w_0 \frac{\partial \rho_0}{\partial r} + \left(\frac{\gamma P_0}{\rho_0} \right) \rho_1 w_0 \frac{\partial \rho_0}{\partial r} + \frac{C \rho_0^2 k_B T_1}{\bar{m}} \;=\; 0 \;\;. \tag{7.90}$$

To investigate the intrinsic behavior of first-order perturbations in a moving medium, a transformation is often made to a coordinate system *comoving* with the zero-order flow. In a constant-velocity medium, this simplifies the equations of motion greatly. In our case, however, the zero-order reference frame is accelerating, thus noninertial, and there is no immediate benefit gained in transforming into the wind's frame. Bogdan et al. (1996) discuss the proper nonflat metric needed to perform this transformation for a general analysis of waves in a radiating and accelerating medium, but this is definitely beyond the scope of this work.

Thus, our independent variables remain r, ϕ, and t. The latter two variables are "homogeneous," since the zero-order solutions vary only in the radial direction. Let us then assume oscillatory solutions of the normal-mode form

$$\frac{w_1}{\tilde{W}(r)} = \frac{u_1}{\tilde{U}(r)} = \frac{\rho_1/\rho_0}{\tilde{D}(r)} = \frac{P_1/\rho_0}{\tilde{\Pi}(r)} = \frac{T_1/T_0}{\tilde{\Theta}(r)} = \exp\left[i(\omega t + m\phi)\right] \quad , \tag{7.91}$$

(see, e.g., Mihalas & Mihalas 1984), where the denominators are complex, radially-dependent amplitudes of the respective perturbed variables, and the frequency ω and azimuthal mode number m are assumed real. Of course, the actual first-order variables u_1, w_1, ρ_1, P_1, and T_1 are obtained in the end by taking the *real part* of any complex quantity. Although global stellar NRPs usually demand m to be an integer, this restriction is not yet imposed. Note that, when differentiating first-order quantities with respect to r, there will be *two* terms for the $\tilde{\Pi}$, $\tilde{D}$, and $\tilde{\Theta}$ amplitudes, because of the assumed dependence on the zero-order density and temperature.

Upon substitution, and dividing all terms by $\rho_0 \exp[i(\omega t + m\phi)]$, the fluid equations become a system of first-order ordinary differential equations. For compactness of notation, let us define the acoustic sound speed,

$$a(r) \equiv \left(\frac{\gamma P_0}{\rho_0}\right)^{1/2} \quad , \tag{7.92}$$

and the density scale height in the wind,

$$H(r) \equiv -\frac{\rho_0}{\partial\rho_0/\partial r} \quad . \tag{7.93}$$

Let us further assume the sound speed a does not vary in the wind, implying an *isothermal* zero-order wind. Because radiative heating and cooling dominates the energy balance in hot-star winds, the time scale for the gas to gain or lose energy is short when compared to the time scale of the flow. This results in the near-constancy of T_0 in the wind (see Section 7.2.4, below, and, e.g., Klein & Castor 1978; Drew 1989). However, this does not prevent first-order temperature *perturbations* from existing.

Under these approximations, the continuity equation thus becomes expressible as

$$i\omega\tilde{D} - \frac{1}{H}\tilde{W} + w_0\frac{\partial\tilde{D}}{\partial r} + \frac{\partial\tilde{W}}{\partial r} + \frac{2}{r}\tilde{W} + \frac{imu_0}{r}\tilde{D} + \frac{im}{r}\tilde{U} \;=\; 0 \;\;, \tag{7.94}$$

and the momentum equations become

$$i\omega\tilde{W} + w_0\frac{\partial\tilde{W}}{\partial r} + \frac{\partial w_0}{\partial r}\tilde{W} + \frac{a^2}{\gamma H}\tilde{D} + \frac{imu_0}{r}\tilde{W} - \frac{2u_0}{r}\tilde{U} - \frac{1}{H}\tilde{\Pi}$$
$$+ \frac{\partial\tilde{\Pi}}{\partial r} - F_1\tilde{W} - \rho_0 F_3\tilde{D} \;=\; 0 \tag{7.95}$$

$$i\omega\tilde{U} + w_0\frac{\partial\tilde{U}}{\partial r} + \frac{imu_0}{r}\tilde{U} + \frac{w_0}{r}\tilde{U} + \frac{im}{r}\tilde{\Pi} \;=\; 0 \;\;. \tag{7.96}$$

The energy equation becomes (after eliminating $\tilde{\Theta}$ in favor of $\tilde{\Pi}$ and $\tilde{D}$, and dividing out another factor of the zero-order density)

$$i\omega\tilde{\Pi} + w_0\frac{\partial\tilde{\Pi}}{\partial r} + \frac{(\gamma-1)\,w_0}{H}\tilde{\Pi} + \left(\frac{\gamma-1}{\gamma}\right)\frac{a^2}{H}\tilde{W} + \frac{imu_0}{r}\tilde{\Pi} - i\omega a^2\tilde{D}$$
$$- a^2 w_0\frac{\partial\tilde{D}}{\partial r} - \frac{ima^2u_0}{r}\tilde{D} + C\tilde{\Pi} - \frac{Ca^2}{\gamma}\tilde{D} \;=\; 0 \;\;. \tag{7.97}$$

The above system of coupled first-order ordinary differential equations is solved most generally as an initial value problem, with values of the complex amplitudes $\tilde{U}$, $\tilde{W}$, $\tilde{D}$, and $\tilde{\Pi}$ specified at a known initial radius. A numerical scheme, such as Runge-Kutta, then integrates this system in radius to obtain the full solution for the first-order wave variations in the wind. Further, any of the radially-dependent complex amplitudes can be written at any radius as

$$\tilde{Z} \;=\; A_Z \exp(i\psi_Z) \;\;, \tag{7.98}$$

where here $\tilde{Z}$ represents either $\tilde{U}$, $\tilde{W}$, $\tilde{D}$, or $\tilde{\Pi}$, and its magnitude A_Z and phase ψ_Z are real. Below, it will be convenient to express various quantities, such as the wave phase speed, as functions of these real components of the complex amplitudes. As in geometrical optics, the function ψ_Z may be regarded, over a small region of space, as an *eikonal,* with the linear wave vector and frequency defined as

$$\mathbf{k} \;\equiv\; -\nabla\psi_Z \;\;, \qquad\qquad \omega \;\equiv\; \frac{\partial\psi_Z}{\partial t} \;\;. \tag{7.99}$$

Here, however, ψ_Z is a function of position only, and not of time. In general, when the properties of the medium at each point in space do not vary in time, the frequency remains *constant* along the wave path. Thus we assume that a stellar atmosphere "driven" at a certain frequency ω should induce coherent modulations throughout the wind at that same frequency.

7.2.3 Local Dispersion Analysis

Before exploring full global solutions to the linearized first-order ordinary differential equations (in Section 7.2.8), it is instructive to examine the limiting cases of various local environments that can be treated in a simpler way:

1. A **homogeneous medium** (constant u_0, w_0, ρ_0, P_0).
2. A **stratified atmosphere** (varying ρ_0 and P_0, $w_0 \ll a$, constant u_0).
3. A **subsonic wind** ($w_0 \ll a$), superimposed on a stratified plane-parallel atmosphere.
4. A **supersonic wind** ($w_0 \gg a$), with sufficiently high frequency or short wavelength modes.

In these cases, let us assume that the *local* radial variation of the complex amplitudes is given by

$$\tilde{Z}(r) \equiv Z \exp(-ik_r r) \ , \tag{7.100}$$

where the radial wavenumber k_r, in the most general formulation, is allowed to be complex. Note that there is a *single* and *constant* value of k_r defined for all four complex amplitudes; this is consistent only when the coefficients of U, W, D, and Π in the linearized equations are *constants* in radius as well. For more complicated situations, the equations demand that k_r itself vary in radius, and one must also question (and usually reject) the entire notion of a single k_r for all four complex amplitudes.

Given the above radial dependence for the first-order amplitudes, the equations of motion can be written in matrix form as

$$\begin{pmatrix} M_{1U} & M_{1W} & M_{1D} & M_{1\Pi} \\ M_{2U} & M_{2W} & M_{2D} & M_{2\Pi} \\ M_{3U} & M_{3W} & M_{3D} & M_{3\Pi} \\ M_{4U} & M_{4W} & M_{4D} & M_{4\Pi} \end{pmatrix} \begin{pmatrix} U \\ W \\ D \\ \Pi \end{pmatrix} = \begin{pmatrix} 0 \\ 0 \\ 0 \\ 0 \end{pmatrix} \ , \tag{7.101}$$

where the numbers 1, 2, 3, and 4 refer to the continuity, r-momentum, ϕ-momentum, and energy equations, respectively. These coefficients are listed here for completeness, but note that only certain limiting cases (discussed below) are completely consistent with this localized analysis:

$$M_{1U} = \frac{im}{r} \tag{7.102}$$

$$M_{1W} = -ik_r - \frac{1}{H} + \frac{2}{r} \tag{7.103}$$

$$M_{1D} = i\omega - ik_r w_0 + \frac{imu_0}{r} \tag{7.104}$$

$$M_{1\Pi} = 0 \tag{7.105}$$

$$M_{2U} = -\frac{2u_0}{r} \tag{7.106}$$

$$M_{2W} = i\omega - ik_r w_0 + \frac{imu_0}{r} + \frac{\partial w_0}{\partial r} - F_1 \tag{7.107}$$

$$M_{2D} = \frac{a^2}{\gamma H} - \rho_0 F_3 \tag{7.108}$$

$$M_{2\Pi} = -ik_r - \frac{1}{H} \tag{7.109}$$

$$M_{3U} = i\omega - ik_r w_0 + \frac{imu_0}{r} + \frac{w_0}{r} \tag{7.110}$$

$$M_{3W} = 0 \tag{7.111}$$

$$M_{3D} = 0 \tag{7.112}$$

$$M_{3\Pi} = \frac{im}{r} \tag{7.113}$$

$$M_{4U} = 0 \tag{7.114}$$

$$M_{4W} = \frac{(\gamma-1)a^2}{\gamma H} \tag{7.115}$$

$$M_{4D} = -i\omega a^2 + ik_r w_0 a^2 - \frac{imu_0 a^2}{r} - \frac{Ca^2}{\gamma} \tag{7.116}$$

$$M_{4\Pi} = i\omega - ik_r w_0 + \frac{imu_0}{r} + \frac{(\gamma-1)w_0}{H} + C \tag{7.117}$$

Of course, all coefficients in this *homogeneous* system have been divided by $\exp(-ik_r r)$. In addition, the homogeneity of the system allows one of the four amplitudes to be chosen as a free parameter. We will assume hereafter that we can arbitrarily assign

$$D = \delta + 0i \ , \tag{7.118}$$

where $\delta \ll 1$, and D is chosen to be *real* to allow convenient comparison with the other variables (which in general all lead or lag each other in complex phase). Also, the complex temperature amplitude is given immediately by

$$\Theta = \frac{\rho_0}{P_0}\Pi - D \ . \tag{7.119}$$

From the equation of ϕ-momentum conservation, the pressure and horizontal velocity amplitudes are directly related by

$$\Pi \;=\; \left(\frac{iw_0 - \omega' r}{m}\right) U \;\equiv\; nU \quad , \tag{7.120}$$

where $\omega' \equiv \omega - k_r w_0 + m u_0/r$, and is an effective comoving or Doppler-shifted frequency. Note that ω' is the frequency in the locally-inertial frame defined by the translations $r \rightarrow (r + w_0 t)$ and $r\phi \rightarrow (r\phi - u_0 t)$. From the mass and r-momentum conservation equations, the remaining two amplitude relations are given schematically by

$$W \;=\; \left[\frac{(M_{2U} + nM_{2\Pi})M_{1D} - M_{1U}M_{2D}}{M_{1U}M_{2W} - (M_{2U} + nM_{2\Pi})M_{1W}}\right] D \tag{7.121}$$

$$U \;=\; -\frac{1}{M_{1U}}\left(M_{1W}W + M_{1D}D\right) \quad . \tag{7.122}$$

In the "one-dimensional" limit of $m = 0$, the above relations contain canceling infinities, and it becomes easier to express them as follows:

$$U \;=\; 0 \;, \qquad W \;=\; -\left(\frac{M_{1D}}{M_{1W}}\right) D \;, \qquad \Pi \;=\; -\frac{(M_{2W}W + M_{2D}D)}{M_{2\Pi}} \quad . \tag{7.123}$$

Finally, if the frequency ω and the azimuthal mode number m are specified arbitrarily, the allowed values for the radial wavenumber k_r can be determined uniquely by considering them eigenvalues of the coefficient matrix `M`. In other words, there can exist a nontrivial solution of eq. (7.101) only if the determinant of `M` vanishes. This determinant results in a fourth-order polynomial equation, and in general there are four allowed solutions for k_r. Let us examine this so-called *dispersion relation* for the four localized cases listed above.

7.2.4 A Homogeneous Medium

Let us assume all zero-order quantities, u_0, w_0, ρ_0, P_0 are constants with position, and that the local medium can be considered nearly Cartesian, or plane-parallel. Thus, the radial and azimuthal variations can be recast into the form

$$\exp(-ik_r r) \;\;\Longrightarrow\;\; \exp(-ik_z z) \tag{7.124}$$

$$\exp(im\phi) \;\;\Longrightarrow\;\; \exp(-ik_x x) \;, \tag{7.125}$$

where x (equivalent to $r[\phi - \phi_0]$) and z (equivalent to $[r - r_0]$) are horizontal and vertical displacement coordinates, respectively. In these conditions, the dispersion matrix becomes

$$\begin{vmatrix} -ik_x & -ik_z & i\omega' & 0 \\ 0 & i\omega' & 0 & -ik_z \\ i\omega' & 0 & 0 & -ik_x \\ 0 & 0 & -i\omega' a^2 - Ca^2/\gamma & i\omega' + C \end{vmatrix} = 0 \ , \tag{7.126}$$

where, of course, all sphericity, stratification, and radiative acceleration terms vanish, and $\omega' \equiv \omega - k_z w_0 - k_x u_0 = \omega - \mathbf{k} \cdot \mathbf{v}_0$. The algebraic dispersion relation is

$$\omega'^3(\omega' - iC) - \omega' a^2 (k_z^2 + k_x^2)(\omega' - iC/\gamma) = 0 \ . \tag{7.127}$$

In a purely static ($u_0 = w_0 = 0$) and adiabatic ($C = 0$) medium, eq. (7.127) reduces to the pure acoustic dispersion relation,

$$\omega^2 = a^2(k_z^2 + k_x^2) \ , \tag{7.128}$$

where two factors of the trivial solution $\omega = 0$ have been eliminated. Waves propagate parallel to the wave vector $\mathbf{k} = k_z \hat{\mathbf{e}}_z + k_x \hat{\mathbf{e}}_x \equiv (k_z^2 + k_x^2)^{1/2} \hat{\mathbf{e}}_k \equiv k \hat{\mathbf{e}}_k$. The phase speed and group velocity are defined as

$$v_p(\hat{\mathbf{n}}) \equiv \frac{\omega}{\mathbf{k} \cdot \hat{\mathbf{n}}} \ , \qquad \mathbf{v}_g \equiv \nabla_k \omega = \frac{\partial \omega}{\partial k_z} \hat{\mathbf{e}_z} + \frac{\partial \omega}{\partial k_x} \hat{\mathbf{e}_x} \ . \tag{7.129}$$

Note that the phase speed (in the arbitrary $\hat{\mathbf{n}}$ direction) cannot be written as a vector velocity, since, e.g., the x and z phase speeds do not vectorially add to the phase speed in the direction of propagation $\hat{\mathbf{e}}_k$. This same property is what prevents the *wavelength* ($\lambda = 2\pi/k$) from being written as a vector quantity. Note that the phase speed in the direction of propagation and the magnitude of the group velocity are the same in this present case, and both equal to $\pm a$. The relative perturbation amplitudes can be found easily, from the individual equations in (7.101), and written in terms of the density amplitude as

$$\Pi = a^2 D \ , \qquad U = \frac{a^2 k_x}{\omega} D \ , \qquad W = \frac{a^2 k_z}{\omega} D \ , \tag{7.130}$$

or as a general velocity amplitude

$$V \equiv \sqrt{U^2 + W^2} = \pm a \, \delta \ . \tag{7.131}$$

Thus, for acoustic waves, the velocity, density, pressure, and temperature all vary *in phase* with one another.

If the adiabatic ($C = 0$) fluid is now examined in a *moving* inertial frame (with u_0, w_0 constant and nonzero), then ω is simply replaced by ω', and the nontrivial solution to the dispersion equation is

$$\omega \;=\; u_0 k_x + w_0 k_z \pm a\sqrt{k_x^2 + k_z^2} \;\;, \tag{7.132}$$

Note, however, that the trivial solution, now $\omega' = 0$, represents a modulation which is passively carried along with the mean fluid motion. This "entropy-mode" solution corresponds to a constant-pressure ($\Pi = 0$) wave which would occur in an incompressible fluid ($\nabla \cdot \mathbf{v} = 0$). This wave solution is incompatible with the arbitrary specification of the frequency ω at a given location in the wind, and we will not pursue these solutions at present.

Although the phase speeds in the x and z directions are not equal to the x and z components of the group velocity, the phase speed in the direction of propagation remains equal to the magnitude of the group velocity:

$$v_p(\hat{\mathbf{e}}_k) \;=\; v_g \;=\; \frac{u_0 k_x + w_0 k_z \pm ak}{k} \;\;. \tag{7.133}$$

In the limit of both $|u_0|, |w_0| \gg a$, as happens in some regions of a supersonic wind, the two oppositely-propagating wave solutions merge into one solution moving at the velocity of the medium. The velocity amplitudes can be written similar to eq. (7.130), with ω' replacing ω, or in vector form, as

$$\mathbf{V} \;=\; \frac{a^2 \mathbf{k}}{\omega'} D \;\;. \tag{7.134}$$

Heuristically, the uniformly moving medium effectively "stretches" an acoustic wave via the Doppler effect. To quantify this, assume a simple *one-dimensional* z-oscillation ($k_x = 0$), in a medium moving only in the z-direction ($u_0 = 0$), which has a frequency

$$\omega \;\equiv\; aK \;=\; w_0 k_z \pm a k_z \;\;, \tag{7.135}$$

with K defined as the vertical wavenumber (or inverse wavelength, $2\pi/\Lambda$) in the case of a stationary medium. Thus, the ratio of wavenumbers, or wavelengths, is

$$\frac{K}{k_z} \;=\; \frac{\lambda_z}{\Lambda} \;=\; \frac{w_0}{a} \pm 1 \tag{7.136}$$

which is precisely the wavelength shift due to Doppler motions.

Finally, let us examine the effect of net heating or cooling ($C \neq 0$) on waves in a homogeneous medium. For simplicity, consider a static medium. The nontrivial dispersion relation can then be written as

$$\omega^2 \;=\; a^2 k^2 \left[\frac{\omega - iC/\gamma}{\omega - iC} \right] \quad . \tag{7.137}$$

If the cooling rate is negligibly slow or absent ($C \ll \omega$), waves propagate acoustically, but if the cooling rate is rapid ($C \gg \omega$), the phase speed approaches

$$v_p^2 \;=\; \frac{\omega^2}{k^2} \;\rightarrow\; \frac{a^2}{\gamma} \;=\; \frac{P_0}{\rho_0} \;\equiv\; a_T^2 \quad , \tag{7.138}$$

where a_T is an effective *isothermal* sound speed (equivalent to setting $\gamma = 1$ in the definition of a). Thus, when the energy balance is dominated by rapid cooling, all perturbations are quickly brought into thermal equilibrium. For intermediate values of the cooling rate ($C \approx \omega$) waves will be damped by the imaginary component of the resulting wavenumber.

As an aside, let us examine several physical mechanisms that can be responsible for a net rate of heating or cooling. If the fluid allows *thermal conduction,* then

$$H(T) \;=\; \nabla \cdot (K_T \nabla T) \;\approx\; K_T \nabla^2 T \quad , \tag{7.139}$$

where K_T is the coefficient of thermal conductivity. Thus, we can write

$$C \;=\; \chi \left(\frac{\gamma}{\gamma - 1} \right) \left(k_x^2 + k_z^2 \right) \;\equiv\; D k^2 \quad , \tag{7.140}$$

where $\chi \equiv K_T / \rho_0 c_P$ is the thermal diffusivity, and the specific heat at constant pressure $c_P = \gamma k_B / (\gamma - 1)\bar{m}$. Mihalas & Mihalas (1984) investigate the solutions to the modified dispersion relation in this case, and find two classes of wave modes. One pair of solutions are standard acoustic modes, only slightly modified by conductive damping terms,

$$k \;\approx\; \begin{cases} \pm(\omega/a)[1 - i(\gamma - 1)\varepsilon/2] \; , & \varepsilon \ll 1 \\ \pm(\omega/a_T)[1 - i(\gamma - 1)/2\varepsilon\gamma^2] \; , & \varepsilon \gg 1 \quad , \end{cases} \tag{7.141}$$

with $\varepsilon \equiv \omega\chi/a^2$, the relative strength of conduction. Thus, the characteristic damping (or e-folding) length L of oscillations scales as $1/\mathrm{Im}(k)$, and is *large* in the extreme limits $\varepsilon \ll 1$ and $\varepsilon \gg 1$. However, when $\varepsilon \approx 1$, the real and imaginary parts of k are comparable, and waves damp out over a small L. The second pair of solutions are the so-called *thermal waves,* with

$$k \;\approx\; \begin{cases} \pm(\omega/a)(2\varepsilon)^{-1/2}(1 - i) \; , & \varepsilon \ll 1 \\ \pm(\omega/a_T)(2\varepsilon)^{-1/2}(1 - i) \; , & \varepsilon \gg 1 \quad , \end{cases} \tag{7.142}$$

which are always heavily damped (over a few wavelengths), and propagate with an extremely *slow* or *fast* phase speed, compared to a, in the two limits $\varepsilon \ll 1$ and $\varepsilon \gg 1$, respectively.

In hot-star winds, radiation can strongly damp out temperature fluctuations by providing an added "sink" for energy exchange, analogous to the transfer of wave energy into *entropy* for the above heat-conducting fluid. For optically thin disturbances ($\kappa \ll k$, see below), the net heat input to the gas is adequately described by Newtonian cooling, with the constant

$$C \equiv \frac{1}{t_{RR}} = \frac{16\sigma_B \kappa T_0^3}{\rho_0 c_V} \quad , \tag{7.143}$$

where t_{RR} is a characteristic radiative relaxation time, σ_B is the Stefan-Boltzmann constant, κ is the opacity (in cm^2/g) of the gas, and c_V is the specific heat at constant volume. For an optically thick disturbance ($\kappa \gg k$), radiation and matter are in thermal equilibrium, and energy is exchanged via a conduction-like diffusion. The resulting wave propagation is then formally identical to the pure conduction case above, but with

$$K_T = K_T^{\mathrm{thermal}} + K_T^{\mathrm{radiation}} \quad . \tag{7.144}$$

Note, however, that K_T in an ionized or radiating fluid is now a function of temperature, and the treatment of such *nonlinear conduction* is an ongoing subject of study in radiation hydrodynamics.

For simplicity, however, we will keep $C = 0$ in all subsequent cases, and either assume that first-order perturbations are adiabatic ($\gamma = 5/3$) or isothermal ($\gamma = 1$). In fact, in preliminary hydrodynamical simulations using VH-1, the strong radiative cooling which keeps the zero-order wind nearly isothermal *also* drives most perturbations to behave as if $\gamma = 1$ in most of the wind. See, e.g., OR-I for further discussion of this heating/cooling parameter in radiatively-driven winds.

7.2.5 A Stratified Atmosphere

The standard theoretical description of waves in a gravitationally-stratified, plane-parallel medium is that of *gravo-acoustic* waves (Lamb 1932; Mihalas & Mihalas 1984). However, there is a simpler formalism that should be understood prior to the general full gravo-acoustic analysis: the extreme limit of gravity forces being much stronger than pressure-gradient forces.

In a medium where *gravity* dominates as the restoring force on perturbations, we can neglect pressure-gradient forces, and write the dispersion matrix under the ansatz that $\Pi = 0$, i.e., all variations remain in pressure equilibrium, and thus all

motions are *adiabatic*. If we also assume the mean state is at rest ($u_0 = w_0 = 0$), and radiative forces and cooling rates are negligible ($C = F_1 = F_3 = 0$), we obtain

$$\begin{vmatrix} -ik_x & -ik_z - 1/H & i\omega & 0 \\ 0 & i\omega & a^2/\gamma H & 0 \\ i\omega & 0 & 0 & 0 \\ 0 & (\gamma-1)a^2/\gamma H & -i\omega a^2 & 0 \end{vmatrix} = 0 \ , \tag{7.145}$$

which is now effectively *uncoupled,* since the determinant is identically zero. Note also that the assumed isothermality of the medium implies that the zero-order equation of hydrostatic equilibrium,

$$\frac{\partial P_0}{\partial z} = \frac{a^2}{\gamma}\frac{\partial \rho_0}{\partial z} = -\rho_0 g \ , \tag{7.146}$$

(which is the limit of $u_0 = w_0 = 0$ in eq. [7.83]) can be integrated to find

$$\rho_0(z) = \rho_0(0)\exp(-z/H) \ , \tag{7.147}$$

and in a plane-parallel atmosphere, g and $H = a^2/\gamma g$ are *constants*. Thus, the upper-left three-fourths of the above dispersion matrix (ignoring all Π terms and the energy equation) can be solved for

$$\omega^2 = igk_z + \frac{g}{H} \ . \tag{7.148}$$

Also note that $U = 0$ is mandated by the x-momentum equation, mainly because there are no restoring forces in the horizontal direction. Finally, if one takes $-a^2$ times the continuity equation, and compares it term-by-term with the energy equation, one obtains a unique solution for the vertical wavenumber, $k_z = ig/a^2$. A purely imaginary wavenumber implies no wave *propagation,* but rather an exponentially growing (unstable) or decaying (stable) oscillation in z. Substituting this imaginary k_z into the dispersion relation provides the definition for the specified frequency of buoyancy oscillations, called the Brunt-Väisälä frequency:

$$\omega_{BV}^2 \equiv \frac{g}{\rho_0}\left(\frac{1}{a^2}\frac{\partial P_0}{\partial z} - \frac{\partial \rho_0}{\partial z}\right) = (\gamma-1)\frac{g^2}{a^2} \ , \tag{7.149}$$

where the latter equality is valid only for our assumed constant-T_0 equilibrium model. This relation is also known as the Schwarzschild criterion for stability against convection: when $\omega_{BV}^2 > 0$ the medium is stably stratified, and when $\omega_{BV}^2 < 0$ the medium is unstable to convective overturning.

It is clear that if *both* the zero-order medium and the first-order perturbations are isothermal (implying $\gamma = 1$ everywhere), buoyancy oscillations cannot occur, and the medium is considered "neutrally stable." This condition can be also understood by examining the oscillation amplitudes, which are given by

$$U = \Pi = 0 \ , \qquad W = \frac{ig}{\omega} D \ , \qquad \Theta = -D \ , \tag{7.150}$$

and it is clear that buoyancy oscillations depend on a nonzero *density* perturbation. If the oscillations are adiabatic (in pressure equilibrium) *and* isothermal ($\gamma = 1$, and $\Theta = 0$), clearly the density oscillation amplitude must also be zero. Note also that for finite amplitude oscillations, the velocity and density are 90° out of phase, and the temperature and density are 180° out of phase.

A significantly more realistic treatment of oscillations in a gravitationally stratified medium takes both pressure-gradient forces and gravity into account. Let us write the dispersion matrix for a stratified, but unmoving mean state ($u_0 = w_0 = 0$), still ignoring the effects of radiative acceleration and net cooling/heating, and still assuming a plane-parallel geometry. In addition, assume the zero-order medium is isothermally stratified, with density given by eq. (7.147). Thus,

$$\begin{vmatrix} -ik_x & -ik_z - \gamma g/a^2 & i\omega & 0 \\ 0 & i\omega & g & -ik_z - \gamma g/a^2 \\ i\omega & 0 & 0 & -ik_x \\ 0 & (\gamma - 1)g & -i\omega a^2 & i\omega \end{vmatrix} = 0 \ , \tag{7.151}$$

which reduces to the (complex) dispersion relation

$$\omega^4 - \omega^2 \left[a^2(k_x^2 + k_z^2) - i\gamma g k_z \right] + g^2 k_x^2 (\gamma - 1) = 0 \ . \tag{7.152}$$

Because we are presently concerned with steady-state oscillations, we will assume a *real* frequency ω. Note, however, that the use of a *complex* frequency would allow some transient wave-energy transport to occur in ways not previously expected (see Wang, Ulrich, & Coroniti 1995). We will also assume that the horizontal wavenumber k_x is real, since the ambient medium is horizontally homogeneous, and no nonlocal variations in x are expected.

However, the vertical wavenumber k_z can be arbitrarily complex, because a wave can grow or decay in amplitude as it propagates vertically in the stratified medium. Defining $k_z \equiv k_r + ik_i$, the *imaginary* part of the dispersion relation can be written

$$\omega^2 \left(\gamma g k_r - 2a^2 k_i k_r \right) = 0 \ , \tag{7.153}$$

which solves simply for k_i (when $k_r \neq 0$)

$$k_i = \frac{\gamma g}{2a^2} = \frac{1}{2H} \quad . \tag{7.154}$$

Thus, all propagating oscillatory solutions contain a factor $\exp(z/2H)$, implying *rapid growth* of wave amplitudes with height, or with decreasing ambient density. Using this value for k_i, the real part of the dispersion relation reduces to

$$\omega^4 - \omega^2 \left[a^2(k_x^2 + k_r^2) + \omega_a^2 \right] + \omega_g^2 a^2 k_x^2 = 0 \quad , \tag{7.155}$$

where ω_a is the so-called "acoutstic cutoff" frequency,

$$\omega_a \equiv \frac{\gamma g}{2a} = \frac{a}{2H} \quad , \tag{7.156}$$

and ω_g is the Brunt-Väisälä frequency for an isothermal medium (eq. [7.149]). Note that $\omega_a \gtrsim \omega_g$ for physically relevant values of γ (between 1 and 5/3). Solving the real dispersion relation for the vertical wavenumber,

$$k_r^2 = \frac{(\omega^2 - \omega_a^2)}{a^2} - \frac{(\omega^2 - \omega_g^2)\, k_x^2}{\omega^2} \quad , \tag{7.157}$$

we find that, for purely vertical waves ($k_x = 0$), k_r approaches the pure acoustic limit of $(\pm\omega/a)$ for $\omega \gg \omega_a$, but grows smaller for finite values of ω_a. When $\omega = \omega_a$, $k_r = 0$, and there can be no vertical propagation. An imposed oscillation at this frequency coherently lifts and drops the entire medium, an effect known as "atmospheric resonance," first noted by Lamb. In numerical wind models, these Lamb oscillations represent a persistent "ringing" of the near-static base boundary conditions, and often hinder or prevent the formation of a steady-state solution (see Feldmeier 1995).

Frequencies below ω_a make k_r imaginary, implying amplitudes which vary exponentially with height. These *evanescent* waves have a formally infinite vertical phase velocity (since we define v_p as a function of only the real, i.e. propagating, part of $\mathbf{k}$), implying *zero* group velocity (since for gravo-acoustic waves, $v_p v_g = a^2$), and thus they transport no energy vertically.

The general two-dimensional case ($k_x \neq 0$) similarly allows three types of solutions for k_r (propagating, resonant, and evanescent), but with these regions separated into distinct areas of (ω, k_x) space (see Figure 7.1). Two "propagation boundary curves" (on which $k_r = 0$) split up the space into three regions, bounded by

$$\omega_{pbc}^2(k_x) = \frac{\omega_a^2 + a^2 k_x^2 \pm \sqrt{(\omega_a^2 + a^2 k_x^2)^2 - 4a^2 k_x^2 \omega_g^2}}{2} \quad . \tag{7.158}$$

These solutions for ω_{pbc} reduce to the two values $\{0, \omega_a\}$ in the limit $k_x = 0$, and approach the asymptotic limits $\{\omega_g, ak_x\}$ in the limit $k_x \rightarrow \infty$. Above the upper branch, $k_r^2 > 0$, and solutions propagate as gravity-modified acoustic waves. Below the lower branch, $k_r^2 > 0$ as well, and waves appear more and more like the gravitationally-dominated buoyancy waves defined above, and here are called *internal gravity waves*. Between the two propagation boundary curves, $k_r^2 < 0$, and this is an evanescent region. Note that in this region, $k_i \neq 1/2H$, and in general, there are two solutions for k_i, one larger and one smaller than $1/2H$ (Wang et al. 1995).

The phase and group speeds of the two varieties of propagating gravo-acoustic waves are given in full by Mihalas & Mihalas (1984), as are the amplitudes and phases of the first-order fluid variables U, W, D, Π, and Θ. In the limits of high and low frequency these quantities approach the purely acoustic or buoyancy wave solutions found previously, and become more complicated for intermediate values. The phase speed in the z-direction is easily computed from eq. (7.157), however, and is

$$\frac{\omega}{k_r} = \pm \frac{a\omega^2}{\sqrt{\omega^2(\omega^2 - \omega_a^2) - a^2k_x^2(\omega^2 - \omega_g^2)}} \ . \tag{7.159}$$

Because most observed pulsation modes in hot stars have relatively low frequencies and long horizontal wavelengths, it may be instructive to analyze gravo-acoustic waves in this limit, as well as the limit of a purely isothermal medium. When $\gamma = 1$, the complex wavenumber k_z is given by

$$2k_zH = i \pm \sqrt{\left(\frac{\omega}{\omega_a}\right)^2 - 1 - 4H^2k_x^2} \tag{7.160}$$

$$\approx 2i \left\{ \left[1 + H^2k_x^2 - \frac{1}{4}\left(\frac{\omega}{\omega_a}\right)^2 \right] , \left[-H^2k_x^2 + \frac{1}{4}\left(\frac{\omega}{\omega_a}\right)^2 \right] \right\} \ , \tag{7.161}$$

where the latter approximation is in the limit of $\omega \ll \omega_a$ and $k_xH \ll 1$. This region is clearly evanescent, as no internal gravity waves are possible when $\gamma = 1$. Note the existence of a rapidly-varying solution ($k_iH \approx 1$) and a slowly-varying solution ($|k_iH| \ll 1$), which take the place of the upward/downward propagating solutions in the evanescent limit. The velocity amplitudes in the $\gamma = 1$ limit are

$$U = \left(\frac{k_xa^2}{\omega}\right) D \ , \qquad W = \frac{iH}{\omega}\left(\frac{\omega^2 - a^2k_x^2}{ik_zH + 1}\right) D \ , \tag{7.162}$$

and the rapidly-varying $(+)$ solution for k_z results in a wave mode with $|W| \gg |aD|$, while the slowly-varying $(-)$ solution results in $|W| \ll |aD|$.

7.2.6 A Subsonic Wind

Finally, consider a plane-parallel stratified medium with a slow (subsonic) wind. In the limit of $w_0 \ll a$, the isothermal density stratification is still exponential, and the zero-order continuity equation demands

$$w_0(z) \;=\; w_0(0)\exp(+z/H) \;\;, \qquad \frac{\partial w_0}{\partial z} \;=\; \frac{\partial w_0}{\partial r} \;=\; \frac{w_0}{H} \;\;. \tag{7.163}$$

Thus, we can generalize the gravo-acoustic wave model above to include this nascent flow. For simplicity, let us neglect any horizontal flow ($u_0 = 0$) and restrict ourselves to a purely isothermal medium ($\gamma = 1$). The nontrivial dispersion relation is then

$$\omega'^2 - a^2(k_x^2 + k_z^2) + igk_z + \frac{iw_0}{H}\left(\frac{a^2k_x^2 - \omega'^2}{\omega'}\right) \;=\; 0 \;\;, \tag{7.164}$$

where $\omega' = \omega - w_0k_z$. After this substitution, this equation becomes a cubic in complex k_z, and can be solved analytically. Much simpler, however, is the vertical propagation limit of $k_x = 0$, which only results in a quadratic in k_z. This is solved by

$$(w_0^2 - a^2)k_z \;=\; \omega w_0 - \frac{i(w_0^2 + a^2)}{2H} \pm \sqrt{\omega^2a^2 - \frac{2i\omega w_0a^2}{H} - \frac{(w_0^2 + a^2)^2}{4H^2}} \;\;, \tag{7.165}$$

and reduces, in the limit $\epsilon \equiv w_0/a \ll 1$, to

$$2k_zH \;\approx\; i - \epsilon\left(\frac{\omega}{\omega_a}\right) \pm \sqrt{\left(\frac{\omega}{\omega_a}\right)^2 - 1 - 4i\epsilon\left(\frac{\omega}{\omega_a}\right)} \;\;. \tag{7.166}$$

Note that, even in the evanescent limit, there will always be a *real* part of k_z, and thus the presence of the wind helps all wave modes to propagate. This result is significant because it provides low-order NRP modes, many of which are evanescent in the photosphere, a mechanism to begin to "tunnel" their way out into the wind. The requirement, of course, is for these modes to have sufficient *amplitude* to survive the static evanescent photosphere.

Acoustic modes are only slightly modified by the wind, while evanescent modes are strongly affected. In the high-frequency limit ($\omega \gg \omega_a$),

$$2k_zH \;\approx\; \frac{\omega}{\omega_a}(\mp 1 - \epsilon) + i(1 \pm 2\epsilon) \;\;, \tag{7.167}$$

and in the low-frequency limit ($\omega \ll \omega_a$),

$$2k_zH \;\approx\; \left\{\left[2i - 3\epsilon\left(\frac{\omega}{\omega_a}\right)\right] \;,\; \left[\epsilon\left(\frac{\omega}{\omega_a}\right)\right]\right\} \;\;. \tag{7.168}$$

For these quasi-evanescent waves, then, the vertical phase speeds are large, but not infinite:

$$v_p \equiv \frac{\omega}{\mathrm{Re}(k_z)} \approx \left\{ -\frac{a^2}{3w_0}\, ,\ \frac{a^2}{w_0} \right\} \quad . \tag{7.169}$$

Note that it is the slowly-varying evanescent solution (here with $k_i H \approx 0$) which corresponds to the outwardly-propagating wave, and the rapidly-varying evanescent solution (here with $k_i H \approx 1$) which corresponds to the inwardly-propagating wave.

7.2.7 A Supersonic Wind

Abbott (1980) examined the physical significance of the critical point in CAK line-driven winds by a linearized wave analysis in the *comoving* frame of the wind. In order for the localized "wavenumber" picture to be valid, however, one must assume wavelengths shorter than the zero-order density and velocity scale lengths, but longer than the Sobolev length L_{Sob} (see Section 2.4). Abbott (1980) assumed that perturbations to the radiative acceleration are dependent only on perturbations in the radial *velocity gradient*. We thus re-cast the first-order expansion variable F_1, which represents the velocity dependence of the force (see eq. [7.80]) as

$$F_1 \ = \ -ik_z F_2 \ , \qquad \text{where} \quad F_2 \equiv (\partial g_{\mathrm{rad}}/\partial[\partial w/\partial r])_0 \ , \tag{7.170}$$

which is a completely equivalent means of expressing the perturbed radiative acceleration (in the approximation that there is no *other* dependence on the velocity w). Thus, ignoring nonlocal sphericity and stratification effects ($1/H \rightarrow 0, \partial w_0/\partial r \rightarrow 0$) and transforming into a comoving frame ($u_0 = w_0 = 0$), the dispersion matrix becomes

$$\begin{vmatrix} -ik_x & -ik_z & i\omega & 0 \\ 0 & i\omega + ik_z F_2 & -\rho_0 F_3 & -ik_z \\ i\omega & 0 & 0 & -ik_x \\ 0 & 0 & -i\omega a^2 & i\omega \end{vmatrix} = 0 \ . \tag{7.171}$$

Abbott (1980) also assumed that $F_3 = 0$, which is valid for a point-star CAK force when $\omega \gg \partial w_0/\partial r$ (which is consistent with the assumption of wavelengths shorter than the local scale heights). Thus, the dispersion relation reduces to

$$\omega^3 + \omega^2(k_z F_2) - \omega(a^2 k_x^2 + a^2 k_z^2) - a^2 k_x^2 k_z F_2 \ = \ 0 \ , \tag{7.172}$$

and is equivalent to Abbott's eq. (45).

Because the radiation is directed in the vertical direction, horizontal ($k_z = 0$) perturbations propagate purely acoustically, but vertical ($k_x = 0$) perturbations propagate at modified real *radiative-acoustic* phase speeds

$$C_\pm \equiv \frac{\omega}{k_z} = -\frac{F_2}{2} \pm \sqrt{\left(\frac{F_2}{2}\right)^2 + a^2} \ . \tag{7.173}$$

In most regions of a line-driven wind, $F_2 \gg a$, so that $C_+ \approx a^2/F_2$, and $C_- \approx -F_2$, signifying slower (subsonic) outward propagation and faster (supersonic) inward propagation in the frame of the wind. At the mCAK critical point, $C_- = -w_0$, implying zero net wave propagation in the inertial frame at this point. Note that Abbott's $C_\pm$ modes are dispersionless (i.e., $C_\pm$ is not a function of k_z) and non-damped (i.e., k_z is real, even for frequencies that would be evanescent in the photosphere), and that wave amplitudes do not vary appreciably on local length scales. This is to be expected: if the local density and velocity stratification is *ignored,* the medium is effectively homogeneous, and no gravo-acoustic evanescence arises. However, we find below (Section 7.2.8) that on the global scale of the entire wind, such modes do vary systematically in amplitude.

Rybicki, Owocki, & Castor (1990) generalized Abbott's linear analysis to the more general case of a perturbed radiative acceleration of the form

$$g_{\mathrm{rad},1,i} = T_{ij}\, v_{1,j} \ , \tag{7.174}$$

where the subscripts i and j refer to radiative acceleration and velocity perturbations in the x, y, and z directions ($i, j = 1, 2, 3$), and T_{ij} is in general a second-rank tensor. An important new result for intermediate-wavelength (i.e., stable) perturbations is that, for the radiative acceleration from a *finite stellar disk,* the horizontal and radial perturbations interact with one another. Purely horizontal ($k_z = 0$) waves propagate at a modified phase speed

$$\frac{\omega}{k_x} = \pm\sqrt{a^2 + \left(\frac{R_*^2}{4r^2}\, F_2\right)^2} \ , \tag{7.175}$$

and purely radial ($k_x = 0$) waves now have three possible modes: two with phase speeds very close to Abbott's $C_\pm$, and one slow inward "interaction" mode,

$$C_{int} \equiv \frac{\omega}{k_z} = -\frac{R_*^2}{4r^2}\, F_2 \ . \tag{7.176}$$

These modes are highly dependent on the sphericity of the stellar *source* of radiation, but not on the overall spherical geometry of the medium. Thus, even in a near-star Cartesian analysis, the limit $r \to R_*$ retains these important interaction terms.

Because high-frequency radiative-acoustic waves occur in an assumed "homogeneous" background, the effect of a moving medium is included by the simple substitution of ω for ω'. For the case of purely vertical Abbott (1980) waves (with $k_x = 0$), the three solutions for the vertical wavenumber are simply

$$k_z = \left(\frac{\omega}{w_0 + C_\pm}\right) \quad , \quad \left(\frac{\omega}{w_0}\right) \quad , \tag{7.177}$$

the latter unphysical solution given by the formerly degenerate case $\omega' = \omega - w_0 k_z = 0$. The C_- solution above creates an asymptote at the CAK critical point, below which $k_z < 0$ (inward propagation), and above which $k_z > 0$ (outward propagation). Owocki, Castor, & Rybicki (1988) found that the most robust wave modes (in the extreme short-wavelength, unstable regime) start out on the stellar surface on the C_+ branch, then switch to the C_- branch further out in the wind, thus always remaining outwardly-propagating.

However, Owocki & Rybicki (1986) also determined that the supersonic inward C_- characteristic carries no true *information,* but is merely a local reconstruction of a smooth (long-wavelength) wave pattern. This effect is a manifestation of the small-scale line-driven instability, and is an example of the generalized case of an unstable medium where information need not necessarily travel at the local group velocity (Bers 1983). In fact, in Owocki & Rybicki's (1986) pure-absorption approximation, the sound speed a remains the true speed of inward information propagation. Thus, Abbott's (1980) interpretation of the CAK critical point as a "dam" below which information cannot propagate is called into question. Macroscopic perturbations in a hot-star wind, however, may still result in some structures advecting along the C_+ and C_- characteristics, but it is still unclear how this subtle technical issue is to be resolved in a more realistic wind model.

Although it is difficult to apply the localized "wavenumber" picture to an accelerating *and* stratified medium, it is possible to examine the simple case of 1D wave propagation ($u_0 = 0$, $k_x = 0$) in an isothermal ($\gamma = 1$) wind, in the absence of radiative forces ($F_1 = F_2 = F_3 = 0$). Let us define the velocity scale height $-J$,

$$\frac{1}{J} = -\frac{1}{w_0}\frac{\partial w_0}{\partial r} = \left(\frac{2}{r} - \frac{1}{H}\right) \quad , \tag{7.178}$$

and write the (3×3) dispersion matrix, neglecting U-terms:

$$\begin{vmatrix} -ik_z + 1/J & i\omega' & 0 \\ i\omega' - w_0/J & a^2/H & -ik_z - 1/H \\ 0 & -i\omega' a^2 & i\omega' \end{vmatrix} = 0 \quad , \tag{7.179}$$

which reduces to

$$(w_0^2 - a^2)\, k_z^2 - 2\omega w_0 k_z - \frac{ik_z}{J}(w_0^2 + a^2) + \omega^2 + \frac{i\omega w_0}{J} \;=\; 0 \quad . \tag{7.180}$$

This equation can be solved for k_z, but it is a complicated expression. In the *supersonic* limit of $w_0 \gg a$, however, the solution simplifies to

$$k_z \;\approx\; \frac{\omega}{w_0} + \frac{i}{2J} \pm \frac{i}{2J} \;\approx\; \frac{\omega}{w_0} + \left\{ -\frac{i}{w_0}\frac{\partial w_0}{\partial r},\; 0 \right\} \quad . \tag{7.181}$$

This solution obviously neglects the acoustic propagation terms which depend on a, and the real part of k_z gives a trivial phase speed of w_0 (instead of $w_0 \pm a$). However, the imaginary part of k_z contains a solution with a decreasing ($k_i < 0$) amplitude in radius. Let us derive this amplitude, and ambitiously apply it to the *global* variation of wave amplitude with radius.

Because wave amplitudes (D, W, etc.) all vary locally as $\exp(k_i r)$ in addition to their sinusoidal oscillations, we can define the nonlocal amplitude as proportional to

$$A(r) \;\propto\; \exp\left[\int_{r_0}^{r} k_i(r')\, dr' \right] \quad . \tag{7.182}$$

Note, however, that there is no guarantee that *all* wave amplitudes will have this same radial dependence. We will find, however, that short-wavelength or high-frequency waves come close to this idealized limit. For the above variation of k_i, then,

$$A(r) \;\propto\; \exp\left[-\int_{r_0}^{r} \frac{\partial}{\partial r'}(\ln w_0)\, dr' \right] \;\propto\; \frac{1}{w_0(r)} \quad . \tag{7.183}$$

This inverse velocity-amplitude dropoff occurs only in the supersonic wind, and acts as a natural limiting factor to the exponential growth of wave amplitude in the near-static photosphere (Section 7.2.5). Preliminary numerical models of supersonic hot-star winds (see Figure 7.2) indeed show this behavior, at least for the highest acoustic frequencies. However, global variations in the zero-order medium result in the macroscopic wave variables ($\tilde{D}$, $\tilde{W}$, etc.) all behaving slightly *differently* in radius, thus invalidating the assumption of a single universal value of k.

7.2.8 Large-Scale Wave Propagation Analysis

Our eventual goal is to incorporate all the above effects – gravity, radiative forces, and a moving medium – into a model of wave propagation in an accelerating stellar wind. Grzędzielski (1971) initially investigated some of these effects in the solar wind, but the neglect of the energy equation (in favor of a universally-applied polytropic index) in that work makes even the results for a stationary medium differ

from ours above. In the limit of a static, plane-parallel atmosphere, Grzędzielski's (1971) dispersion relation predicts purely *acoustic* waves, as in eq. (7.128) above, for *all* frequencies in the isothermal propagation limit of $\gamma = 1$ (i.e., no evanescence at all). This is clearly unphysical, but the remainder of Grzędzielski's predictions (such as the existence of zero-density-amplitude "gravity-shear" waves) still remain to be examined.

A useful formalism for analyzing the global variation of wave amplitudes is the *conservation of wave action.* This is a generalization of the conservation of wave energy density in the case of a moving medium. Also, it is the fluid-continuum analogue of Hamilton's classical principle of least action for, e.g., the motion of a discrete harmonic oscillator.

Landau & Lifshitz (1987) give the wave energy density for acoustic waves in a moving medium,

$$\mathcal{E} \;=\; \frac{1}{2}\rho_0 v_1^2 + \rho_1 \mathbf{v}_0 \cdot \mathbf{v}_1 + \frac{a^2 \rho_1^2}{2\rho_0} \;\;, \tag{7.184}$$

where the vector velocity $\mathbf{v} = u\hat{\mathbf{e}}_x + w\hat{\mathbf{e}}_z$, and the above is a second-order perturbation quantity. Using eq. (7.134) above for $\mathbf{v}_1$, this energy density can be rewritten as

$$\mathcal{E} \;=\; \mathcal{E}_0 \left(\frac{\omega}{\omega - \mathbf{v}_0 \cdot \mathbf{k}} \right) \;\;, \tag{7.185}$$

where $\mathcal{E}_0$ is the wave energy density in the comoving frame (i.e., when $\mathbf{v}_0 = 0$). We can conveniently define the wave action $\mathcal{S} \equiv \mathcal{E}_0/(\omega - \mathbf{v}_0 \cdot \mathbf{k})$, and note that it is this quantity that is conserved throughout the wind. Landau & Lifshitz (1987) interpret this from a quantum standpoint, as the number of wave "phonons" being independent of the choice of inertial reference frame.

Bretherton & Garrett (1968) and Jacques (1977) derive the equation of conservation of wave action,

$$\frac{\partial \mathcal{S}}{\partial t} + \nabla \cdot (\mathbf{v}_g \mathcal{S}) \;=\; 0 \;\;, \tag{7.186}$$

which reduces in our case of a steady-state and spherical mean wind to

$$\frac{1}{r^2}\frac{\partial}{\partial r}\left(v_{g,r} \mathcal{S} r^2 \right) \;=\; 0 \;\;. \tag{7.187}$$

The quantity in parentheses is constant in radius. For pure acoustic waves propagating in the radial direction, this quantity is

$$v_{g,r} \mathcal{S} r^2 \;=\; (w_0 \pm a) \left[\frac{\rho_0 w_1^2}{\omega} \left(1 \pm \frac{w_0}{a} \right) \right] r^2 \tag{7.188}$$

$$\propto \;\; \pm \frac{(w_0 \pm a)^2 \, w_1^2}{w_0} \;\;, \tag{7.189}$$

and this implies

$$|w_1| \propto \sqrt{\frac{w_0}{(w_0 \pm a)^2}} \ , \tag{7.190}$$

or that, in the supersonic limit, $|w_1| \propto w_0^{-1/2}$. Parker (1966) derived this result in the WKB limit for outwardly-propagating waves in an isothermal wind, but the wave action picture is potentially more general. Note that this result is qualitatively similar, but not identically the same as eq. (7.183), which predicted wave amplitudes to drop off as w_0^{-1}.

Figure 7.2 shows the radial variation of the density amplitude D for preliminary numerical VH-1 models of winds perturbed by radial ($k_x = 0$) gravo-acoustic base oscillations. The density and pressure at the base are varied in time according to the static isothermal gravo-acoustic modes derived in Section 7.2.5, with $\gamma = 1$, and the radial velocity is allowed to "float" so the wind can determine a unique mass flux. The hydrodynamical simulation was allowed to evolve in time until all transient variations propagated away, leaving only the periodic oscillations. The lower boundary of the model was driven with a small linear amplitude ($D = 0.01$), and the straight lines at negative values of z in Figure 7.2 show the ideal (static limit) growth of the imaginary part of the wavenumber k_i. Note that for evanescent modes, the more *slowly* growing solution matches the numerical variation of amplitude in the wind, and in Section 7.2.5 we determined that this solution was *outwardly-propagating* in the subsonic wind. Note also that, past the sonic point of the flow (at $z/R_* \approx 0.008$), the amplitude variations for all modes behave similarly, and begin to drop off as w_0^{-1}, as approximated above in Section 7.2.7.

Another important consideration in global wind wave propagation is the effect of first-order waves on the *mean* zero-order flow. In general, the wave action equation and the zero-order equations of motion are a coupled system of differential equations, but in many cases the effect of waves can be modeled by a "wave pressure tensor" which provides a source of momentum to the mean flow. This formalism has been applied to solar wind models by, e.g., Jacques (1978) and Leer, Holzer, & Flå (1982); to general Alfvén-wave driven winds by Hartmann & MacGregor (1980), Velli (1993), and MacGregor & Charbonneau (1994); and to early-type stellar winds by Koninx & Hearn (1992). However, for acoustic waves of reasonable base amplitude, there is only a minimal wave-pressure impact on the mean wind, and we will not explicitly include these terms in our linear analysis. Of course, the full hydrodynamic solution of the equations of motion may contain a slightly-altered "mean" state (w_0, ρ_0), and it will be interesting to see how important radiative-acoustic waves are in altering the unperturbed zero-order wind.

Another type of wave-impact on the mean flow has been suggested for Be stars

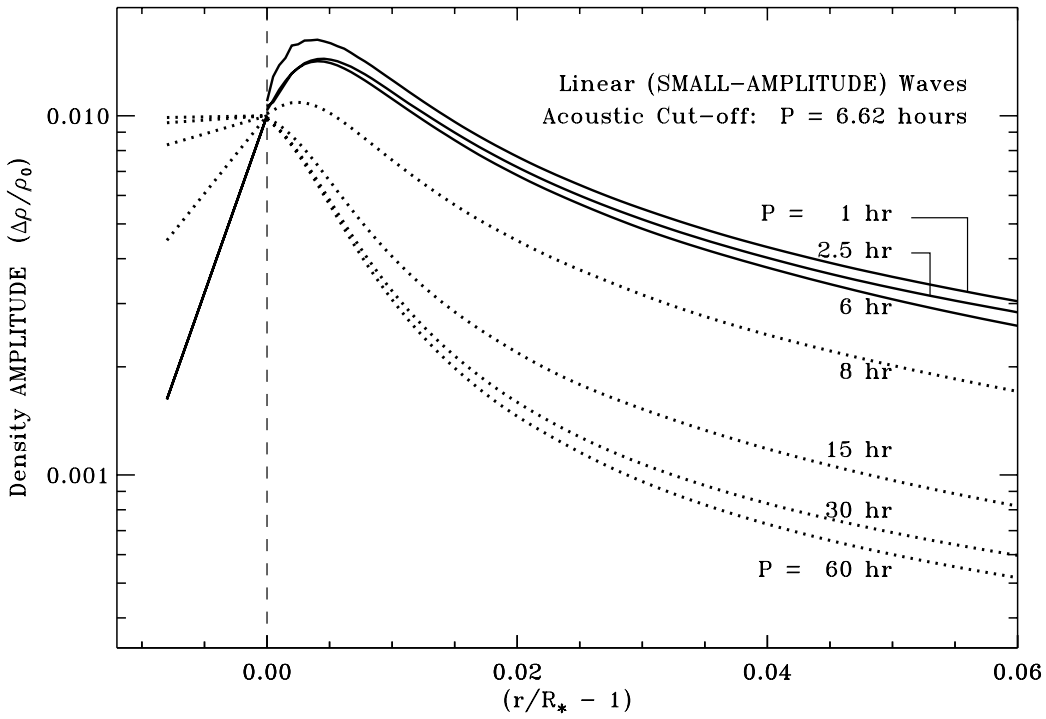

Figure 7.2: Fractional density amplitudes for near-star wind oscillations of a B supergiant (see, e.g., $\ell = 0$ modes in Figure 7.1). Solid lines represent modes that are able to propagate in the static isothermal photosphere, and dotted lines represent evanescent modes. Note that as the wind accelerates, the solid and dotted lines behave similarly and only differ by a constant factor in the supersonic wind.

by Osaki (1986): angular momentum transport from a rotating star. In the corotating equatorial plane, the radial flux of angular momentum is given by $r\rho_0\langle u_1 w_1\rangle$, where the angle-brackets denote an average over one oscillation period. Stars exhibiting adiabatic nonradial pulsations, however, have u_1 and w_1 varying 90° out of phase – implying zero mean angular momentum flux. Saio (1994) suggests that prograde nonaxisymmetric ($m < 0$) and *nonadiabatic* modes can transport significant amounts of angular momentum outward to form a dense "decretion" disk around the star. In our present wind models, nonadiabaticity is *not* necessary to produce a phase difference other than 90° between U and W. The acceleration, stratification, and radiative terms can produce this effect. It will be interesting to see if self-consistent wave models can be made to exhibit azimuthal velocities different enough from $u_0 \sim 1/r$ to show this transport.

7.3 Nonlinear Wave Effects

The theory of wave motion developed above applies well to small-amplitude (linear, first-order) perturbations in a fluid. However, *larger* amplitude disturbances are affected by the *nonlinear* terms in the hydrodynamic equations. Finite-amplitude acoustic waves "steepen" into shock discontinuities, while finite-amplitude internal gravity waves steepen and "break," like ocean waves, into dissipative turbulent motions. Also, since we know that linear wave trains must eventually steepen into nonlinear structures, we need to analyze what types of discontinuities can occur in the fluid variables and their gradients in an accelerating stellar wind. For example, the "kinks" in the radial velocity and density in the CIR models of Chapter 6 are a qualitatively new phenomenon which we hope to better understand by analyzing these nonlinear effects.

7.3.1 Weak-Shock Wave Steepening

Let us examine the principal steepening effects of nonlinear waves in a heuristic way. It is possible, via the theory of Riemann invariants (see, e.g., Landau & Lifshitz 1987), to derive a nonlinear correction term for the phase speed of a wave in the direction of propagation. For dispersionless acoustic waves, the nonlinear generalization of the simple amplitude relation

$$V = \pm aD \tag{7.191}$$

is the integral expression

$$\int dv = \pm \int a(\rho)\frac{d\rho}{\rho} \ , \tag{7.192}$$

where for large amplitudes, the phase speed $\pm a$ of such "simple waves" is now a function of the instantaneous velocity or density. This relation is coupled with the

kinematic fact that the true definition of the "phase speed" in a disturbance is now given, for different points in the wave profile, by slightly different values:

$$v_p(\hat{\mathbf{n}}) \equiv \frac{\omega}{\mathbf{k}\cdot\hat{\mathbf{n}}} + [\mathbf{v}_1(\mathbf{r},t)\cdot\hat{\mathbf{n}}] \quad . \tag{7.193}$$

For simplicity, assume purely radial propagation. We can then write, schematically,

$$v_{p,r}(\text{nonlinear}) = v_{p,r}(\text{linear}) + \zeta w_1 \quad , \tag{7.194}$$

where ζ is an order-unity correction factor that takes into account the higher-order dependence of the phase speed on the density or velocity. For pure-acoustic and adiabatic waves, $\zeta = (\gamma+1)/2$ (Landau & Lifshitz 1987). For Abbott (1980) waves, in the supersonic limit of $F_2 \gg a$, the Riemann invariant theory gives $\zeta \approx 1 \pm \alpha$, for the $C_\pm$ modes (see Chapter 2 for the CAK definition of α).

In the linear limit of $|w_1/v_{p,r}| \ll 1$, this correction is negligible. When w_1 is larger, however, the nonlinear phase speed can be strongly affected. For $w_1(r) \propto \text{Re}[\exp(-ik_r r)]$, the "crests" of this sinusoid propagate *faster* than the linear phase speed, and the "troughs" propagate *slower*. In a finite time, or over a finite distance, the crests eventually overtake the troughs and form a sawtooth-pattern train of weak shocks. This nonlinear effect competes, in some cases, with the exponential growth of wave amplitude in a stratified photosphere. When, say, $D \sim \Theta \sim 1$, or when $|U|$ or $|W|$ surpass the local sound speed, then the linearized fluid equations no longer are valid. We find, however, that the presence of the wind naturally can limit this wave growth, and in fact causes amplitudes to begin to decrease around the sonic radius.

Let us estimate the distance Z over which a wave of a specified amplitude will steepen into a shock. Consider an initial waveform propagating in the radial, or $+z$ direction, with

$$w_1(z) = \frac{\tilde{w}_1}{2}\cos\left(\frac{2\pi z}{\lambda}\right) \quad , \tag{7.195}$$

where $k_z = 2\pi/\lambda$. A wave crest will meet and overtake its next highest "zero-point" (where $w_1 = 0$) when the crest travels a distance $(Z + \lambda/4)$ in the same time the zero-point travels a distance Z. This occurs when

$$\frac{\lambda}{4} = \int_0^T \Delta v_p(t)\,dt \approx \int_0^Z \Delta v_p(z)\,\frac{dz}{v_p^{(0)}} \quad , \tag{7.196}$$

where $v_p^{(0)}$ is the linear (unperturbed) value of the phase speed, and

$$\Delta v_p = \zeta\,[w_1(0) - w_1(\lambda/4)] = \frac{\zeta\tilde{w}_1}{2} \quad . \tag{7.197}$$

In a *homogeneous* medium, $\tilde{w}_1$ is constant in z, and it is trivial to solve for

$$Z \;=\; \frac{v_p^{(0)}\lambda}{2\zeta\tilde{w}_1} \;\; . \tag{7.198}$$

Similarly, for an exponentially-stratified static atmosphere, we find that

$$\tilde{w}_1 \;=\; \tilde{w}_1(0)\exp(z/2H) \tag{7.199}$$

and

$$Z \;=\; 2H\,\ln\left[\frac{v_p^{(0)}\lambda}{4H\zeta\tilde{w}_1(0)} + 1\right] \;\; . \tag{7.200}$$

Castor (1987) developed a different scaling estimate for the height Z of shock formation, which roughly agrees with the above analysis. By assuming the medium is disturbed by the motion of an upward-moving "piston," the creation of a shock is incumbent upon there being a net *change* in the piston's acceleration. If the piston were constantly accelerating, it would only produce an atmospheric "standing wave," with the atmosphere's acceleration matching that of the piston. For the piston position given by $z(t) = z_0 + z_1\cos(\omega t)$, its velocity amplitude is $W \propto \omega z$, and its rate of change of acceleration is

$$\frac{\partial^3 z}{\partial t^3} \;=\; \omega^2 W \;\; . \tag{7.201}$$

At each instant during the piston's motion, it emits sound waves, where later-departing waves have a larger absolute velocity (due to the exponential growth of gravo-acoustic modes). Thus, waves necessarily begin to cross each other when a "cusp" forms in the r-t diagram, and a shock forms at the height

$$Z \;\approx\; \frac{1}{3}\sqrt{\frac{a^3}{\partial^3 z/\partial t^3}} \;\approx\; \frac{\gamma g}{3\omega\sqrt{aW}}\,H \;\; , \tag{7.202}$$

for acoustic waves, with $v_p^{(0)} = a$. For either this or the above analysis, Z is of the order $(1-10)H$ for plausible early-type star values.

Gravo-acoustic waves, which inevitably grow with height, have an additional *local* means of reaching nonlinear amplitudes. This provides us with further ways to estimate where either shock formation or wave breaking occurs. First of all, the first-order linearized fluid equations break down when the amplitudes grow too large:

$$|D| \;\approx\; 1 \;\; , \qquad |\Pi| \;\approx\; \frac{a^2}{\gamma} \;\; , \qquad |\Theta| \;\approx\; 1 \;\; , \tag{7.203}$$

and, for acoustic-like waves, when the velocity amplitudes $|U|$ and $|W|$ surpass the sound speed a. For internal gravity waves, Mihalas & Toomre (1981) discuss various criteria for the onset of nonlinearity. The most clear condition is when the second-order *buoyancy* terms in the energy equation grow to the magnitude of the first-order terms, or when

$$\frac{|\partial\rho_1/\partial z - (1/a^2)\partial P_1/\partial z|}{|\partial\rho_0/\partial z - (1/a^2)\partial P_0/\partial z|} \approx \left|\frac{g}{\omega_{BV}^2}\left(\frac{1}{\rho_0}\frac{\partial\rho_0}{\partial z} - ik_z\right)\left(D - \frac{\Pi}{a^2}\right)\right| \approx 1 \ . \qquad (7.204)$$

When this condition is satisfied, the convective stability is significantly increased in some parts of the atmosphere, and decreased in others, leading to local instabilities and eventual dissipative mixing.

7.3.2 Discontinuities in Fluid Variables

In order to determine whether a given fluid quantity can be discontinuous across a small spatial interval at radius r, we must integrate the conservation equations of these quantities across this interval. Because this interval is assumed to be vanishingly small, any smoothly-varying function f_0 (such as a function of radius only) is considered *constant* across the interval. Thus, between r_1 and r_2 (where $\Delta r \equiv (r_2 - r_1) \rightarrow 0$),

$$\int_{r_1}^{r_2} f_0(r)dr \approx f_0\Delta r \rightarrow 0 \ . \qquad (7.205)$$

Variables allowed to be discontinuous across Δr can be approximated by the piecewise continuous form

$$f \approx \begin{cases} f_1 & , \quad r \leq r_1 \\ f_1 + (r - r_1)(\Delta f/\Delta r) & , \quad r_1 < r < r_2 \\ f_2 & , \quad r \geq r_2 \end{cases} , \qquad (7.206)$$

where $\Delta f \equiv f_2 - f_1$. The integral of such a variable across Δr is similarly negligible,

$$\int_{r_1}^{r_2}\left[f_1 + \frac{\Delta f}{\Delta r}(r - r_1)\right]dr = \left(\frac{f_1 + f_2}{2}\right)\Delta r \rightarrow 0 \ . \qquad (7.207)$$

However, the integral of the *radial gradient* of this discontinuous variable does not vanish, and

$$\int_{r_1}^{r_2}\frac{\partial f}{\partial r}\,dr = \left(\frac{\Delta f}{\Delta r}\right)\Delta r = \Delta f \ . \qquad (7.208)$$

Also, if we assume that the discontinuity is moving with a velocity $s \equiv \delta r/\delta t$ (with $\delta r \ll \Delta r$ and $\delta t \equiv t_f - t_i$), we find that the integral of the time derivative of f is finite. We can approximate

$$\int_{r_1}^{r_2} \frac{\partial f}{\partial t}\, dr \;=\; \frac{\partial}{\partial t} \int_{r_1}^{r_2} f\, dr \;\approx\; \frac{\int f(t_f) dr - \int f(t_i) dr}{t_f - t_i} \quad , \tag{7.209}$$

and for t_i and t_f occurring when the assumed pattern (eq. [7.206]) is a distance $\delta r/2$ below and above its given location, one obtains

$$\int_{r_1}^{r_2} f(t_i) dr \;=\; \frac{\Delta r}{2}(f_1 + f_2) + \frac{\delta r}{2}\Delta f - \frac{(\delta r)^2}{8\Delta r}\Delta f \tag{7.210}$$

$$\int_{r_1}^{r_2} f(t_f) dr \;=\; \frac{\Delta r}{2}(f_1 + f_2) - \frac{\delta r}{2}\Delta f + \frac{(\delta r)^2}{8\Delta r}\Delta f \quad . \tag{7.211}$$

Thus,

$$\int_{r_1}^{r_2} \frac{\partial f}{\partial t}\, dr \;\approx\; -s\Delta f + \frac{1}{4} s\Delta f \left(\frac{\delta r}{\Delta r}\right) \;\approx\; -s\Delta f \quad . \tag{7.212}$$

The 1D (spherically-symmetric) mass continuity equation (eq. [7.67], neglecting the $\partial/\partial\phi$ terms), when integrated over Δr, becomes

$$-\, s\Delta\rho + \Delta(\rho v) \;=\; 0 \quad , \tag{7.213}$$

or in a more familiar form,

$$(v_2 - s)\, \rho_2 \;=\; (v_1 - s)\, \rho_1 \quad . \tag{7.214}$$

The momentum equation can be integrated similarly, but special care must be taken when integrating the radiative acceleration term. For a simple Sobolev force from a point star, for example,

$$g_{rad} \;=\; \frac{GM,\, k}{r^2} \left(\frac{1}{\sigma_e v_{th} \rho} \frac{\partial v}{\partial r}\right)^{\alpha} \;\equiv\; C(r) \left(\frac{1}{\rho} \frac{\partial v}{\partial r}\right)^{\alpha} \quad , \tag{7.215}$$

and

$$\int_{r_1}^{r_2} \rho\, g_{rad}\, dr \;=\; C(r) \int_{r_1}^{r_2} \rho^{1-\alpha} \left(\frac{\partial v}{\partial r}\right)^{\alpha} dr \tag{7.216}$$

$$\approx\; C(r) \int_{r_1}^{r_2} \left[\rho_1 + \frac{\Delta\rho}{\Delta r}(r - r_1)\right]^{1-\alpha} \left(\frac{\Delta v}{\Delta r}\right)^{\alpha} dr \tag{7.217}$$

$$\approx\; \frac{C(r)}{2-\alpha} (\Delta v)^{\alpha} \frac{\Delta(\rho^{2-\alpha})}{\Delta\rho} (\Delta r)^{1-\alpha} \quad , \tag{7.218}$$

which, because $\Delta r \to 0$, vanishes for $\alpha < 1$. The slowly-varying finite disk correction factor $\eta = \eta(r, v, \partial v/\partial r)$ does not alter this result, since if the velocity v is represented by the piecewise continuous eq. (7.206), η becomes a simple function of r only:

$$\eta \equiv \frac{1-(1-\chi)^{1+\alpha}}{\chi(1+\alpha)} \ , \tag{7.219}$$

$$\chi = \frac{R_*^2}{r^2}\left(1 - \frac{v}{r\partial v/\partial r}\right) \approx \frac{R_*^2}{r^3}\left(\frac{r_1\Delta v - v_1\Delta r}{\Delta v}\right) \approx \frac{R_*^2 r_1}{r^3} \ , \tag{7.220}$$

the last approximation being that $\Delta r \ll r_1\Delta v/v_1$. Thus, for our present purposes, $\eta(r)$ can be assimilated into $C(r)$, and the finite disk factor ignored.

Thus, the momentum jump condition is unaffected by the radiative acceleration, and is given by integrating eq. (7.68) over Δr,

$$-s\Delta(\rho v) + \Delta[\rho(v^2 + a^2)] = 0 \ , \tag{7.221}$$

or, using eq. (7.214) to rewrite,

$$\rho_2[(v_2 - s)^2 + a^2] = \rho_1[(v_1 - s)^2 + a^2] \ . \tag{7.222}$$

The assumed isothermality (i.e., constancy of a) admits the simplified solutions,

$$(v_1 - s)(v_2 - s) = a^2 \ , \qquad \frac{\rho_2}{\rho_1} = \left(\frac{v_1 - s}{a}\right)^2 \ , \tag{7.223}$$

or, if the inertial-frame velocities v_1 and v_2 are known, the shock velocity is given by

$$s = \left(\frac{v_1 + v_2}{2}\right) \pm \sqrt{\left(\frac{v_1 - v_2}{2}\right)^2 + a^2} \ . \tag{7.224}$$

The density contrast ρ_2/ρ_1 can reach arbitrarily high values, as shown by the fact that the limiting value of this ratio for adiabatic shocks, $(\gamma+1)/(\gamma-1)$, diverges for $\gamma = 1$. Note also that *contact discontinuities,* where $v_1 = v_2 = s$, $P_1 = P_2$, but $\rho_1 \neq \rho_2$, are not allowed in the isothermal case, because if $P_1 = P_2$, then $\rho_1 = \rho_2$ automatically.

7.3.3 Discontinuities in Gradients

Abbott (1980) expressed the equations of motion in "quasi-linear" form by taking the radial derivative $\partial/\partial r$ of every term. Defining the velocity and density gradients as two new variables, the differentiated equations of motion become

$$\frac{\partial v}{\partial r} = x \tag{7.225}$$

$$\frac{\partial \rho}{\partial r} = y \tag{7.226}$$

$$\frac{\partial y}{\partial t} + \rho \frac{\partial x}{\partial r} + v \frac{\partial y}{\partial r} = -2xy - \frac{2\rho x}{r} - \frac{2vy}{r} + \frac{2\rho v}{r^2} \tag{7.227}$$

$$\frac{\partial x}{\partial t} + v \frac{\partial x}{\partial r} - \frac{\partial g_{rad}}{\partial x}\frac{\partial x}{\partial r} + \frac{a^2}{\rho}\frac{\partial y}{\partial r} = -x^2 + \frac{a^2 y^2}{\rho^2} - \frac{\partial g}{\partial r} + \frac{\partial g_{rad}}{\partial r} + x\frac{\partial g_{rad}}{\partial v} + y\frac{\partial g_{rad}}{\partial \rho} \tag{7.228}$$

Let us now consider discontinuities in the gradient variables x and y, but only those cases where v and ρ themselves remain *continuous*. This ansatz isolates weak discontinuities, or "kinks" in the flow density and velocity, and distinguishes their behavior from the shocks discussed above.

Integrating over the small interval Δr is done in a similar way as for the original equations of motion, and and the above eqns. (7.227) and (7.228) are written such that their left-hand sides contain the "jump" terms which remain finite upon integration. The quasi-linear mass continuity equation becomes

$$\rho \Delta x + (v - s)\Delta y = 0 \ , \tag{7.229}$$

and the quasi-linear momentum equation becomes

$$(v - s)\Delta x + \frac{a^2}{\rho}\Delta y - \Delta g_{rad} = 0 \ , \tag{7.230}$$

where

$$\Delta g_{rad} \equiv g_{rad}(r, v, \rho, x_2) - g_{rad}(r, v, \rho, x_1) \ . \tag{7.231}$$

Note that these jump-condition equations result from an integral of the differential of the original conservation equations, and thus have the same dimensionality as the original equations. It is, however, the choice of which variables to keep continuous (ρ and v) and which to let "jump" (x and y), that distinguishes these equations from the original conservative forms. Finally, if we define the "nonlinear Abbott speed" V_A as

$$V_A \equiv \frac{\Delta g_{rad}}{\Delta x} \ , \tag{7.232}$$

then the momentum equation can be written as

$$\left[(v - s)^2 - a^2 - V_A(v - s)\right] \Delta x = 0 \tag{7.233}$$

(where Δy has been eliminated via eq. [7.229]). This equation provides a constraint on the kink propagation velocity s, since in order for a nontrivial kink to exist at all ($\Delta x \neq 0$), we must have

$$(v - s)^2 - a^2 - V_A(v - s) = 0 \ , \tag{7.234}$$

or

$$s = v - \frac{V_A}{2} \pm \sqrt{\left(\frac{V_A}{2}\right)^2 + a^2} \tag{7.235}$$

$$= v + C_\pm \ . \tag{7.236}$$

This is an alternate means of proving that weak discontinuities must propagate along fluid characteristics. These characteristics are specified by V_A, which is the nonlinear generalization of the linear "Abbott speed" F_2 for small perturbations. It is simple to see that for a vanishingly small value of Δx, V_A would approach the partial derivative of the unperturbed g_{rad} with respect to x, which is precisely the linear F_2.

Note that the quasi-linear mass continuity equation can now be written simply as

$$\frac{\Delta y}{\Delta x} = \frac{\rho}{C_\pm} \ , \tag{7.237}$$

which helps to determine the sense of the gradient discontinuities. For kinks propagating along the positive ($C_+ > 0$) characteristics, Δx and Δy must have the same sign. For kinks propagating along the negative ($C_- < 0$) characteristics, Δx and Δy must be of opposite sign. This is a nonlinear generalization of the velocity-density correlation of simple linear acoustic (or modified radiative-acoustic) waves. Outwardly propagating (C_+) waves have their velocity and density oscillations *in phase*, and inwardly propagating (C_-) waves have their velocity and density oscillations 180° *out of phase*. This is in qualitative agreement with the sharp velocity and density kinks produced in the models of corotating stream structure in Chapter 6.

With the present development of velocity-gradient discontinuities as "shocks" in the quasi-linear dynamical variables x and y, we hope to bring to bear the extensive theory of shock waves developed over the last century to understand better these important and possibly *observable* features. Whether these idealized structures survive in the actual unstable and non-Sobolev winds is still to be determined. This is an example, however, of the value of the study of hot-star winds to the field of radiation hydrodynamics as a whole: providing a "laboratory" to explore regions of physics that are inaccessible under terrestrial conditions.

Chapter 8

SUMMARY AND CONCLUSIONS

Small and transitory is man.
Already he is behind you, and
once again ye find yourselves in endless space,
in the smaller or innermost infinity.

At immeasurable distance standeth
one single Star in the zenith.

C. G. Jung, *Septem Sermones ad Mortuos*

8.1 Overview of Current Work

The purpose of this dissertation has been to explore how rapid stellar rotation and pulsation affect the radiation-driven winds around early-type stars. Here I present the most important results and conclusions from this work and outline some ongoing and future projects related to the topic of rotating hot-star winds.

After a brief motivational introduction in Chapter 1, the theory of radiatively driven winds was presented in Chapter 2. One important new result is the impact of *limb darkening* on the line radiation force as discussed in Section 2.2.4. The intensity distribution from a limb-darkened star is intermediate between a purely-radial "point source" and the traditional uniformly-bright "finite disk." We thus expect a $\sim$ 10–15% increase in theoretical mass loss rates, and a similar decrease in theoretical terminal velocities compared with the current standard mCAK-type models. Also, in Section 2.3.2, I introduced a new approximation method for estimating the terminal velocity v_∞ (eq. [2.120]) which, despite a relatively insensitive

dependence on the assumed β exponent, gives results of similar accuracy as the more complicated (but widely used) Kudritzki et al. (1989) so-called "cooking recipe." In addition, the present approximation for v_∞ (in, e.g., eq. [2.123]) concisely illustrates the phenomenon of the loss of steady-state wind solutions for large mass loss rates.

In Chapter 4 we began to examine the interaction between stellar rotation and winds, and we found that the presence of von Zeipel *gravity darkening* governs the latitudinal variation of mass flux from a rotating oblate star. The resulting decrease in the equatorial mass loss runs counter to the expected increase due to the centrifugal weakening of gravity. The accurate computation of *nonradial* Sobolev line forces in Chapters 4 and 5, which tend to point latitudinally away from the equator and azimuthally opposite the rotation, seems to lead to the weakening or inhibition of the Bjorkman & Cassinelli (1993) "wind compressed disk" phenomenon. More work needs to be done to ensure that all relevant physics has been included, and Owocki, Gayley, & Cranmer (1996) have constructed preliminary two-dimensional hydrodynamical models incorporating these effects.

The intrinsic time variability of rotating hot-star winds is beginning to be addressed by use of dynamical models, and in Chapter 6 we verified Mullan's (1984a) suggestion that corotating interaction regions (CIRs) can give rise to spectral variability very similar to the observed discrete absorption components (DACs) in ultraviolet lines. By varying the Sobolev radiation force over a bright (dark) "star spot" in the equatorial plane, we produce an increase (decrease) in the localized mass loss. This in turn affects the wind's acceleration and leads to nonlinear shocks and "kinks" in the radial velocity. These kinks, or gradient discontinuities, contain the greatest optical depth, and their supersonic inward propagation (in the frame of the wind; see Abbott 1980) results in a *slow* outward propagation that reproduces well the $\beta \approx 2$–4 acceleration seen in DACs.

An interesting link between the meridionally-symmetric rotation models of Chapters 4 and 5 and the CIR models of Chapter 6 is the importance of the nonlinear *feedback* in line-driven winds between the radiative flux, the mass flux, and the wind acceleration. Darker regions on a star, for example, are given a lower mass flux and density, but the resulting velocity depends sensitively on various competing terms in the equation of motion. When von Zeipel gravity darkening causes the flux dimunition, the wind velocity will probably decrease along with the escape speed, but if some other mechanism leads to a dark, but finite, star-spot, the velocity will eventually increase as it leaves the spot's influence. A recurring theme of these models, then, is that the *dynamics* (i.e., the accurate computation of forces and their impact on the wind) must be modeled consistently to be able to predict the consequences of any large or small scale perturbations on a wind.

The physical mechanisms responsible for producing the wind structure that

leads to time variability, however, are far from clear. In Chapter 7 we outlined the theory behind nonradial stellar pulsations and their wavelike propagation into the wind, and in some cases this can provide the required "photospheric connection" between interior and wind variability. There are three current projects with which I am involved that apply this pulsational theory to currently unexplained spectroscopic wind data:

1. **IUE "MEGA" Observations of HD 64760:** In addition to slow DACs, many stars also exhibit a faster periodic type of wind modulation that appears to simultaneously accelerate and decelerate in time. Owocki, Cranmer, & Fullerton (1995) explained these "banana" shaped modulations in terms of corotating spiral streams passing in and out of the absorption column in the line of sight towards the star. For the B supergiant HD 64760, variations appear to occur on a time scale of 1/4 of the rotation period, and it is unclear whether these are $|m| = 4$ modulations rooted to the star, or are due to some other NRP mode with only $\omega_{\rm observed} \approx 4\Omega$ (see eq. [7.66]).

2. **IUE Observations of BW Vul:** The slowly-rotating β Cephei pulsator BW Vulpeculae has been observed to exhibit transient mass loss in the form of strong DACs which propagate out to $\sim 1000\,{\rm km\ s^{-1}}$ every pulsation period ($P \approx 4.8\,{\rm hr}$). Cranmer, Massa, & Owocki (1996) constructed a 1D time-dependent dynamical model of a B-star wind perturbed by a strong nonlinear gravo-acoustic wave at the subsonic wind base. The resulting spherical kink/shock structures (similar to the "dark spot" Model 2 of Chapter 6) qualitatively reproduce the DAC variability and discontinuous radial velocity curve of BW Vul, but more work needs to be done to accurately determine the wind and pulsation parameters from detailed fits to the spectra.

3. **GHRS and ORFEUS Observations of γ Cas:** In collaboration with M. A. Smith, I am assisting in the interpretation and modeling of highly-variable absorption line spectra from this bright Be star. By comparing DACs and other "migrating subfeatures" in lines from many different ions, the wind dynamics can be traced as a function of velocity/distance from the star. For example, by use of the "Van Hoof effect" (see Mathias & Gillet 1993), the phase lag between different ions can provide accurate information about the propagation of waves and shocks through the wind.

In addition to exploring the effects of rotation and pulsation on hot-star winds, I have worked on various other projects relating to observations of early-type stars. The radiative transfer in close and contact binary systems is a fascinating and complex field. Incident light from one photosphere to the other can heat up the

upper regions of each stellar atmosphere and alter observed light and polarization variations (Cranmer 1993). Also, in binaries containing an O star and a Wolf-Rayet star, the ram pressure balance between the two *winds* can be strongly affected by the momentum flux of photons from the (usually brighter) O star (Gayley, Owocki, & Cranmer 1996).

8.2 Future Research Goals

There remains much work to be done, both in continuing the theoretical work outlined in this dissertation and in incorporating new physics into models of rotating hot-star winds. Ongoing research is focused into two major areas: the effects of rapid rotation (i.e., models with meridional r,θ symmetry) and the photospheric mechanisms responsible for time variability (usually, models in the equatorial plane, varying r,ϕ). As mentioned earlier, Owocki, Gayley, & Cranmer (1996) have constructed 2D hydrodynamical models which incorporate the oblateness, gravity darkening, and nonradial Sobolev forces into the computation of the wind around an axisymmetric rotating star. In contrast with the WCD paradigm of Bjorkman & Cassinelli (1993), these models show a net *poleward* deflection of wind streamlines, resulting in enhanced density and mass flux over the poles and a low-density depletion around the equator. In addition to O and B stars, these models may be pertinent to the evolution of luminous blue variables (LBVs) such as η Carinae, which exhibits very prominent bipolar lobes in addition to an equatorial disk-like structure (see, e.g., Mac Low, Langer, & Garcia-Segura 1996).

Although the WCD model was originally intended to explain the dense disks around Be stars, it is growing clearer that some other mechanism is necessary to produce this dramatic phenomenon. We plan to investigate the physics responsible for these Keplerian ($v_\phi \propto r^{-1/2}$) and negligibly expanding ($v_r \lesssim a$) disks from the standpoint of three possible effects. First, magnetic fields are suspected to exist in all stars, and even fields below current observational thresholds (typically 100 Gauss) can have a significant influence in channeling the wind in complex ways. Specifically, a dipole field aligned with the rotation axis may redirect wind streamlines toward the equatorial plane as in the solar model of Pneuman & Kopp (1971). Second, Osaki (1986) and Saio (1994) discuss the outward transport of angular momentum by nonadiabatic NRPs, and we suspect that even *adiabatic* pulsations can spin up the equatorial wind if they have the proper phase behavior. The presence of the accelerating medium and the existence of complex toroidal oscillations may result in the gradual buildup of dense, critically-rotating circumstellar material. Third, the actual rotational velocity fields of Be stars need to be re-examined carefully; differential rotation and gravity darkening can alter observed $V_{\rm eq} \sin i$ values to mask a possibly "super-breakup" rotating equator (see, e.g., Collins & Truax 1995).

Besides this current work on the effects of rotation on winds, we are also continuing efforts to better understand observed *variability* (DACs, blue-edge variations, "bananas," Wolf-Rayet emission subfeatures) in terms of physical processes linking the interior, photosphere, and wind. Over the past decade, as observations of spectral wind diagnostics have improved, the sheer complexity of these quasi-regular large-scale variations have become evident (Massa et al. 1995; Kaper et al. 1996; Prinja et al. 1996). Many stars, such as HD 64760 (see above), have shown epochal variations in both their photospheric pulsations (e.g., individual modes appearing and disappearing) and their wind variability. Other stars, like EZ CMa (HD 50896; WN5) have preserved a consistent, possibly rotational "clock" over the years, but the variations have appeared qualitatively different. St-Louis et al. (1995) interpret this in terms of small-scale evolving magnetic field regions carried around with the stellar rotation. Whether most DAC-like variability is due to NRPs or magnetic fields, it is important to better understand both the periodic *and* transient behavior that is expected in such winds (see Wang, Ulrich, & Coroniti 1995).

One "transient" physical mechanism neglected in this dissertation has been the line-driven instability of hot-star winds (OR-I, II, III; Owocki 1991, 1992, 1994). Despite the conjecture that this intrinsic instability will result only in *small-scale* variability (which gets averaged out over the entire stellar disk), it is not clear how the various large-scale photospheric perturbations mentioned above will react with the instability. Fullerton & Owocki (1992) and Owocki, Fullerton, & Puls (1994) performed numerical experiments with large 1D base perturbations in an unstable wind, and found significant, possibly observable transient spectral variability. It is now becoming possible to incorporate the full non-Sobolev line force (e.g., Owocki & Puls 1996) into 2D and 3D hydrodynamical models, and it will be important to verify the results from the multidimensional Sobolev models presented in this dissertation.

The importance of simple physical models, however, should not be underestimated. Breakthroughs in computer technology allow us to simulate nature in more and more detail, but this demands more and more critical understanding of the physics behind these models. The standard progression in theoretical astrophysics from a simple "cartoon" paradigm to numerical simulations should be followed whenever possible by a *return* to an analysis of the basic physics of the problem. Hopefully in this dissertation I have laid the necessary groundwork for such understanding of the selected aspects of rotating and pulsating winds.

Finally, then, the research presented here raises many more questions than it answers. This may surprise those that consider stellar astrophysics to be a "mature" field with few fundamental issues left unknown. In fact, this characterization refers only to the standard, early twentieth century picture of stars as spherical, static, and

closed systems. The *actual stars,* however, continue to reveal new and fascinating physical processes with each new observation, and this enlivens the development of new theory and insight.

REFERENCES

Abbott, D. C. 1979, in *IAU Symp. 83, Mass Loss and Evolution of O-type Stars,* ed. P. S. Conti & C. deLoore (Dordrecht: Reidel), 237.

Abbott, D. C. 1980, *Astrophys. J.*, **242**, 1183.

Abbott, D. C. 1982a, *Astrophys. J.*, **259**, 282.

Abbott, D. C. 1982b, *Astrophys. J.*, **263**, 723.

Abbott, D. C., & Lucy, L. B. 1985, *Astrophys. J.*, **288**, 679.

Abney, W. de W. 1877, *Mon. Not. Roy. Astron. Soc.*, **37**, 278.

Adams, W. S., & MacCormack, E. 1935, *Astrophys. J.*, **81**, 119.

Aerts, C. 1993, Ph.D. Dissertation, Katholieke Univ. Leuven, Belgium.

Allen, R. H. 1899, *Star-Names and their Meanings* (New York: G. E. Stechert).

Anderson, L., & Shu, F. H. 1977, *Astrophys. J.*, **214**, 798.

Andriesse, C. D. 1981, in *Effects of Mass Loss on Stellar Evolution,* IAU Colloquium 59, ed. C. Chiosi & R. Stalio (Dordrecht: Reidel), 213.

Ando, H. 1991, in *ESO Workshop on Rapid Variability of OB-Stars: Nature and Diagnostic Value,* ed. D. Baade (Garching: European Southern Obs.), 303.

Babel, J. 1995, *Astron. Astrophys.*, **301**, 823.

Babel, J. 1996, *Astron. Astrophys.*, **309**, 867.

Baker, N., & Temesváry, S. 1966, *Tables of Convective Stellar Envelope Models,* 2nd ed. (New York: NASA Goddard Institute for Space Studies).

Batchelor, G. K. 1967, *An Introduction to Fluid Dynamics,* (Cambridge: Cambridge U. Press), 598-603.

Beals, C. S. 1929, *Mon. Not. Roy. Astron. Soc.*, **90**, 202.

Beals, C. S. 1931, *Mon. Not. Roy. Astron. Soc.*, **91**, 966.

Bers, A. 1983, in *Handbook of Plasma Physics: Vol. 1: Basic Plasma Physics,* ed. A. Galeev & R. Sudan (Amsterdam: North Holland), 451.

Bevington, P. R. 1969, *Data Reduction and Error Analysis for the Physical Sciences,* (New York: McGraw-Hill).

Bjorkman, J. E. 1992, Ph.D. Dissertation, University of Wisconsin.

Bjorkman, J. E. 1995, *Astrophys. J.*, **453**, 369.

Bjorkman, J. E., & Cassinelli, J. P. 1993, *Astrophys. J.*, **409**, 429.

Bjorkman, J. E., Ignace, R., Tripp, T. M., & Cassinelli, J. P. 1994, *Astrophys. J.*, **435**, 416.

Blake, W. 1795, "The Book of Ahania," in *The Poems of William Blake,* ed. W. Stevenson (New York: W. W. Norton, 1971). (Chapter 5 quotation)

Bogdan, T. J., Knölker, M., MacGregor, K. B., & Kim, E.-J. 1996, *Astrophys. J.*, **456**, 879.

Bohlender, D. A. 1994, in *IAU Symp. 162, Pulsation, Rotation, and Mass Loss in Early-Type Stars,* ed. L. A. Balona, H. F. Henrichs, & J. M. Le Contel (Dordrecht: Kluwer), 155.

Brandt, J. C. 1970, *Introduction to the Solar Wind* (San Francisco: W. H. Freeman).

Bretherton, F. P., & Garrett, C. J. R. 1968, *Proc. Roy. Soc.,* Ser. A, **302**, 529.

Brown, J. C. 1994, *Astrophys. Space Sci.*, **221**, 357.

Brown, J. C., McLean, I. S., & Emslie, A. G. 1978, *Astron. Astrophys.*, **68**, 415.

Bunn, J. C., & Drew, J. E. 1992, *Mon. Not. Roy. Astron. Soc.*, **255**, 449.

Burlaga, L. F. 1993, *Adv. Space Res.,* **13**, no. 6, 27.

Buta, R. J., & Smith, M. A. 1979, *Astrophys. J.*, **232**, 213.

Cannon, C. J., & Thomas, R. N. 1977, *Astrophys. J.*, **211**, 910.

Carlberg, R. G. 1980, *Astrophys. J.*, **241**, 1131.

Casse, M., & Paul, J. A. 1982, *Astrophys. J.*, **258**, 860.

Cassinelli, J. P. 1979, *Ann. Rev. Astron. Astrophys.*, **17**, 275.

Castor, J. I. 1970, *Mon. Not. Roy. Astron. Soc.*, **149**, 111.

Castor, J. I. 1974, *Mon. Not. Roy. Astron. Soc.*, **169**, 279.

Castor, J. I. 1986, *Publ. Astron. Soc. Pacific*, **98**, 52.

Castor, J. I. 1987, in *Instabilities in Luminous Early Type Stars,* ed. H. J. G. L. M. Lamers & C. W. H. de Loore (Dordrecht: Reidel), 159.

Castor, J. I., Abbott, D. C., & Klein, R. I. 1975, *Astrophys. J.*, **195**, 157 (CAK).

Castor, J. I., Abbott, D. C., & Klein, R. I. 1976, in *Physiques des Mouvements dans les Atmospheres Stellaires,* ed. R. Cayrel & M. Steinberg (Paris: CNRS), 363.

Castor, J. I., & Lamers, H. J. G. L. M. 1979, *Astrophys. J. Supp.*, **39**, 481.

Catala, C., Czarny, J., Felenbok, P., Talavera, A., & Thé, P. S. 1991, *Astron. Astrophys.*, **244**, 166.

Chamberlain, J. 1961, *Astrophys. J.*, **133**, 675.

Chandrasekhar, S. 1933, *Mon. Not. Roy. Astron. Soc.*, **93**, 462.

Chandrasekhar, S. 1946, *Astrophys. J.*, **103**, 351.

Chandrasekhar, S. 1964, *Astrophys. J.*, **139**, 644.

Chen, H., & Marlborough, J. M. 1994, *Astrophys. J.*, **427**, 1005.

Chiosi, C., & Maeder, A. 1986, *Ann. Rev. Astron. Astrophys.*, **24**, 329.

Clement, M. J. 1994, in *Pulsation, Rotation, and Mass Loss in Early-Type Stars*, ed. L. Balona, H. Henrichs, J. Le Contel (Dordrecht: Kluwer), 117.

Cohen, D. H., Cooper, R. G., MacFarlane, J. J., Owocki, S. P., Cassinelli, J. P., & Wang, P. 1996, *Astrophys. J.*, **460**, 506.

Collela, P., & Woodward, P. R. 1984, *J. Comput. Phys.,* **54**, 174.

Collins, II, G. W. 1963, *Astrophys. J.*, **138**, 1134.

Collins, II, G. W. 1988, *Mon. Not. Roy. Astron. Soc.*, **234**, 417.

Collins, II, G. W. 1989, *The Fundamentals of Stellar Astrophysics* (New York: Freeman).

Collins, II, G. W., & Cranmer, S. R. 1991, *Mon. Not. Roy. Astron. Soc.*, **253**, 167.

Collins, II, G. W., & Harrington, J. P. 1966, *Astrophys. J.*, **146**, 152.

Collins, II, G. W., & Truax, R. J. 1995, *Astrophys. J.*, **439**, 860.

Collins, II, G. W., Truax, R. J., & Cranmer, S. R. 1991, *Astrophys. J. Supp.*, **77**, 541.

Conti, P. S., & Underhill, A. B. 1988, eds., *O Stars and Wolf-Rayet Stars,* NASA Monograph SP-497 (Washington, DC: NASA Sci. & Tech. Inf. Division).

Cooper, R. G., & Owocki, S. P. 1994, *Astrophys. Space Sci.*, **221**, 427.

Cowling, T. G. 1941, *Mon. Not. Roy. Astron. Soc.*, **101**, 367.

Cox, J. P. 1980, *Theory of Stellar Pulsation* (Princeton: Princeton U. Press).

Coyne, G. V., & McLean, I. S. 1982, in *IAU Symp. 98, Be Stars,* ed. M. Jaschek & H. Groth (Dordrecht: Reidel), 77.

Cranmer, S. R. 1993, *Mon. Not. Roy. Astron. Soc.*, **263**, 989.

Cranmer, S. R., & Collins, II, G. W. 1993, *Astrophys. J.*, **412**, 720.

Cranmer, S. R., Massa, D., & Owocki, S. P. 1996, *Bull. Amer. Astron. Soc.*, **28**, 918 (59.07).

Cranmer, S. R., & Owocki, S. P. 1995, *Astrophys. J.*, **440**, 308.

Cranmer, S. R., & Owocki, S. P. 1996, *Astrophys. J.*, **462**, 469.

Crowley, E. A. 1904, "Liber AL Vel Legis, Sub Figura CCXX," in *The Holy Books of Thelema* (York Beach, Maine: Samuel Weiser, 1983), 107. (Chapter 1 quotation)

De Greve, J. P. 1986, *Space Sci. Rev.*, **43**, 139.

Denissenkov, P. 1994, in *IAU Symp. 162, Pulsation, Rotation, and Mass Loss in Early-Type Stars,* ed. L. A. Balona, H. F. Henrichs, & J. M. Le Contel (Dordrecht: Kluwer), 145.

Deutsch, A. J. 1956, *Astrophys. J.*, **123**, 210.

Dorland, H., & Montmerle, T. 1987, *Astron. Astrophys.*, **177**, 243.

Dowling, T. E., & Spiegel, E. A. 1990, *Annals NY Acad. Sci.,* **617**, 190.

Drew, J. E. 1989, *Astrophys. J. Supp.*, **71**, 267.

Dziembowski, W. 1971, *Acta Astron.,* **21**, 289.

Dziembowski, W. 1994, in *IAU Symp. 162, Pulsation, Rotation, and Mass Loss in Early-Type Stars,* ed. L. A. Balona, H. F. Henrichs, & J. M. Le Contel (Dordrecht: Kluwer), 55.

Ebbets, D. 1982, *Astrophys. J. Supp.*, **48**, 399.

Eddington, A. S. 1929, *Mon. Not. Roy. Astron. Soc.*, **90**, 54.

Eggleton, P. P., & Pringle, J. E. 1985, *Interacting Binaries* (Dordrecht: Reidel).

Eliot, T. S. 1930, "Ash Wednesday," in *The Complete Poems and Plays: 1909–1950,* (New York: Harcourt, Brace, & Company, 1952). (Chapter 4 quotation)

Feldmeier, A. 1995, *Astron. Astrophys.*, **299**, 523.

Friend, D. B., & Abbott, D. C. 1986, *Astrophys. J.*, **311**, 701.

Friend, D. B., & Castor, J. I. 1983, *Astrophys. J.*, **272**, 259.

Friend, D. B., & MacGregor, K. B. 1984, *Astrophys. J.*, **282**, 591.

Fullerton, A. W. 1990, Ph.D. Dissertation, University of Toronto.

Fullerton, A. W., Gies, D. R., & Bolton, C. T. 1996, *Astrophys. J. Supp.*, **103**, 475.

Fullerton, A. W., & Owocki, S. P. 1992, in *Nonisotropic and Variable Outflows from Stars,* ed. L. Drissen, C. Leitherer, & A. Nota (ASP Conf. Series 22), 177.

Garcia-Segura, G., Mac Low, M.-M., & Langer, N. 1996, *Astron. Astrophys.*, **305**, 229.

Gayley, K. G. 1995, *Astrophys. J.*, **454**, 410.

Gayley, K. G., & Owocki, S. P. 1994, *Astrophys. J.*, **434**, 684.

Gayley, K. G., & Owocki, S. P. 1995, *Astrophys. J.*, **446**, 801.

Gayley, K. G., Owocki, S. P., & Cranmer, S. R. 1995, *Astrophys. J.*, **442**, 296.

Gayley, K. G., Owocki, S. P., & Cranmer, S. R. 1996, *Bull. Amer. Astron. Soc.*, **28**, 922 (60.16).

Gerasimovič, B. P. 1934, *Mon. Not. Roy. Astron. Soc.*, **94**, 737.

Gouttebroze, P., & Toutain, T. 1994, *Astron. Astrophys.*, **287**, 535.

Grady, C. A., Bjorkman, K. S., & Snow, T. P. 1987, *Astrophys. J.*, **320**, 376.

Grinin, V. P. 1978, *Soviet Astron.-A.J.*, **14**, 301.

Grzędzielski, S. 1971, *Solar Phys.*, **21**, 225.

Hamann, W.-R. 1981, *Astron. Astrophys.*, **93**, 353.

Hansen, C. J., & Kawaler, S. D. 1994, *Stellar Interiors: Physical Principles, Structure, and Evolution* (New York: Springer-Verlag New York).

Harmanec, P. 1991, in *ESO Workshop on Rapid Variability of OB-Stars: Nature and Diagnostic Value,* ed. D. Baade (Garching: European Southern Obs.), 265.

Harries, T. J., & Howarth, I. D. 1996, *Astron. Astrophys.*, **310**, 533.

Hartmann, L., & MacGregor, K. B. 1980, *Astrophys. J.*, **242**, 260.

Haser, S. M., Lennon, D. J., Kudritzki, R.-P., Puls, J., Pauldrach, A. W. A., Bianchi, L., & Hutchings, J. B. 1995, *Astron. Astrophys.*, **295**, 136.

Henrichs, H. F. 1984, in *Fourth European IUE Conference,* ed. E. Rolfe & B. Battrick (ESA SP-218), 43.

Henrichs, H. F., Hammerschlag-Hensberge, G., Howarth, I. D., & Barr, P. 1983, *Astrophys. J.*, **268**, 807.

Henrichs, H. F., Kaper, L., & Nichols, J. S. 1994, *Astron. Astrophys.*, **285**, 565.

Henrichs, H. F., Kaper, L., Nichols, J. S., Bohlender, D., Cao, H., Gordon, K., Hill, G., Jiang, Y., Kolka, I., Neff, J., & Telting, J. H. 1995, in *IAU Symp. 176, Stellar Surface Structure,* ed. K. G. Strassmeier (Dordrecht: Kluwer), 229.

Henrichs, H. F., Kaper, L., & Zwarthoed, G. A. A. 1988, in *A Decade of UV Astronomy with IUE,* ed. ESA (ESA SP-281), **2**, 145.

Holt, J. R. 1893, *Astron. & Astro-Physics,* **12**, 646.

Holzer, T. E. 1977, *J. Geophys. Res.*, **82**, 23.

Holzer, T. E. 1989, *Ann. Rev. Astron. Astrophys.*, **27**, 199.

Howarth, I. D. 1992, in *Nonisotropic and Variable Outflows from Stars,* ed. L. Drissen, C. Leitherer, & A. Nota (ASP Conf. Series 22), 155.

Howarth, I. D., & Prinja, R. K. 1989, *Astrophys. J. Supp.*, **69**, 527.

Hummer, D. G. 1969, *Mon. Not. Roy. Astron. Soc.*, **145**, 95.

Hummer, D. G., & Rybicki, G. B. 1992, *Astrophys. J.*, **387**, 248.

Humphreys, R. M., & Davidson, K. 1994, *Publ. Astron. Soc. Pacific*, **106**, 1025.

Hundhausen, A. J. 1972, *Coronal Expansion and Solar Wind* (Berlin: Springer-Verlag).

Hundhausen, A. J. 1973, *J. Geophys. Res.*, **78**, 1528.

Ignace, R., Cassinelli, J. P., & Bjorkman, J. E. 1996, *Astrophys. J.*, **459**, 671.

Jacques, S. A. 1977, *Astrophys. J.*, **215**, 942.

Jacques, S. A. 1978, *Astrophys. J.*, **226**, 632.

Johnson, M. C. 1925, *Mon. Not. Roy. Astron. Soc.*, **85**, 813.

Johnson, M. C. 1926, *Mon. Not. Roy. Astron. Soc.*, **86**, 300.

Joyce, J. 1922, *Ulysses,* critical and synoptic edition, prep. by H. W. Gabler (New York: Garland Publishing, 1984), 7:999. (Chapter 2 quotation)

Jung, C. G. 1916, "Septem Sermones ad Mortuos," in *The Gnostic Jung,* ed. R. A. Segal (Princeton: Princeton U. Press, 1992), 193. (Chapter 8 quotation)

Kambe, E., Ando, H., & Hirata, R. 1993, *Astron. Astrophys.*, **273**, 435.

Kaper, L. 1993, Ph.D. Dissertation, University of Amsterdam.

Kaper, L., & Henrichs, H. F. 1994, *Astrophys. Space Sci.*, **221**, 115.

Kaper, L., Henrichs, H. F., Nichols, J. S., Snoek, L. C., Volten, H., & Zwarthoed, G. A. A. 1996, *Astron. Astrophys. Supp.*, **116**, 257.

Kemp, J. C., Henson, G. D., Barbour, M. S., Kraus, D. J., & Collins, G. W. 1983, *Astrophys. J. Letters*, **273**, L85.

Klein, R. I., & Castor, J. I. 1978, *Astrophys. J.*, **230**, 902.

Koninx, J. P. M. 1992, Ph.D. Dissertation, Rijksuniversiteit Utrecht.

Koninx, J. P. M., & Hearn, A. G. 1991, in *ESO Workshop on Rapid Variability of OB-Stars: Nature and Diagnostic Value,* ed. D. Baade (Garching: European Southern Obs.), 279.

Koninx, J.-P., & Hearn, A. G. 1992, *Astron. Astrophys.*, **263**, 208.

Kopp, R. A., & Holzer, T. E. 1976, *Solar Phys.*, **49**, 43.

Kudritzki, R.-P., & Hummer, D. G. 1990, *Ann. Rev. Astron. Astrophys.*, **28**, 303.

Kudritzki, R.-P., Hummer, D. G., Pauldrach, A. W. A., Puls, J., Najarro, F., & Imhoff, J. 1992, *Astron. Astrophys.*, **257**, 655.

Kudritzki, R. P., Pauldrach, A. W. A., & Puls, J. 1987, *Astron. Astrophys.*, **173**, 293.

Kudritzki, R.-P., Pauldrach, A. W. A., Puls, J., & Abbott, D. C. 1989, *Astron. Astrophys.*, **219**, 205.

Lamb, H. 1932, *Hydrodynamics* (New York: Dover Publications).

Lamers, H. J. G. L. M. 1994, *Astrophys. Space Sci.*, **221**, 41.

Lamers, H. J. G. L. M., Cerruti-Sola, M., & Perinotto, M. 1987, *Astrophys. J.*, **314**, 726.

Lamers, H. J. G. L. M., Gathier, R., & Snow, T. P. 1982, *Astrophys. J.*, **258**, 186.

Lamers, H. J. G. L. M., & Leitherer, C. 1993, *Astrophys. J.*, **412**, 771.

Lamers, H. J. G. L. M., & Pauldrach, A. W. A. 1991, *Astron. Astrophys.*, **244**, L5.

Landau, L. D., & Lifshitz, E. M. 1987, *Fluid Mechanics,* 2nd ed. (Pergamon: Oxford U. Press).

Langer, N., Hamann, W.-R., Lennon, M., Najarro, F., Pauldrach, A. W. A., & Puls, J. 1994, *Astron. Astrophys.*, **290**, 819.

Ledoux, P. 1951, *Astrophys. J.*, **114**, 373.

Ledoux, P., & Walraven, T. 1958, *Handbuch der Physik*, ed. S. Flügge (Berlin: Springer-Verlag), **51**, 353.

Lee, U., & Saio, H. 1990, *Astrophys. J.*, **349**, 570.

Leer, E., Holzer, T. E., & Flå, T. 1982, *Space Sci. Rev.*, **33**, 161.

Limber, D. N. 1964, *Astrophys. J.*, **140**, 1391.

Lucy, L. B. 1967, *Zeit. Astrophys.*, **65**, 89.

Lucy, L. B. 1982, *Astrophys. J.*, **255**, 278.

Lucy, L. B. 1983, *Astrophys. J.*, **274**, 372.

Lucy, L. B. 1984, *Astrophys. J.*, **284**, 351.

Lucy, L. B., & Abbott, D. C. 1993, *Astrophys. J.*, **405**, 738.

Lucy, L. B., & Solomon, P. 1970, *Astrophys. J.*, **159**, 879.

MacGregor, K. B. 1988, *Astrophys. J.*, **327**, 794.

MacGregor, K. B., & Charbonneau, P. 1994, *Astrophys. J.*, **430**, 387.

MacGregor, K. B., & Friend, D. B. 1984, *Bull. Amer. Astron. Soc.*, **16**, 406 (36.17).

MacGregor, K. B., Hartmann, L., & Raymond, J. C. 1979, *Astrophys. J.*, **231**, 514.

Mac Low, M.-M., Langer, N., Garcia-Segura, G. 1996, *Bull. Amer. Astron. Soc.*, **28**, 882 (38.06).

Maeder, A. 1981, *Astron. Astrophys.*, **101**, 385.

Marston, A. P. 1995, *Astron. J.*, **109**, 1839.

Massa, D., et al. (32 co-authors), 1995, *Astrophys. J. Letters*, **452**, L53.

Mathias, P., & Gillet, D. 1993, *Astron. Astrophys.*, **278**, 511.

Mazzali, P. A. 1990, in *Properties of Hot Luminous Stars,* ed. C. D. Garmany (San Francisco: Astron. Soc. Pacific), 300.

McCarthy, J. K., Lennon, D. J., Venn, K. A., Kudritzki, R.-P., Puls, J., & Najarro, F. 1995, *Astrophys. J. Letters*, **455**, L135.

Mihalas, B. W., & Toomre, J. 1981, *Astrophys. J.*, **249**, 349.

Mihalas, D. 1978, *Stellar Atmospheres,* 2nd ed. (San Francisco: W. H. Freeman).

Mihalas, D., Kunasz, P. B., & Hummer, D. G. 1975, *Astrophys. J.*, **202**, 465.

Mihalas, D., & Mihalas, B. W. 1984, *Foundations of Radiation Hydrodynamics* (Oxford: Oxford U. Press).

Miller, W. W., & Cox, D. P. 1993, *Astrophys. J.*, **417**, 579.

Milne, E. A. 1924, *Mon. Not. Roy. Astron. Soc.*, **84**, 354.

Milne, E. A. 1926, *Mon. Not. Roy. Astron. Soc.*, **86**, 459.

Moffat, A. F. J., Owocki, S. P., Fullerton, A. W., & St-Louis, N. 1994, eds., *Instability and Variability of Hot-Star Winds* (Dordrecht: Kluwer), repr. in *Astrophys. Space Sci.*, **221**.

Morton, D. C. 1967a, *Astrophys. J.*, **147**, 1017.

Morton, D. C. 1967b, *Astrophys. J.*, **150**, 535.

Morton, D. C., Jenkins, E. B., & Brooks, N. 1969, *Astrophys. J.*, **155**, 875.

Moss, D., & Smith, R. C. 1981, *Rep. Prog. Phys.,* **44**, 832.

Mullan, D. J. 1984a, *Astrophys. J.*, **283**, 303.

Mullan, D. J. 1984b, *Astrophys. J.*, **284**, 769.

Mullan, D. J. 1986, *Astron. Astrophys.*, **165**, 157.

Ness, N. F. 1987, in *Essays in Space Science,* eds. R. Ramaty, T. Cline, & J. Ormes, NASA Pub. N87-24247 (Greenbelt, MD: NASA Goddard Sp. Fl. Center).

Okazaki, A. T. 1991, *Publ. Astron. Soc. Japan*, **43**, 75.

Olson, G. L. 1982, *Astrophys. J.*, **255**, 267.

Orlov, A. A. 1961, *Soviet Astron.-A.J.*, **4**, 845.

Osaki, Y. 1970, *Mon. Not. Roy. Astron. Soc.*, **148**, 391.

Osaki, Y. 1986, *Publ. Astron. Soc. Pacific*, **98**, 30.

Owocki, S. P. 1991, in *Stellar Atmospheres: Beyond Classical Models,* eds. L. Crivellari, I. Hubeny, & D. G. Hummer, (Dordrecht: Kluwer), 235.

Owocki, S. P. 1992, in *The Atmospheres of Early-Type Stars,* ed. U. Heber & S. Jeffrey (Berlin: Springer), 393.

Owocki, S. P. 1994, in *IAU Symp. 162, Pulsation, Rotation, and Mass Loss in Early-Type Stars,* ed. L. A. Balona, H. F. Henrichs, & J. M. Le Contel (Dordrecht: Kluwer), 475.

Owocki, S. P., Castor, J. I., & Rybicki, G. B. 1988, *Astrophys. J.*, **335**, 914 (OCR).

Owocki, S. P., Cranmer, S. R., & Blondin, J. M. 1994, *Astrophys. J.*, **424**, 887.

Owocki, S. P., Cranmer, S. R., & Fullerton, A. W. 1995, *Astrophys. J. Letters*, **453**, L37.

Owocki, S. P., Fullerton, A. W., & Puls, J. 1994, *Astrophys. Space Sci.*, **221**, 437.

Owocki, S. P., Gayley, K. G., & Cranmer, S. R. 1996, *Bull. Amer. Astron. Soc.*, **28**, 881 (38.01).

Owocki, S. P., & Puls, J. 1996, *Astrophys. J.*, **462**, 894.

Owocki, S. P., & Rybicki, G. B. 1984, *Astrophys. J.*, **284**, 337 (OR-I).

Owocki, S. P., & Rybicki, G. B. 1985, *Astrophys. J.*, **299**, 265 (OR-II).

Owocki, S. P., & Rybicki, G. B. 1986, *Astrophys. J.*, **309**, 127 (OR-III).

Owocki, S. P., & Zank, G. P. 1991, *Astrophys. J.*, **368**, 491.

Papaloizou, J., & Pringle, J. E. 1978, *Mon. Not. Roy. Astron. Soc.*, **182**, 423.

Papaloizou, J. C. B., & Whelan, J. A. J. 1973, *Mon. Not. Roy. Astron. Soc.*, **164**, 1.

Parker, E. N. 1958, *Astrophys. J.*, **128**, 664.

Parker, E. N. 1963, *Interplanetary Dynamical Processes* (New York: Interscience Publishers).

Parker, E. N. 1966, *Astrophys. J.*, **143**, 32.

Pauldrach, A. W. A. 1987, *Astron. Astrophys.*, **183**, 295.

Pauldrach, A. W. A., & Herrero, A. 1988, *Astron. Astrophys.*, **199**, 262.

Pauldrach, A. W. A., Kudritzki, R. P., Puls, J., & Butler, K. 1990, *Astron. Astrophys.*, **228**, 125.

Pauldrach, A. W. A., Puls, J., & Kudritzki, R.-P. 1986, *Astron. Astrophys.*, **164**, 86 (PPK).

Peart, N. 1980, "Natural Science," on album *Permanent Waves,* by the musical group *Rush,* produced by Rush and Terry Brown, Mercury/PolyGram Records, 822-548-2 M-1. (Chapter 7 quotation)

Pekeris, C. L. 1938, *Astrophys. J.*, **88**, 189.

Petrenz, P., & Puls, J. 1996, *Astron. Astrophys.*, in press.

Pizzo, V. J. 1982, *J. Geophys. Res.*, **87**, 4374.

Pneuman, G. W., & Kopp, R. A. 1971, *Solar Phys.*, **18**, 258.

Poe, C. H. 1987, Ph.D. Dissertation, University of Wisconsin.

Poe, C. H., & Friend, D. B. 1986, *Astrophys. J.*, **311**, 317.

Poe, C. H., Owocki, S. P., & Castor, J. I. 1990, *Astrophys. J.*, **358**, 199.

Poeckert, R., & Marlborough, J. M. 1976, *Astrophys. J.*, **206**, 182.

Press, W. H., Flannery, B. P., Teukolsky, S. A., & Vetterling, W. T. 1989, *Numerical Recipes: The Art of Scientific Computing* (Cambridge: Cambridge U. Press).

Prinja, R. K. 1988, *Mon. Not. Roy. Astron. Soc.*, **231**, 21p.

Prinja, R. K. 1994, in *IAU Symp. 162, Pulsation, Rotation, and Mass Loss in Early-Type Stars,* ed. L. A. Balona, H. F. Henrichs, & J. M. Le Contel (Dordrecht: Kluwer), 507.

Prinja, R. K., Balona, L. A., Bolton, C. T., Crowe, R. A., Fieldus, M. S., Fullerton, A. W., Gies, D. R., Howarth, I. D., McDavid, D., Reid, A. H. N. 1992, *Astrophys. J.*, **390**, 266.

Prinja, R. K., Barlow, M. J., & Howarth, I. D. 1990, *Astrophys. J.*, **361**, 607.

Prinja, R. K., & Howarth, I. D. 1988, *Mon. Not. Roy. Astron. Soc.*, **233**, 123.

Prinja, R. K., Massa, D., Fullerton, A. W., Howarth, I. D., & Pontrefract, M. 1996, *Astron. Astrophys.*, in press.

Puls, J. 1987, *Astron. Astrophys.*, **184**, 227.

Puls, J., Kudritzki, R.-P., Herrero, A., Pauldrach, A. W. A., Haser, S. M., Lennon, D. J., Gabler, R., Voels, S. A., Vilchez, J. M., Wachter, S., & Feldmeier, A. 1996, *Astron. Astrophys.*, **305**, 171.

Puls, J., Owocki, S. P., & Fullerton, A. W. 1993, *Astron. Astrophys.*, **279**, 457 (POF).

Robert, C. 1994, *Astrophys. Space Sci.*, **221**, 137.

Rossiter, R. A. 1924, *Astrophys. J.*, **60**, 15.

Rucinski, S. M. 1970, *Acta Astron.,* **20**, 1.

Rybicki, G. B. 1987, in *Instabilities in Luminous Early Type Stars,* ed. H. J. G. L. M. Lamers & C. W. H. de Loore (Dordrecht: Reidel), 175.

Rybicki, G. B., & Hummer, D. G. 1978, *Astrophys. J.*, **219**, 654.

Rybicki, G. B., & Lightman, A. P. 1979, *Radiative Processes in Astrophysics* (New York: John Wiley and Sons).

Rybicki, G. B., Owocki, S. P., & Castor, J. I. 1990, *Astrophys. J.*, **349**, 274.

Saio, H. 1994, in *IAU Symp. 162, Pulsation, Rotation, and Mass Loss in Early-Type Stars,* ed. L. A. Balona, H. F. Henrichs, & J. M. Le Contel (Dordrecht: Kluwer), 287.

Schlesinger, F. 1909, *Publ. Allegheny Obs.,* **1**, 134.

Schlesinger, F. 1910, *Publ. Allegheny Obs.,* **3**, 28.

Schmidt, G. D. 1988, in *Polarized Radiation of Circumstellar Origin,* ed. G. Coyne, S. Magalhen, A. Moffat, R. Schulte-Ladbeck, S. Tapia, & D. Wickramasinghe (Tucson: U. of Arizona Press), 641.

Shajn, G. A., & Struve, O. 1929, *Mon. Not. Roy. Astron. Soc.*, **89**, 222.

Shimada, M. R., Ito, M., Hirata, R., & Horaguchi, T. 1994, in *IAU Symp. 162, Pulsation, Rotation, and Mass Loss in Early-Type Stars,* ed. L. A. Balona, H. F. Henrichs, & J. M. Le Contel (Dordrecht: Kluwer), 487.

Shklovskij, I. S. 1956, *Astron. Zh.,* **33**, 315.

Slettebak, A. 1949, *Astrophys. J.*, **110**, 498.

Slettebak, A., & Snow, T. P., eds., *Physics of Be Stars,* IAU Colloquium 92 (Cambridge: Cambridge U. Press).

Smeyers, P. 1984, in *Theoretical Problems in Stellar Stability and Oscillations,* proc. of 25th Liège International Astrophysical Colloquium (Liège: Universite de Liège), 68.

Smith, R. C. 1987, in *Physics of Be Stars,* ed. A. Slettebak & T. P. Snow (Cambridge: Cambridge U. Press), 123.

Snow, T. P. 1977, *Astrophys. J.*, **217**, 760.

Snow, T. P. 1981, *Astrophys. J.*, **251**, 139.

Sobolev, V. V. 1957, *Soviet Astron.-A.J.*, **1**, 678.

Sobolev, V. V. 1960, *Moving Envelopes of Stars* (Cambridge: Harvard U. Press).

Springmann, U. 1994, *Astron. Astrophys.*, **289**, 505.

Springmann, U., & Pauldrach, A. W. A. 1992, *Astron. Astrophys.*, **262**, 515.

Stamford, P. A., & Watson, R. D. 1981, *Astrophys. Space Sci.*, **77**, 131.

St-Louis, N., Dalton, M. J., Marchenko, S. V., Moffat, A. F. J., & Willis, A. J. 1995, *Astrophys. J. Letters*, **452**, L57.

Štefl, S., Baade, D., Harmanec, P., & Balona, L. A. 1995, *Astron. Astrophys.*, **294**, 135.

Stewart, G. C., & Fabian, A. C. 1981, *Mon. Not. Roy. Astron. Soc.*, **197**, 713.

Stokes, G. G. 1852, *Trans. Cam. Phil. Soc.,* **9**, 399.

Story, T. R. 1996, Ph.D. Dissertation, University of Delaware.

Struve, O. 1930, *Astrophys. J.*, **72**, 1.

Struve, O. 1931, *Astrophys. J.*, **73**, 94.

Sweet, P. A. 1950, *Mon. Not. Roy. Astron. Soc.*, **110**, 548.

Swings, P., & Struve, O. 1940, *Astrophys. J.*, **91**, 546.

Tassoul, J.-L. 1978, *Theory of Rotating Stars* (Princeton, NJ: Princeton U. Press).

Telting, J. H., & Kaper, L. 1994, *Astron. Astrophys.*, **284**, 515.

Tempchin, J., & Strandlund, R. 1974, "Already Gone," on album *On the Border,* by the musical group *The Eagles,* produced by Bill Szymczyk, Asylum Records, 1004. (Chapter 3 quotation)

Townsend, R. H. D. 1996, *Mon. Not. Roy. Astron. Soc.*, submitted.

Underhill, A. B., & Doazan, V. 1982, eds., *B Stars with and without Emission Lines,* NASA Monograph SP-456 (Washington, DC: NASA Sci. & Tech. Inf. Division).

Underhill, A. B., & Fahey, R. P. 1984, *Astrophys. J.*, **280**, 712.

Unno, W., Osaki, Y., Ando, H., & Shibahashi, H. 1979, *Nonradial Oscillations of Stars* (Tokyo: University of Tokyo Press).

Velli, M. 1993, *Astron. Astrophys.*, **270**, 304.

Villata, M. 1992, *Astron. Astrophys.*, **257**, 677.

von Zeipel, H. 1924, *Mon. Not. Roy. Astron. Soc.*, **84**, 665.

Waldron, W. L., Klein, L., & Altner, B. 1994, *Astrophys. J.*, **426**, 725.

Wang, Z., Ulrich, R. K., & Coroniti, F. V. 1995, *Astrophys. J.*, **444**, 879.

Waters, L. B. F. M. 1986, *Astron. Astrophys.*, **159**, L1.

Waters, L. B. F. M., Coté, J., & Lamers, H. J. G. L. M. 1987, *Astron. Astrophys.*, **185**, 206.

Waters, L. B. F. M., Taylor, A. R., van den Heuvel, E. P. J., Habets, G. M. H. J., & Persi, P. 1988, *Astron. Astrophys.*, **198**, 200.

Weaver, R., McCray, R., Castor, J. I., Shapiro, P., & Moore, R. 1977, *Astrophys. J.*, **218**, 377.

Whitman, W. 1874, "Song of the Universal," in *Leaves of Grass* (New York: Vintage Books, 1992). (Chapter 6 quotation)

Willis, A. J. 1991, in *IAU Symposium 143, Wolf-Rayet Stars and Interrelations with Other Massive Stars in Galaxies,* ed. K. A. van der Hucht & B. Hidayat (Dordrecht: Kluwer), 265.

Willson, L. A. 1986, *Publ. Astron. Soc. Pacific*, **98**, 37.

Wood, K., Bjorkman, J. E., Whitney, B., & Code, A. 1996, *Astrophys. J.*, **461**, 847.

Wood, K., Brown, J. C., & Fox, G. K. 1993, *Astron. Astrophys.*, **271**, 492.

York, D. G., Vidal-Madjar, A., Laurent, C., & Bonnet, R. 1977, *Astrophys. J. Letters*, **213**, L61.

Yorke, H. W. 1986, *Ann. Rev. Astron. Astrophys.*, **24**, 49.

Zellner, B., & Serkowski, K. 1972, *Publ. Astron. Soc. Pacific*, **84**, 619.

Zhou, D.-Q., & Leung, K.-C. 1990, *Astrophys. J.*, **355**, 271.

Zirker, J. B. 1977, ed., *Coronal Holes and High Speed Wind Streams* (Boulder: Colorado Associated U. Press).